UNIVERSITY COLLEGE LONDON

Development of a Novel Multiwavelength, Time Resolved, Near Infrared Spectrometer

Luke Timothy Dunne

A thesis submitted in partial fulfillment for the
degree of Doctor of Philosophy

in the
Multimodal Spectroscopy Group
Department of Medical Physics and Biomedical Engineering

November 2016

Declaration of Authorship

I, Luke Timothy Dunne, confirm that the work presented in this thesis is my own. Where information has been derived from other sources, I confirm that this has been indicated in the thesis.

Signed:

Date:

Abstract

During this PhD I have designed, built, and tested a multiwavelength, multi-channel, time resolved, near infrared optical spectrometer. The system uses a supercontinuum laser which is coupled to two acousto-optic tuneable filters (AOTFs) to produce very short pulses (∼4ps) with a narrow spectral bandwidth of 2 - 4 nm in the near infrared region (690 - 900 nm). This narrow band of light is vital in order to accurately resolve chromophore concentrations. The output light from the AOTFs is coupled to biological tissue using two single mode fibre optics. Light escaping the tissue is then collected using up to four fibre bundles, which guide the photons to the system's detectors via custom-designed connectors. Custom built variable optical attenuators are used to control the amount of light that enters the photomultiplier tubes (PMTs) to prevent over exposure. The PMTs convert the optical signal into an electrical pulse, which is fed through a router to a time correlated single photon counting card (TCSPC). The TCSPC card measures the times of flight of the photons in tissue, which can be used to build up a temporal point spread function (TPSF). This is done at multiple wavelengths using precise timing electronics, with a resolution of 6 ps. This measurement directly allows the mean time of flight to be obtained, and the coefficients of absorption and scattering to be resolved. The novel elements of the system include that it can measure the absorption and scattering of up to 16 wavelengths simultaneously with a total collection time as low as 1 second. The wavelengths are also completely selectable and any combination of 16 in the near infrared region can be used in a single measurement. The system also has custom AOTF crystals that uniquely provide narrowband light.

In this thesis I detail the design, development and characterisation of novel hardware and software. The system is then tested and calibrated on tissue-like phantoms to verify

performance, before performing several in vivo measurements on the arm and head, including a cuff occlusion and a preliminary visual cortex study.

Acknowledgements

First of all, I would like to thank my supervisors, Ilias Tachtsidis and Jem Hebden for their continued support, encouragement and guidance throughout my PhD. I am incredibly grateful to them for giving me the opportunity to work on this project.

I would also like to thank Salavat Magazov and Marta Varela for their invaluable help and advice at the beginning of my PhD.

I am grateful to work with many friends and colleagues in Medical Physics and Biomedical Engineering at UCL who have supported me throughout my time in the department. In particular I would like to thank Nick Everdell and Sam Powell for their encouragement and advice during my PhD. I am also honored to have worked alongside Gemma Balé who has supplied the tea, bad jokes and dog photos that have made this PhD possible.

I would like to especially thank Teedah Saratoon for all her incredible support and encouragement over the last few years.

Finally, this PhD would not have been possible without the constant support of my parents and family throughout all of my university studies.

Contents

List of Figures

List of Tables

Abbreviations

ADC	Analogue-to-digital converter
AOTF	Acousto-optic tunable filter
ATP	Adenosine triphosphate
CCO	Cytochrome c oxidase
CFD	Constant fraction discriminator
CSF	Cerebrospinal fluid
CW	Continuous wave
DPF	Differential pathlength
ETC	Electron transport chain
FD	Frequency domain
HHb	Deoxyhaemoglobin
HbO_2	Oxyhaemoglobin
ICCD	Intensified charged coupled device
IRF	Instrument response function
LED	Light emitting diode
NA	Numerical aperture
NIRS	Near infrared spectroscopy
MCP	Multichannel plate
OD	Optical density
PMT	Photomultiplier tubes
SER	Single electron response
SPAD	Single photon avalanche diode
TAC	Time-to-analogue converter
TCSPC	Time correlated single photon counting

TD Time domain

TPSF Temporal point spread function

List of Symbols

Symbol	Name	Unit
λ	Optical wavelength	nm
μ_{a}	Optical absorption coefficient	mm^{-1}
μ_{s}	Optical scattering coefficient	mm^{-1}
μ_{s}'	Reduced optical scattering coefficient	mm^{-1}
μ_{eff}	Effective attenuation coefficient	mm^{-1}
D	Diffusion coefficient	mm
σ_{a}	Absorption cross-section	mm^{-2}
σ_{s}	Scattering cross-section	mm^{-2}
g	Anisotropy factor	
Θ	Scattering phase function	
Φ	Optical fluence	$\mathrm{J\ mm}^{-2}$
ϕ	Optical radiance	$\mathrm{J\ mm}^{-2}\ \mathrm{sr}^{-1}$
c_{vacuum}	Speed of light in a vacuum	$= 299\ 792\ 458\ \mathrm{ms}^{-1}$

Chapter 1

Introduction

This chapter discusses the motivation and aims of the project, detailing some of the key aspects of the work. An introduction to near infrared spectroscopy and its application to optical motoring of the brain is also given. This project sees the design, development, and testing of a novel multiwavelength time-resolved near infrared spectrometer based on a supercontinuum laser source.

This work was carried out in the Multimodal Spectroscopy Group at the Biomedical Optics Research Laboratory, UCL. It was funded by the the Wellcome Trust, an independent global charitable biomedical foundation dedicated to improving health through science, research and engagement with society.

The Multimodal Spectroscopy Group aims to develop novel physiological monitoring systems and modalities, focusing on combining near infrared spectroscopy with magnetic resonance imaging and spectroscopy. A key area of research for the group is the monitoring of tissue oxygenation and cellular metabolism in the brain. These techniques are used for monitoring the brain function and health of neonates and brain injury patients to improve understanding of biological mechanisms in order to improve diagnosis and patient care.

1.1 Motivation and aims

Over the last few decades near infrared spectroscopy has become an important tool for the non-invasive monitoring of haemodynamics and oxygenation of the brain. While near infrared spectroscopy is mostly used for research purposes, a major aim of patient care and diagnosis is the ability to monitor the brain at the bedside. Near infrared spectroscopy offers the ability to assess the recovery and health of brain tissue from patients with a wide range of health concerns, without affecting other treatments and patient care. The systems are relatively inexpensive and portable, making them suitable for a broad range of measurements.

In the Biomedical Optics Research Laboratory (BORL) at UCL, the understanding of injury and recovery in preterm infants suffering from hypoxic-ischaemia is a major research goal. Hypoxic-ischemia is caused by a lack or reduction of the oxygen to the brain during birth, which can result in severe disability or death of the infant.

Near infrared spectroscopy is a valuable tool to monitor the recovery of the brain after an injury to determine how the haemodynamics and metabolism change over this period, both naturally and due to clinical interventions. The non-invasive nature of near infrared spectroscopy means that the concentrations of chromophores cannot be measured directly. In order to calculate the concentrations of molecules in tissue, data types or a combination of data types such as attenuation, temporal spread point functions, mean time of flight, or variance must be extracted from measurements of the light escaping tissue in order for a solution to be found. Therefore, accurate monitoring of these biological changes relies on a good understanding of tissue optics.

The most common technique for measuring these changes in clinical settings is continuous wave near infrared spectroscopy. This technique is well suited for measurements in clinical environments, as the instrumentation itself can be relative simple, benefiting from compact designs and ease of use. The limitations of the data collected from these

devices, however, means that several assumptions have to be made in order to calculate changes of chromophore concentrations. Most significantly, these measurements have to assume that the scattering of light remains constant throughout the duration of a measurement. While this assumption will be adequate for many studies, this condition may not hold true for severe brain injury patients, and as such might introduce errors into the measurement.

By measuring the times-of-flight of photons as they travel through tissue, time resolved near infrared spectroscopy allows the absorption of light to be separated from the scattering, so that the absorption and scattering coefficients of tissue can be resolved individually. The main aim of this project is to develop a novel multiwavelength, time resolved near infrared spectrometer to provide a 'gold standard' of near infrared measurements. The ability to accurately measure the times-of-flight of photons means that significantly more information about the propagation of light in tissue can be determined, providing greater accuracy in determining the biological condition of the brain.

As continuous wave instruments only measure the attenuation of light, only the relative changes in chromophore concentrations can be calculated. Time resolved measurements, however, can resolve the absorption coefficient of light, from which absolute concentrations of oxyhaemoglobin and deoxyhaemoglobin in tissue can be obtained. While time domain spectroscopy has been used in research for several decades, the majority of research studies have used a limited number of wavelengths for measuring concentration changes of oxyhaemoglobin and deoxyhaemoglin.

The redox state of cytochrome c oxidase can be used as a biomarker for the rate of cellular metabolism in tissue. Measurement of this chromophore is significantly more difficult than that of haemoglobin, as the overall concentration in tissue is an order of magnitude less. Investigations show that in order to accurately measure the redox dependence of cytochrome c oxidase with little error, more than eight wavelengths in the near infrared region are required [3]. The objective of this project is to develop a

system with the ability to simultaneously measure the absorption and scattering of light at multiple wavelengths, in order to determine sufficiently accurate redox state changes of cytochrome c oxidase.

1.2 Instrumentation requirements

To produce time resolved measurements of absorption and scattering at multiple wavelengths, the main requirements of the system developed in this research are as follows:

- The system must be able to resolve the absorption and scattering of light within tissue.
- The wavelengths used in the measurements should be adjustable within the near infrared region, and the bandwidth of the light should be less than 5 nm to provide sufficient accuracy when calculating chromophore concentrations. As the peaks in the absorption spectrum can be relatively narrow, a smaller bandwidth of light than 5 nm will enable accurate measurement of any change in absorption of these peaks.
- The system must be portable to allow movement around a clinical unit, and optics and electronics must not be affected by this movement.
- To resolve cytochrome c oxidase, the system must be able to simultaneously measure the times-of-flight of photons at more than eight wavelengths.
- The system should have four detector channels and two independent light sources in order to allow simultaneous measurements of different areas of the brain.
- The light must be delivered to the patient via optical fibres and held firmly in place with an optode holding system.

1.3 Near infrared spectroscopy

The application of near infrared spectroscopy (NIRS) to physiological monitoring was demonstrated in 1977 by Jobsis et al. at Duke University by measuring the attenuation spectrum of light across the brain in order to determine the oxygenation of blood [4]. Visible and ultraviolet light are highly attenuated by tissue due to high levels of absorption by haemoglobin and water. Light at these wavelengths does not penetrate the skull and brain tissue adequately for spectroscopic measurements, however, near infrared light between 700 and 1000 nm can penetrate deep into tissue, making it suitable for in-vivo measurements. The absorption spectra of substances in tissue that contribute to the attenuation of light in the near infrared region are well defined. By comparing the absorption of light at different wavelengths to the known absorption spectra of chromophores in tissue, the concentrations of oxy- and deoxyhaemoglobin, and hence the oxygen saturation of blood can be calculated.

Light absorbing compounds in the near infrared region include water (H_2O), lipids, melanin, oxyhaemoglobin (HbO_2), deoxyhaemoglobin (HHb) and cytochrome c oxidase. The concentrations of water, lipid and melanin are generally thought to remain constant throughout the course of a measurement, resulting in a constant absorption spectrum. The concentrations of oxyhaemoglobin, deoxyhaemoglobin and the redox state of cytochrome c oxidase will change in response to the energy requirements of the tissue. By measuring the absorption of light in tissue and resolving the concentrations of these molecules, insight into the oxygenation and cellular metabolism of tissue can be obtained.

Near infrared spectroscopy measures the concentration changes of oxyhaemoglobin and deoxyhaemoglobin in order to monitor the haemodynamics in tissue. It can also monitor the metabolism on a cellular level by observing the behaviour of cytochrome c oxidase, the terminal electron acceptor enzyme in the electron transport chain (ETC). The ETC

synthesises adenosine triphosphate (ATP) through a series of redox reactions, transferring electrons from electron donors to electron acceptors. Therefore the redox state of cytochrome c oxidase gives insight into the availability of cellular oxygen. As the oxidised and reduced forms of cytochrome c oxidase have different absorption spectra, changes to its rate of optical absorption can indicate increased or reduced cellular metabolism.

The first clinical studies using NIRS were performed in 1985 by Brazy et al. and Ferrari et al. [5, 6], where bedside NIRS monitoring was used to measure changes in cerebral oxygenation and cellular metabolism in preterm infants and brain-injured patients. These initial studies, made at the bedside, measured relative changes in the concentrations of HbO_2, HHb and redox state of cytochrome c oxidase in arbitrary units. The modified Beer-Lambert law allowed quantitative concentration changes by estimating the pathlength of light in tissue [7].

The non-invasive nature, low cost and portability means that the application of NIRS to bedside clinical studies and haemodynamic monitoring has increased dramatically in the last few decades, with the number of papers published over the last few year growing almost exponentially. One of the main uses of NIRS technology in a clinical setting is the cerebral haemodynamics monitoring of premature infants, stroke and head injury patients in intensive care. NIRS is also used for study into brain and muscle function [8], including functional activation studies [9], sports science monitoring of muscle oxygenation during exercise [10], and cognitive development studies [11].

The two main mechanisms that act on light as it propagates through a diffuse media are absorption and scattering, with the latter the dominant cause of attenuation. The combination of absorption and scattering means that in tissue, the intensity of light will approximately decrease by an order of magnitude every 10 mm it travels [12]. This high level of scattering means that the penetration depth, and therefore imaging depth of NIRS, is limited, and the diffusion of light means that high resolution images, such

as those acquired with magnetic resonance imaging cannot be achieved using a solely optical imaging modality.

The large majority of NIRS measurements are made using continuous wave (CW) systems (Chapter 3.1.1). This method uses measurements of attenuation changes in tissue to calculate changes in the concentration of chromophores [13]. This method is popular, since it is relatively straightforward to observe quantitative changes in haemodynamics, however, the technique requires several assumptions, such as the assumption that the differential pathlength of light in tissue and the scattering coefficient is constant throughout the duration of the measurement. To address these issues, time resolved NIRS can be used to resolve the absolute absorption and scattering of tissue by measuring the times-of-flight of individual photons. In addition to continuous wave and time resolved techniques, frequency domain NIRS can also be used to resolve absorption and scattering. However, due to the superior depth resolution achievable by time resolved spectroscopy, the frequency domain technique is not used in this work.

1.3.1 Time resolved near infrared spectroscopy

Whereas continuous wave NIRS measures the intensity of light, time resolved NIRS measures the times-of-flight of individual photons in the tissue. Comparing the data to theoretical models of light propagation in tissue allows the absorption and scattering of light to be separated and individually resolved. This technique also provides information about the depth resolution of the change in absorption, as the late-arriving photons which have travelled through deeper tissue can be isolated.

1.4 Thesis outline

In this thesis I have aimed to provide a detailed background on the physiological and technical aspects of near infrared spectroscopy. As the major aim of this project involved developing a novel, multiwavelength, time resolved spectrometer, the majority of this thesis discusses the system design, with later chapters evaluating the characterisation and performance of the instrument using phantoms and in vivo studies.

Chapter 2 contains an introduction to the anatomy and physiology of the human head, focusing on aspects that impact near infrared spectroscopy measurements. I include an overview of the properties of blood and the mechanisms of cellular metabolism. Finally, the basis of light propagation through tissue is described, and the mathematics behind the absorption and scattering of light in a scattering medium are explained.

Chapter 3 introduces the history of near infrared spectroscopy before discussing particular modalities which have used the technique. The current state of the art time resolved systems developed by other research groups and collaborative groups are discussed, before moving on to describe the most commonly used instrumentation in time resolved spectroscopy.

Chapter 4 discusses the major contribution of this work: the design and development of a novel, multiwavelength, near infrared time resolved spectrometer. The instrumentation chosen for the system are described in detail, and individual components are characterised. The design choices of the technical aspects are described and improvements are evaluated and documented. Finally, the development of software written for the control of the system is explained.

Chapter 5 explains how the data from a time resolved measurement can be used to resolve the absorption and scattering of tissue, and how these influence the times-of-flight of photons. A study into the possible techniques for improving the depth resolution

from time resolved measurements and validation of the best gating methods for achieving deeper sensitivity in tissue is included in this chapter.

Whereas Chapter 4 characterised each component of the system individually, Chapter 6 aims to characterise the system as a whole. The stability and accuracy of measurements is documented, and phantom studies show the ability of the system to resolve absorption and scattering in tissue.

Finally, in Chapter 7, the system is used to perform in vivo studies on the arm and forehead of several volunteers. A cuff occlusion measurement is performed and preliminary visual cortex measurements are described.

Chapter 2

Fundamentals of tissue optics

This chapter gives an overview to parts of the anatomy and physiology of the human body and head which are involved in near infrared spectroscopy. The structure of the integumentary system and the human head are discussed before cell metabolism and the mechanics of the electron transport chain are briefly explained. The chapter then discusses the basis for near infrared spectroscopy with background on the absorption and scattering of light in scattering media leading to the derivation of the Beer-Lambert law.

2.1 Anatomy

As with all diffuse optical measurements of the head, the entire anatomy, from the surface through to the brain, needs to be considered. While the aim is to measure biological changes occurring in the brain tissue, near infrared measurements are affected considerably by minor changes at the surface which can produce major changes to the optical signal. There are four main biological structures to consider for the human head that affect the optical absorption and scattering measured using near infrared

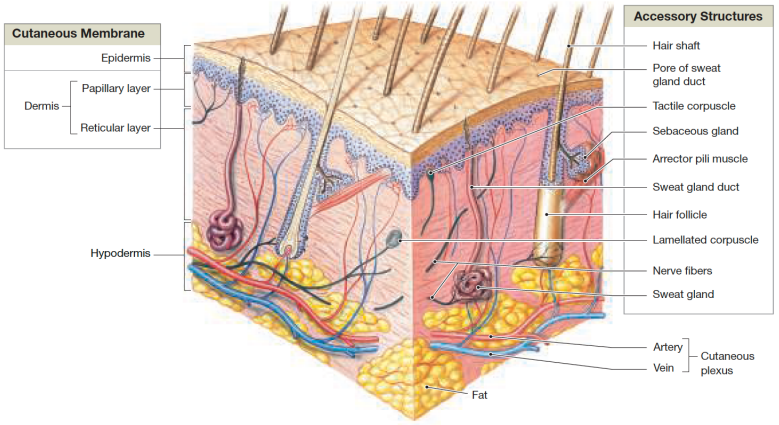

FIGURE 2.1: Diagram of the skin showing the structure of the top layers including the epidermis and dermis and the accessory structure of hair follicle, nerve fibres and sweat glands [14].

spectroscopy. This chapter contains a brief description of the skin, skull, meninges, and brain tissue.

2.1.1 Skin

The integumentary system is the organ responsible for providing protection for the internal organs and is formed of the skin, hair follicles, and nails. The top layer of the skin, the epidermis, consists of epithelial cells providing protection and homeostasis (regulation of a body's internal environment, i.e. temperature). Below these cells is the squamous epithelium, consisting of mainly keratinocytes, which produce keratin, a waterproofing and protective protein. Other common cells in this layer are melanin and merkel cells. This layer also provides a blood supply to the epithelial cells which contain no blood vessels. The dermis, situated below the epidermis, comprises of a dense connective tissue which forms the stretchy layer of the skin. The structure of the skin layers and accessory structures can be seen in Figure 2.1.

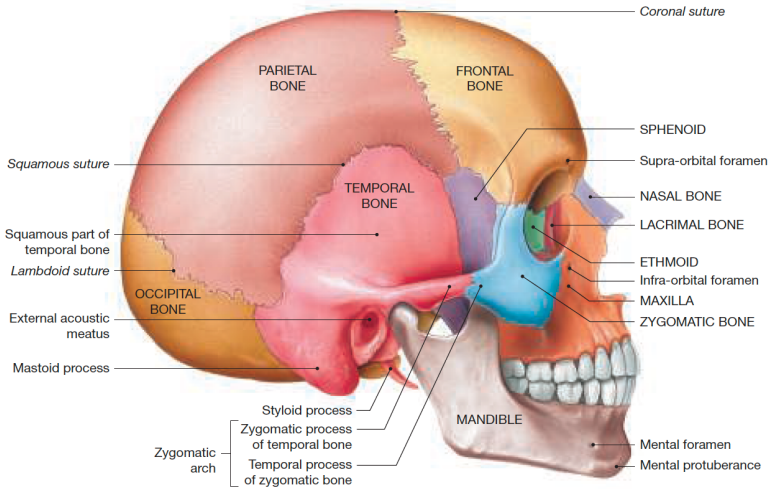

FIGURE 2.2: Laterial view of the adult skull showing the structure of the cranial and facial bones [14].

2.1.2 Skull

The skull can be classified into two separate parts: the neurocranium and the viscerocranium, the former comprising bones protecting the brain and the latter supporting the face. The cranium comprises of 8 bones, and 14 bones form the facial bones. The cranium consists of the occipital, parietal, frontal, temporal, sphenoid, and ethmoid bones as can be seen in Figure 2.2. These support and enclose the brain and cranial cavity which contains the cerebrospinal fluid. Of these bones, the two parietal and two frontal bones form the large top four sections. There are two types of bone in the body: the dense and smooth compact bone, and the much more porous and needle-like spongy bone. In flat sections of bone, such as the parietal bone, there are two layers of relatively solid compact bone that protect an inner layer of spongy bone. The inner spongy bone is an irregular meshwork of sheets and spikes called trabecule, between which lies red bone marrow which contains stem cells and blood cells in different stages of development.

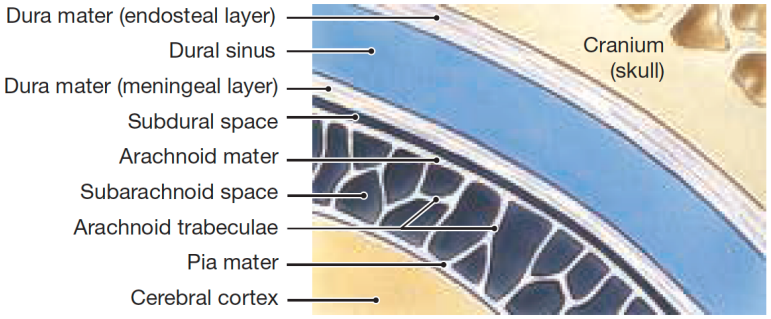

FIGURE 2.3: Cross section view of the layers of the meninges and how it connects to the cranium and the brain [14].

2.1.3 Meninges

The cranial meninges are membranes of connective tissue that surround the brain and protect it from contact with the inside of the skull. There are three layers of tissue that form the meninges called the dura mater, arachnoid mater and pia mater, forming a complete enclosure around the brain and the spinal cord. The three layers of meninges can be seen in Figure 2.3. The inner most layer is the pia mater which is tightly wrapped around the brain and spinal cord. It is impermeable to fluid, containing the cerebral fluid around the central nervous system. The pia mater also supports the large blood vessels that supply the brain. The middle arachnoid mater attaches itself to the pia mater by a web-like structure across the subarachnoid space. The dura mater is made up of two fibrous layers which are in some areas separated by a small gap of fluid and blood vessels including large veins. The dura mater provides a tough exterior to the meninges limiting the movement of the brain.

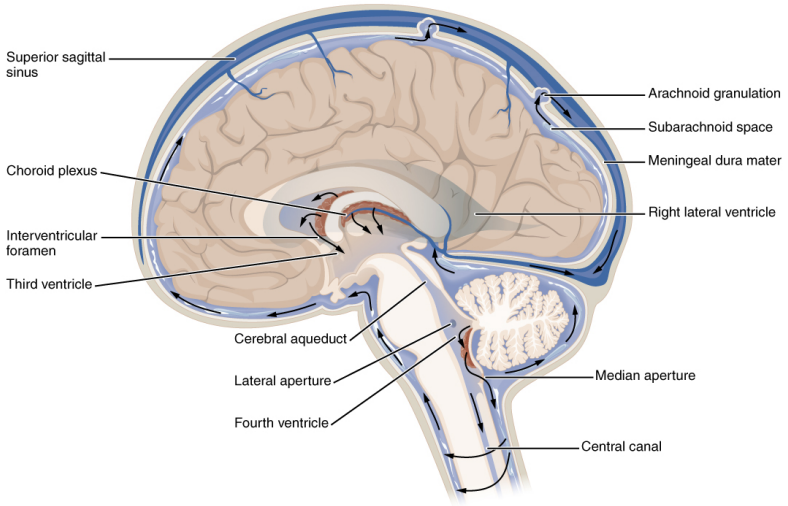

FIGURE 2.4: Cross section diagram of the head show the location of the choroid plexus and the circulation of the CSF. Image reproduced from [15].

2.1.4 Cerebrospinal fluid

In the subarachnoid space, cerebrospinal fluid (CSF), a cushioning liquid providing protection for the brain, is produced and circulated. The fluid consists of a watery mixture containing a small amount of protein, blood and nutrients for the brain. The CSF provides cushioning for the brain and surrounding bones and is produced in the choroid plexus which is situated in the ventricles. The choroid plexus produces around 500 ml/day, completely replacing the entire volume of CSF every eight hours. The circulation of the CSF starts in the four ventricles of the brain before entering the subarachnoid space circulating around the outside of the brain and the spinal cord.

2.1.5 Brain

The four major regions of the brain are the cerebral hemisphere, cerebellum, diencephalon, and the brain stem. The cerebral hemispheres make up the largest region at about 80% of the total volume of the brain [16]. The two hemispheres are separated by the longitudinal fissure, and are formed of 4 lobes that are responsible for controlling different tasks.

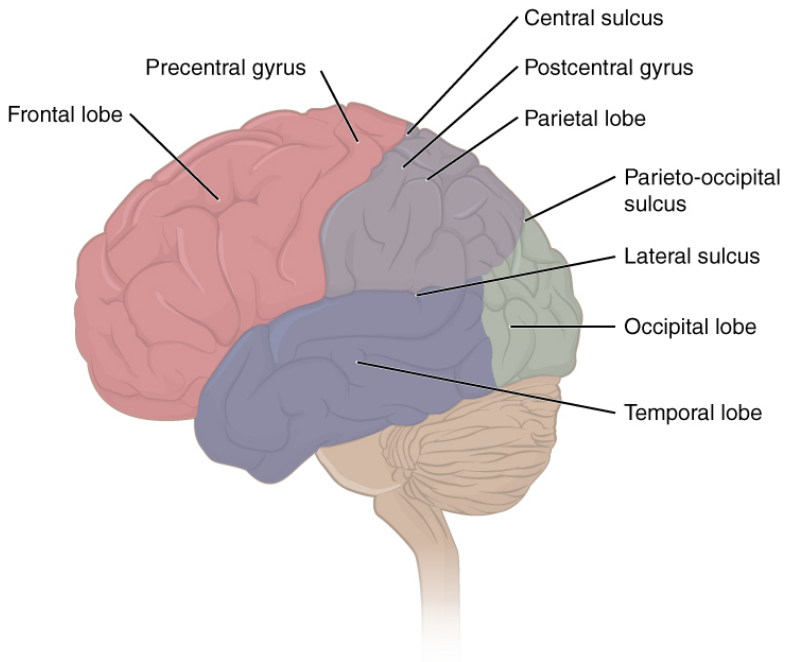

FIGURE 2.5: Diagram showing the lobes of the cerebral cortex [15].

As seen in Figure 2.5 the frontal, parietal, temporal and occipital lobes surround and enclose most of the diencephalon and brain stem. The tissue near the surface of the cerebral hemispheres forms a ridged and grooved structure of grey matter known as the cerebral cortex where most of the neurons responsible for the brain function are found. Below this is the cerebral white matter, formed of nerve fibres and responsible for carrying impulses from the cortex.

The posterior of the frontal lobes contains the region responsible for controlling the motor functions of the body, whereas the visual area is found in the occipital lobe. With a similar structure to the spinal cord the brain stem at around 3 inches long provides a pathway for signals to and from the body to the brain. It is comprised of similar grey matter to the cerebral cortex.

Above the brain stem sits the diencenephalon which acts as a pathway for sensory impulses to be passed to the sensory cortex in the centre of the cerebral hemispheres. The diencephalon consists of the epithalamus, and right and left thalamus and the hypothalamus.

Tissue	μ_a [mm^{-1}]	μ_s' [mm^{-1}]
Skin	0.012 ± 0.005	1.91 ± 0.3
Fat	0.008 ± 0.003	1.14 ± 0.293
Muscle	0.0283	0.699
Brain grey matter	0.02	0.80

TABLE 2.1: Values of μ_a and μ_s' for different tissues in the human body [1, 2]

Toward the rear of the brain is the cerebellum formed also of grey matter surrounding white matter. The function of the cerebellum, is to correct the timing of outgoing motor signals from the brain in correspondence to the current body position.

Table 2.1 shows some typical values for scattering and absorption for different tissues in the human body including muscle and brain matter. These values stated are measured at at 800 nm.

2.1.6 Cell metabolism and the electron transport chain

The digestive system breaks down food to various forms of nutrients for the body, one of these being glucose, which is used as a source of energy. Glucose enters the circulatory system through the small intestine and is transported around the body by the blood stream. Cells will then take up the glucose in order to convert it into Adenosine diphosphate (ADP) to form Adenosine triphosphate (ATP), which is sometimes refered to as the the "molecular unit of currency" of cellular energy. There are several different mechanisms used in order to achieve this, the first being a process called glycolysis. The chemical interactions can be seen in Figure 2.6. Glycolysis has two phases: the first consumes energy, as the glucose requires 2 ATP molecules to initiate the reaction. The second phase creates energy, producing 4 ATP molecules resulting in a net gain of 2 ATP. The chemical process of glycolysis can be expressed with the equation:

$$\text{Glucose} + 2\text{ATP} + 2\text{NAD}^+ + 4\text{ADP} + 2\text{P}_i \Rightarrow 2\text{Pyruvate} + 4\text{ATP} + 2\text{NADH} + 2\text{H}^+. \quad (2.1)$$

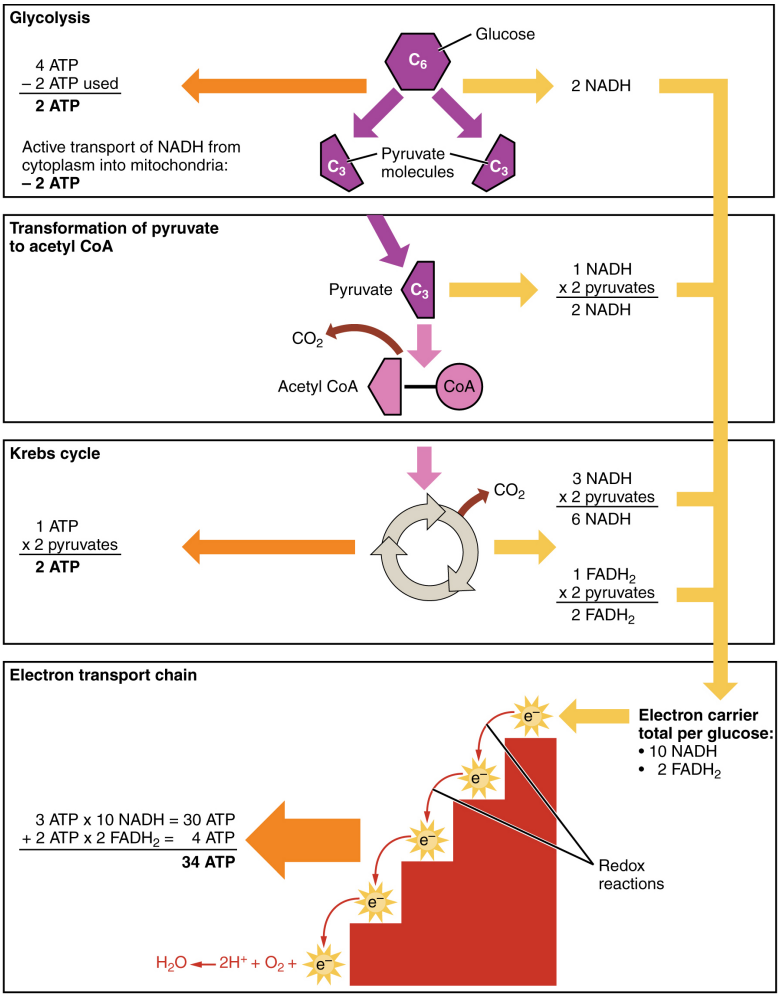

FIGURE 2.6: Cellular metabolism showing the oxydation of glucose to form ATP through glycolysis, the Krebs cycle and the electron transport chain [15].

The glycolysis process, in addition to creating 2 ATP molecules, produces 2 Nicotinamide adenine dinucleotide (NADH) energy containing molecules which are used later in the cellular metabolism mechanism to produce ATP. Also produced, are two pyruvate molecules which are transported across the mitochondrial membrane to be metabolised in the kreb cycle.

The Krebs cycle, also know as the citric acid cycle, creates more energy in the form of ATP and other energy containing molecules such as NADH and Flavin adenine dinucleotide ($FADH_2$). The Krebs cycle is a complex mechanism, and detailed information can be found in [14, 17, 18]. The cycle produces $FADH_2$ molecules in addition to more NADH

molecules which are both used in the electron transport chain.

2.1.6.1 The electron transport chain

The electron transport chain is a system occurring in the mitchondrial membrane. It uses NADH and $FADH_2$ molecules produced in glycolysis and the Krebs cycle to produce ATP molecules. The chain uses four enzyme complexes called Complex I-IV, and coenzymes called ubliquinone and cytochrome c as ion pumps and electron carriers to move the H^+ through mitochondrial membranes.

In the process, NADH is broken down to NAD+ and H+, releasing 2 electrons, which are then transported through a series of transition molecules, lowering the energy state of the electrons before combining with hydrogen and oxygen to produce water. The last 'transition molecule' in this electron transport chain, and the molecule of interest for near infrared spectroscopy, is cytochrome c. As the transport chain moves the electron, cytochrome c becomes reduced and oxidised, which leads to changes in its absorption spectrum. This means the change in concentration of oxidised cytochrome c oxidase will give an biomarker for the rate of metabolism on a cellular level. The oxidised and reduced forms of cytochrome c have different absorption spectra in the near infrared region which mean we can use near infrared spectroscopy to observe this change. The absorption of light by cytochrome c oxidase is discussed in the Section 2.3.0.4.

2.2 Tissue optics

This section discusses the interaction mechanisms which occur as light travels through biological tissue. The main two optical phenomena that describe the propagation of light in a scattering medium are optical absorption and optical scattering.

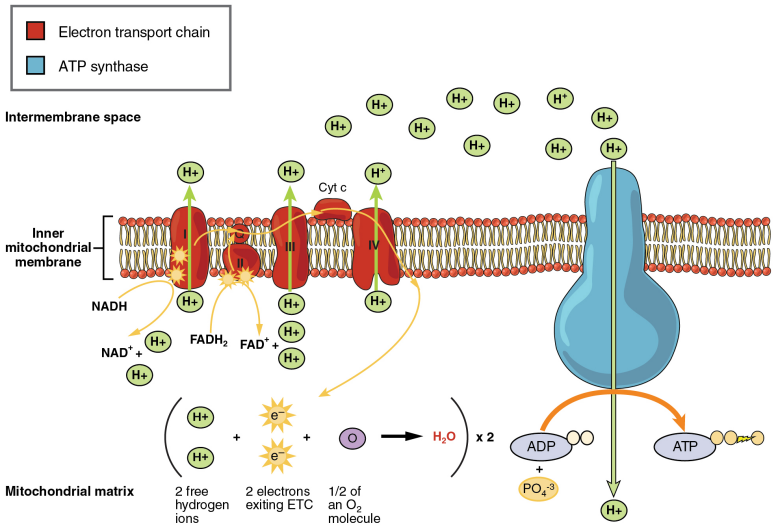

FIGURE 2.7: Diagram of the electron transport chain showing the mechanism of electron carriers and ion pumps to create ATP. Figure from [15].

2.2.1 Absorption of light

In 1729 Bouguer observed that there is an exponential relationship between the intensity of light and the length of the path that light travels through a uniformly absorbing medium. This led to Lambert's Law, formed in 1760, which states that every layer of the medium dx will absorb the same fraction dI/I of light where the absorption coefficient μ_{a} is constant. Therefore if the medium has a greater absorption coefficient, the light will not travel as far in the material, and the intensity at a distance away from the source will be reduced. The absorption coefficient can be described as the product of the density of the material (ρ) which has units mm^{-3} and, if only one chromophore is considered, the absorption cross section of the chromophore σ_a, such that

$$\mu_{\mathrm{a}} = \rho\sigma_a. \tag{2.2}$$

If we consider a non-scattering medium, we can write the change in intensity of light for a depth dx as:

$$dI = -I\mu_{\mathrm{a}}dx, \tag{2.3}$$

which can be rearranged to give

$$\frac{dI}{I} = -\mu_{\mathrm{a}} dx. \tag{2.4}$$

By integrating with respect to x, we can calculate the intensity of light I, at distance x using

$$ln(I) = \mu_{\mathrm{a}} x + C, \tag{2.5}$$

where C is a constant. If the above equation is evaluated at the source of the light and a distance d away from the source (i.e. x = 0 and d) and calculate the difference between the two we find that

$$ln(I_d) - ln(I_0) = -\mu_{\mathrm{a}} d + C + \mu_{\mathrm{a}}.0 - C, \tag{2.6}$$

which can be rearranged to give

$$I_d = I_0 e^{-\mu_{\mathrm{a}} d}, \tag{2.7}$$

where I_d is the intensity at distance d away from the source and I_0 the intensity at the source. Beer discovered in 1852 the relationship between the absorption of light and the concentration (c) of absorbing molecules diluted in a non absorbing solution:

$$\mu_{\mathrm{a}}(d, \lambda) = \alpha(\lambda) c(d), \tag{2.8}$$

where $\alpha(\lambda)$ is the specific absorption coefficient of the absorber for a unit concentration at wavelength λ. We can then substitute this into the equation above to get the Beer-Lambert law, which can be written as:

$$I(d) = I_0 e^{-\alpha c d}. \tag{2.9}$$

The specific absorption coefficient is the level of absorption per micromole of compound per millimetre (mm). Alternative units of millimole per centimetre are also used.

The specific absorption coefficient, ϵ, is also used to describe the Beer-Lambert law and arises when base 10 log units are used whereas the absorption coefficient is used in natural logarithm units. The the specific extinction coefficient has the units μmole^{-1}mm^{-1}.

$$\alpha = ln(10)\epsilon. \tag{2.10}$$

The Beer-lambert Law in log base 10 units is therefore written as

$$A = \log\left(\frac{I_0}{I}\right) = \epsilon.c.d, \tag{2.11}$$

where A is the absorbance of the medium, also called optical density (OD), and is a dimensionless quantity.

The modified Beer-Lambert law can be used to calculate the changes in concentrations of chromophores by measuring the attenuation of light, A_t [7]. This law uses an additive term, G, to account for scattering losses, and a scaling factor, the differential pathlength factor (DPF), to take into account the distance travelled in tissue by the light, resulting in equation

$$A_t = \epsilon.c.d.DPF + G. \tag{2.12}$$

The differential pathlength factor is calculated by dividing the optical pathlength by the source-detector separation. As the constant G is unknown and cannot be measured, the Beer-Lambert law can be used to measure changes in the chromophore concentrations

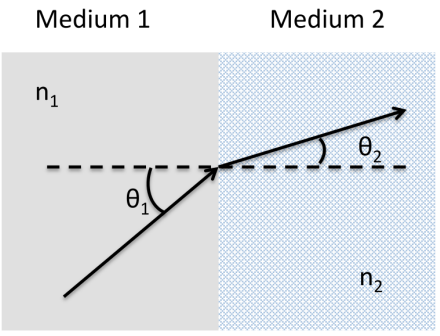

FIGURE 2.8: Refraction of light at the boundary of two media with different refractive indices.

by measuring the changes in attenuation:

$$\Delta A_t = \epsilon.\Delta c.d.DPF. \tag{2.13}$$

2.2.2 Scattering of light

The scattering of light in tissue occurs in media due to the heterogeneity of the medium in which the light is travelling. It can be described in terms of interactions with single particles, and the size of the particle and wavelength of the light will affect the nature of scattering events. Rayleigh scattering describes the scattering of light off of particles with a very small radius in comparison to its wavelength [19]. Where the particle is of similar size to the wavelength, Mie theory applies, and is therefore the dominant type of scattering in biological tissue [20]. In tissue at visible and infrared wavelengths it is sufficient for our application to describe the scattering in terms of the bulk refractive index of the medium.

In biological tissue, variations and mismatches in the refractive index at cell and structural boundaries are responsible for the scattering of light. Snell's law states the relationship between the refracted angle and the refractive indices of the mediaat a boundary,

and is given by

$$n_1 sin\theta_1 = n_2 sin\theta_2, \tag{2.14}$$

where n_1 and θ_1 are the refractive index of the medium the light is entering from and the angle incident to the normal of the surface of the incoming light, respectively. n_2 and θ_2 are the refractive index of the medium the light is entering and the defracted angle to the normal. The speed of light in any medium, ν, is defined as

$$\nu = \frac{c_{vacuum}}{n}, \tag{2.15}$$

where c$_v acuum$ is the speed of light in a vacuum and n is the refractive index of the medium. Light scattering can be thought of as deflection from a straight path due to irregularities in the medium or due to refractive index mismatches at tissue boundaries. The probability of a photon in the medium being scattered per unit length. If we consider a non-absorbing medium, we can write

$$dI = -\mu_{\mathrm{s}} I dx, \tag{2.16}$$

where dI is the change in intensity at distance dx due to the effect of scattering. By integrating and evaluating the equation at a distance x from the source analogously to the Beer-Lambert law for absorption we get

$$I(x) = I_0 e^{-\mu_{\mathrm{s}}(\lambda)x}. \tag{2.17}$$

This states that in a purely scattering, homogeneous medium, the intensity of light will decrease exponentially as the distance away from the source increases. When light meets a mismatch in the refractive index of the media the photon will be scattered in a different direction. In tissue, when a scattering event occurs the light is not scattered

isotropically but has a preference toward forward scattering in the direction of travel [21]. Scattering does not become entirely diffuse (isotropic) until after a few scattering events have occurred.

The angle that the light is scattered is dependent on the wavelength of light and the shape and size of the particle. Each particle will have a different phase function depending on its size and shape, so for simplification the average phase function is used. The average scattering phase function is the probability that the light travelling in direction $\hat{r}$ will be scattered into a direction $\hat{r}'$. As the phase function does not describe the absorption of light it is sometimes referred to as the scattering phase function, although it would perhaps be more sensible to simply use the term 'scattering function' since it is not related to phase in the usual sense. The phase function is assumed symmetric along the initial propagation direction. Therefore the phase function can be written as a function of the angle φ in which the light is scattered from its incident propagation direction

$$\Theta(\hat{r} \cdot \hat{r}') = \Theta(cos(\varphi)) \tag{2.18}$$

The anisotropy factor g represents the likelihood of the light being scattered in a forward direction and is defined by

$$g = \int_{-1}^{1} \Theta(cos(\varphi))\ cos\varphi\ d\varphi. \tag{2.19}$$

The value of g ranges from -1 to 1; a value of $g = 1$ indicates entirely forward scattering, $g = -1$ indicates backward scattering, and if $g = 0$ the scattering is entirely isotropic. In tissue the scattering has a preference for forward scattering where a typical value for g is around 0.69 to 0.99 [22]. Due to this anisotropic scattering in tissue it can be useful to concider the reduced scattering coefficient (μ_{s}'), which is derived as

$$\mu_{\mathrm{s}}' = \mu_{\mathrm{s}}(1 - g), \tag{2.20}$$

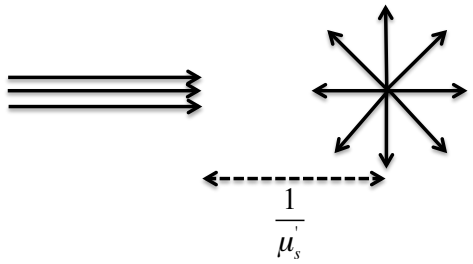

FIGURE 2.9: The reciprocal of μ_s' is the distance at which light becomes purely isotropic

The reciprocal of the reduced scattering coefficient can be thought of as the distance at which the light becomes purely isotropic and loses any memory of its initial direction 2.9.

Scattering in tissue is by far the greater contributor to the attenuation of light in tissue, where μ_s' is typically around two orders of magnitude greater than μ_a [23].

2.3 Tissue absorption of light

Near infrared spectroscopy can be performed on biological tissue due to the wavelength dependence of the absorption of light by different molecules in the body. These light absorbing molecules are called chromophores, and each has a specific wavelength-dependent absorption spectrum. By exploiting this characteristic of each separate chromophore, we can deduce the absolute concentrations or change in concentrations of the individual compounds from the data by comparing it to controlled measurements.

This chapter discusses the absorption spectra for the main chromophores in tissue that affect near infrared measurements: water, oxyhaemoglobin, deoxyhaemoglobin, lipids, cytochrome c oxidase and melanin. Table 2.2 shows the average percentage composition of compounds in the human head.

	Skeletal muscle (%)	Whole Brain (%)
Water	75	77
Lipids	5	11
Protein	19	8
Carbohydrates	1	1
Soluble organic substances	4	2
Inorganic salts	1	1

TABLE 2.2: Composition of the human head [24].

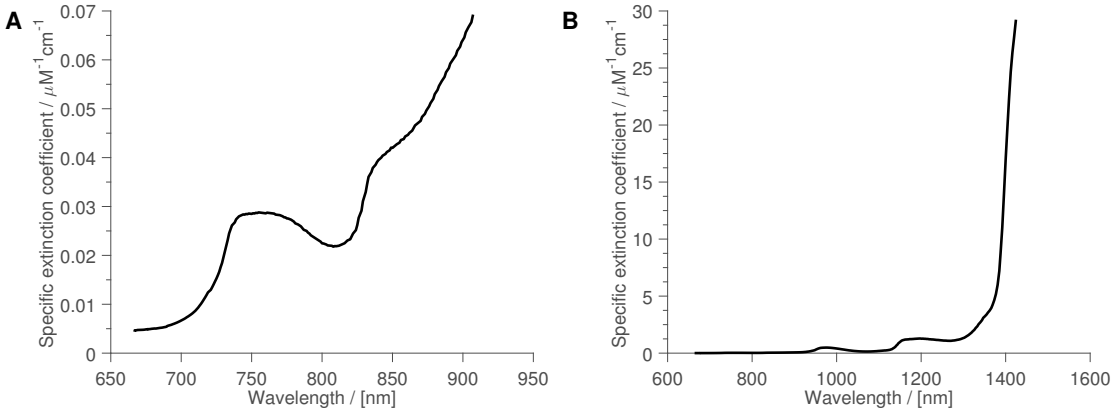

FIGURE 2.10: (A) Extinction spectrum of water between 667 and 920 nm, (B) Extinction spectrum of water over greater range showing vary large rise in absorption over 1400 nm. Data from [25].

2.3.0.1 Water

At around 80% of the mass of the human adult brain, water is by far the most abundant compound, and its effecton spectroscopic measurement limit their capability significantly [24]. As seen in Figure 2.10 the absorption coefficient is relatively low between 200 nm and 900 nm before increasing to a peak at 970 nm. Due to the high concentration of water in the human brain and the high absorption of light for wavelengths longer than 900 nm, near infrared spectroscopy does not often use wavelengths higher than 950nm. Since the attenuation of the light would severely limit the maximum penetration depth. From 700 to 900 nm the absorption coefficient varies from 0.001 to 0.006 mm^{-1}.

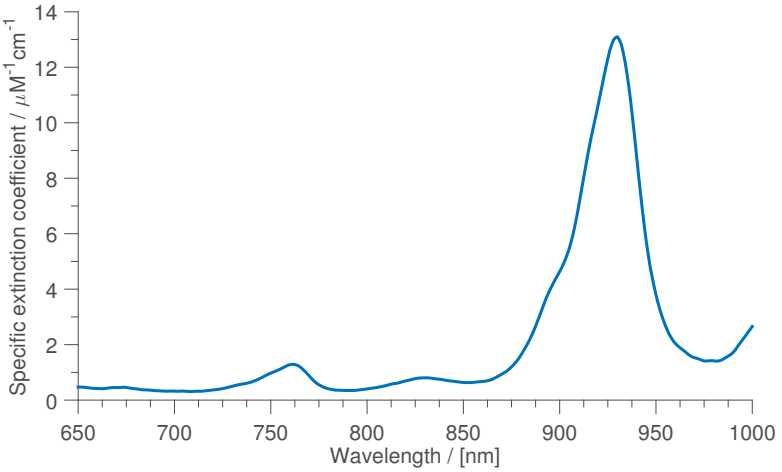

FIGURE 2.11: Absorption spectrum of lipids. Data from [27].

2.3.0.2 Lipid

Lipids have very similar absorption properties to water with a low μ_a from 200 nm rising to a peak at around 930 nm as seen in Figure 2.11 [26]. However, due to the low concentration of lipids in the brain of about 10%, the total absorption of light is less significant than that of water [24]. The distribution of lipids varies in tissue depending on the area being illuminated.

2.3.0.3 Haemoglobin

Blood has three main constituents: plasma, blood cells and platlets. Plasma constitutes between 46-63% of the total blood volume, blood cells 37-54%, while platelets only account for a very small amount. Red blood cells account for nearly all of the total volume of blood cells, with white blood cells accounting for only 0.01%. Red blood cells, or *erythrocytes*, transport oxygen and carbon dioxide around the body through a network of blood vessels. The average red blood cell measures 7.7 μm wide by 2.85 μ m and forms a biconcave shape which creates a large surface area in order to maximise the ability to take on oxygen and carbon dioxide. The red blood cells lack mitochondria, which means that they rely on anaerobic metabolism from glucose taken from the plasma

to obtain energy. This mechanism ensures that the red blood cells do not use any of the oxygen that they carry.

Red blood cells contain approximately 280 million molecules of Haemoglobin each, which accounts for 95% of all proteins in the cell. The molecule has a complex shape made of four polypeptide subunits, two α and two β chains, each containing a single heme molecule. The heme molecule has an atomic structure which contains an iron ion in such a way that it can easily interact with an oxygen molecule. There is only a weak interaction between the iron ion and the oxygen molecule which allows the two to easily bond and separate without damage to the heme molecule. Carbon dioxide binds to different subunits of the haemoglobin protein so does not compete with oxygen for the binding with iron.

Haemoglobin gives blood its distinctive red pigment, oxygenated blood (HbO_2) appears bright red while deoxyegenated blood (HHb) a deep red colour. This difference in colour is due to the arterial oxygenated blood and deoxygenated blood possessing different absorption spectra, both containing distinct features. By exploiting these features we can separate the absorption due to each compound by near infrared spectroscopy, calculating either the relative change or absolute concentration of both oxyhaemoglobin and deoxyhaemoglobin.

At wavelengths less than 600 nm, both the absorption coefficients for the two types of haemoglobin are relatively high at around 0.005 mm^{-1}, which along with water creates what is known as the window of transparency from 600 nm to 950 nm. Between these two wavelengths, near infrared spectroscopy measurements can penetrate the tissue further due to the relatively low absorption of light by all chromophores, enabling measurements at deeper regions to be made and therefore providing information of the tissue properties at depth. Figure 2.12 shows the different absorption spectra of HbO_2 and HHb . With only a few wavelengths, concentrations of these compounds can be

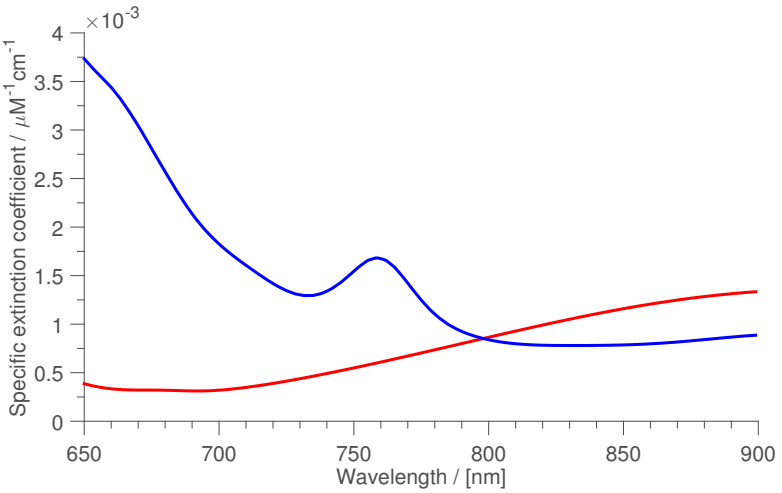

FIGURE 2.12: Extinction coefficient spectrum of oxyhaemoglobin (HbO_2)and deoxyhaemoglobin (HHb) between 650 and 1000 nm. Data from [28].

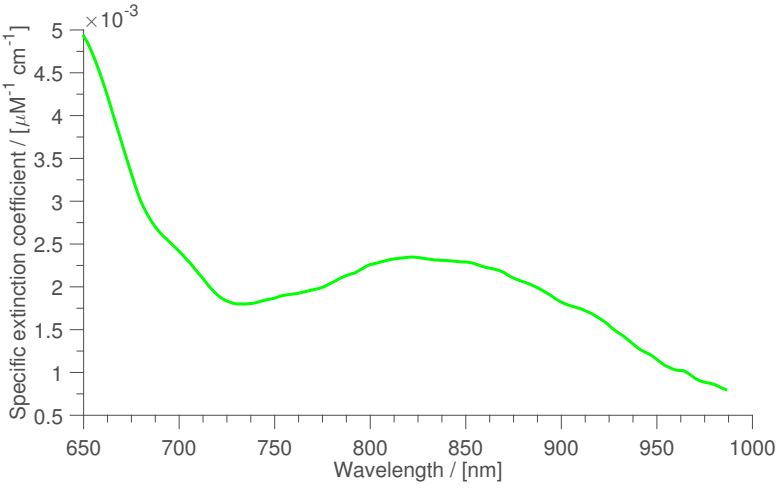

FIGURE 2.13: Difference in the extinction coefficient spectrum between the oxidised and reduced forms of cyctochrome c oxidase.

obtained, although a combination of multiple and specifically chosen wavelengths can yield more accurate results.

2.3.0.4 Cytochrome c oxidase

Unlike oxy- and deoxyhaemoglobin, the concentration of cytochrome oxidase remains constant in tissue, but the absorption spectrum differs depending on whether the compound is in its reduced or oxidised state.

Figure 2.13 shows the difference in absorption spectra of the oxidised and reduced forms of cytochrome. The production of Adenosine triphosphate (ATP) and energy usage in the brain can be deduced by monitoring the amount of cytochrome c oxidase in each redox state. The concentration of cytochrome c oxidase in tissue is significantly less than that of blood by an order of magnitude, and as a result monitoring the changes of redox state requires many more wavelengths to be used in spectroscopy than in HbO_2 and HHb measurements [29, 30]. The difference in the absorption spectrum between the oxidised and reduced forms of cytochrome c oxidase has a broad peak at 820 nm and increases at the lower wavelengths in the near infrared range.

2.4 Chapter summary

This chapter presents an overview to the anatomy of the human head and the challenges various biological tissues pose the collection of near infrared spectroscopy measurements. An introduction to the scattering and absorption of light in tissue shows how measurements of light absorption can be used to calculate the changes in concentrations of light absorbing molecules.

Chapter 3

Near infrared spectroscopy techniques and instrumentation

This chapter gives a background of near infrared spectroscopy and different techniques used. A review of the state of the art time resolved near infrared systems from several research groups is given. The chapter then reviews the most common currently in use electronics associated with time resolved NIRS spectrometers such as pulsed light sources, wavelength filters, single photon detectors and time of flight single photon counting techniques.

3.1 Near infrared Spectroscopy

The attenuation of light in tissue is due to the combined effect of absorption and scattering of light. Light is absorbed by many different chromophores in tissue which are described in Section 2.3. The concentrations of these chromophores can be constant (e.g. water, lipids) or dynamic such as haemoglobin (HbO_2, HHb) or the redox state of cytochrome c. Near infrared systems aim to quantify the concentrations of these dynamic chromophores in tissue by measuring the optical properties of tissue. One of the first

in vivo continuous measurements of HbO_2 and HHb was performed by Jobsis in 1977, who described how the apparent transparency of biological materials at near infrared wavelengths means that changes in the spectrum across the head relates to changes in chromophore concentrations [4]. The paper discusses the complexity of providing absolute quantification of concentrations changes due to the unknown pathlength of light in tissue. A major problem of quantifying concentration changes by measuring the attenuation variation in tissue is that light loss is not only due to absorption but also scattering. We find in tissue a much greater loss of light due to scattering than from absorption with the reduced scattering coefficient in humans ranging from 0.5 - 1.5 $mm^{-1}$and the coefficient of absorption ranging from 0.0052 - 0.02 mm^{-1}[22].

The Modified Beer-Lambert law enabled continuous wave measurements to quantify changes in the chromophore concentrations by making an assumption of the differential pathlength of light in tissue and assume that the scattering remains constant for the duration of the measurement [7]. While these assumptions can yield relative changes reasonably, other techniques were developed such as frequency domain and time domain NIRS which can separate the scattering from absorption measurements to measure absolute chromophore concentrations. Figure 3.1 illustrates the light input and measurements of these three techniques and sections 3.1.1, 3.1.2 and 3.1.3 describe them in detail.

3.1.1 Continuous wave NIRS

Continuous wave (CW) instruments operate by emitting light with a constant intensity onto the tissue. They measure the change in intensity or attenuation of the light exiting a short distance away. In order to convert this measurement of attenuation into a quantification of chromophore changes, the pathlength of light must be estimated [31]. The differential pathlength factor (DPF) which is related to the source detector separation is

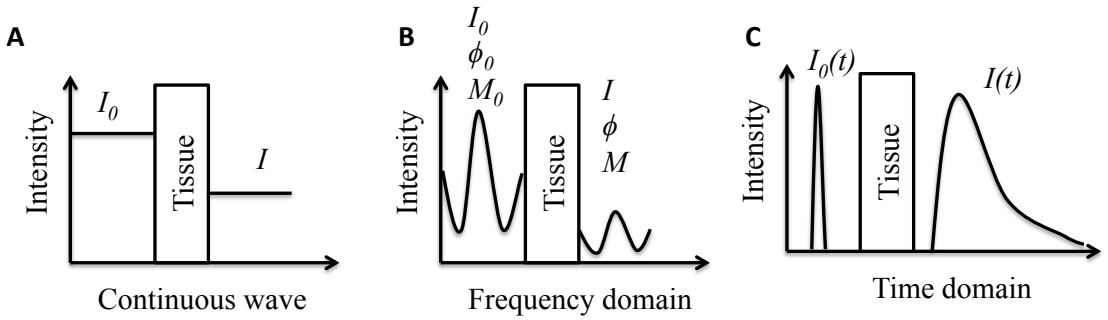

FIGURE 3.1: Illustration of the three methods of near infrared spectroscopy. (A) Continuous wave NIRS emits light a constant intensity I_0, measuring only the change in intensity or the attenuation of light due to both scattering and absorption in tissue. (B) Frequency domain instruments modulate the intensity of light that enters the tissue, and measure the intensity (I), phase shift of the light ϕ and amplitude M. (C) Time domain measurements input a short pulse of light to the tissue and measure the time of photons as they travel through the media.

used in order to calculate the effective or differential pathlength,

$$\textit{differential pathlength} = \textit{s-d separation} * DPF. \tag{3.1}$$

If this estimate is known, with measurements of attenuation of light at multiple wavelengths the modified Beer-Lambert law can be used to calculate changes in chromophore concentrations.

The first commercial system to use this technique was the NIRO 1000 developed be Hamamatsu Photonics in collaboration with Dave Delpy at UCL in 1987. Since this first system, many versions of the NIRO spectrometer have been developed with the NIRO-200NX being the current model. The two channel NIRO-200NX uses three LEDs at wavelengths 735 nm, 810 nm and 850 nm measuring the tissue oxygenation index (TOI), normalized tissue haemoglobin index (nTHI), oxyhaemoglobin change (ΔHbO_2), deoxyhaemoglobin change (ΔHHb) and the total haemoglobin change.

Imaging continuous wave systems uses multiple sources to perform optical tomography or tomography on the head, breast or arm. Topography uses an array of sources and detectors to determine the optical properties of tissue a constant depth below the surface.

This yields a 2D map of the chromophore concentration changes in the tissue near the surface, where multiple channels are measured from different pairings of source and detectors. The mean penetration depth of the light is dependent on the source detector separation; short distances will measure changes near the surface (i.e. skin), whereas greater separations will measure changes deeper in the tissue [32].

The majority of systems use a discrete number of narrowband light sources to illuminate the tissue [13]. Where there are multiple sources and detectors used, in order to distinguish which source the light has come from, frequency multiplexing can be used. This means that all sources can be illuminated at all times, maximising the collection time for each detector. The light is modulated at a different frequency for each wavelength and source at around 2 kHz and measured by high sensitivity detectors such as avalanche photodiodes (APDs). The measured light is passed through to analogue-to-digital converters to separate the different source signals.

One system that implements this technique is the NTS Optical Imaging System in Figure 3.2 from UCL [33]. Light at two wavelengths (780 and 850 nm) are used to image oxy- and deoxyhaemoglobin. The system uses 32 laser diodes which are used to provide 16 source locations on the skin using bifurcated fibre optics. The source frequencies are all derived from a main 20 MHz oscillator. By using frequency dividers the modulation frequency is reduced to one octave between 2 and 4 kHz. This reduces interference between harmonics. 16 Hamamatsu C5460-01 avalanche photodiodes measure the light leaving the tissue through fibre optics and pass the signal through low pass filters to analogue-to-digital converters sampling each channel at 20 kHz. Performing a fast Fourier transform on the data allows the signals to be separated and used to generate spatial maps of haemodynamic changes at a rate of 20 Hz. Small portable systems like this offer a wide range of applications such as measuring the haemodynamics of neonates during seizures [34], simultaneous EEG measurements [35], and functional activation in infants due to social perception and facial recognition [36–38]. Due to the portable

FIGURE 3.2: NTS optical imaging system designed and build at UCL [39].

nature of the system it has been used to assess cognitive function in rural Africa and Bangladesh [11].

Another method of continuous wave measurement uses a white light source, typically a halogen bulb. The light is coupled to an optical fibre which is placed on the skin. As the source provides a broadband spectrum the light is collected though a charged coupled device (CCD) measuring the attenuation of the spectrum due to a combination of absorption and scattering in the medium. This data is then used to calculate the concentrations of chromophores in the tissue [40, 41]. The advantage of this technique is that it effectively uses as many wavelengths as the spectrometer resolution and therefore can more accurately resolve for chromophores such as cytochrome c oxidase [42].

3.1.2 Frequency domain NIRS

Continuous wave instruments are limited in their applications since they measure the attenuation of light, meaning that the scattering and absorption of light cannot be separated. Frequency domain systems solve this problem by modulating the intensity of the light source, enabling not only the attenuation of light to be detected but also the phase shift. Scattering and absorption will have an independent effect on the phase shift of the signal. This means that by fitting analytical models to the data, independent values for μ_{a} and μ_{s}' can be derived [43]. Frequency domain measurements were first demonstrated in 1990 by Lakowicz, where the time dependent migration of photons through the arm and finger was measured [44].

Frequency domain instruments appear similar to frequency multiplexed continuous wave systems as they both modulate the source light. However, frequency multiplexed continuous wave instruments are modulated at much lower frequencies in the order of 2 kHz whereas frequency domain systems modulate the light source in the 100 MHz range. This means that there will be a measurable phase change at short source-detector separations.

The first commercial frequency domain instrument, the Oxiplex, was introduced in 1998 by ISS. Since then, ISS have also brought out a multichannel imaging system, the Imagent, which can use up to 64 source fibres and 8 detector fibres. The popularity of frequency domain systems has yet to match the uptake of continuous wave systems possibly due to additional complexity of the measurement and data analysis.

3.1.3 Time domain NIRS

The first time resolved measurements were recorded in 1988, where Delpy et al. reported the use of an ultrafast dye laser and a streak camera to measure the time-of-flight of photons across the rat head in order to calculate the differential path length factor [7].

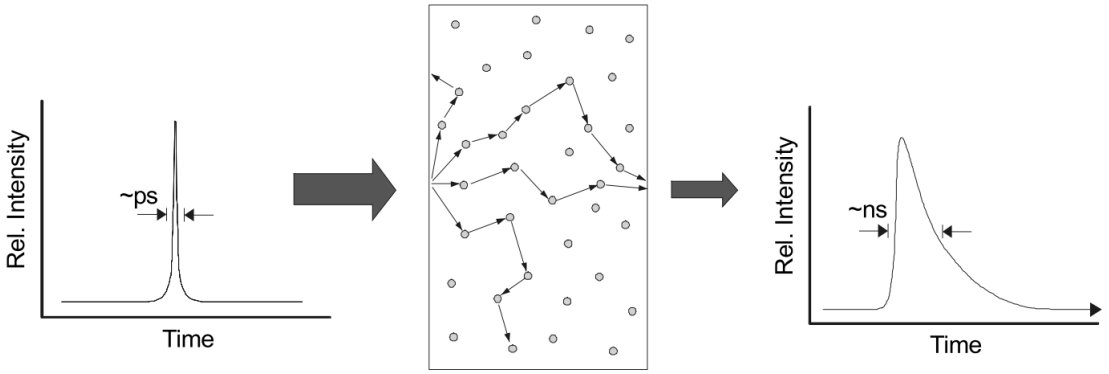

FIGURE 3.3: Time domain spectroscopy illuminates the surface of tissue with short picosecond pulses. As the light propagates through tissue the photons experience multiple scattering events, which result in the temporal broadening of the recorded pulse (right). The measured broadened pulse is called the temporal point spread function (TPSF). Figure from [48].

They reported a pathlength of 5.3 $\pm$0.3 times the width of the rat head. Chance et al. in the same year used a two wavelength tunable dye laser operating at 760 nm and 790 nm to measure the extent of oxyhaemoglobin deoxygenation during mild ischemia/hypoxia in a cat brain [45]. In the same year, Chance also measured changes of haemoglobin and myoglobin in resting and ischemic muscle [46].

Time domain spectroscopy systems measure the transit time of individual photons as propagating through tissue. By injecting an ultrashort (picosecond) pulses of light, the temporal response of tissue can be measured. The recorded pulse of light that emerges from the tissue will have been temporally broadened to a few nanoseconds due to scattering and the different paths taken by each photon, as shown in Figure 3.3. The temporal distribution of detected photons is called the temporal point spread function (TPSF), the shape of which provides information about the absorption and scattering of light in tissue [47]. An increase in the absorption of light will result in a decrease in the total intensity but a decrease in the temporal distribution of photons and the mean time-of-flight. An increase in the scattering coefficient will decrease in total intensity. However, unlike the absorption, the mean time-of-flight and temporal distribution of photons will increase.

As the TPSF is effectively a histogram of the flight times of all the photons detected, the integral of the TPSF over flight times gives the measured intensity of light detected similar to continuous wave measurements. From the TPSF the mean time of flight can be calculated, and together with the integrated intensity, these are the Fourier equivalent to phase and amplitude measured with frequency domain instruments. Whilst continuous wave systems only measure the intensity of light emerging from the tissue surface, the data types obtained from time domain measurements such as mean time of flight, variance, along side intensity provide depth-selective information from a single source that is not achievable with CW measurement unless multiple detectors are used.

The first time domain systems used streak cameras to measure the pulse of light emerging from the tissue surface [49]. Now it is much more common for time resolved measurements to be made using the time correlated single photon counting (TCSPC) technique [50]. This method uses high repetition rate lasers (40-80MHz) to illuminate the tissue with short picosecond pulses. The light source is often coupled to the tissue via optical fibres. Similarly, fibre optics collect the photons escaping from the tissue surface a short distance away depending on the geometry required, and direct the light to single photon detectors. There is a wide range detector available for this task, including photomultiplier tubes (PMT), multichannel plate PMTs, single photon avalanche diodes (SPAD) and silicon photomultipliers (SiPM) [51].

The detectors measure the arrival of a photon, convert it to an electronic pulse and amplify the signal so that TCSPC timing electronics can measure the arrival time of the photon. Figure 3.4 displays how for each period (time between pulses of light from source), either one or zero photons are detected and their flight time recorded. When the photon is detected the event is recorded by adding a '1' to a histogram bin at the measured arrival time. Through the detection of multiple photons over many signal periods, the temporal distribution of flight times builds up to form a TPSF.

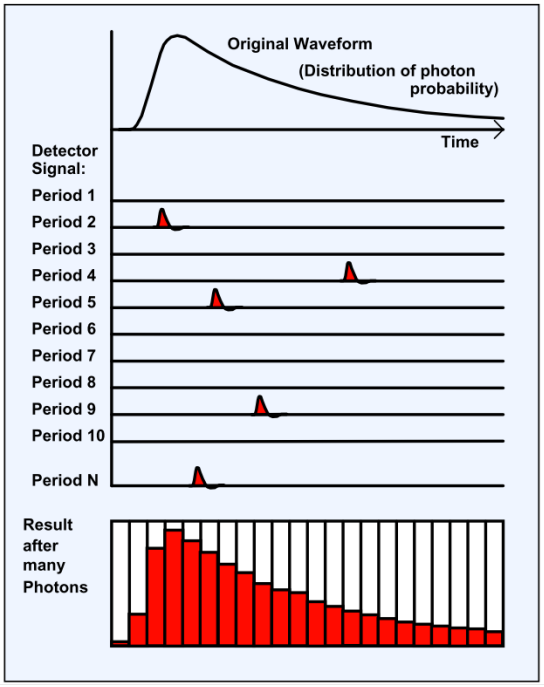

FIGURE 3.4: Time correlated single photon counting. When a photon is detected, the flight time is measured and added to the histogram of all the the arrival times. Image from [52].

3.1.3.1 Current time resolved near infrared systems

This section discusses a selection of near infrared time resolved systems recently developed and their technical aspects.

In 2008 the nEUROPt project (Non-invasive imaging of brain function and disease by pulsed near infrared light) was set up to develop advanced optical methodologies for monitoring of brain function and diagnosis and prognosis of neurological diseases such as stroke, ischemia and epilepsy using pulsed near infrared light [53]. This project led to the development of many time resolved instruments being developed across Europe, with different aims for their function and application [54–56].

One of the systems developed in this project is the MONSTIR-II system at UCL [57]. The Biomedical Optics Research Lab built the first MONSTIR (multi-channel opto-electronic

near-infrared system for time-resolved image reconstruction) system in 2000 for optical bedside monitoring of premature infants [58]. The system used 32 source and 32 detector fibres to illumine the infants head with light from a Ti:sapphire Tsunami laser. Segmented 8-anode multichannel plates detected the light and flight times of photon measured by a picosecond timing analyser (PTA). Whilst the system was technically portable the system consisted of two large full height rack systems and required water cooling. MONSTIR was successfully used to image the premature infant brain and perform whole head tomography of functional responses to passive arm movements [59, 60].

The second generation of MONSTIR, MONSTIR-II (Figure 3.5), was developed in the nEUROPt project to investigate the use of new instrumentation including a supercontinuum laser source and acousto-optic tunable filters (AOTF). The system, described in detail in Cooper et al. [57], employs 32 source fibres to sequentially transmit the light from a Fianium supercontinium laser and acousto-optic tunable filter at four wavelengths between 650 and 900 nm. 32 thermoelectrally cooled photomultiplier tubes provide the detection of light with four time correlated single photon counting cards measuring the flight time of photons in tissue. The system requires a warm up period of approximately 1 hour to reach thermal equilibrium and exhibits a temporal jitter of 5-10 ps. The new generation of instrument significantly reduced the cross talk in the measurement from 0.3% to a negligble amount due to the use of individual PMT modules in place of the MCP-PMTs used in the original system. The PMTs in the system, however, reduce the temporal resolution in the system due to an increased transit time spread in the module. The instrument response function measured in the system has a full width half maximum of 345 ps compared to 125 ps in MONSTIR. As MONSTIR-II is an imaging system fast acquisition of data is important. At the time of publication the time required to obtain good quality TPSFs for a full sequence of 32 sources was 99 s. Further developments are ongoing to reduce the acquisition time and a reduction of acquisition time to 75 s

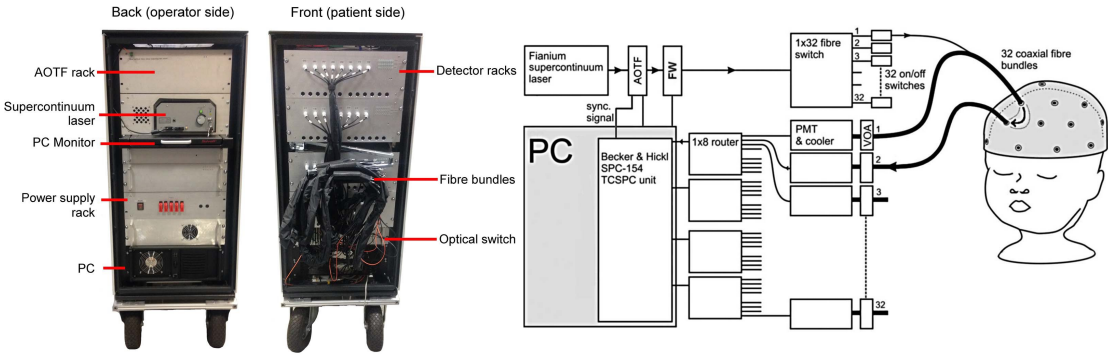

FIGURE 3.5: Photos and diagram of MONSTIR-II. Figure from [57].

is currently anticipated. Preliminary studies have shown haeomodynamic response to functional activation in the infant brain [61].

In 2006, Contini et al. reported the development of a 16 source, 16 detector time domain functional imaging system capable of sub 5 ms collection times per channel [62]. Two pulsed laser diodes at 690 and 820 nm, operating at a frequency of 80 MHz were used as light sources. A timing delay in the output created by the use of different length fibre optics allowed both TPSFs from each source to be captured in the same TCSPC collection window. 4-channel PMT modules were used for photon detection (Hamamatsu R5900-20-M4). Based on this design a compact two channel dual wavelength system was developed to improve the signal to noise ratio and decrease the potential cross talk of the measurement. The first system collected both TPSFs from each source in the same temporal window. This potentially introduces cross talk in the distribution of photons and due to the non-linearity of the time-to-amplitude converter of the TCSPC system the time interval available for photon collection may be reduced. To compensate for these issues, Re et al. developed a system that injects and collects the light to and from the head alternatively [63]. As the wavelengths are no longer simultaneously detected, a fast switch rate of 5 Hz was required in order to measure haemodynamic changes in the brain. The system was used to asses the effectiveness of time domain measurements in separating deep and superficial fNIRS signals [64].

A novel time domain fNIRS system developed at the Politecnico di Milano uses a fibre switch to space multiplex the light from two laser diodes (687 nm and 826 nm) to 18 source positions [65]. Eight hybrid photomultiplier tubes (PMTs) are used for the multichannel detection of photons. The hybrid PMTs eliminate any after-pulsing in the PMT, increasing the dynamic range of TCSPC measurements [52].

A laboratory based time domain system utilising fast-gated single photon avalanche diodes was developed by Puszka et al. in 2013, displaying the advantage of gated detection for improved depth localisation and sensitivity [66]. The system uses a 4 wave mixing Fianium laser produces light at 820 nm with a repetition rate of 40 MHz and a full width half maximum of 26 ps. Gated single photon avalanche diodes allow the detection of elements of the TPSF with a much higher dynamic range than if the entire TPSF is recorded. The single photon avalance diodes used, have a switch on time 200 ps and timing jitter of 30 ps [67]. This technique gives the possibility to increase the light source power, and reduce the source detector separation in order to improve the signal to noise ratio.

A non-contact time-resolved diffuse reflectance imaging system based on the fast gated detection technique and using small source detector separation has been recently developed by Sieno et al. across multiple research facilities in Europe and Japan [68–70]. The system utilises fast-gated single photon avalanche diodes to measure optical signal with high dynamic range and extract data from the late arrival of photons, thereby increasing the amount of depth information collected. The system uses a supercontinium laser (SC500-6, Fianium, Ltd) at a repetition rate of 40.5 MHz and an eight channel acousto-optic tunable filter for the near infrared range. The non-contact optics direct the light onto the surface of the tissue using a galvanometer scanner that produces a spot size of 1 mm in diameter. Due to the non-contact optical imaging technique and the small active area of the single photon avalanche diode the responsivity is much smaller than that of a ‘conventional’ time domain imaging systems that use PMTs. However the fast gating

technique, not possible with PMTs and image intensified CCD cameras, provides higher dynamic range, and the non-contact optics have advantages in allowing measurement on patients with wounds or burn injuries. The short separation technique and ability to efficiently measure late photons improves spatial and depth sensitivity.

Another single photon avalanche diode (SPAD) based time domain imaging device has been developed by Mata Pavia et al. containing a non-contact 128 x 128 pixel detector array [71]. Each pixel in the array is capable of providing independent timing information and has a resolution of 97 ps. This large number of detectors has been shown to provide better spatial resolution in reconstructed images. The large amount of data generated by the 16,384 pixels however means that conventional image reconstruction algorithms cannot be used and the long readout time of the SPAD array results in long acquisition time.

An intensified CCD (ICCD) camera based time domain spectrometer was developed by Selb et al. in 2005 at the Massachusetts General Hospital, using a Ti:sapphire laser producing a single tunable single output in the near infrared range, (750-850 nm) [72, 73]. Since then the light source has been upgraded to a Fianium supercontinuum laser outputting 9 W of power at 60 MHz [74, 75]. The light from the laser source is split using a diachronic filter at 776 nm to allow two independent sources. The wavelength of light in each source channel is then selected by a motorised filter wheel containing different bandpass filters. Both 40 mn and 12-13nm wide bandpass filters are used depending on whether fast functional activation measurements are being made or slower baseline studies. The light is then focused into a custom made switching system. A dual axis galvanometer with scanning mirrors directs the light into one of sixteen graded-index fibres held in a 4x4 array. This technique results in a 75-80% coupling efficiency. The ICCD is used in a gated detection mode similar to the Milan system to record different temporal sections of the TPSF. The gate width of the ICCD is set at 400ps with a 25 ps

resolution. Detection fibre of varying lengths allow the simultaneous measurement of multiple fibre locations.

The only commercially available time domain system specifically designed for fNIRS monitoring is the TRS-20 designed and sold in Japan by Hamamatsu Photonics [76, 77]. The two channel system uses laser diodes to provide pulses at 760, 800 and 830 nm with a mean intensity of 200 μm and propriety photomultipliers and TCSPC electronics.

A medical device for measuring blood flow and oxygenation in infants is being developed across Europe by a multi facility 3 year research project called BabyLux [78]. The aim of the project is to design and build an optical neuro-monitor of cerebral oxygen metabolism and blood flow for neonatology. The system design combines diffuse correlation and time domain near infrared spectroscopy into an optical bedside monitor for premature infants. The main objective of the project is to lower the risk of brain legions in premature babies from 25% to 20% thus lowering the number of children with disabilities in Europe be 1000. This work shows that there is a positive move to use time resolved spectroscopy in clinics and aid in medical treatment. As of yet time resolved spectroscopy has been solely used for research purposes.

3.2 Lights sources

There are several choices for light sources in near infrared spectroscopy across the three techniques of continuous wave, frequency domain, and time domain; light emitting diodes (LED), broadband lamps, laser diodes, solid-state lasers, and supercontinium lasers are all used in the field. Broadband lamps and LEDs are not discussed in detail in this thesis as they do not fulfil the requirements needed from time domain spectroscopy and as such are only used in continuous wave and frequency domain techniques. Time domain spectroscopy relies solely on laser technology due to the ability to produce short pulses of light at specific wavelengths.

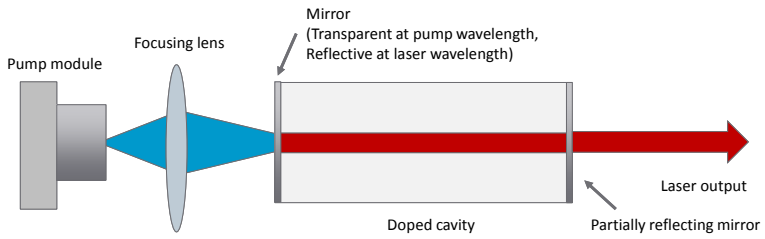

FIGURE 3.6: Diagram showing the function of a solid state laser.

Lasers (light amplification by stimulated emission of radiation) emits coherent light through the process of stimulated emission of electromagnetic radiation which is optically amplified. Temporal coherence of lasers means that they emit light with a very narrow bandwidth, which allows the generation of very short (femtosecond) pulses of light. Spatial coherence means that the light will stay in a narrow beam without divergence, allowing the propagation of light over long distances while remaining focused to a small spot. Light from a laser can be emitted continuously or pulsed, which makes it suitable for all near infrared methods.

3.2.1 Solid state lasers

Early time domain instruments used solid state lasers for the optical light sources. They produce coherent light at single wavelengths by stimulated emission. Solid state lasers use a crystal or glasses doped with rare earth or metal ions as a gain media. The optical cavity containing the gain media has two mirrors at either end: one to let in light from the pumping source, whilst the other is partially reflective to let out a fraction of the light while maintaining stimulated emission within the cavity. An optical pump such as a laser diode excites ions within the media maintaining a population inversion and amplifying the light, shown in Figure 3.6. Stimulated emission occurs when an excited atom or ion decays into a lower state in response to an external electromagnetic field. Several time domain systems have used Ti:Saphire Solid state lasers for light sources described in [58, 73], which produce a high output power of 700 mW at 80 MHz and 1 W at 80

MHz respectively. Ti:Sapphire lasers are tunable in the near infrared range which suits near infrared spectroscopy, however the long delay required to switch wavelength and large size of the laser means they are not ideal for portable fNIRS devices.

3.2.2 Laser diodes

Laser diodes, developed in 1962, are based semiconductor gain media to achieve stimulated emission of light at a semiconducting boundary [79, 80]. Figure 3.7 shows the patented design of the first laser diode. Semiconductor lasers contain two substrates of p- and n-doped substrates sandwiched between two electrodes. An electrical current pumps the p-n junction where these two meet, exciting electrons which then decay due to stimulated emission. Mirrors on either side of the p-n junction contain and amplify the light with one side letting a fraction of the photons escape the diode forming the laser beam.

When provided with enough energy the electrons in the p-n junction are excited and move from the valence band to the conduction band. The electrons decay to the bottom of the conduction band and holes are created in the top of the valence band. When the electron annihilates with the hole in the valence band a photon is emitted. The wavelength of light that is emitted is dependent on the band gap between in the valence and conduction band. By engineering different materials for the p and n doped regions the wavelength can be chosen. The main advantages of laser diodes for use in near infrared applications are that they are relatively inexpensive, they are packaged in very small devices, and they produce coherent light with narrow bandwidth <10 nm. The pulse duration is long compared to solid state laser systems but this can be improved by lowering the output power. While different wavelengths can be achieved by changing the semiconductor gain media, obtaining laser diode at specific wavelengths is not always possible.

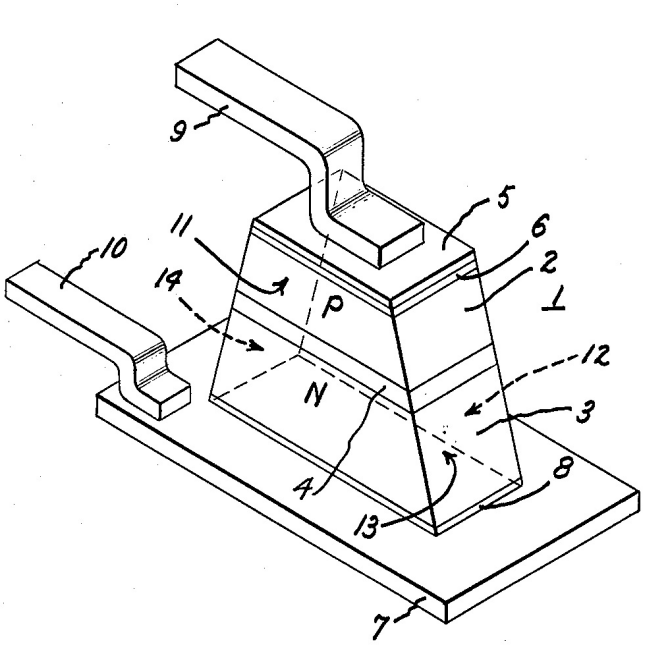

FIGURE 3.7: Diagram of first laser diode construction from [80]. **2** doped P-type region, **3** doped N-type region, **4** P-N junction which is 1 μm wide, **5, 6, 7** and **8** electrode and electrical connection layers to P and N-doped regions, **9** and **10** electrode connectors, **11** polished front surface, **12** polished rear surface, **13** and **14** angles cuts to prevent transverse waves forming within the semiconductor crystal.

3.2.3 Supercontinuum light sources

Frequency broadening of light in crystal and glass was first observed in 1970 by Alfano and Shapiro by firing picosecond pulses into borosilicate glass [81]. The pulses of light, transmitted through the bulk media with an intensity of 1 GWcm^{-2}, were spectrally broadened from 400 nm to 700 nm. Supercontinium generation is not limited to glass and can be achieved in other media including solid state material, liquids, and gasses [82–84]. As the non-linearity of glass is relatively low, Alfano's experiment required a relative high power light source to generate the supercontinuum. While spectral broadening had been observed before [85], Alfano reported a broadening an order of magnitude greater than had been seen previously [86]. The mechanism responsible for spectral broadening in this first experiment was mainly due to self-phase modulation where an ultra short (femtosecond) pulse of light will induce a intensity dependent refractive index in the

medium due to the Kerr effect [87, 88]. The term supercontinuum was coined later in [89].

To produce the supercontinuum in a bulk media, high peak powers are required. The time-dependent shift of light is proportional to the length of the material, therefore, by increasing the interaction length, the spectral broadening of the light can be achieved at lower peak powers [90]. To extend the interaction length, optical fibres can be used. This method was the basis for the second generation supercontinuum generation light sources. The non-linearity of optical fibres means that there is a significant reduction in pump power required compared to bulk materials [91].

In fibre optic supercontinuum generation systems, the self-phase modulation mechanism has a smaller role in spectral broadening due to the longer pulse widths used (10 ps - 10 ns). Therefore the main mechanisms of supercontinuum generation are stimulated Raman scattering (SRS) and four-photon parametric generation [92]. The asymmetric broadening of stimulated Raman scattering, however, results in the extension of the pump source to higher wavelengths only. As most pump sources are at around 1064 nm, the visible and near infrared spectrum are not populated using this method. This makes the sole use of optical fibres unsuitable for supercontinuum lasers and hence not useful for near infrared spectroscopy, as the required wavelengths are not present.

Development of supercontinuum generation sources was significantly improved in the 1990s with the invention of Photonic Crystal Fibres (PCF) by Knight and Russell [93]. There are two main types of PCFs, categorised by their high and low index guiding properties. High index guiding fibres have a solid core similar to convention optical fibres, which is surrounded by an air filled microstructure 'lattice' [94]. The microstructure air-filled region has a lower refractive index than the solid core and internal reflection is maintained from this. Low index guiding fibres have a hollow core and rely on the photonic bandgap effect to confine the light in the fibre as it is unable to propagate in

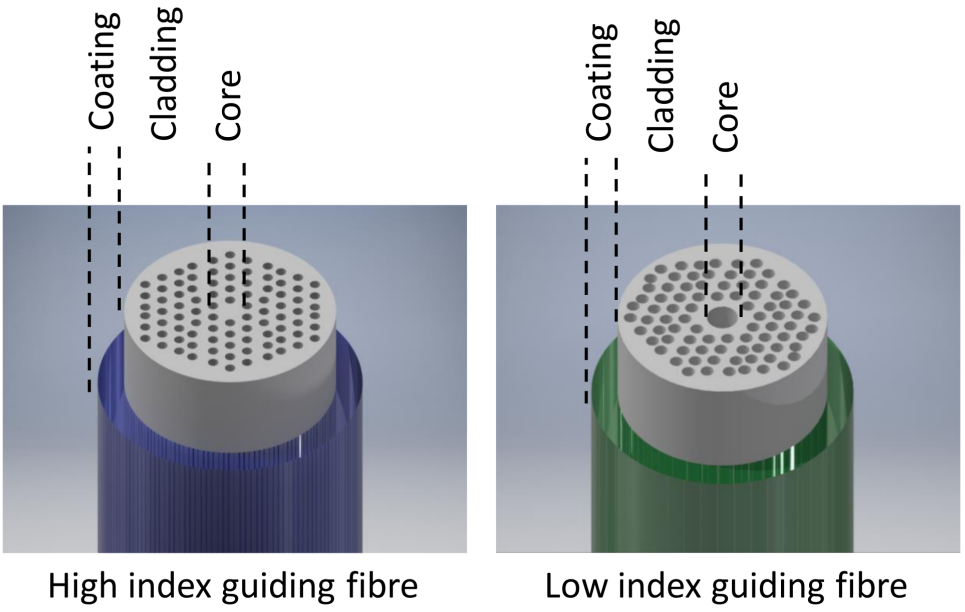

FIGURE 3.8: Diagram of the internal structure of photon crystal fibres. High index guiding fibres (left) consist of a solid core at the centre, micro structured cladding, and an external coating. Low index guiding fibres (right) have a hollow core.

the microstructure region in the cladding [94]. The structures of the two fibre types can be seen in Figure 3.8.

Supercontinuum lasers utilise the high index guiding fibres due to the high non-linearity making it efficient at low pump powers. The large difference in refractive index of the core and cladding in the fibre and linear lattice structure means that the fibres have properties ideal for supercontinuum generation. Due to the core and cladding structure, the light is concentrated into a very small spot size, increasing the non-linearity of the fibre two orders of magnitude over traditional fibres [95].

The structure of the PCFs means the dispersion characteristics can be tuned, and alteration of the group-velocity dispersion (GVD) properties achieved. The GVD of an optical fibre describes the dispersion of a pulse along its length. By using PCFs, the zero group-velocity dispersion wavelength, the wavelength at which there is no dispersion of the pulse, can be set in the 1000 nm region. Using a pump source at the zero group-velocity dispersion wavelength will result in symmetrical non-linear spectral broadening at longer

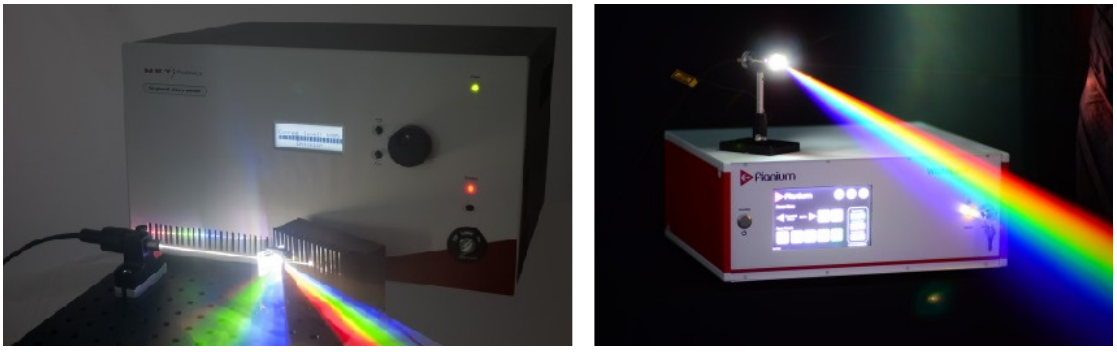

FIGURE 3.9: Supercontinuum light sources from NKT (left), and Fianium (right).

and shorter wavelengths. Supercontinuum lasers can therefore provide 'white' light with a broad spectrum ranging from 400 nm to 2400 nm. There are two major companies that produce supercontinuum sources for use in research and industry: Fianium (UK), and NKT Photonic (Denmark). Both produce a wide range of light sources with different power and spectral specifications (3.9). Detailed specifications and options of lasers from both companies is reported in Section 4.1.

3.2.4 Filtering the broadband spectrum

The time domain optical spectrometer developed in this research uses a supercontinuum laser for a light source and photomultiplier tubes for detectors, as described in Sections 3.2.3 and 3.3.1, respectively. Although supercontinuum lasers offer a broad spectrum of light across the near infrared range, photomultiplier tubes cannot differentiate between wavelengths of light and as such, effective time resolved measurements require a narrowband light source to be used. In order to use both technologies together, the light from the supercontinuum laser must be filtered into narrowband pulses. The light can be filtered before or after the subject or phantom, however, by filtering the light before the tissue, higher source powers can be used due to safety limitations.

There are three techniques that can be used to filter the light from the supercontinuum laser: bandpass filters, prisms, and acousto-optic tunable filters.

3.2.4.1 Bandpass filters

Bandpass filters allow the transmission of light with a defined wavelength band while preventing wavelengths that are outside this region from being transmitted. Bandpass filters use a Fabry-Perot cavity which, through constructive interference, allow a central wavelength and a small band of wavelengths close to the central wavelength, to be transmitted. Destructive interference blocks light with wavelengths outside the specified band from passing through the filter. An absorption layer is also used to absorb light with wavelengths far from the central wavelength as the destructive interference of the optical cavity has limited range.

Bandpass filters are used in the time domain system described by Selb et al. [75]. In this system bandpass filters with a FWHM of 11 to 13 nm were used in a fast change filter wheel. While bandpass filters can have a wide range of central wavelengths and relatively small bandwidths in the order of 2-3 nm, a limitation of their use is that specific wavelength choices cannot be made as the central wavelength depends on the materials used for its construction.

3.2.4.2 Prism

An alternative to using bandpass filters is to use a prism to spatially disperse the spectrum. By using a series of lenses, a narrow band of the light can be focused into an optical fibre. By mounting the prism onto a rotational stage the wavelength of light can be selected [96]. The system developed by Bassi et al. is capable of achieving a minimum bandwidth of 5 nm. However, this method requires fast moving mechanical parts creating technical challenges where high levels of accuracy are needed for alignment of the light into the optical fibre. As a result, use in a portable system is not suitable as considerable suspension of the optics would be required.

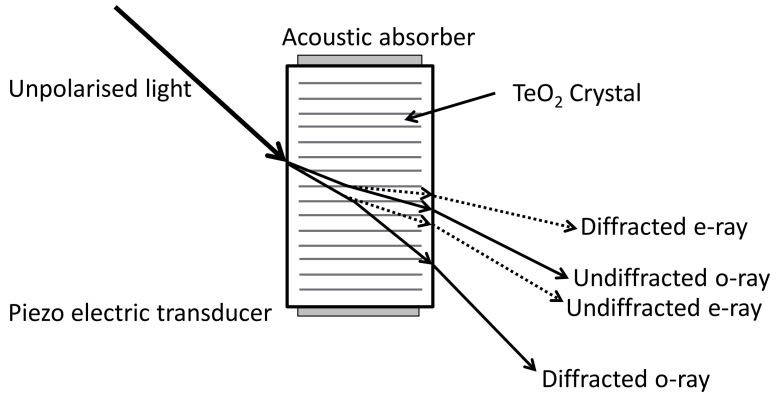

FIGURE 3.10: Shear waves in an acousto-optic tunable filter leading to the diffraction of light into its ordinary-ray and extraordinary-rays.

3.2.4.3 Acousto-optic tunable filters

The first acousto-optic tunable filter (AOTF) was developed by Harris and Wallace in 1969 using collinear acousto-optic diffraction in optically anisotropic media [97]. In 1974 Chang developed the concept to produce a noncollinear AOTF [98]. AOTF devices are based on elasto-optic effects of the crystalline structures which are optically transparent at the wavelength band of interest.

AOTFs use piezoelectric transducers bonded to compress quartz crystals, launching shear waves in the semi-translucent material. Operating in the hundreds of megahertz range the transducers create a series of wavefronts traversing the crystal, shown in Figure 3.10. The compression waves propagate through the crystal creating refraction 'wavefronts'. As light propagates through the crystal the refraction shear wave will refract light at a specific wavelength into a different direction to the incident light. The incident, ordinary-ray (o-ray) will be refracted into an extraordinary-ray (e-ray), whose polarisation is rotated 90 degrees. The diffracted white light will pass through the crystal in its original direction. AOTFs can then focus the diffracted wavelength into an optical fibre and transmit the light to the subject [99].

3.3 Photon detectors

The function of optical detectors in near infrared spectroscopy is to convert the arrival of light into a useful electrical signal that can be measured. In time domain near infrared spectroscopy single photons are counted, which means that detectors must have sufficient gain in order to convert the arrival of a photon into a usable electrical pulse. Time domain systems measure the time of flight of the photons. In order to accurately record the arrival times of photons, the output pulse from the detector must be free from significant timing jitter in the pulse width (transit time spread). The pulse must also be short enough to accurately resolve timing information of single photons at high count rates. Three types of detectors commonly used in current time domain spectroscopy devices (see 3.1.3.1) are photomultiplier tubes (PMTs), single photon avalanche diodes (SPADs), and intensified CCD (ICCD) cameras. Streak cameras were used in early time domain systems as they can provide very good temporal resolution, however due to their large size and cost they are no longer used in favour of cheaper, more compact devices.

3.3.1 Photomultiplier tubes

Secondary emission of electrons from a surface was first observed in 1901 by Austin and Stark [100]. In 1936, Zworykin et al. developed the first photomultiplier tube with multiple dynodes for secondary emission amplification [101]. Three years later, Zworykin and Rajchman developed a photomultiplier tube with electrostatically focusing dynodes [102]. With this design the electrons are electrostatically focused from one dynode to the next, increasing amplification of the signal and minimising the width of the pulse. While many improvements to this initial design of the photomultiplier tube have been made, the basic structure of current PMTs is the same.

Figure 3.11 shows the basic design of a PMT. There are three main components that constitute a PMT: a photocathode, multiple dynodes for secondary emission of photons, and

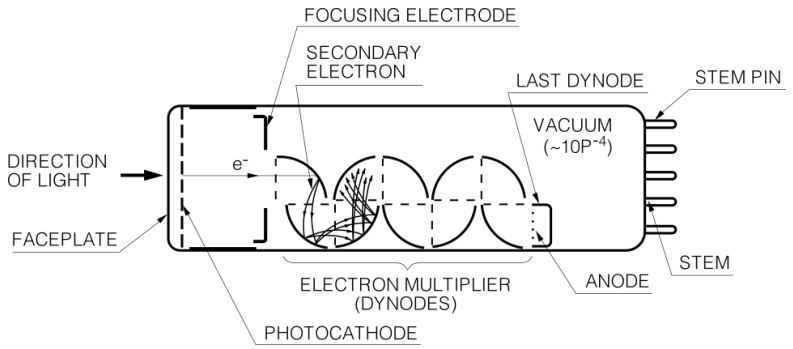

FIGURE 3.11: Typical structure of a photomultiplier tube. Figure reproduced with courtesy of Hamamatsu Photonics [103].

an anode to collect the electrons. The process of light detection using a PMT starts with light entering the input window of the tube. Light incident on the negatively charged photocathode exites electrons within the material causing the emission of photoelectrons due to the external photoelectric effect. These photoelectrons are emitted into a vacuum, where they are focused and accelerated by a focusing electrode onto the first dynode. Secondary photon emission occurs at the dynode multiplying the electrons in the vacuum. The electrons are electrostatically focused onto a series of dynode with increasing multiplication of the electrons through secondary emission. After multiple dynodes the electrons are collected by the anode and an output the electrical pulse.

The photoelectric effect describes the emission of electrons when light with the right conditions is incident on the material. In the case of PMTs, the external photoelectric effect results in the emission of a photoelectron into a vacuum from the surface of a photocathode. Other detectors such as SPADs rely on the internal photoelectric effect which results in the excitation of a photoelectron into the conduction band of a material. As the photocathode in a PMT is a semiconductor, the quantum efficiency (QE), a ratio of the number of incoming photons to emitted photons, is dependant on the material selected and the wavelength of the incident light. For visible light detection, multialkali photocathodes are typically used since Gallium Arsenide (GaAs) provides better quantum efficiency at longer wavelengths in the near infrared range (380-890 nm) [104].

The photocathode can be use in two different modes; reflective or transmission mode. The reflective mode cathodes normally used in side-on PMTs, consist of a metal plate, where emitted photoelectrons are reflected onto the first dynode. The transmission mode cathodes used in head-on PMTs are formed of a semi-transparent material which allows the electron to be emitted in the same direction as the incoming photon. The choice of cathode used depends on the layout required of the PMT, but head-on transmission mode PMTs allow a much larger detection area.

3.3.1.1 Dynodes

The function of the dynodes within a PMT is to multiply the number of photoelectrons in the vacuum in order to provide an amplified signal. The design of the dynode section is critical to provide optimum electron trajectory through the PMT in order to minimise the transit time spread. A current amplification of 10 to 108 times can be achieved in the dynode section.

The ratio of secondary electrons emitted per incident electron is called the secondary emission ratio (δ). Figure 3.12 shows the secondary emission ratio of different dynode materials for different acceleration voltages. The dynodes require a high voltage of over 1000 V to achieve maximum quantum emission ratio.

The shape and layout of the dynodes determine the electron trajectory through the PMT and the time response of the detector. The output signal from the anode is greatly affected by the electron transit time spread (TTS) within the PMT. Figure 3.13 shows the transit time and transit time spread of the electrons in the PMT. The time taken for the electrons to travel from the cathode to the anode in the PMT will vary from electron to electron. The FWHM of the frequency distribution of electron transit times is called the transit time spread. The temporal response of the PMT will depend on the dynode structure and the accelerating voltages used.

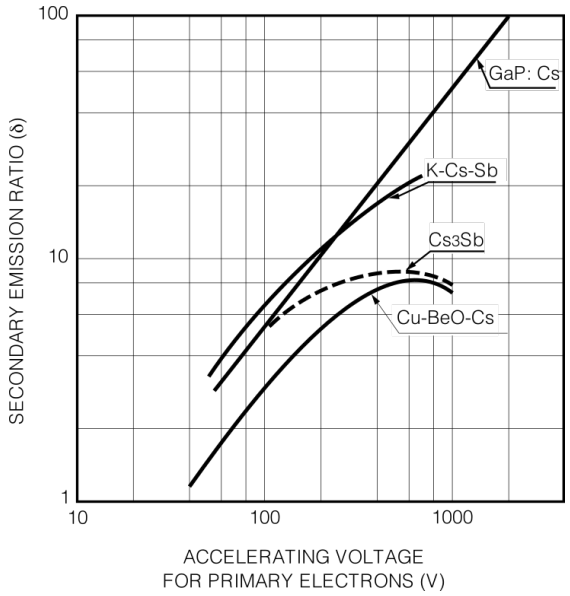

FIGURE 3.12: Secondary emission ratio of different dynode materials at different accelerating voltages. Figure reproduced with courtesy of Hamamatsu Photonics [103].

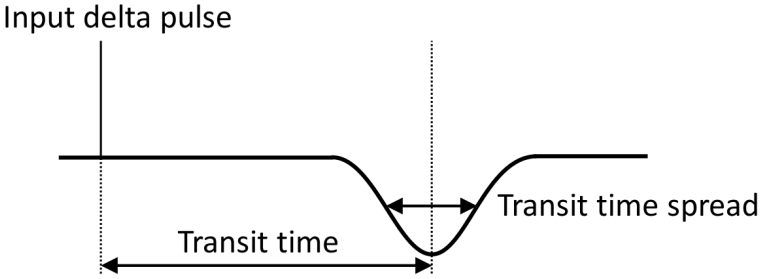

FIGURE 3.13: Transit time and transit time spread of electrons within the PMT. Figure reproduced with courtesy of Hamamatsu Photonics [103].

Three different PMT designs are shown in Figure 3.14. The electron multiplier section of the PMT typically contains 8 to 19 dynodes [103]. Box-and-grid type PMTs use transmission mode photocathodes and quarter circle shaped dynodes achieving high collection efficiency. Linear-focused detectors also use transmission mode cathodes, and the shape and design of the dynode provides high time resolution and high output current. Circular-cage type dynodes are used for compact PMT designs which provides fast response and high gain for low gain voltages.

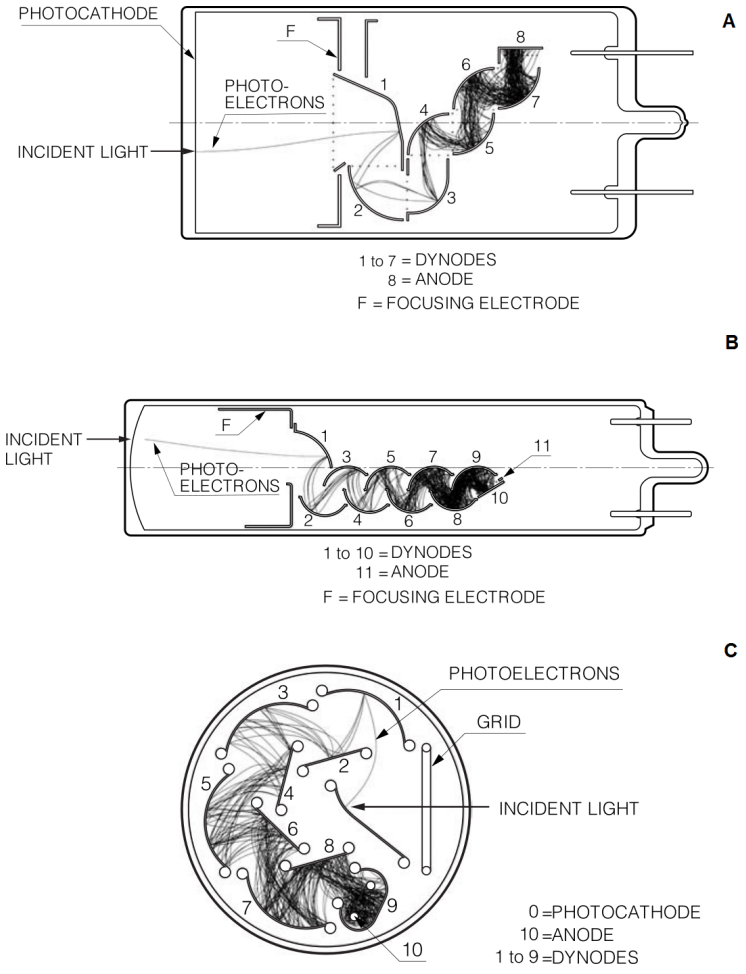

FIGURE 3.14: Different PMT dynode structures. (A) Box-and-grid type, (B) Linear-focused type, (C) Circular-cage type. Figure reproduced with courtesy of Hamamatsu Photonics [103].

3.3.1.2 Quantum efficiency of the photocathode

The quantum efficiency of a photocathode is the probability that a pulse will be generated at the output of the PMT due to the arrival of a particular photon. This efficiency depends on the material of the photocathode. The relationship between sensitivity and quantum efficiency is given by

$$\text{Quantum efficiency} = \frac{h.c}{\lambda.e} \times S = \frac{S \times 1240}{\lambda} \times 100, \tag{3.2}$$

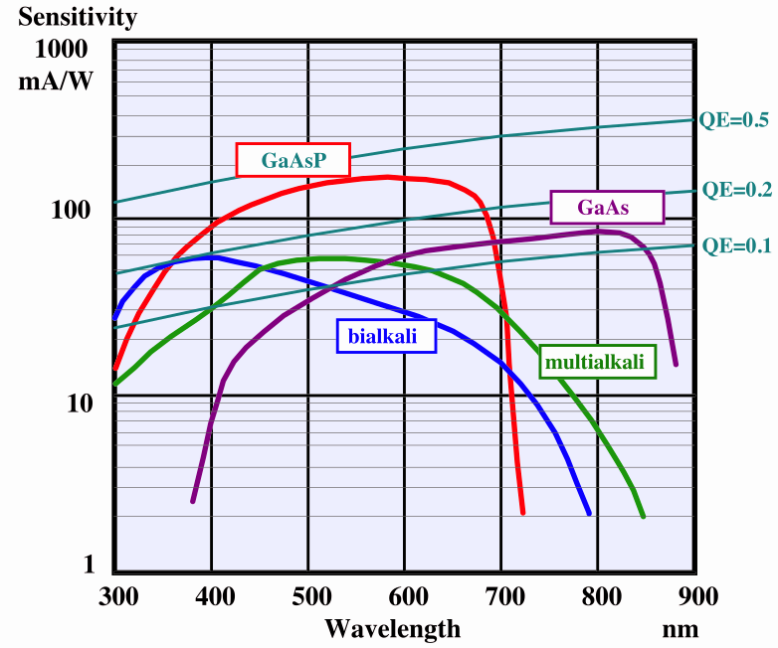

FIGURE 3.15: Quantum efficiency of different photocathodes. Figure reproduced with courtesy of Hamamatsu Photonics [103].

where S is the sensitivity in $AW^{-}1$ and λ is the wavelength (nm). Figure 3.15 shows the quantum efficiency of commonly used photocathodes. The bialkali and multialkali cathodes used in visible light collection reach a quantum efficiency of 20-25%. GaAsP cathodes provide the highest quantum efficiency of 45% however are not suitable for use in the near infrared spectrum as the sensitivity drops off significantly at 700 nm. GaAs cathodes provide greater spectral range with high sensitivity up to 890 nm.

3.3.1.3 Dark counts

A small number of pulses will be generated by PMTs in the absence of light. These pulse are called dark counts and will produce noise in the measured TPSF. The majority of dark counts will be due to spontaneous thermionic emission of electrons from the cathode. Temperature will greatly affect the number of dark counts and an increase of 10 degrees Celsius at the cathode can increase the number of dark counts by and order of magnitude

[103]. Peltier coolers are often implemented in PMTs to decrease the temperature of the cathode reducing the noise due to dark counts.

3.3.1.4 Microchannel plate

Microchannel plates (MCP) consist of a thin disk with a large number of glass capillaries placed in parallel shown in Figure 3.16. The process of electron multiplication is similar to that of PMTs with dynodes, where the inner walls of the glass channels produce secondary electron emission. The thin diameter of the microchannels, in the order of tens of microns, means that the electron trajectory is restricted and results in a small transit time spread of the signal. The ratio of the channel length to the diameter of the microchannel is $\alpha = L/d$. Typical MCPs have an α value of 40 to 60. Due to the small diameter of the channels the transit time spread of a typical MCP is less than 50 ps which offers very good temporal resolution for TCSPC applications. However, the efficiency of MCPs are much lower than PMTs and significantly more expensive. MONSTIR implemented MCPs for multichannel detection of light, though experienced difficulties with cross talk and short detector lifetime [48].

3.3.2 Single photon avalanche diode

Single photon avalanche diodes (SPADs) offer a solid state alternative to photomultiplier tubes for single photon detection and TCSPC applications [106]. The avalanche photodiode was developed in 1960 at the Shockley Laboratory by Goetzberger et al., where detection of a single photon at a p-n junction was first made [107].

In photodiodes, when the photon hits the semiconductor the internal photoelectric effect causes an electron-hole pair to be created. Due to the inbuilt electric field of the depletion region in the p-i-n junction, the electrons and holes move in opposite directions, each flowing towards the cathode and anode respectively. In optical spectroscopy, however,

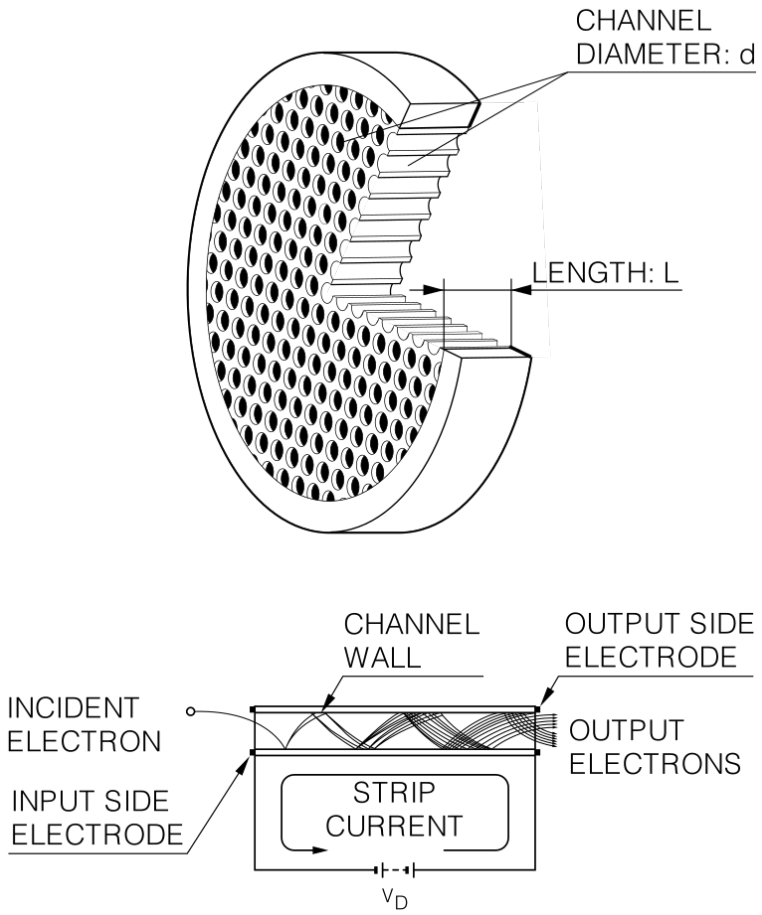

FIGURE 3.16: Structure of a microchannel plate (MCP) and electron trajectory within a channel. Figure from [105].

the light intensity is far too low to create a measurable current at the photodiode, so the avalanche effect is utilised. The semiconductor lattice is held at a reverse bias so that the electrons excite new electron hole pairs as they move in the materials to amplify the signal.

Figure 3.17 shows the production of electron hole pairs and the avalanche effect though the SPAD. SPADs differ from APDs as they allow detectable signals to be triggered by light down to a single photon. This is achieved by operating the reverse bias at a higher voltage than would be used in an avalanche photodiode, where this voltage would normally destroy the diode. SPADs utilise a quenching circuit to recover the semiconductor material after each photon, preventing breakdown.

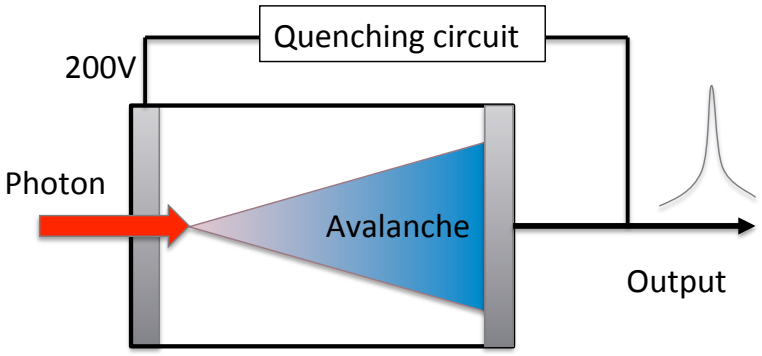

FIGURE 3.17: Avalanche effect in a single photon avalanche diode. Figure adapted from [51].

There are two different methods of quenching circuits; the first is passive quenching where a capacitor automatically discharges through the diode when photons are detected. This then lowers the voltage of the material below breakdown, stopping the avalanche effect until the voltage across the diode returns to the initial bias ready for the next photon. This type of quenching is relatively slow and unsuitable for applications where the incoming photon rate is higher than 1 MHz. The second method is called active quenching. The signal produced by the diode is detected by a circuit in the SPAD which then triggers the bias across the diode to be rapidly decreased below breakdown allowing the diode to recover before reapplying the reverse voltage. The active quenching SPADs are more preferable as they have a much faster recovery time, which is in the order of a few tens of ns in comparison with passive quenching diodes which recover in a few ms.

3.3.3 Intensified charged coupled devices

Another option for photon detection are intensified CCD (ICCD) cameras. Charge coupled device (CCD) cameras have been quite extensively used in continuous wave spectroscopy [42, 108], as they are an easy and efficient way of measuring the intensity of detected light, and require little extra equipment such as variable attenuators in order to make measurements. Conventional CCD's are too slow to be used as single photon devices and

so cannot be utilised in time domain measurements. However, if an image intensifier is used in conjunction with the CCD fast photon counting can be achieved [109]. The image intensifier is formed of a photocathode which is placed in front of a small microchannel plate. This generates a cascade from a single electron and enables a significant electrical pulse to be counted by the CCD. One major benefit of this set up is that the image intensifier can effectively be used as a shutter to gate the measurement. By reversing the voltage on the photocathode and the MCP, the electrons will be attracted back to the cathode and no signal will reach the CCD.

3.4 Time correlated single photon counting

Time correlated single photon counting (TCSPC) is relies on the detection of single photons from a pulsed light source. The times-of-flight of individual photons are measured and through collection of many photons a 'waveform' can be reconstructed [50, 110, 111]. The TCSPC measurements requires a constant, stable, fast repetition rate light source and reference pulse in order to measure the time of flight of the photons. The intensity of light needed at the detectors is relatively low and TCSPC measurements require the number of photon detection in a pulse period to be between 1 and 0. The detected signal will be a random spread of pulses over the time axis. The detected pulses only have relevance in relationship to the reference pulse of the light source. With both these signals a TCSPC measurement system can measure the time of flight of each individual photon (i.e. the time taken for the photon to travel from the light source to the detectors). In TCSPC systems when a photon is detected, the time between the photon arriving and a reference pulse being measured and the time-of-flight for that photon is calculated. The events are then stored in memory by adding '1' to a time channel corresponding to the time detected. This process repeats for every pulse of the light source and a 'waveform' is generated from the photon arrival times. This waveform is

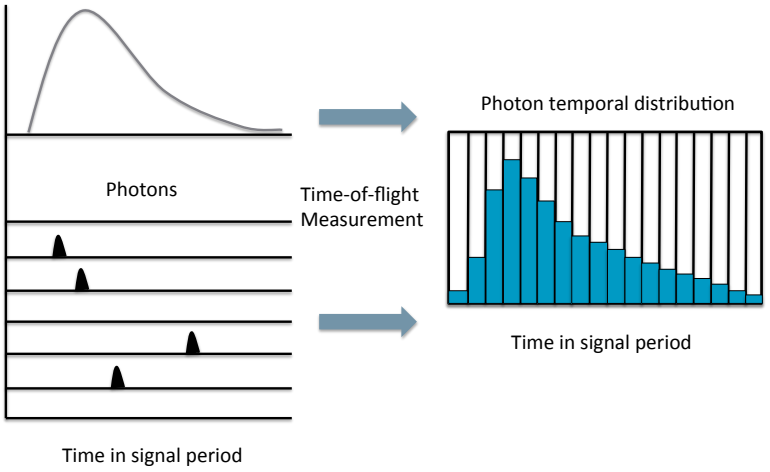

FIGURE 3.18: Single channel time correlated single photon counting technique.

actually a distribution or histogram of photon flight times and is called a temporal point spread function (TPSF). The process is shown in Figure 3.18 for single and multichannel TCSPC systems. In a multichannel TCSPC recording system the flight times of photons from different detector channels are stored in different TPSFs.

The output pulse form a detector is called the single electron response (SER). TCSPC is not limited by the width of the SER for its timing resolution but the transit time spread of the detector and high accuracy at which the arrival time of the photon can be measured. This section discusses the process of time correlated single photon counting as performed by Becker and Hickl photon counting cards.

3.4.1 TCSPC electronics

The general architecture of TCSPC electronics is outlined in Figure 3.19. TCSPC require two input pulses, one from the detector indicating the arrival of a photon, and a timing reference pulse from the laser. These signals are passed into two constant fraction discriminators (CFD) which remove timing jitter from the pulse. These signals trigger the start and stop of a time-to-amplitude converters (TAC) which generates a voltage proportional to the time separation of the two pulses. The voltage is amplified and an

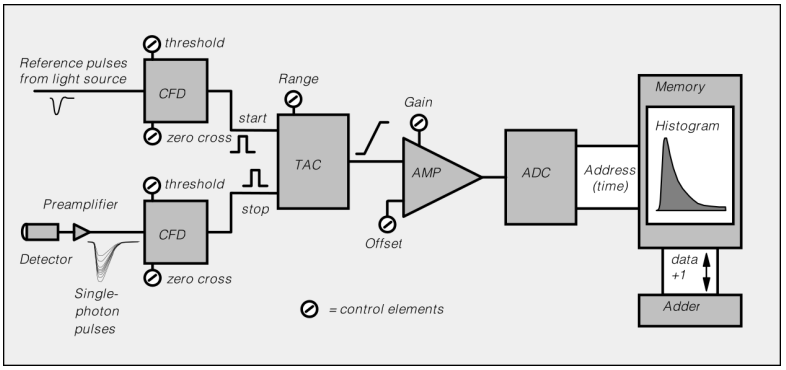

FIGURE 3.19: Basic architecture of an modern TCSPC device. The pulses from the detector and pulse reference enter two constant fraction discriminators (CFD) which trigger the start stop operation of the time to amplitude converter (TAC). The voltage generated by the TAC is amplified and the analogue to digital converter (ADC) allocates the information to the memory generating a histogram of photon flight times. Figure from [51].

analogue-to-digital converter (ADC) reads the voltage and converts it into an address in the memory. Each photons time-of-flight is recorded in the memory and a distribution of photon flight times can be generated.

3.4.1.1 Constant fraction discriminators

The function of TCSPC electronics is to measure the time between a pulse generated by a detector from the arrival of a photon and a reference pulse from the light source. If the detectors and laser reference produced perfectly uniform pulses with identical pulse width and amplitude a leading edge trigger could be used to start and stop the timing. However, due the random amplification mechanism of the detectors used in TCSPC measurements (PMTs, SPADs, MCPs) the pulses produced are far from uniform. As can be seen in Figure 3.20 which shows the output from a standard PMT module, the pulse has considerable fluctuation in amplitude and pulse width. A leading edge trigger set at a trigger threshold as shown in Figure 3.21(left) would introduce significant time jitter in the measurement as the start time of the TAC would be dependant on the amplitude and rise time of the pulse from the detector.

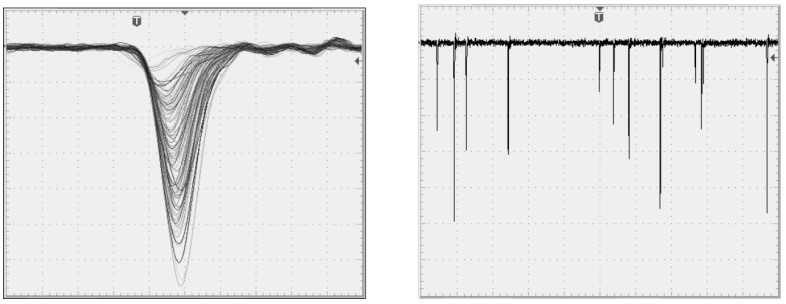

FIGURE 3.20: Output pulses triggered from a Hamamatsu R5900 PMT (Left), Pulse output over time (right). Figure from [51].

To prevent error due to timing jitter in the measurement due to pulse height and rise time, constant fraction discriminators are use in the signal path of the TCSPC cards. A constant fraction of the pulse height of the signal pulse is used as the trigger and therefore does not depend on the amplitude, eliminating pulse height jitter. In order to mark the trigger point of the signal, the CFDs convert the pulse shape so that a zero cross point can be used as a trigger. To achieve this, the input pulse is duplicated, inverted and delayed. By summing the pulse and the duplicated pulse a zero cross point will be created as shown in Figure 3.21. The zero cross point does not depend on the amplitude of the detector pulse, minimising any timing jitter.

The reference pulse from the laser can be generated using several methods, a common technique is to use a fast photodiode at the source output. This signal may be subject to amplitude jitter or drift over time, therefore, a second CFD is also used on this signal.

The CFDs contain a discriminator for cutting off low amplitude pulses from the detectors or pre-amplifiers. If PMTs are used this will reduce noise from small pulses generate from spontaneous electron emission within the PMT.

3.4.1.2 Time-to-analogue converters

The time-to-amplitude converter (TAC) measures the time between the pulse produced from the detector, and the reference pulse from the light source. The TAC is triggered

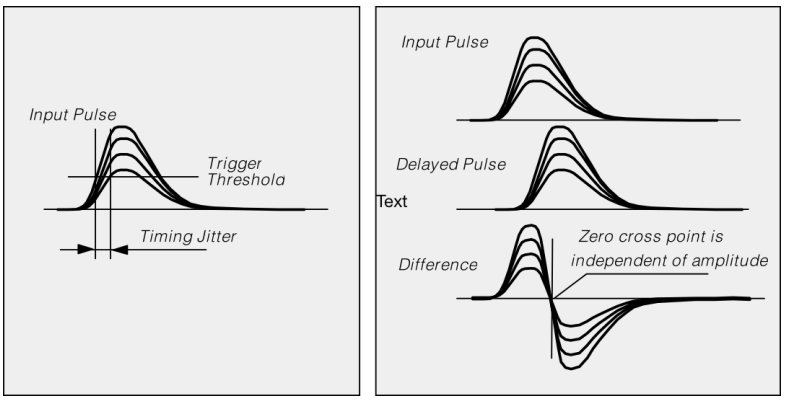

FIGURE 3.21: Leading edge triggering (left), signal processing of the constant fraction discriminators (right). Figure from [51].

by the zero cross over point created by the CFDs, and starts a charging a capacitor to generate a linear ramp voltage. When the second zero cross over point occurs, the TAC stops the linear ramp voltage. Charging the capacitor with a constant current source means that the voltage generated is proportional to the time between pulses. This method is highly accurate and sub-picosecond resolutions can be achieved.

3.4.1.3 Reversed start-stop technique

At low frequencies a TAC could operate in a conventional way where the linear ramp voltage is started at each reference pulse. The TAC would then stop at the detection of a photon and the voltage will be proportional to the time from the reference pulse to detected pulse.

However, in TCSPC measurements there is a low probability of a photon detection event occurring for each pulse period (time between pulses). Therefore the TAC will begin the process of charging the capacitor without being stopped. The TAC then is required to reset before the next pulse period. At high frequencies used in TCSPC this process would mean a significant workload for the TAC. For a source frequency of 60 MHz the TAC would be required to reset every 16.6 ns, whereas we typically expect a count rate

of more that an order of magnitude less. Therefore, a reversed start-stop configuration is used, reducing the requirements on the electronics.

In reversed start-stop mode the TAC is started at the arrival of a pulse due to the detection of a photon. The TAC then measures the time between the detected photon and the next synchronisation pulse. This significantly reduces the workload of the TAC. The voltage measured by the TAC is therefore inversely proportional to the time-of-flight of the photon and this inversion can easily be made in the ADC. The voltage on the TAC is then amplified by a programmable gain amplifier before being measured by the ADC.

3.4.1.4 Analogue-to-digital converters

The analogue-to-digital converter, measures the voltage on the TAC and converts it to an address in the memory. The ADC measures the voltage with very high precision resolving the signal into one of 4096 time channels with a sub picosecond resolution.

3.4.1.5 Router

If a single channel system is developed (i.e. one source and one detector) the pulses generated by the detectors can be passed directly to the CFDs in the TCSPC electronics. All time-of-flight data will be processed and allocated into a single memory location. However, when a multichannel detector system is used, the TCSPC electronics must separate the pulse into separate waveforms. As the pulses themselves do not contain any information about their origin, a router must be used to encode the detector channel with each pulse.

The basic architecture of a routing module and its function in the TCSPC system is shown in Figure 3.22. The routing modules developed by Becker and Hickl allow up to eight detectors to be connected to a single TCSPC card [112]. The pulses from the detectors

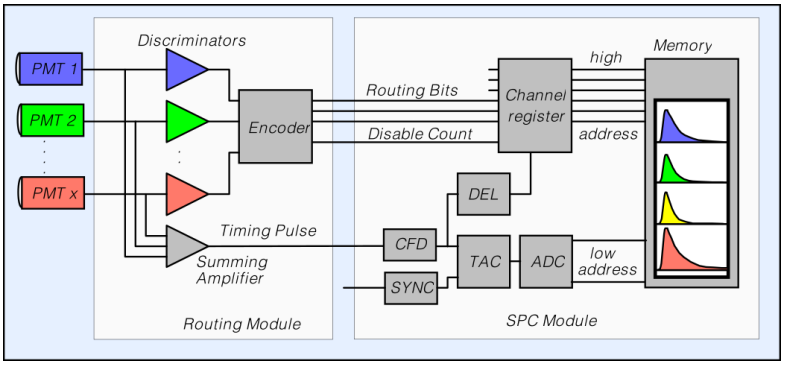

FIGURE 3.22: Function of the routing module, The router registers the detector channel which the pulse originates from and encodes this information for the channel register to sort the pulses into their respective channels. Figure from [51].

are fed through amplifiers before a discriminator eliminates noise in the channel by only allowing pulses greater than a reference voltage pass through. The signals that exceed the reference voltage are encoded and a channel indication signal is sent to the TCSPC card indicating which detector each pulse is from. While this is happening the original is passed through a summing amplifier and sent to the TCSPC card for the measuremt of the time-of-flight.

With the timing signal and the channel information from the router, the TCSPC card can allocate the signal to a specific time channel in the TPSF, corresponding to the appropriate detector. The process of encoding the channel in the router and sending the 'counting bit' to the TCSPC cards takes 10 to 20 ns longer than the time taken for the timing pulse to arrive. Therefore a routing delay is used in the channel register. This means that when a timing pulse is triggers the TAC and ADC, the TCSPC electronic wait for a specified time (longer than 20ns), to receive the channel 'count bit' from the router. It then allocates the photon detection event to the correct channel in the memory.

3.4.1.6 Dead time

One of the largest sources of error in a TCSPC is dead time in the system. Dead time is the period after a detection of a photon where the system is unable to count another

photon and is effectively blind to any incoming photons. The major consequence of dead time is the reduction of the maximum count rate, but it can also introduce distortions in the shape of the TPSF.

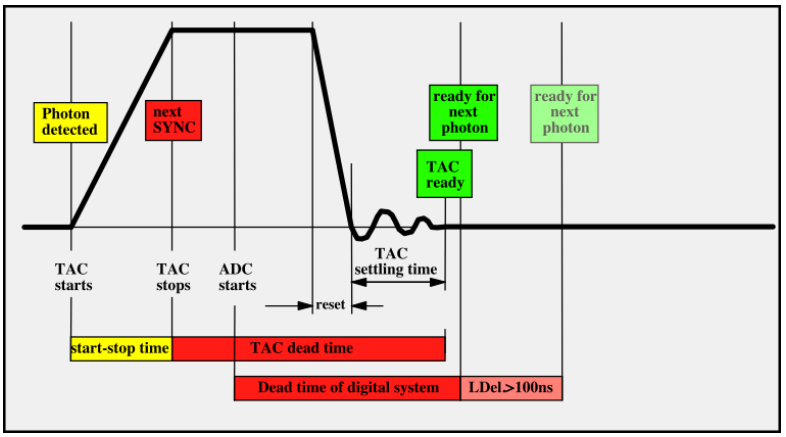

FIGURE 3.23: Dead time of the TCPSC electronics. Figure from [51].

The dead time occurs after a photon is detected. When the CFD initiates the start stop mechanism, the TAC starts charging a capacitor resulting in a ramp voltage. When the next reference pulse arrives the CFD stops the TAC voltage increasing. At this point another pulse of light has been injected into the tissue and a pulse from a detected photon could arrive at any time. However, the TCSPC electronics is unable to register the photon as the TAC is still at high voltage. Around 10 ns after the TAC stops the ADC starts reading the voltage on the TAC requiring a small amount of time before the TAC can begin to reset. When the ADC is finished the TAC is able to discharge and recover. Both of which require a short time period in the order of nanoseconds to reset as shown in Figure 3.23.

This process results in a dead time in the order of 100 ns for a source frequency of 60 MHz. The maximum count rate of the system is calculated as the reciprocal of the dead time. Measurements with dead time of 100 ns will have a maximum count rate of 10 MHz.

3.5 Discussion

This chapter gives a broad overview of the current state of near infrared spectroscopy, and reviews in detail, state of the art systems developed by research groups around the world. The individual electronics used in these systems are then described, especially in relation to use in time resolved NIRS.

3.6 Chapter summary

This chapter give a background on near infrared spectroscopy, detailing the three measurement modalities; continuous wave, frequency domain and time domain. The technology and design for existing systems developed globally for all three techniques are reviewed, focusing on state of the art time resolved instrumentation.

The review of existing time domain near infrared spectrometers and imaging systems shows that there are many different solutions to the instrumentation used. The chapter therefore describes some of the commonly used technologies which are suitable for use a light source, wavelength filtering, photon detection and the timing electronics.

Chapter 4

System development

This chapter describes the design and development of a multichannel, multiwavelength, time resolved near infrared spectrometer. A schematic of the completed system is shown in Figure 4.1. It is based on a supercontinuum laser with a AOTF module which produce short pulses of light in the near infrared region. The design choices and considerations when building and calibrating the system are described in detail, and results from the testing of individual components are discussed.

The requirements for the system are as follows:

- The system should be able to measure the times of flight of photons with pico second resolution as they pass through tissue, in order to calculate the absorption and scattering of light in tissue at single wavelengths.
- The system should be able to measure at least 8 wavelengths sequentially in a short period of time, so that data for multiple wavelengths can be assumed to occur over the same biological conditions. Analysing broadband near infrared measurements has shown the advantage of using many wavelengths, increasing the accuracy of calculating certain chromophores from 10% error to 2 % [3].

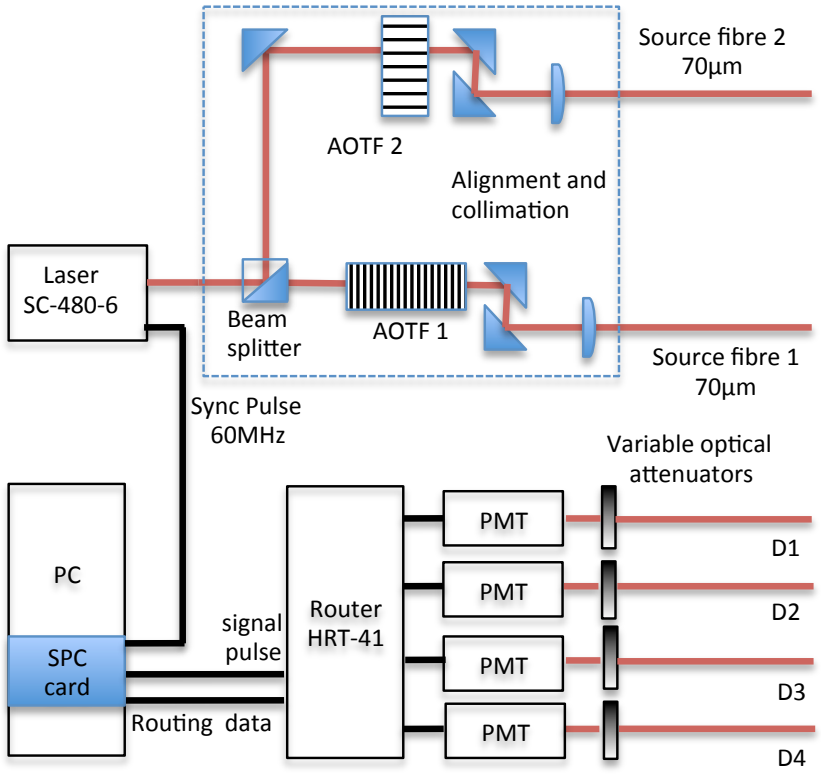

FIGURE 4.1: Schematic of the completed multichannel, multiwavelength, time resolved near infrared spectrometer.

- The system will be able to detect wavelengths in the range 650-900 nm, within which absorption from water and haemoglobin is relatively low. This range is known as the near infrared window.

- The system will have four detector channels and two source channels to acquire data from different areas of the head in order to obtain spatial information.

- The wavelengths of light should be adjustable so that different configurations and combinations can be used.

- The light source should produce pulses shorter than 10ps. The pulse width will contribute to the full width half maximum of the IRF, and by minimising this the accuracy of the measurement will be increased.

- The system will use some form of variable optical attenuation to increase the dynamic range of the system.

4.1 Light source

The technical requirements for the light source in the system are:

- Pulsed light source producing pulses of duration <10ps.
- Optimised for NIR wavelengths in the region of 600nm to 900nm.
- Narrowband single wavelengths below 5 nm.
- Fast switching between 16 wavelengths up to 100Hz.
- Produce up to 3mW of power for a single wavelength at the 100μm single mode fibre tip connected to the output of the AOTF.
- Stable power output over this range for at least 10h.
- Repetition rate between 40Mhz and 80Mhz.

4.1.1 Choice of Supercontinuum Laser

Spectral broadening using non-linear optics has been studied for many decades, with supercontinuum generation in bulk glass being first observed in 1970 by Alfano et. al [81]. Supercontinuum lasers, however, have only been commercially available for around the last decade and there are only a few companies that produce supercontinuum lasers globally, with two of the largest being Fianium and NKT photonics. Both sell high powered supercontinuum sources with various mechanisms for wavelength selection, and have been extensively used with other biomedical laboratories for time resolved spectroscopy

[55–57, 74, 75, 96, 113–115]. The aim of this project was not to develop a light source for this application, but to buy a commercial laser that requires little development or modification to operate in the system. Therefore the choice of laser was narrowed down to Fianium and NKT, who produce supercontinuum lasers FemtoPower1060 and SuperK EXTREME, respectively. The two lasers can be seen in Figures 4.2 and 4.3.

FIGURE 4.2: Fianium supercontinuum laser Femtopower1060.

FIGURE 4.3: NKT Photonics supercontinuum laser SuperK EXTREME.

4.1.1.1 Laser size

The Fianium and NKT lasers are significantly different with respect to the form factor. The dimensions of the NKT are 440 x 243 x 380 mm, where as the Fianium laser measures 524 x 300 x 216 mm and enclosed in a 19 inch 4U rack mountable box. On form factor alone the Fianium laser has significant benefits as no additional mounting is needed in order to be fixed to the system.

4.1.1.2 Spectral power density

Both NKT and Fianium lasers have a master source at 1060nm producing a peak in the spectral power density seen in the specification of the lasers (4.4 and 4.5). As we only require the laser output to lie in the range 600-1000nm, the 1060nm peak and above will have no impact on our measurements. In the 600-100nm range both lasers have similar spectral output, the Fianium SC480-6 varying between 3 and 5 mW/nm, and the EXR-15 (scaled EXR-20 for power) producing between 3 and 6 mW/nm. While these spectral power densities are representative of the standard laser options, NKT and Fianium will both adapt the photonic crystal fibre in the laser in order to produce a flatter spectrum in the near infrared region.

4.1.1.3 Fianium

At the time of purchasing a laser for the system, Fianium had 3 options for high powered supercontinuum lasers: the SC480-4, SC480-6 and SC480-8, each with total power 4W, 6W, and 8W respectively. All three supercontinuum lasers are based on a master source, which is a passively modelocked Yb-doped fibre laser, a high power fibre amplifier and a supercontinuum generator using photonic crystal fibres. The key differences between the three options are detailed in Table 4.1.

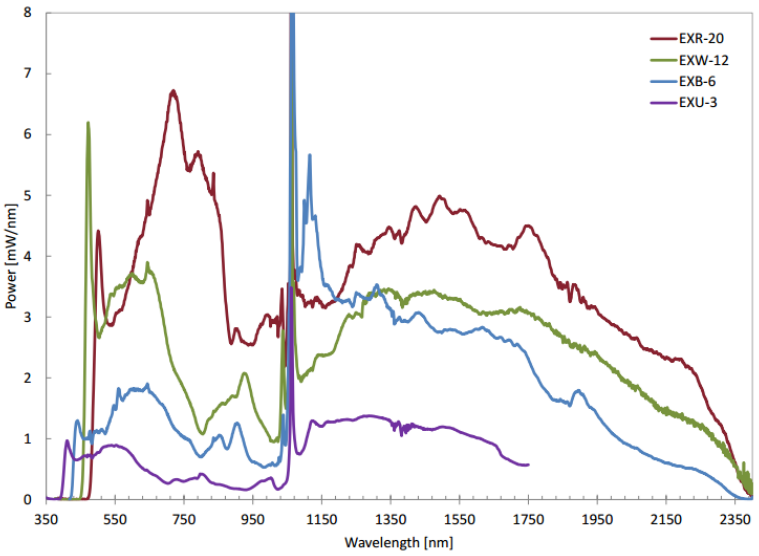

FIGURE 4.4: NKT Photonics Power spectral density form laser data sheet. The legend specifies lasers calibrated for different wavelength ranges. EXR-20 is the laser calibrated for the near infrared region.

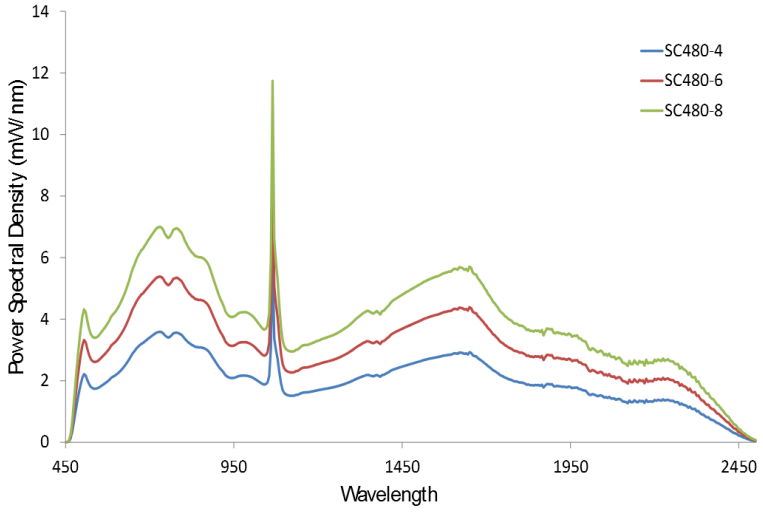

FIGURE 4.5: Fianium Power spectral density from laser datasheet, showing a peak at 1060nm due to the master source.

Fianium has an AOTF-Dual system that houses two AOTF crystals in order to avoid loss of power due to polarisation of light. The AOTF-Dual system can therefore be used with two near infrared AOTF crystals to produce two source outputs without the need for splitting the light at a later stage. While the same laser is providing power for both AOTF crystals, they can be controlled independently with software and external DAQ cards to

Parameter	SC480-4	SC480-6	SC480-8
Total output power	>4W	>6W	>8W
Average Spectral power density	>2mW/nm	>3mW/nm	>4mW/nm
Repetition rate	40MHz	60MHz	80MHz
Visible power (400-850nm)	900mW	1300mW	1700mW
Minimum wavelength	480nm	480nm	480nm
Maximum Wavelength	2400nm	2400nm	2400nm

TABLE 4.1: Specifications of different Fianium lasers

effectively provide two independent sources.

The AOTF system comes in a form factor shown in Figure 4.6, with the addition of the two RF drivers for the crystals. However, on request Fianium were able to provide the AOTF optical setup and drivers in separate 19in 2U rack mount enclosures. This would result in the entire light source system taking up 8U of space in the rack.

At the time of purchasing the laser, no specific software was available, and so the laser communicates to the computer through serial commands which can be easily incorporated into custom software.

FIGURE 4.6: Fianium AOTF-Dual system standard enclosure.

4.1.1.4 NKT

The NKT laser utilises similar technology for supercontinuum generation as the Fianium laser, with a 1060nm master source, amplifier and photonic crystal fibre for supercontinuum generation. The repetition rate on the master source is user selected using a pulse picker with range of 2-78 MHz. The power stability of the laser is $\pm 1.5\%$ and has a master seed pulse duration of $\sim$5 ps.

All SuperK Extreme lasers have a broad spectral range of 400-2400nm (Figure 4.4), and the supercontinuum generation can be customised so the the maximum power can be achieved in the near infrared range. The NKT SuperK laser comes with a propriety SuperK SELECT system (Figure 4.7(A)) for selecting wavelength using AOTF technology. The laser is connected to the AOTF module using propriety connectors called SuperK CONNECT (Figure 4.7(B)), offering simple alignment and "plug'n'play" capability. At the time of purchasing the light source, there was not the option of using two near infrared crystals to give the same output range, as polarising beam splitters were not used in the system. The Command box seen in Figure 4.7(C) provides easy access to the AOTF crystal drivers for fast switching, which would require a DAQ card to provide TTL signals.

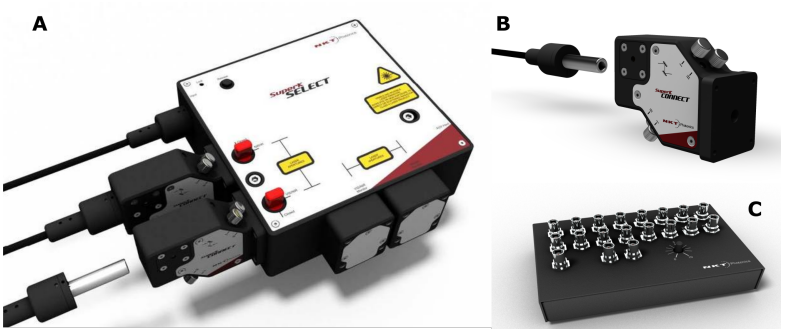

FIGURE 4.7: NKT SuperK Extreme accessories, (A) SuperK SELECT AOTF module, (B) SuperK CONNECT proprietary fibre connection and alignment system, (C) SuperK COMMAND wavelength selection and fast switching module.

Laser	Manufacturer	Power	Pulse rate	Pulse duration
Femtopower 1060	Fianium	6W	60Mhz	4ps
SuperK EXTREME	NKT	6W	60Mhz or pulse picked	5ps

TABLE 4.2: Specifications of the Fianium and NKT laser sources

4.1.1.5 Summary

The Fianium SC480 and NKT SuperK Extreme both rely on very similar technology for supercontinuum generation, and therefore the output from the lasers are similar in power and spectral density over the near infrared range. As can be seen in Table 4.2, there is very little difference in the key specifications of the lasers alone. Deciding which laser to use in the system came down to form factor and the available options for wavelength selection. The system enclosure will be based on a 19 inch rack cabinet, which means that the Fianium has a major advantage over the NKT, since no extra adaptation is needed for mounting. The AOTF system utilised in the Fianium also gives a significant advantage over the NKT, as the AOTF module will not only provide two outputs but will also provide twice the power output due to the 90 degree AOTF design. After considering these points the Fianium laser was chosen to be used in the system for the power advantage and the ease of installation.

4.1.2 Laser temporal stability

The Fianium SC480-6 Laser has a seed pulse that is produced by an internal fast photodiode that monitors the master source via a polariser. A clear uniform signal is key for high quality time resolved data. The SYNC pulse is used in the timing electronics to measure the time between the photon arrival at the PMT to the next synchronisation pulse, in order to measure the times of flight of the photons (stop-start mode is explained in Section 3.4.1.3). The raw output from the seed pulse can be seen in Figure 4.8. The TCSPC card used in the system requires a negative SYNC pulse, and so an A-PPI inverter is used to invert the signal (Figure 4.9). There is a small post peak in the inverted signal,

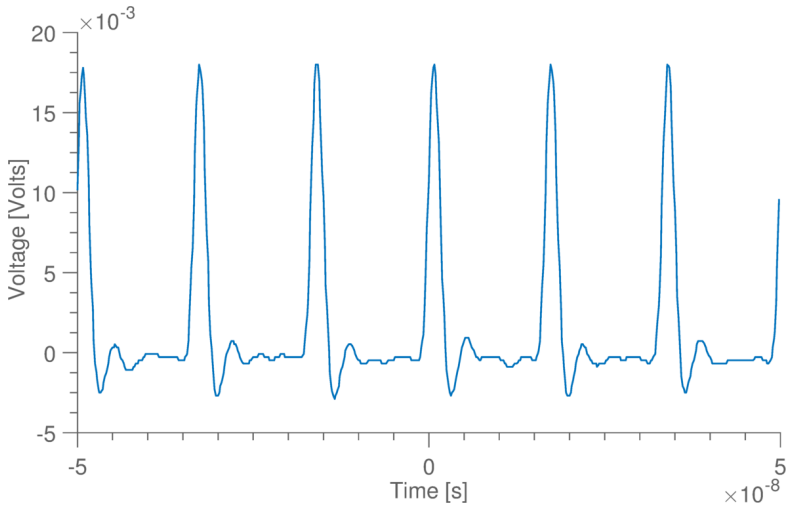

FIGURE 4.8: Raw seed pulse from Fianium laser using a 200MHz oscilloscope with an inline 50Ohm 3db attenuator.

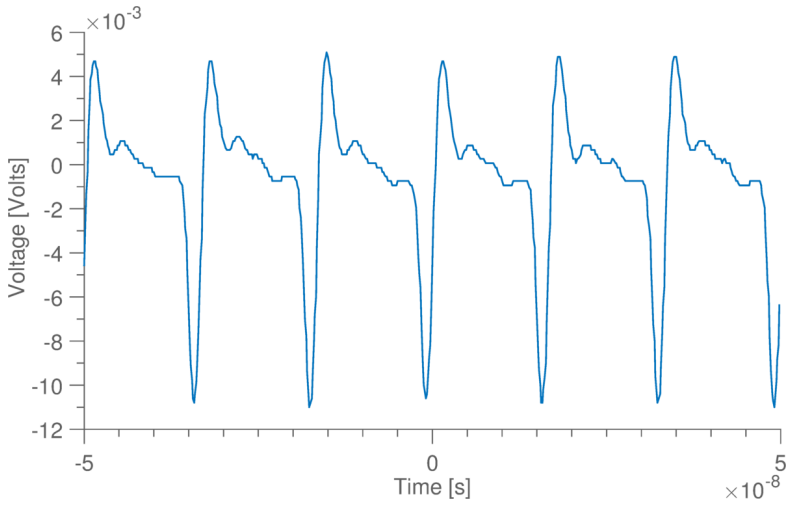

FIGURE 4.9: Inverted seed pulse from Fianium laser using the addition of an in line Becker and Hickl A-PPI inverter.

however when using the TCSPC software there has not been any variability to the sync pulse frequency, so it is not expected that this pulse will affect the measurement.

The laser produces a sync pulse at 60.03 MHz, which is within the expected limits set out by Fianium 57-63 Mhz. The stability of the seed can be seen in Figure 4.10. This is measured with the Becker and Hickl SPC-130 EM which is described later in this chapter. The pulse is generated by a photodiode in the laser and used as a reference for measuring the time of flight of photons. There is a very slight variation in the frequency of the pulse

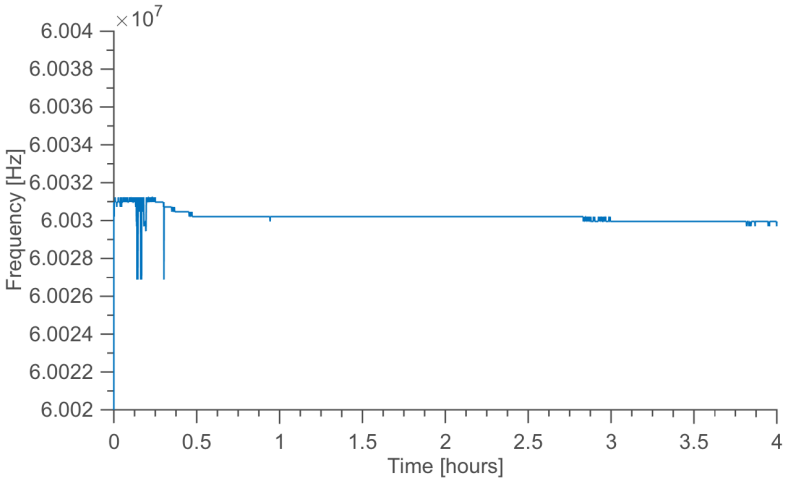

FIGURE 4.10: Laser seed pulse stability measured through a Beker and Hickl TCSPC card.

for the initial 30 minutes of operation, and then it remains very stable over several hours. While it is advisable for the entire system to be left for 20 minutes from start up to measurement to ensure temperature stability, the small changes seen in the frequency would not significantly affect the measurement.

4.1.3 Laser power stability

The Fianium laser has a specific operation procedure to ensure the master source and amplifiers are switched on in the correct order, and to allow the master source to stabilise before the gain is turned up. The normal operation of the laser requires a 10 minute warm up period before the master oscillator can be enabled via the 'laser enable' key (Figure 4.2). With the master source and low power amplifier active the laser output can then be controlled by software to set the gain on the high power amplifiers.

The laser output power stability can be seen in Figure 4.11 for both AOTF source channels. The power was measured from the point of setting the gain to maximum immediately after the 10 minute warm up and master oscillator activation, and measured for 16 hours. Both data series were measured after the AOTF output at 800 nm using a Thorlabs PM100A power meter on two separate occasions to ensure repeatability. A significant

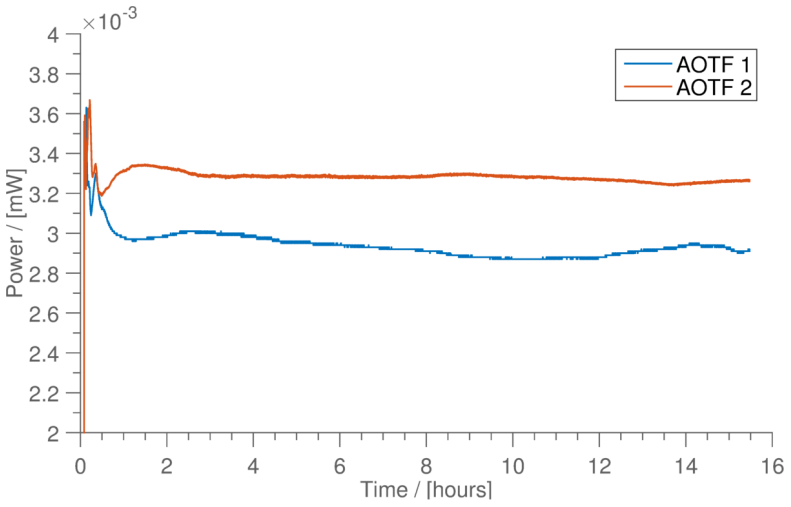

FIGURE 4.11: Power output from AOTF 1 through a 100μm fibre at 800nm, measured using a Thorlabs PM100A power meter with a S120VC photodiode and sampled at 1Hz.

power fluctuation can be seen in both measurements immediately after the laser output is enabled. However, after this initial period, the laser (and AOTFs) remains stable with very little change in output for the following 16 hours. If the initial 1 hour period is ignored, the average power output of AOTF 1 is 2.93 mW with a stability of $\pm 3\%$ over the subsequent 15 hours. The mean output of AOTF 2 is measured as 3.28 mW with $\pm 2\%$ change over the 15 hours. There is a small difference in the mean power outputs, which is most likely due to the alignment of the laser path to the fibre collimators, which is explained in greater detail in Section 4.2.3.

4.2 Acousto-optic tunable filters

The AOTFs used in the system are two modified Gooch and Housego Acousto-optic modulators (2986-01). These crystal are made from tellurium dioxide (TeO2) and allow rapid selection of specific wavelengths within a specified region from a broadband source. The key specifications of the standard AOTF crystal are detailed in Table 4.3. The standard bandwidth of the AOTF crystal is 5 nm, however, in order to improve on

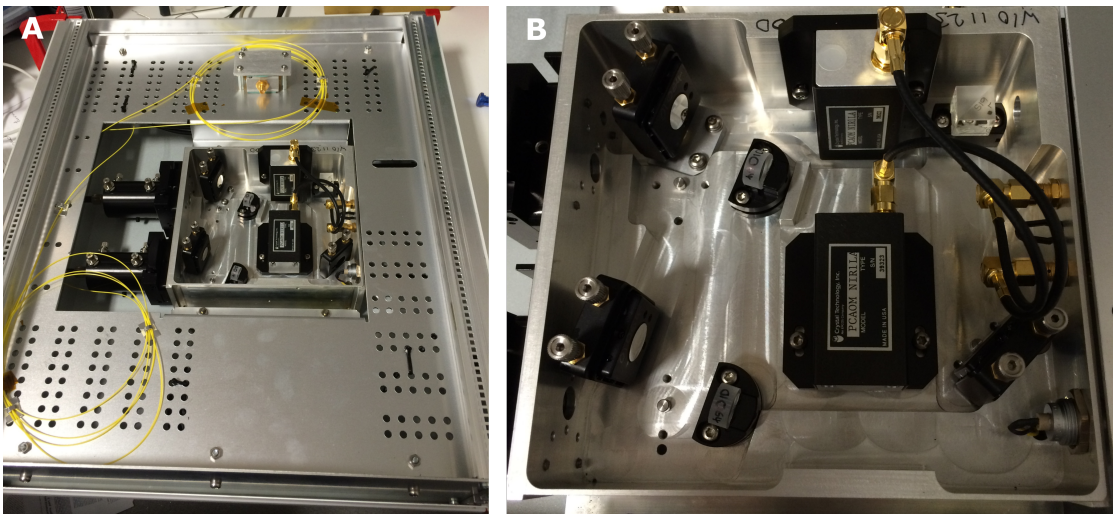

FIGURE 4.12: (A) Internal mounting of optical AOTF setup inside a 19inch subrack. (B) Close-up of optical setup.

the accuracy of the measurements a modified crystal, that the manufacturers claim has a bandwidth of 2-3 nm over the near infrared, is used.

Acoustic Medium	TeO2
Acoustic velocity	.68mm/μs
Active Apeture	2.5$\varnothing$mm
Bandwidth	5nm
Freq. range	49-98MHz
Wavelength range	650-1100nm
Temperature sensitivity	0.05 nm/C
Input polarisation	Vertical
Output polarisation	Horizontal
Diffraction efficiency	min 90 %

TABLE 4.3: Specifications of standard Gooch and Housego 2986-01 acousto-optic tunable filters.

4.2.1 Spectral density

Figure 4.5 shows the output from the laser itself. Whilst this is important for selecting a laser, the spectral density of the output used for spectroscopy will always be first convolved with the efficiency of the AOTF crystals. The spectral density has therefore been measured by filtering the laser into individual wavelengths using both AOTF crystals

(Figure 4.13). The measurement was performed at 100% laser power and the AOTF on the most efficient power. Comparing the output of the AOTF to the laser output in Figure 4.5, we see a similar shape in the near infrared range, with a peak in power around 760nm. There should be little spectral change due to the AOTF filtering, however, both crystals are calibrated for a range of 600-1100 nm, which may account for the drop in power at 600 nm. The difference in outputs is most likely due to the alignment of the optical paths entering the fibre collimator in the AOTF module and will be explained further in Section 4.2.3.

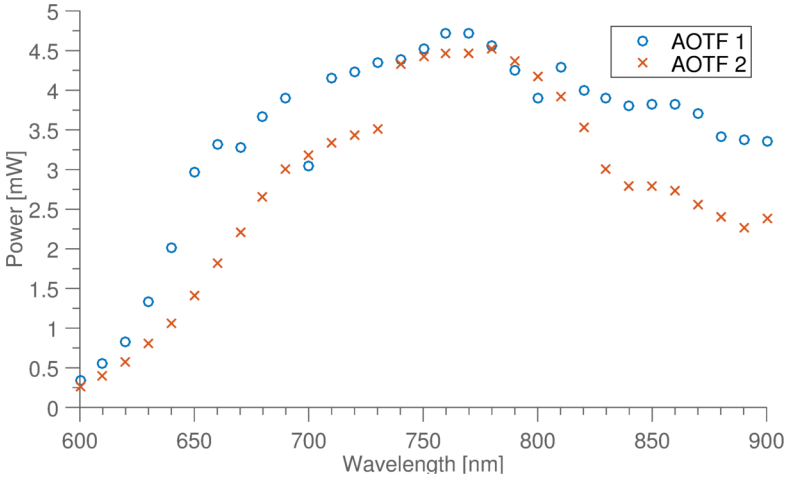

FIGURE 4.13: Power of light from the output of both AOTFs measured with a Thorlabs P-100 calibrated power meter.

4.2.2 Wavelength selection

The AOTF crystals used in the Fianium modules are designed for narrowband wavelength selection, with manufacturer specifications stating a bandwidth of 2-3 nm throughout the near infrared range. Figure 4.14 shows a selection of 31 wavelengths from 600 nm to 910 nm with a 10 nm separation. The spectrum was acquired using four discrete measurements, with 8 wavelengths selected by the AOTF at a time. The background noise was removed and spectra combined. The FWHM of each wavelength can be seen

to increase as the wavelength increases (Figure 4.15). The FWHM ranges from 1.40 to 4.40 nm in the 600-900 nm range, with a mean value of 2.59 nm.

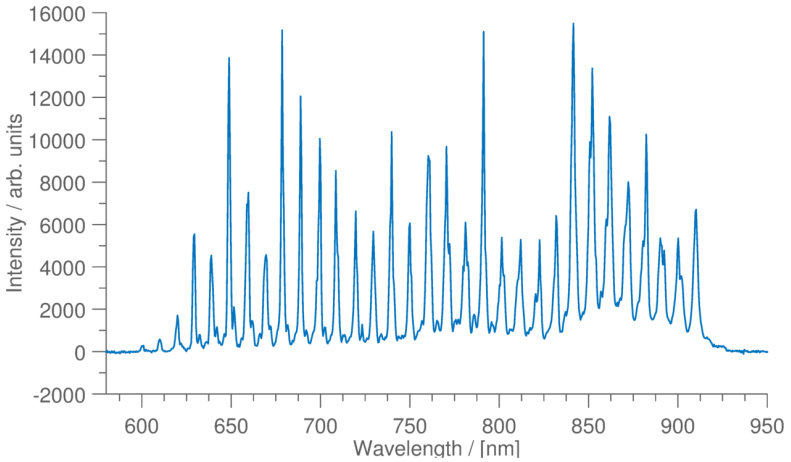

FIGURE 4.14: Spectrum of wavelengths selected at 10nm separation. The measurement was recorded using an Ocean Optics USB 4000HR spectrometer over four measurements with background correction.

This FWHM of the light filtered by the AOTFs are slightly larger than the system specifications set out, the wider bandwith will may introduce a small error on the measurement calculations. However, this is unlikely to have a significant impact of the final concentration values as the majority of light pulses have a FWHM around 2.5 nm or less.

4.2.3 AOTF alignment

The optical path from the laser requires high precision in order to maximise the laser power output achieved at the end of the optical fibre. There are two effective enclosures for the AOTF: a main case which is 19 inch rack mountable, and an internal optical enclosure to mount the optical components. In order to protect these components from vibrations which could lead to misalignment of the optics, mechanical damping was incorporated in the design for the internal enclosure. However, during the course of this study, the power output of one source decreased from 4.12 mW to 1.15 mW due to a misalignment of the optical path (Figure 4.16). In order for the collimator to achieve maximum coupling efficiency with the optical fibre, the laser beam needs 4 axis

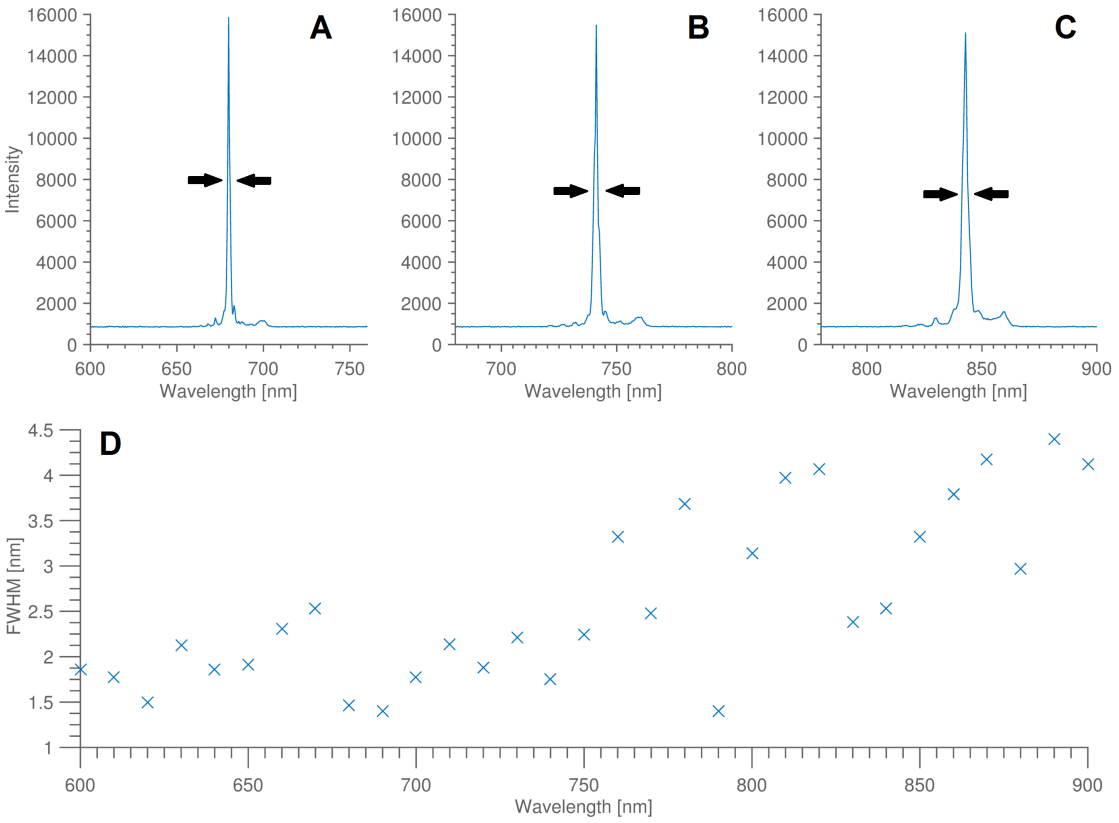

FIGURE 4.15: Single wavelength spectrum for A) 680nm, B)740nm, C) 840nm measured with Ocean Optics 4000HR Spectrometer. D) FWHM of all wavelengths as seen in 4.14.

alignment. This is achieved by 'walking' the laser beam across the face of the collimator in the x and y axes separately using two of the four output alignment screws on the laser output. There should be very little need to alter the laser path more than this, but in cases where the beam has diverted by a greater amount the input alignment screws may need to be adjusted.

4.3 Fibres

The bespoke fibre optics used in the system are obtained from Loptek GmbH&Co., Germany. There are two different types of fibres used: single mode, single-core source fibres and fibre bundles for light collection from the head.

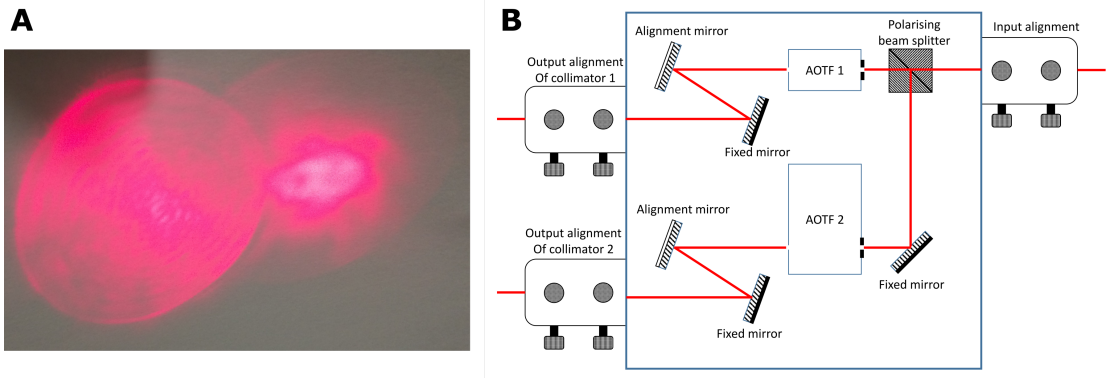

FIGURE 4.16: (A) Raw output seen from both sources at 670 nm, with the unfocused path seen on the left of image. (B) AOTF enclosure optics.

4.3.1 Source Fibres

The source fibres used are Loptek single core 70 μm fibres with a lightweight PVC hose and a numerical aperture (NA) of 0.54. One connector is a standard APC FC connector to connect to the output from the AOTF module, and the other end uses a straight 3mm x 30mm metal ferrule. Most of the testing of the system was conducted using a 2m long source fibre. The Fibre is a single core glass fibre and therefore very delicate. Previous versions of this fibre had a thick protective hose. However, due to the weight of the fibre pulling on the ferrule, this was prone to breaking.

4.3.2 Detector fibres

The detector fibres are 2 metre long glass fibre bundles with a high NA of 0.64. One end is terminated with a 4.5mm x 30mm plastic ferrule for applying to phantoms or tissue, and the other has a long metal ferule with dimensions 4mm x 140mm in order to fit it to the system using the custom fibre connector described in Section 4.4.6. The high numerical aperture of the detector fibres is very important in order to maximise the light collected and guided into the detectors. The maximum angle of light acceptance i_m

(Figure 4.17) can be calculated using Snell's law, which upon rearrangement leads to

$$\text{NA} = \sqrt{n_1^2 - n_2^2}, \tag{4.1}$$

where n_1 and n_2 are the refractive indices of the fibre core and the fibre cladding, respectively. In air, the detector fibre has a maximum acceptance angle of 39.8 degrees and in tissue, which has been shown to have a refractive index of 1.4, it has a maximum angle of acceptance of 27.2 degrees [116].

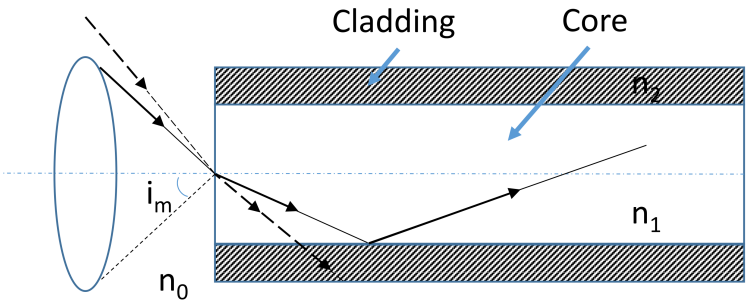

FIGURE 4.17: Cone of light acceptance into a cladded optical fibre. n_0, n_1 and n_2 are the refractive indices of air, the fibre core and the fibre cladding, respectively, and i_m is the maximum angle of light acceptance.

4.4 Detector box

The detector subrack houses the variable optical attenuators (VOA) drivers, variable optical attenuator module, photomultiplier tubes (PMT) and their power supplies, and the photomultiplier tube controllers. The requirements needed to be met by the design of the detector box are as follows:

- Variable optical attenuators and photomultiplier tubes must be optically aligned, and the distance between the two minimised.

- The detector fibres must be easily removable and swappable to allow easy transport of the system and flexibility with regards to the length of fibres used.
- The light path must be shielded from external light.
- The photomultiplier tubes must have sufficient cooling.
- The data acquisition (DAQ) cards and PMT power and temperature controllers must be housed in the rack along with a suitable USB hub.
- The rack must be no bigger than 4U height.

The VOA drivers used in the system were originally designed for use in the MONSTIR-II system [57], utilising a modular design so that each motor and driver are independent of one another. The VOAs allow the light levels detected by the PMT to be within the dynamic range of the detector and enable different source detector separations to be used.

4.4.1 Custom optode holders

Optode holders are required to maintain a stable contact with the phantom or skin and keep the source and detector fibres a set distance apart. This is especially important with time resolved spectroscopy where only a small amount of light is being detected. Another major concern when applying NIRS to the head is avoiding trapped hair between the fibres and the scalp, which could hinder the measurement and also increase the attenuation of light, thereby reducing the signal. Ideal optodes for time resolved NIRS will be able to maintain a stable grip onto the source and detector fibre, and be able to have the fibre protrude a short distance through the optode holder in order to 'comb' hair out of the way allowing for a good contact with the skin.

4.4.2 3D design

Many different methods have been implemented for optode holder design, including full head caps and rubber pads [9, 117, 118]. One technique which is increasingly being used for this application is 3D printing. 3D printing has had a major influence on rapid prototyping, especially in the last decade where large technological improvements have been made and, perhaps most crucially, the overall cost has decreased significantly [119]. Typically 3D printers have been used to print rigid material such as ABS or PLA, although recently UCL gained access to a Stratasys Objet Connex 500 printer which prints both rigid and flexible materials. Furthermore, any combination of these two can produce materials with a range of strengths and flexibilities. This capability was used to design and create optode holders which posess a rigid part to hold the fibres, while a flexible base pad is used to cushion the skin and allow the optode holder to adapt to the curvature of the head.

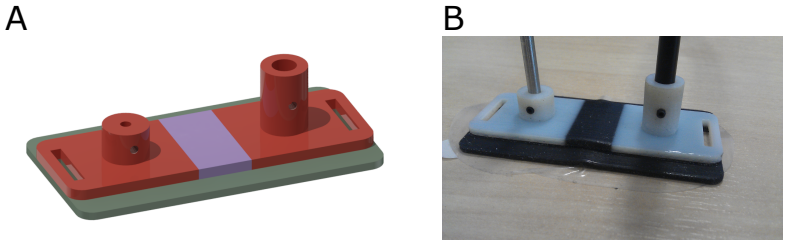

FIGURE 4.18: (A) 3D design of a single channel optode holder with a source detector separation of 30mm. (B) 3D printed version of design A. The white parts are a rigid hard plastic, while the black part is a softer, rubber-like material.

The first design of this optode holder can be seen in Figure 4.18. This is a single channel optode holder with a 30mm source detector separation. The design works well on flat surfaces such as phantoms and arms, however, when placed on the head the base of the optode holder does not sit flat with the skin, as demonstrated on a head-like phantom in Figure 4.19. Version 2 of the optode holder solves this problem by reducing the size of the rigid parts around the fibres seen in Figure 4.20. This resulted in good contact between the entire base of the optode holder and the skin when placed onto the forehead.

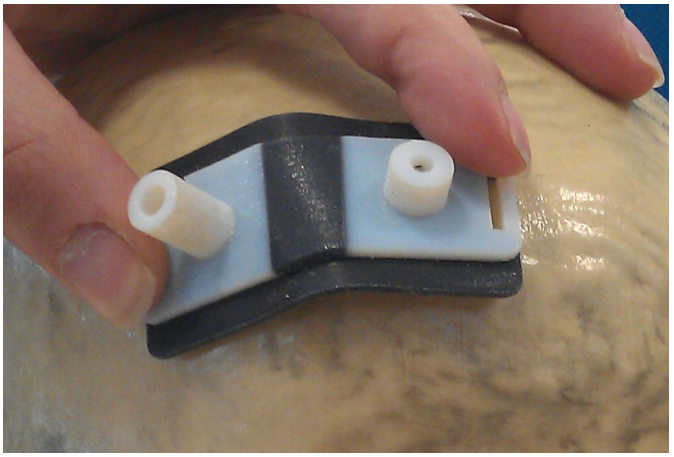

FIGURE 4.19: Demonstration of the first version of the optode holder on a head phantom; the base does not sit flat against the skin.

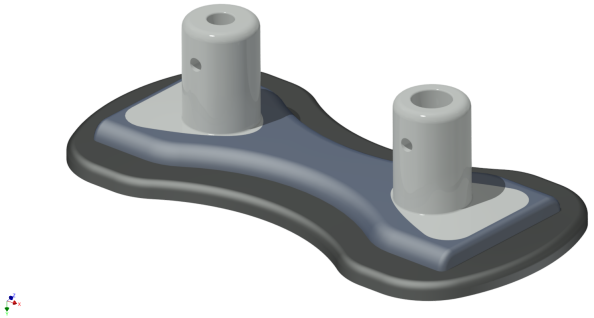

FIGURE 4.20: 3D CAD of the second version of the single channel optode holder.

Following on from this, two additional designs were made with the same design principles as version 2 of the optode holder. The first was a simple two-channel design with a single source and dual detectors mounted 30mm apart, as seen in Figure 4.21(A). The upper layer (seen in red) is made from a material with a greater rigidity than the lower part to provide additional strength to the optode holder. Figure 4.21(B) and (C) show the design and 3D print of a four-channel optode holder with a central source position and four detectors placed 30mm radially.

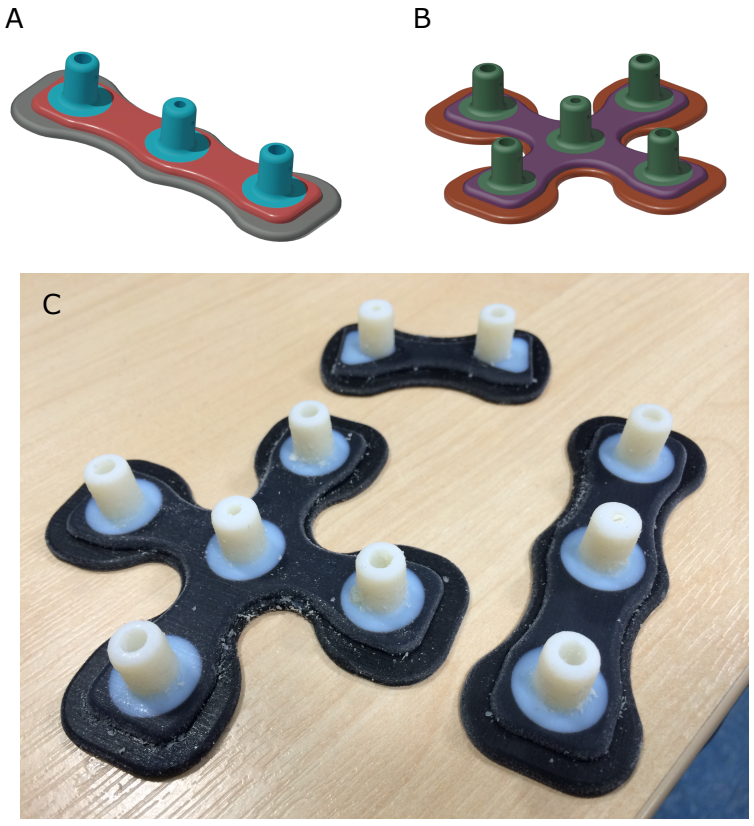

FIGURE 4.21: (A) 3D CAD of the two-channel optode holder; (B) 3D CAD of the four-channel optode holder; (C) 3D printed optode holders of the designs shown in (A), (B) and Figure 4.20.

4.4.3 Variable optical attenuators

Variable optical attenuators are required in order to control the amount of light entering the PMT. This prevents over exposure, which can damage the PMT. Figure 4.23 shows the modelled relative intensity of photons detected at different source-detector separations for reflectance and transmission geometries using the Green's function solution of the diffusion approximation with typical absorption and scattering properties of tissue ($\mu_a = 0.015$ mm^{-1}, $\mu_s' = 1$ mm^{-1}). As can be seen for both geometries, the number of photons detected decreases by an order of magnitude for every centimetre the source-detector separation is increased. In order to allow for flexible arrangement of source and detector separation, each PMT must have a variable optical attenuator that has a wide

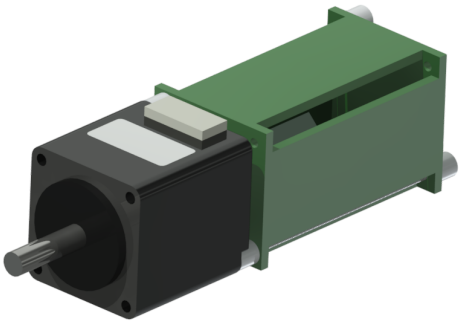

FIGURE 4.22: 3D CAD drawing of the variable optical attenuators motor and driver unit.

dynamic range and individually-selectable attenuation. The VOA must also have little impact on the spectral density of the light.

4.4.3.1 Design

The VOAs used are based on the original design made for MONSTIR-II and are composed of X-Ray film with variably exposed sections. The manufacture of these films is described in detail in a thesis by Jennions [120]. The variably exposed film was created by constructing a stepped mask made from PMMA and exposing the film to an x-ray beam (Figure 4.24). The centre line of the beam was lined up with the highest step to prevent shadowing, which would cause blurring between sections. The film is then glued onto a metal washer and fixed onto the shaft of the stepper motor. Stepper motors allow very precise rotation of the VOA and are driven by individual custom build drivers. The stepper motors and VOAs are then housed in a delrin case to provide mounting for the motors and a shield from external light.

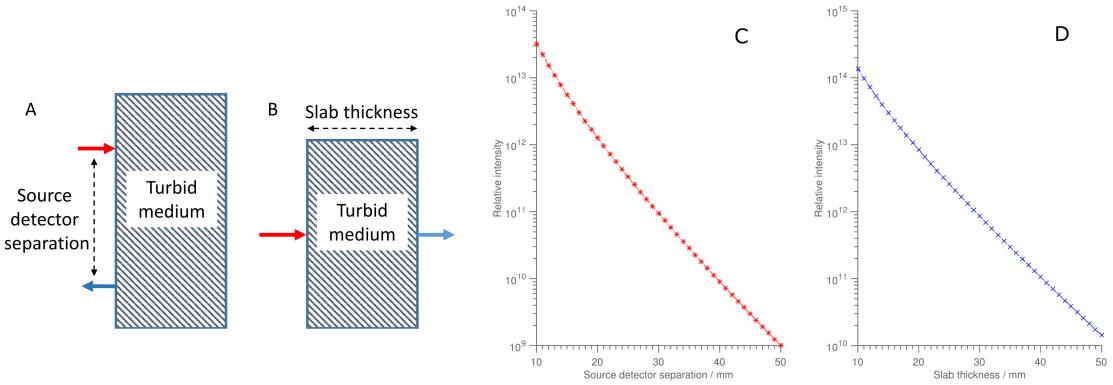

FIGURE 4.23: Modelled reflectance and transmission intensities using the Green's solution to the diffusion approximation. (A) Reflectance slab geometry; (B) Transmission slab geometry; (C) Photon relative intensity for refection geometry seen in (A) over varying source detector separations; (D) Photon relative intensity for transmission geometry seen in (B) for varying slab thicknesses.

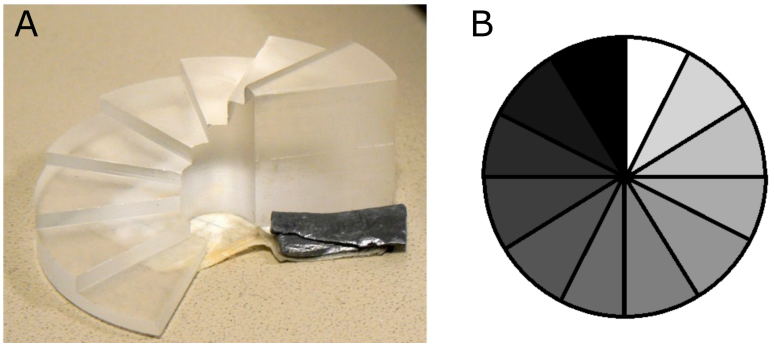

FIGURE 4.24: (A) VOA stepped mask made from PMMA [120]; (B) 12 segment VOA layout.

4.4.3.2 Performance

The VOAs were designed to achieve a very large dynamic range to account for large variations in the source detector separation. The optical density (OD) or absorbance of the VOAs is calculated using

$$OD = \log_{10}\left(\frac{I_i}{I_t}\right), \tag{4.2}$$

where I_i and I_t are the intensity of incident and transmitted, respectively. The number of counts and optical density of the VOAs can be seen in Figure 4.25. The maximum optical density achieved by the the VOAs is 3.5 at position 12. The VOA was designed

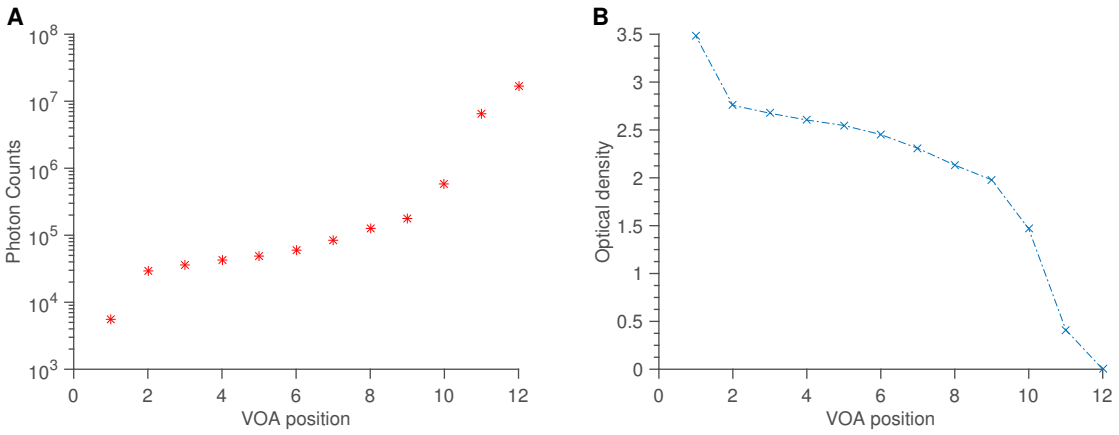

FIGURE 4.25: (A) Attenuation of light by the VOAs; (B) Optical density of VOAs by position.

to have a linear optical density between 0 and 3.7, which is the maximum attenuation achievable using the x-ray film. The effective optical density does not show a linear decrease through the range of VOA steps. While this is not ideal, the system will not have very large variations in source detector separations, and therefore the attenuations provided by the VOA are adequate.

In order to measure the instrument response function (IRF) at different VOA positions, the x-ray film must have very little effect on the spectral density of the light. Figure 4.26 shows the optical density of the VOA for different wavelengths in position 11 (where the film has been blocked from exposure to x-rays) and position 10 (where the film has been exposed). Section 11 of the VOA has a variation of 11.3%, while section 10 has a variation in OD of 7.8%. This spectral variation will not affect any measurements which the system is designed for as the VOA position will not be altered during a single measurement. If an adequate IRF is measured at the beginning or end of a study the n the spectral variation in the VOA will be accounted for in the calculations of absorption and scattering.

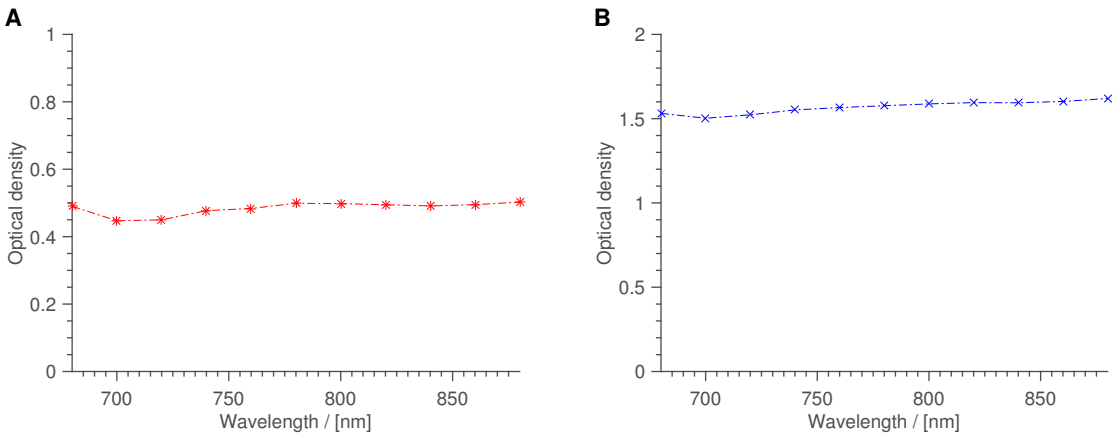

FIGURE 4.26: (A) Optical density of the VOA at position 11 (A) and position 10 (B) over the near infrared range.

FIGURE 4.27: Hammamatsu H7422P-50 photomultiplier tube module with heatsink and fan.

4.4.4 Photomultiplier tubes

Hamamatsu H7422P-50 photomultiplier tube modules (Figure 4.27) were used for the measurement of photon flight times.

These specific PMTs were chosen due to their very high sensitivity in the 380-890nm range, and their ability to detect the arrival of single photons. The H7422P-50 is maintained at a constant temperature of 5 degrees Celcius by a Peltier cooling element next to the photocathode, in order to reduce thermal noise and dark counts. The photocathode is made from Gallium arsenide phosphide (GaAsP) and has a quantum efficiency of 12%

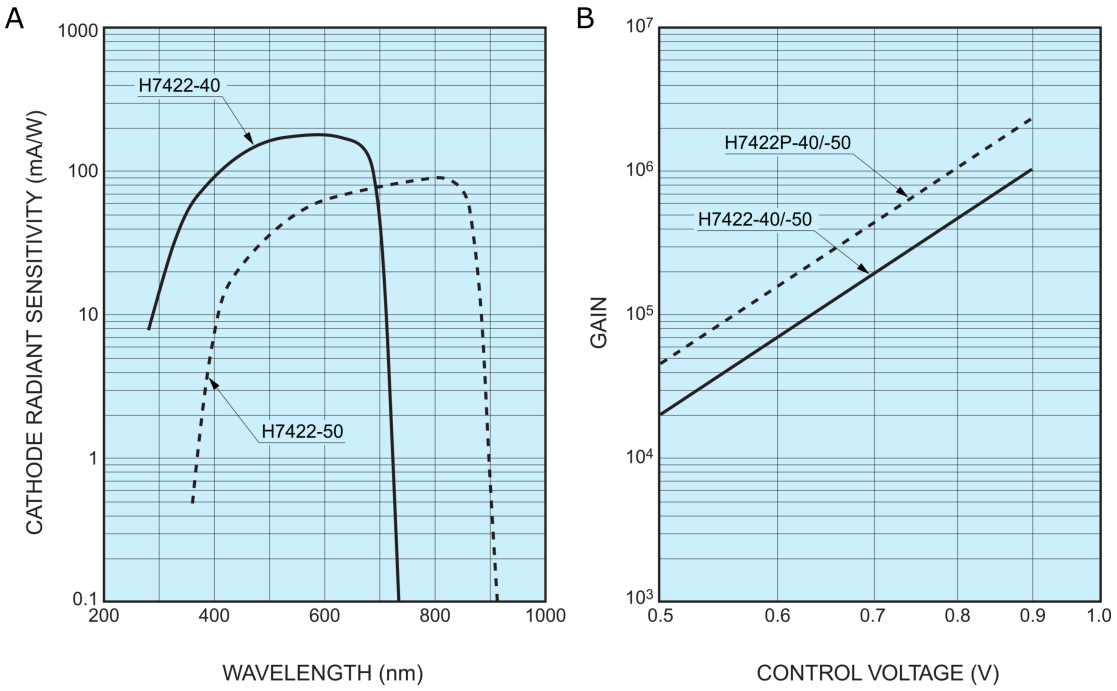

FIGURE 4.28: Manufacturer data sheet of (A) cathode radiant sensitivity and (B) gain.

at its peak wavelength of 800nm. The cathode radiant sensitivity and gain can be seen in Figure 4.28, and key information about the module seen in Table 4.4.

The PMT module is designed to work with an individual heat sink and fan (Hamamatsu - A7423), which is controlled along with the cooling and gain voltages by a power supply unit with a temperature control (Hamamatsu - M9012). The M9012 unit is controlled by a series of I/O TTL signals which are generated by a combination of DAQ cards (National instruments - USB-6501 and USB-6008), which are operated using the LabView software described in Section 4.8. The PMT is based on a head-on type layout as explained in Section 3.3.1.

4.4.4.1 Characterisation of the photomultiplier tubes

The PMT gain is controlled by an analogue output on the National instruments DAQ card, with the maximum gain achieved by outputting a voltage of 0.9V to the PMT power

Parameter	H7422P-50	Units
Input voltage	11.5 - 15.5	V
Max output signal current	2	μA
Max control voltage	+0.9	V
Effective area	$\varnothing$5	mm
Peak sensitivity wavelength	800	nm
Dark count	125	s^{-1}

TABLE 4.4: Key specifications of the Hamamatsu H7422P-50 photomultipier tube module.

supply controller. Figure 4.29 shows the TPSFs (A) and the total counts for different PMT gains (B). The experimental set-up consisted of a tissue-like phantom, with a source-detector separation of 30mm and a constant fully open VOA position of 12. The wavelength used for both measurements in Figures 4.29 and 4.30 was 780nm, which is near the peak of quantum efficiency for the PMT as seen in Figure 4.28. The PMT gain can be set with a reference voltage of 0-0.9V, which corresponds to a voltage between 0-900 V across the anode and cathode. There is no response from the PMT when the reference voltage is below 0.65V, and a steady increase in counts when above a 0.75V reference voltage. The maximum voltage stated in the specifications of the PMT is 0.9V, however, there is also a recommended setting of 0.8V which should help prolong the life of the PMT. As seen by Figure 4.29, the PMT gain will affect the mean arrival time of the photon, as a higher gain will cause the photoelectron to travel in a more direct path inside the PMT.

The number of photon counts is also shown to be linearly dependent on collection time (Figure 4.30). This is expected as double the collection time yields double the number of collected photons. The limiting factor in this collection time measurement of 46.4s is due to the maximum number of photon counts being reached in the photon counting module.

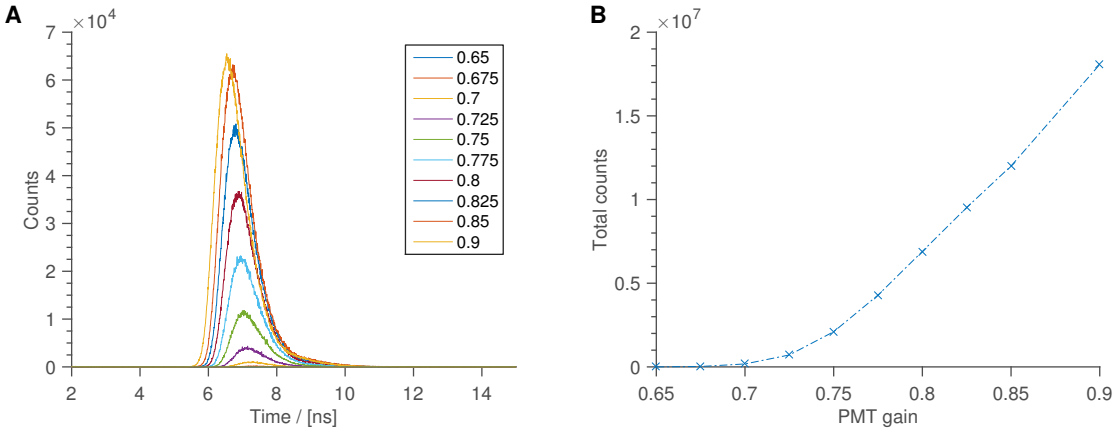

FIGURE 4.29: (A) TPSFs for differing gain settings; (B) Number of photon counts for increased gain.

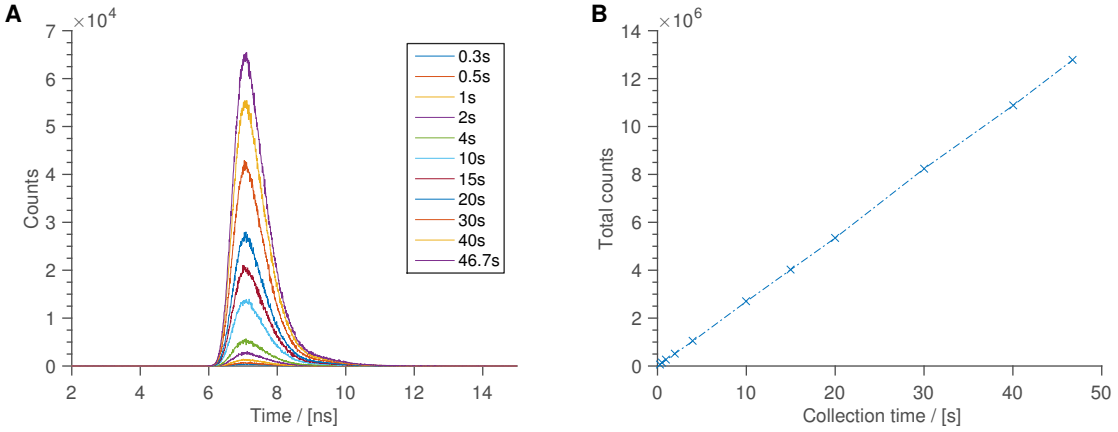

FIGURE 4.30: (A) TPSFs for differing collection times; (B) Number of photon counts for increased collection time.

4.4.5 Router

A router is required in the system to route the pulses produced by the four PMTs into a time-correlated single-photon counting card (TCSPC), which is explained in section 4.5. For this process, a Becker and Hickl HRT-41 router is used, which is designed to work with low current output PMTs and Becker and Hickl photon timing electronics Figure 4.31(B). The HRT module allows simultaneous operation of the PMT modules by first combining the pulses from all channels onto a common pulse line, which is then passed to the main TCSPC card directly to provide timing information. The router also passes the pulses from the PMTs to amplifiers and a comparator, and the pulse is then passed through to

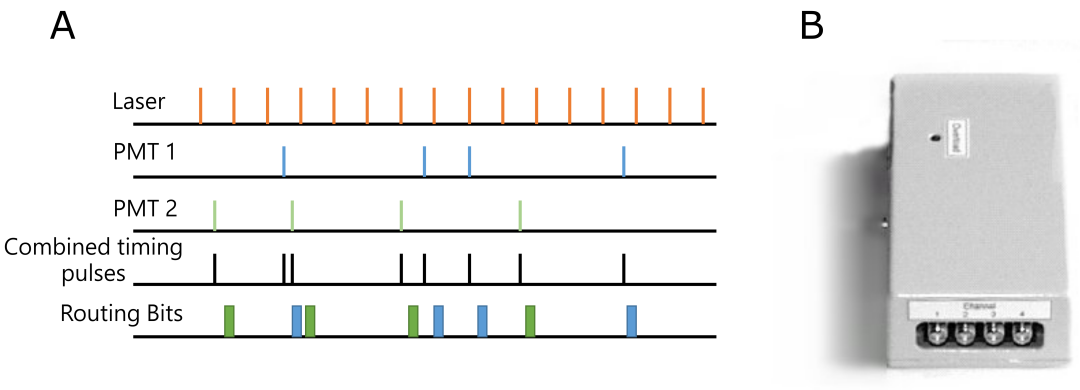

FIGURE 4.31: (A) Pulses from different PMTs and combination of signals with routing information; (B) Beckl and Hickl HRT-41 router.

an encoder if it exceeds a reference voltage set by an adjustable threshold value. This has the advantage of filtering dark counts from the PMT as the electron multiplication process will not originate from the cathode, and therefore will be a lower voltage than pulses generated from the arrival of a photon. The encoder then outputs two routing bits to indicate which channel the detected pulse in the timing line originated from, and one 'count-enabled' bit which reads true if routing information is available. The routing and count-enabled bits are delayed by 30ns from the detected pulse, so that the counting card can then allocate the photon count to the relevant memory block and histogram.

4.4.6 Custom fibre connector

A fibre connector is required to provide the ability to use interchangeable fibres from the outside of the system without the need to open the detector subrack. This is a challenging mechanical problem due to the design of the VOA drivers. Ideally, the length of the optical connection from the VOAs to the PMTs is kept at a minimum to reduce light loss. Two configurations are possible as seen in Figure 4.32. Configuration (A) has the shortest path between the VOAs and the PMT, which will reduce the loss of light in the light guide connecting the two, though this will increase the complexity of using exchangeable fibres. Configuration (B) will simplify the connection to an external fibre,

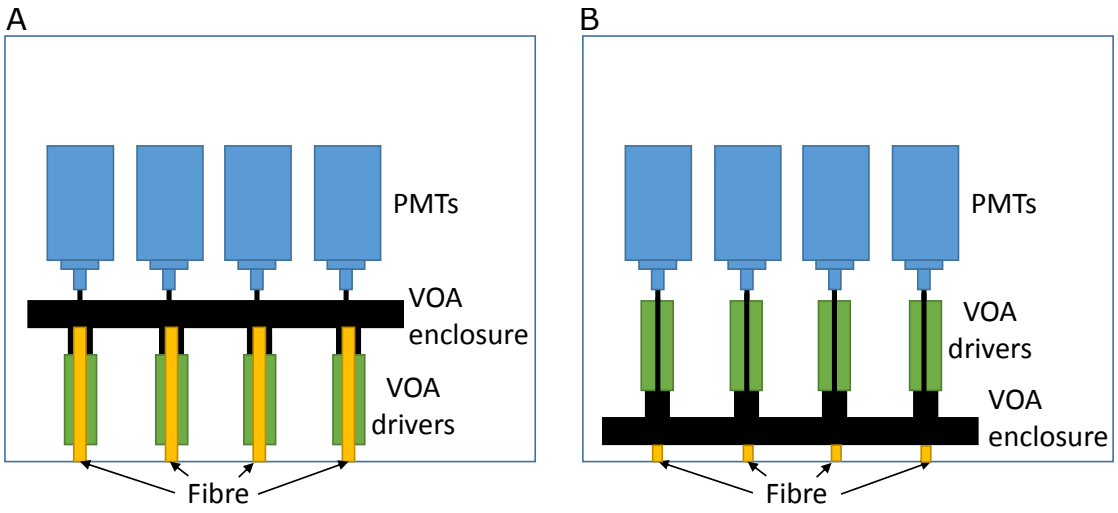

FIGURE 4.32: (A) Configuration of detector box with shortest path between PMT and VOAs, (B) Configuration with short path to VOA from external connector.

but will increase the length of the light guide to over 150mm compared to 40mm for configuration (A). Configuration (A) was chosen as the fibres can be custom made with long ferrules. In order to use this configuration, custom fibre connectors are required. They must be able to accurately align the fibre in the VOA housing in line with the exit light guide, as well as provide a locking mechanism to ensure the fibre is not easily pulled out of the system.

4.4.6.1 Design of the fibre connector

The final design of the fibre connector is seen in Figure 4.33. The design allows a fibre with a 4.0mm diameter and 140mm length ferrule to be used with the system. In order to accurately align the end of the fibre with the VOA, a locking piece (seen in green) is attached to the fibre by two grub screws. The fibre can then be inserted into the connector and rotated to lock the fibre in place.

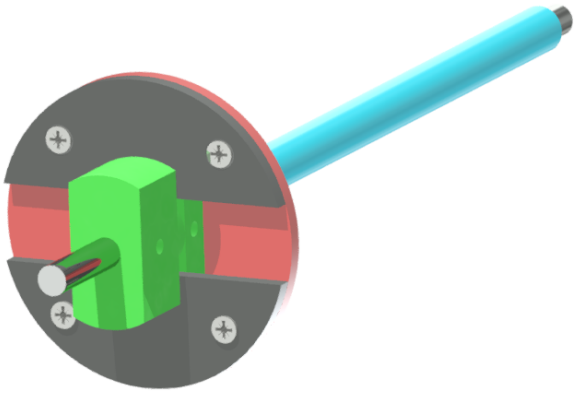

FIGURE 4.33: Single channel of the custom fibre connector. A locking mechanism (green) is attached to the fibre (silver) with a guide tube (blue).

4.4.6.2 Modification

The initial design used metal for the locking mechanism, but three design flaws were found:

- The tight tolerance of the aluminium locking part (Figure 4.34) against the housing caused the entire fibre to occasionally become stuck inside the system, the removal of which required disassembly of the entire connector.
- The internal edges of the locking part could hit the flanges of the connector preventing the piece from rotating and correctly locking the fibre in place.
- The upper part of the locking mechanism, which is used as a 'handle', was too small to hold on to easily.

These issues led to a re-design of the locking mechanism. The part was 3D printed, as this is easily replicable for additional fibres. The second version of the locking part is seen in Figure 4.34(D-F). The top section of the part has increased in size, and the entire piece made narrower to reduce the chance of the part binding in the connector. Finally, in order to increase the ease to which the part rotates, the leading edge of the locking

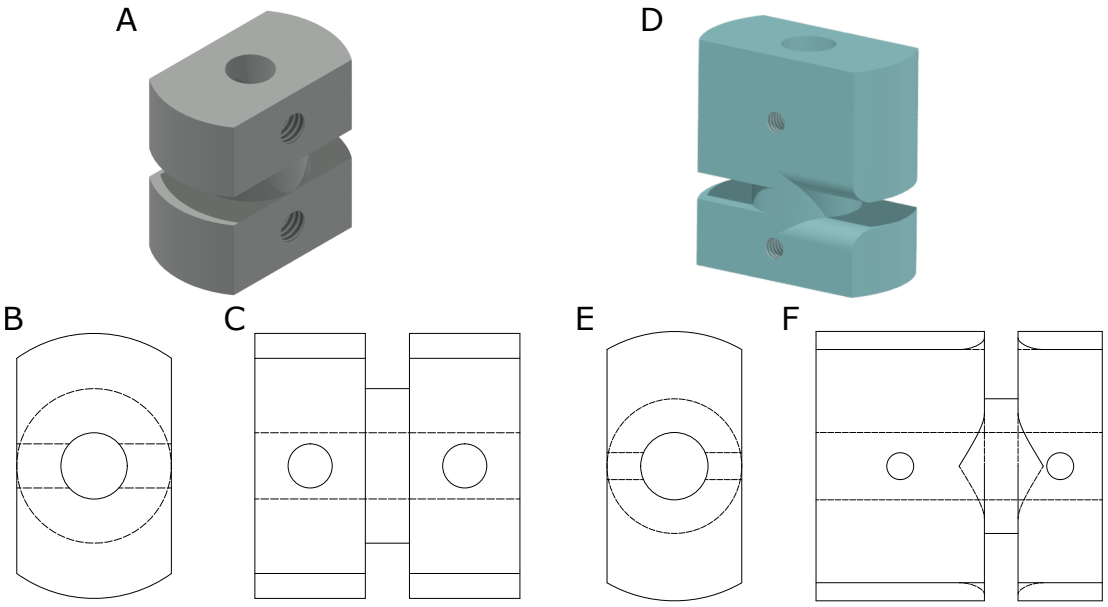

FIGURE 4.34: (A) 3D CAD of version one of the locking part for the custom fibre connector; (B) and (C) Technical drawings of version one; (D) 3D CAD of version 2 of the locking part; (E) and (F) Technical drawings of version two.

part was rounded to increase the ease of rotation. In future iterations an increase to a 3mm screw will help secure the fibre ferrule and ensure that the grub screw has sufficient thread in the 3D printed part.

4.5 Time-correlated single-photon counting card

The timing and counting electronics of the system is all controlled by a single PCI card from Becker and Hickl called a time-correlated single-photon counting card (TCSPC). The card used in the system is the SPC-130-EM, since the SPC-130 range of cards are designed for applications where a large number of TCSPC channels are required. The EM version of the card was chosen as it has a faster bus interface and a larger memory than the standard model, allowing up to 64 simultaneous TPSFs to be recorded in conjunction with a router module. The TCSPC card has a minimum time channel width of 813 fs and a time window resolution of up to 4096 channels. The electrical time resolution is less than 3ps RMS with a 6.5ps FWHM which will be negligible compared to the systems

IRF. The card operates in a reversed start/stop mode (explained in Section 3.4.1.3), with laser rates up to 150MHz, and has a saturated count rate of 10MHz. However, the usable count rate is limited to 5MHz. For our application this is limited further, as when four channels are used the maximum counts in a single time bin is limited to 65536. The card has two constant fraction discriminators for the synchronisation pulse, and the photon count signals to ensure that the amplitude of the pulse does not affect the timing of the photon arrival time.

4.6 Power supply

The system's requirements for AC and DC supplies are as follows:

- Medical-rated isolation transformer with sufficient power for the whole system.
- 240V AC supplies for main computer, monitor, supercontinuum laser and AOTF drivers.
- 12V DC low ripple for 4 PMT power supple controllers.
- 7-9V DC for VOA drivers.
- 5V DC for USB hub.

An isolation transformer is required for all medical equipment to be connected to the mains. A 1000VA Reo medical isolation transformer which complies with the EN60601 standard (3rd edition) is used to achieve a low general earth leakage current to protect the system. The power requirements for the system were measured and recorded below (Table 4.5). A 1000VA isolation transformer was selected to provide adequate power without the likelihood of blowing a fuse in regular operation.

Equipment	Current draw / [A]	Power Consumption / [W]
PC	0.5	120
Monitor	0.12	30
Laser start up	0.5	
Laser full power	0.9	216
AOTF (rest)	0.15	
AOTF (max)	0.16	38.4
PMTs		100 (PSU max)
VOA		60 (PSU max)
USB hub		12.5 (datasheet max)
Total		615.3

TABLE 4.5: Power consumption of all electronics in the system.

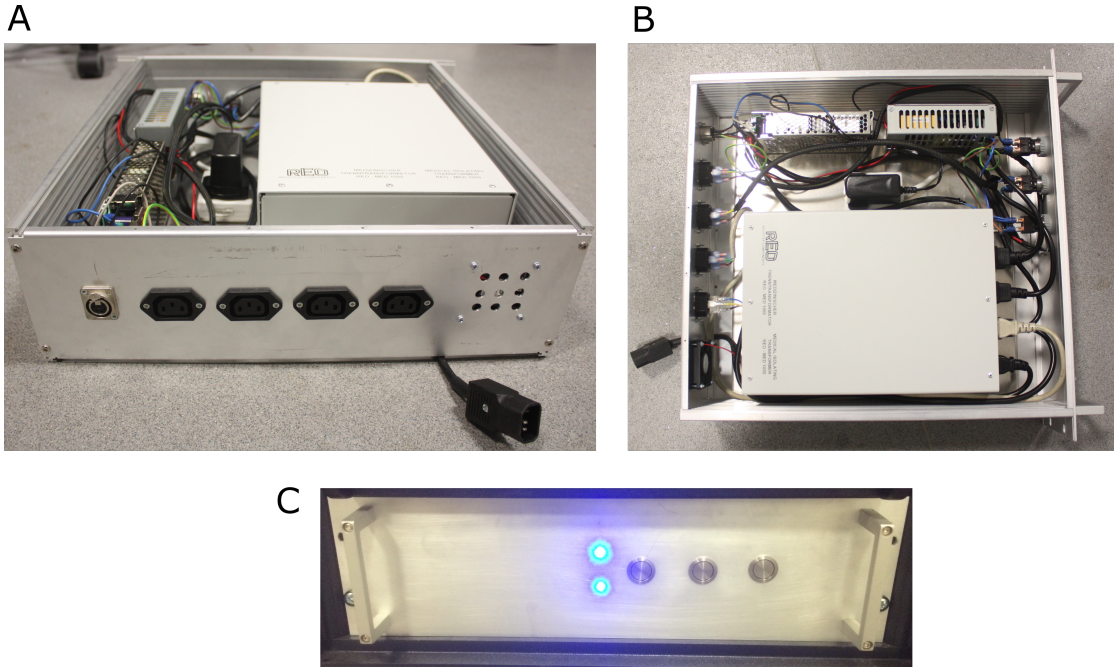

FIGURE 4.35: (A) Back panel with 4 240V AC IEC sockets for PC, Monitor, Laser and AOTFs, and a 6 way DIN connector for low voltage DC power; (B) Top-down view of the power supply case; (C) Front panel of the power supply enclosure.

4.7 Mechanical hardware

To enable the clinical use of the system, the design uses a standard 19 inch rack mount cabinet to house all of the components. A 950mm high, 600mm deep 20U Novastar cabinet with 400Kg castors, which accepts 19 inch subracks, is used. Including the castors, the system has a total height of 1100mm, and the layout of the system can be

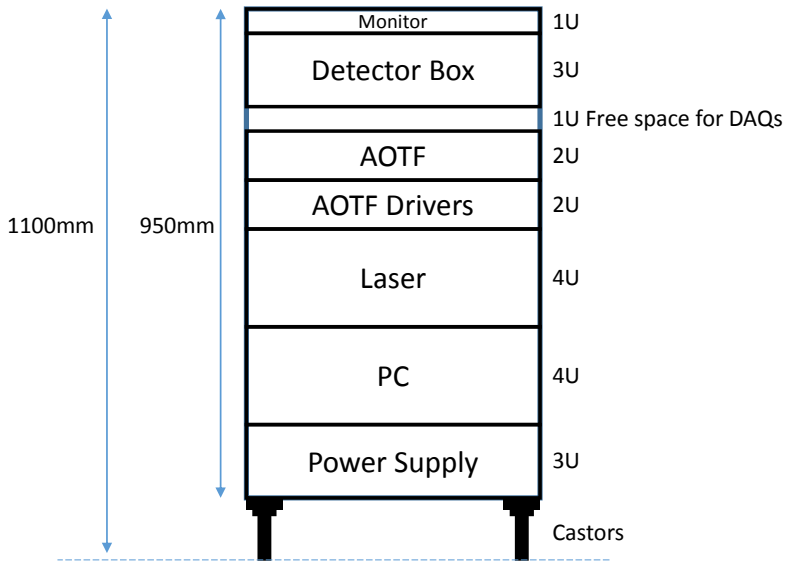

FIGURE 4.36: Subrack and system layout in the 20U Novastar cabinet.

seen in Figure 4.36. The power supply subrack, PC and laser were kept as low as possible, as they are the three heaviest sections and have no fibre connections. The AOTFs and the detector subrack are at the top of the system, as these provide the fibre connections.

4.8 Software

Software was developed to enable control of the PMTs, VOAs, laser (except high power key), AOTFs, and the acquisition of data via the TCSPC card. The software is written in LabView, a visual language which utilises data flow programming due to the ease at which it can interface with the IO DAQ multifunction cards, and the availability of drivers and Dynamic Link Libraries (DLLs) for the platform. LabView divides the code into Virtual Instruments (VIs), similar to how text-based programming uses functions to perform separate tasks. There are four main VIs that control the system: the PMT and VOAs are controlled in a single VI, and the AOTFs, the supercontinuum laser and the TCSPC card are controlled in another three.

4.8.1 PMT and VOA software

The control of the VOAs and the PMTs is achieved in a single VI as shown in Figure 4.37. The PMTs require a standard procedure when switching on to produce reliable results. Firstly, +12V must be applied to the PMT power supply via an external switch on the power subrack; the light on the GUI will indicate that this has been successful. The Peltier cooling elements are then switched on to cool the anode of the PMT, which will take between 60-100 seconds depending on the temperature of the room. During the cooling period the 'Status' light will flash with a 2 second interval, and when the cooling is complete the rate of flashing will increase to 0.5 seconds. At this point the PMT button can be pressed, and a reference for the high voltage selected with the slider.

The VOAs communicate with the computer via a serial interface, where the position is selected with the vertical sliders and closed either by returning the slider to 0 or pressing the close button. The errors from the PMTs are handled in a number of ways depending on the type of error occurring. There are two main errors that are likely to happen: a) the PMT overheats and the peltier cooling element cannot cool the module down to the desired temperature, or b) the PMT is overloaded with light and needs to switch off. If the first error occurs, the PMT high voltage and the peltier cooling element will switch off, which is indicated by a flashing error light. In the second case, the high voltage will switch off and will also trigger the VOA to close, so that the when the gain is switched back on the same situation does not occur again.

4.8.2 Laser and AOTF software

Fianium have provided basic drivers for both the laser and AOTFs, which are controlled independently; the AOTF GUI as provided by the manufacturer is seen in Figure 4.38.

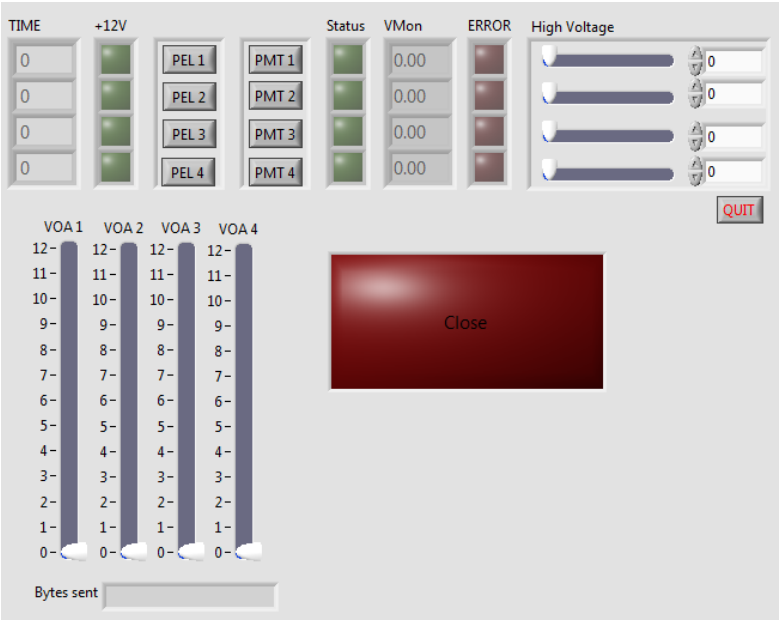

FIGURE 4.37: GUI for the control of the PMTs and VOAs. At the top of the panel, four indicators show whether there is power to the PMTs, and the time since they had power. The PEL push buttons operate the individual cooling element in the modules. The PMT buttons allow the high voltage reference to be set with the slider. The vertical sliders control the VOA position.

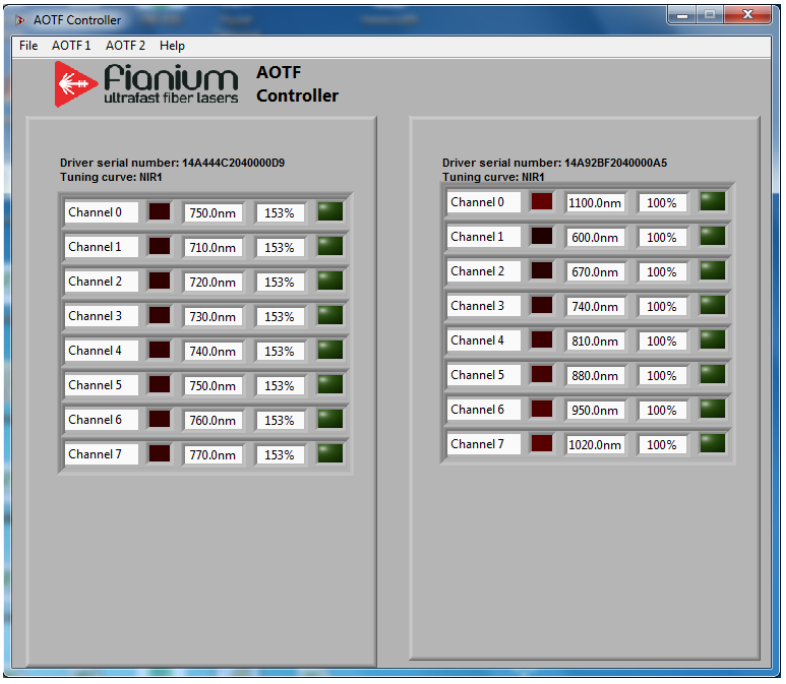

FIGURE 4.38: GUI for control of the AOTF drivers. In this window, eight channels for the two AOTFs can be seen. For each channel the drive power and wavelength can be selected.

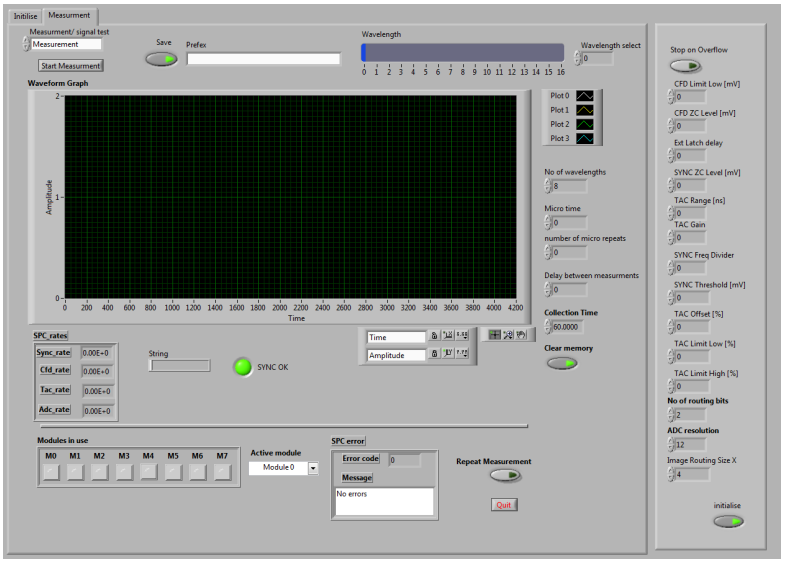

FIGURE 4.39: GUI for main control of the data acquisition of the system. The main panel consists of a large graph to display the TPSF of all PMTs for a single wavelength. Different wavelengths are displayed in wavelength select.

The switching of the wavelengths with the AOTFs can be achieved in two ways. The wavelength can be selected in the software and switched on and off with the push-buttons, although this is a very slow mechanism for switching. To rapidly switch the wavelengths, the FSK mode needs to be enabled, which releases the control of the wavelengths to external TTL inputs on the driver boards. These are then controlled by the data acquisition software shown in Section 4.8.3. The laser software is much more straightforward, with a simple serial interface that provides information about the warm up period of the master source (10 minutes) and then switches to full power via a push button.

4.8.3 Data acquisition software

The data acquisition VI is by far the most complicated code in the system, as it performs many operations and is required to be fast when implementing the tasks in order to meet the general system requirements. The measurement tab of the GUI can be seen in Figure 4.39.

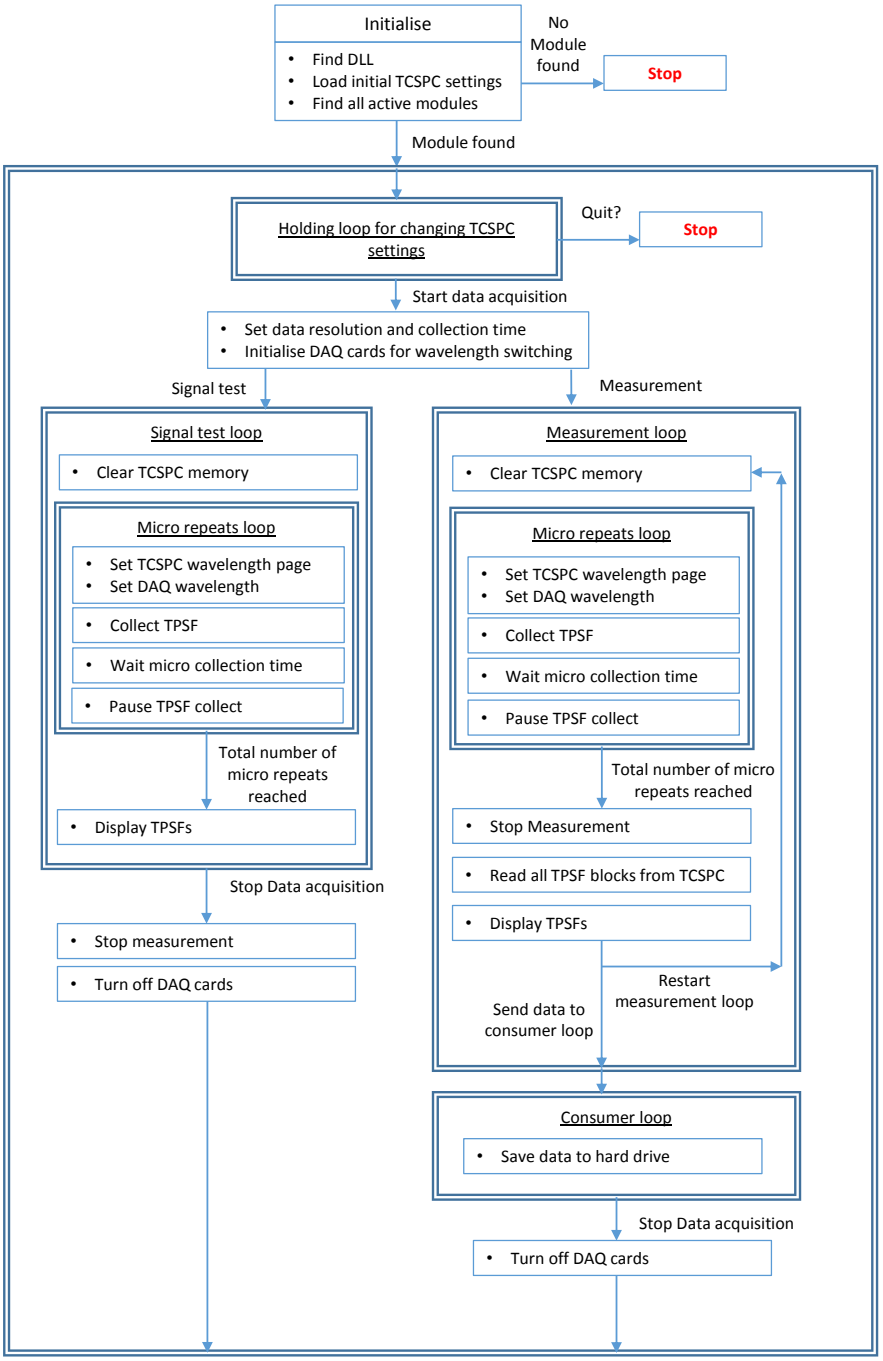

FIGURE 4.40: Simplified data and operation flow of the system.

The settings on the TCSPC card are selected on the right hand side of the GUI, and the TPSFs for a single wavelength from all PMTs are displayed on a the main graph display. The operation and data flow of the main VI is shown in Figure 4.40.

The first process the program undertakes is detecting the TCSPC card and going through the initialisation process. If there is an error during this process, the software will stop and indicate why the card cannot be initialised. If there are no errors the software will proceed to a holding loop, which allows the user to make changes to the setting of the TCSPC card and the data collection settings, such as the number of wavelengths used, micro time, number of micro repeats, and any delay between measurements.

4.9 Chapter summary

This chapter describes the design and development of a multichannel, multiwavelength, time resolved near infrared spectrometer. A Fianium supercontinuum laser produces pulses of broadband light into two acousto-optic tunable filters via a bandpass beam splitter. The light is filtered into a narrowband wavelength and collimated into two source fibres which transmit to the surface of the tissue. The optical fibres are held in place on the tissue by custom-designed 3D printed flexible optode holders. The light is collected by four optical fibres, and the arrival of single photons are detected by four photomultiplier tube modules. The light entering these detectors can be attenuated by individual variable optical attenuators achieving an attenuation of 3.7 OD to protect from overexposure. The arrival time of the pulses generated in the PMTs are then measured against a reference pulse from the laser. A Becker and Hickl TCSPC card measures the times-of-flight of all the detected photons, and generates a temporal point spread function for each PMT at every wavelength. The performance of each component in the system has been individually evaluated and the temporal stability, output power and sensitivity has been characterised.

Figure 4.41 shows the completed multiwavelength time resolved near infrared spectrometer. Figure 4.41(A) shows the front of the system which contains the user controls and monitor. From this side of the system, the power to the laser, AOTFs, PMTs, VOAs and PC are all controlled from the bottom subrack, which houses an isolation transformer. The laser master oscillator key switch can be seen, and the individual switches for the AOTFs are located above. The system is laid out so that the operator can stand at the front of the system controlling the experiment, with the fibre optics, which deliver and collect the light to and from the subject, are connected at the rear (4.41(B)). Four heavy duty castors make the system relatively easy to move, and the monitor can be retracted for transport. The cables and power connections are managed internally and the exterior of the system is electrically grounded.

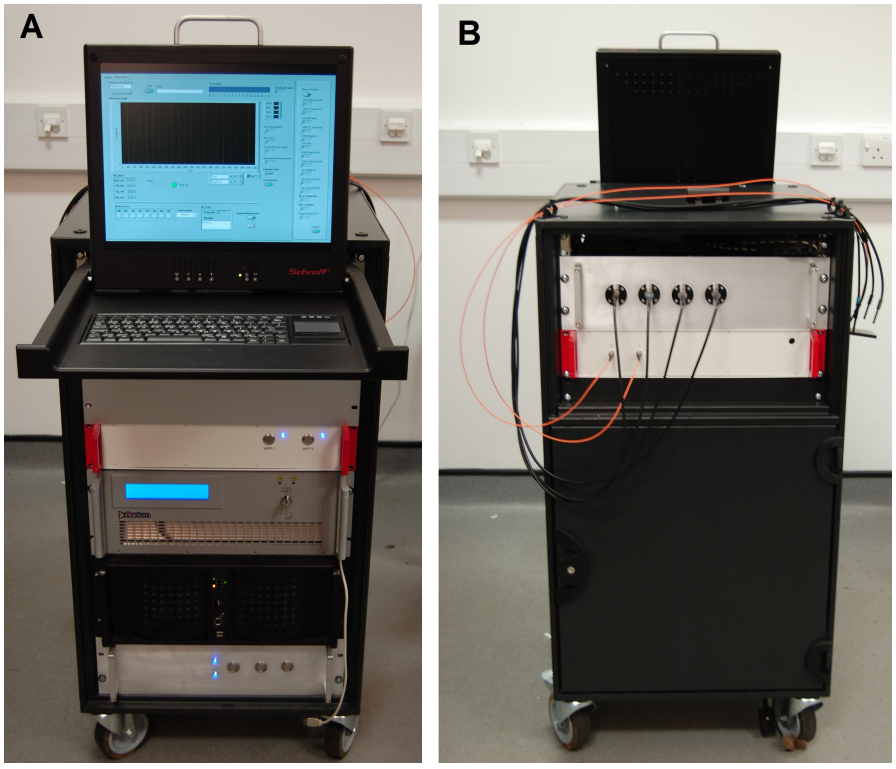

FIGURE 4.41: (A) Front of time resolved NIRS system, (B) Rear of system, showing fibre optic connections.

Chapter 5

Light transport models and data analysis

This chapter starts by describing light transport models for tissue and gives an overview of mathematics of each model. The method of data analysis using the Green's function solution to the diffusion equation is then discussed. Finally, a short study into alternative methods for improved mean penetration depth and sensitivity is reported.

5.1 Light transport models

The propagation of light through tissue can be described in several ways, including stochastic models such a Monte Carlo method, or deterministic models such as the radiative transfer equation. Stochastic methods describe the mathematical movement of particles by modelling individual scattering and absorption interactions using probability density functions. Deterministic models use partial differential equations to describe the transport of particles in tissue as a continuous wave of energy.

5.1.1 Monte Carlo method

A common method for modelling the propagation of light through tissue is the Monte Carlo method [121]. This highly accurate stochastic method is often used as the gold standard in modelling light transport. The Monte Carlo method considers light as individual particles moving in tissue, whereby the light packets are injected into the medium with an initial 'weight', where they then move in straight lines until interactions occur. The particles can be either absorbed, scattered, internally reflected or transmitted out of the medium during the flight. At each interaction, the energy of the photon is reduced until it falls below a threshold due to absorbed, or is transmitted out of the tissue domain. The path of each photon is tracked throughout the tissue and the location that it is absorbed or transmitted is recorded. The process is repeated for a very large number of photons to ensure convergence to a solution. Monte Carlo methods can be computationally inefficient due to the larger number of photons required to converse to a solution, though improvements in computational speed can be made through parallelisation of the method, providing a far more tractable model. However, for optimisation methods, where the absorption and scattering parameters are perturbed until a good fit to the measured data is obtained, Monte Carlo methods would require a large amount of computational time and resource.

5.1.2 The Radiative Transfer Equation

The propagation of light in tissue can be described by an integro-differential equation called the radiative transfer equation (RTE). The RTE provides a highly accurate description of the absorption, scattering and emission of light in a small volume of the medium, and is derived by the principle of conservation of energy. In order to derive the RTE, the rate of change of photons entering a small volume ΔV in a particular direction $\hat{\mathbf{s}}$ at time

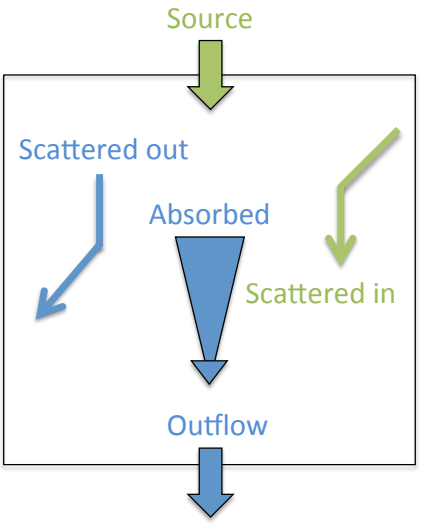

FIGURE 5.1: Schematic describing the processes which contribute to the terms in the radiative transfer equation (adapted from [122]).

t is considered. The directional photon density of the photons travelling in direction $\hat{\mathbf{s}}$ at time t at point $\mathbf{r}$ can be denoted as $\mathbf{P}(\mathbf{r}, \hat{\mathbf{s}}, t)$.

The RTE contains five terms which balance the rate of change of energy with the gain or loss of photons travelling in a small volume in a direction $\hat{\mathbf{s}}$, as seen in Figure 5.1.

As the photons can travel $(\Delta t \Delta V)$ during a time Δt, the rate of change of photons is given by $(\Delta t \Delta V)\partial \mathbf{P}(\mathbf{r}, \hat{\mathbf{s}}, t)/\partial t$. Using the principal of conservation of energy, this term can be equated to:

- the inflow of photons from the source q travelling in a direction $\hat{\mathbf{s}}$ into a volume ΔV during a time Δt, which is equal to $(c\Delta t \Delta V) q(\mathbf{r}, \hat{\mathbf{s}}, t)$,
- minus the number of photons that are scattered out of the direction $\hat{\mathbf{s}}$ within the volume ΔV during a time Δt, equal to $(c\Delta t \Delta V)\mu_{\mathrm{s}}(\mathbf{r})\mathbf{P}(\mathbf{r}, \hat{\mathbf{s}}, t)$,
- minus the photons travelling in a direction $\hat{\mathbf{s}}$ in a volume ΔV that are absorbed in the tissue over a time Δt, equal to $(c\Delta t \Delta V)\mu_{\mathrm{a}}(\mathbf{r})\mathbf{P}(\mathbf{r}, \hat{\mathbf{s}}, t)$,

- minus the net outflow of photons that leave the volume ΔV in time Δt due to the gradient $\nabla \mathbf{P}$, equal to $(c\Delta t \Delta V)\ \hat{\mathbf{s}} \cdot \nabla \mathbf{P}(\mathbf{r}, \hat{\mathbf{s}}, t)$,

- plus the number of photons travelling in a different direction $\hat{\mathbf{s}}'$ to the source, which are scattered *into* the direction $\hat{\mathbf{s}}$ over a time Δt. Since photons can travel from any direction into the direction of interest, this term is integrated over the set of all possible directions S^{n-1}. This term is therefore equal to $(c\Delta t \Delta V)\mu_{\mathrm{s}} \int_{S^{n-1}} \Theta(\hat{\mathbf{s}}, \hat{\mathbf{s}}')\mathbf{P}(\mathbf{r}, \hat{\mathbf{s}}', t)\, \mathrm{d}\hat{\mathbf{s}}'$, where Θ is the scattering phase function.

The directional photon density $\mathbf{P}$ is equal to $h\nu\phi$ where $h\nu$ is the energy of the photon and ϕ is the radiance. The radiance is the energy deposited by light at a position $\mathbf{r}$ in direction $\hat{\mathbf{s}}$ at time t. Substituting this into the above terms and rearranging leads to

$$\frac{1}{c}\frac{\partial \phi}{\partial t}(\mathbf{r}, \hat{\mathbf{s}}, t) = q(\mathbf{r}, \hat{\mathbf{s}}, t) - (\hat{\mathbf{s}} \cdot \nabla + \mu_{\mathrm{a}}(\mathbf{r}) + \mu_{\mathrm{s}}(\mathbf{r}))\phi(\mathbf{r}, \hat{\mathbf{s}}, t) + \mu_{\mathrm{s}}(\mathbf{r}) \int_{S^{n-1}} \Theta(\hat{\mathbf{s}}, \hat{\mathbf{s}}')\phi(\mathbf{r}, \hat{\mathbf{s}}', t)\, \mathrm{d}\hat{\mathbf{s}}', \tag{5.1}$$

which is the time-dependent RTE. The RTE is a complex problem to solve, and analytical solutions only exist for very simple geometries and conditions. Its complexity is due to the angular dependence of the phase function in the last term and the additional dependence on time, which means that numerically solving the RTE over a two-dimensional spatial domain is in fact a five-dimensional problem. Similarly, a three-dimension domain will become a six-dimensional problem. The RTE can be simplified by making approximations which remove the dependence on angle, which vastly reduces the complexity of the problem whilst maintaining sufficient accuracy in the solution over the majority of the spatial domain.

5.1.3 Diffusion approximation to the Radiative Transfer Equation

The first step in simplifying the RTE is to make the $\mathbf{P}_n$ approximations. Using spherical harmonics, the RTE can be written as an infinite sum, which can then be rearranged as an infinite set of coupled equations [123]. Truncating this infinite sum at n leads to a set of n coupled equations known as the $\mathbf{P}_n$ approximations. While the accuracy of the $\mathbf{P}_n$ approximations increases with the value of n, truncating the series at $n = 1$ provides sufficient accuracy and removes the dependence on angle entirely, leading to the diffusion approximation to the radiative transfer equation [124, 125]. The diffusion approximation can be written as

$$\frac{1}{c}\frac{\delta}{\delta t}\phi(\mathbf{r},t) - D\nabla^2\phi(\mathbf{r},t) + \mu_{\mathrm{a}}\phi(\mathbf{r},t) = Q(\mathbf{r},t), \tag{5.2}$$

where D is the diffusion coefficient, defined by

$$D = \frac{1}{3(\mu_{\mathrm{a}} + \mu_{\mathrm{s}}(1-g))} \tag{5.3}$$

and where Q($\mathbf{r}$, t) is an isotropic photon source.

Equation 5.2 is accurate at calculating the fluence rate in the case where $\mu_{\mathrm{a}} \ll \mu_{\mathrm{s}}'$ [123]. This is generally true for most biological tissues in the near infrared region [7]. An analytical solution to the diffusion equation, called the Green's function solution, can be derived from equation 5.2 if the source is considered to be an infinitely short pulse (i.e. Q($\mathbf{r}$, t) becomes a delta function) in an infinite medium, where μ_{a} and μ_{s} are homogeneous [125]. The Green's function solution is given by

$$\phi(\mathbf{r},t) = \frac{c}{(4\pi Dct)^{3/2}} \exp\left(-\frac{r^2}{4Dct} - \mu_{\mathrm{a}}ct\right). \tag{5.4}$$

Using the Green's function solution, the reflectance and transmission of the tissue can be calculated by making several assumptions about the boundary conditions. Considering

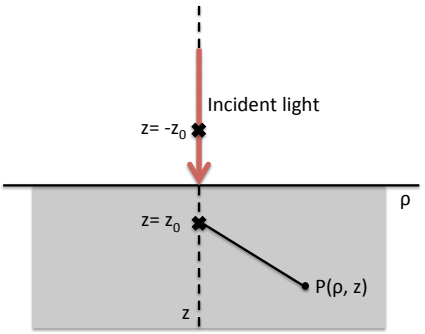

FIGURE 5.2: Diagram showing the calculation of the reflectance for a semi-infinite homogeneous medium.

the geometry shown in Figure 5.2, where a beam of light is incident on the surface of the homogeneous medium, the reflectance can be obtained analytically by making two assumptions: (i) the photons are initially scattered at depth z_0 below the surface of the tissue, where
$z_0 = ((1-g)\mu_s)^{-1}$, and (ii) a boundary condition is set so that at the surface so the radiance at the boundary is zero [125].

Using this boundary condition, the radiance at a point ρ away from the source at depth z can be written as

$$\phi(\rho,z,t) = \frac{c}{(4\pi Dct)^{3/2}}\exp(-\mu_a ct)\left\{\exp\left[-\frac{(z-z_0)^2+\rho^2}{4Dct}\right]-\exp\left[-\frac{(z+z_0)^2+\rho^2}{4Dct}\right]\right\}. \tag{5.5}$$

Fick's law tells us the number of photons reaching the surface area per unit time is equal to

$$\mathbf{J}(\rho,0,t) = -D\nabla\phi(\rho,z,t)|_{z=0}d. \tag{5.6}$$

This can be used to calculate the reflectance $R(\rho,t)$ from

$$R(\rho,t) = \frac{1}{(4\pi Dc)^{3/2}}z_0 t^{-5/2}\exp\left(-\frac{\rho^2+z_0^2}{4Dct}\right). \tag{5.7}$$

5.1.4 Comparison between Monte Carlo method and the diffusion approximation

Figure 5.3 compares the temporal point spread function (TPSF) calculated using a Monte Carlo method with the TPSF calculated using the diffusion approximation to the RTE [31, 126]. The TPSFs were calculated for a source-detector separation of 30 mm, with μ_a= 0.015 mm^{-1}, μ_s = 1 mm^{-1}and g = 0.9, which are typical values for biological tissue [45].

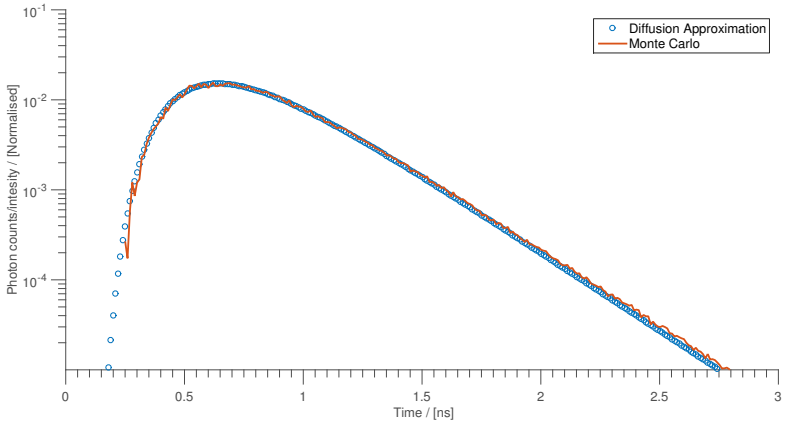

FIGURE 5.3: Comparison between the the temporal point spread function generated using the Green's function solution to the diffusion equation (circles) and a Monte Carlo method (solid line).

Both TPSFs are normalised, and a good correlation can be seen between the models. The Monte Carlo simulation was designed to produce a TPSF with a similar number of photons to that typically measured in tissue. The signal to noise will therefore vary, depending on the number of photons launched into the medium. However, increasing the number of photons will also increase the computational time. The TPSF shown in Figure 5.3 took approximately 20 minutes to acquire on a high performance computer, whereas the TPSF from the Green's function can be calculated in <1 second.

Given the agreement between the two models and difference in computation time, the Green's function solution is a suitably accurate and efficient model used to resolve coefficients of absorption and scattering from the measured data. The analytical model

however is limited to solving for homogeneous layers only.

5.2 Data analysis techniques

There are several different methods for analysis of time resolved data [127–129]. The data measured by the system described in this thesis has been analysed by fitting the Green's function solution to the measured TPSF, in order to resolve μ_{a} and μ_{s}'. This method has yielded accurate values for μ_{a} and μ_{s}' in phantom measurements. While faster methods for data analysis can be used for large amounts of data, such as fitting the mean time-of-flight and intensity, as this system only has a small number of channels, the need for faster data analysis was not required. The steps taken in this method to correct for the instrument response function (IRF) are described in Section 5.2.1, and it is this method that is used in the analysis of data measured in Chapters 6 and 7.

Other methods of data analysis are then investigated for quantifying the mean penetration depth of time resolved NIRS measurements. In (Section 5.3), data is used from a different study by Gunadi et al. for gated intensity calculations and fitting of the TPSF [130]. The findings of this work will hopefully be used for future data analysis of the multiwavelength time resolved NIRS system.

5.2.1 Green's function fitting of the temporal spread point function

This section explains how the Green's function solution to the diffusion approximation is fitted to the measured data, and can be used in order to resolve μ_{a} and μ_{s}' of the tissue.

A complication in fitting the Green's function to the measured data is that the diffusion equation models the light propagation in tissue from a perfect delta source. In reality, the laser in the system does not produce an infinitely short pulse, but a pulse with width in the order of picoseconds. In addition, the detector will introduce a broadening of the

measured TPSF due to the transit time spread within the detector. Therefore, in order to account for this, an instrument response function (IRF) is acquired before or after each measurement. The method of acquiring the IRF is described in detail in Section 6.2. The source and detector fibres are placed 'end on' to acquire a distribution of photons due to the system itself. This IRF can ether be deconvolved from the measured TPSF or convolved into the model before fitting.

Deconvolving the IRF from the TPSF has been found to produce undesirable results due to the complexity of filtering the noise from the Fourier transform. In this work the data is therefore analysed by convolving the IRF to the model before fitting to the measured TPSF. A diagram of this method is shown in Figure 5.4. The steps taken to resolve the values of μ_{a} and μ_{s}' in the tissue are as follows:

- The IRF and the Green's function solution are convolved by multiplying their Fourier transforms and applying the inverse Fourier transform to the result.
- The convolved model is then fitted to the measured TPSF using a least squares fitting regime based on the Levenberg-Marquardt method [131, 132].
- The fitting method minimises the squared deviation between the data, resolving the coefficient of absorption and scattering.

5.3 Depth sensitivity of time resolved data

Time resolved systems can offer much better mean penetration depth than continuous wave systems, as the photons that have travelled to a great depth in tissue can be isolated. The photons that make up the late part of the temporal point spread function have travelled further in the tissue, and are therefore more likely to have penetrated the

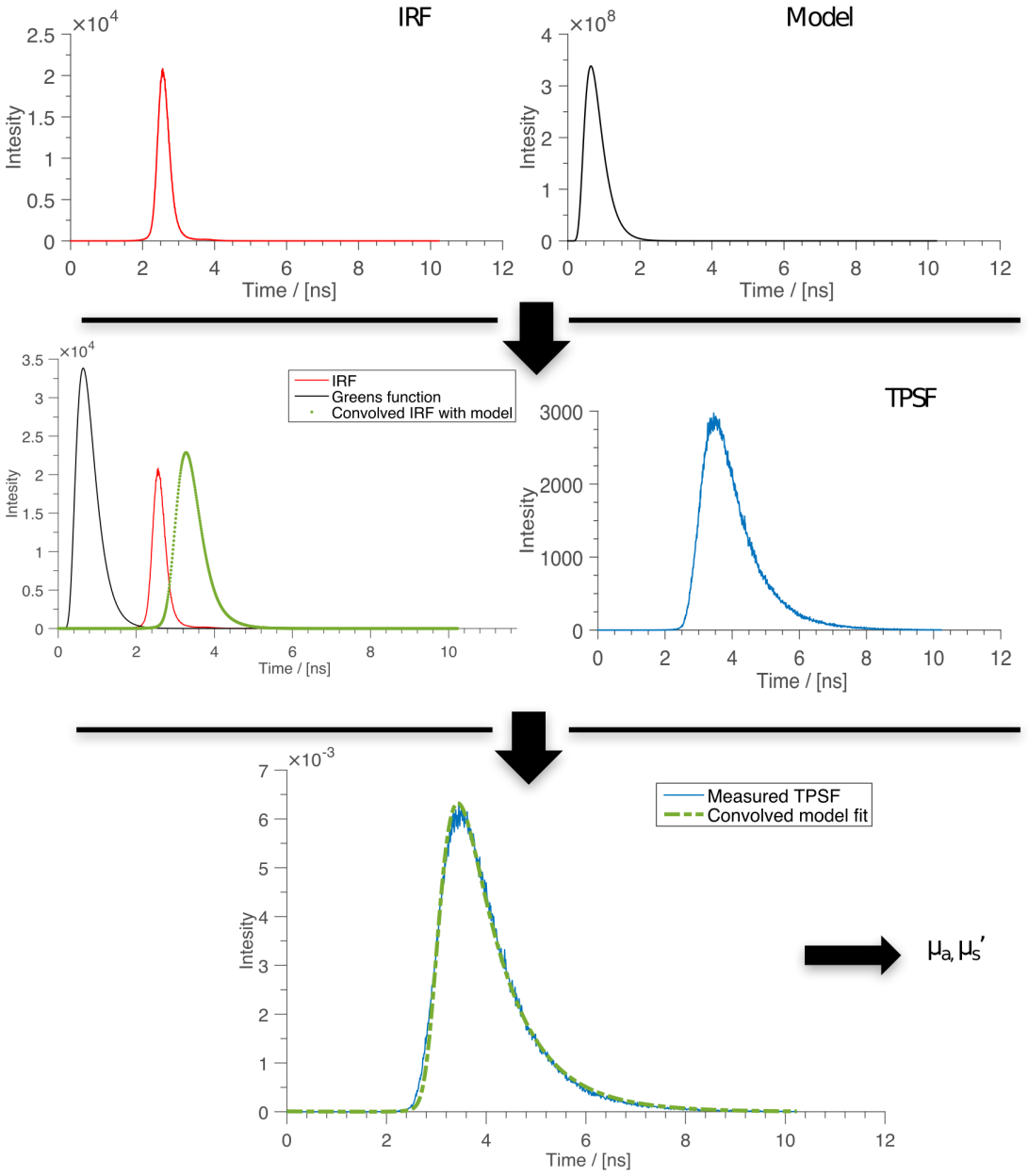

FIGURE 5.4: Procedure used to fit the Green's function solution to the diffusion approximation to the measured data, accounting for the IRF.

tissue at greater depth. This study aims to validate this assumption using experimental data.

Several methods utilising time resolved measurements have been developed to remove or separate the superficial layers from the deeper tissue. These have included utilising time

delays on the measurement by either gating the detector or using multiple detectors with optical delays [73, 115], and using a layered model to reconstruct absorption changes at different depths in the tissue [133–136]. Further quantitative experimentation is necessary to describe the advantage of time resolved fNIRS measurements in improving the sensitivity to deeper structures.

The perturbation method can be used to measure the spatial (both layer and depth) sensitivity of NIRS systems by relocating a local absorber in a homogeneous medium, and detecting the change in light attenuation compared to when the absorber located outside of the intralipid [137]. This procedure can then be repeated systematically throughout the liquid phantom to generate a two dimensional mean penetration depth profile of the area in plane with the source and detector positions [138].

5.3.1 Depth sensitivity data

The data used in this section was collected by Sonny Gunadi for a separate study into the depth sensitivity of different commercial NIRS devices [130]. This work however analyses the data use new methods. One of these was the Hamamatsu TRS-20, a time resolved system described in Section 3.1.3.1. The data collected in this study was used to investigate the impact of gated analysis of TPSFs on the mean penetration depth of the measurement.

5.3.1.1 Instrumentation and phantom

The instrumentation and phantom setup used to collect the data for this investigation are described in detail in [130]. Briefly, a TRS-20 near infrared spectrometer (Hamamatsu Photonics KK) was used to measure time resolved data on a liqud intralipid phantom. The TRS-20 is a two-channel, three-wavelength (760, 800, 830 nm) system, with an

average IRF FWHM of 360 ps for the three wavelengths and produces a mean power of 200 μW.

Figure 5.5 shows the IRF and a typical temporal spread point function measured by the TRS-20 in the experiment. The intensities of both the IRF and TPSF are controlled by variable optical attenuators to ensure the count rate is within the optimal operating range of the photomultiplier tube of 40-150 thousand counts per second. The collection time of each TPSF was set at 2 seconds for the entire experiment.

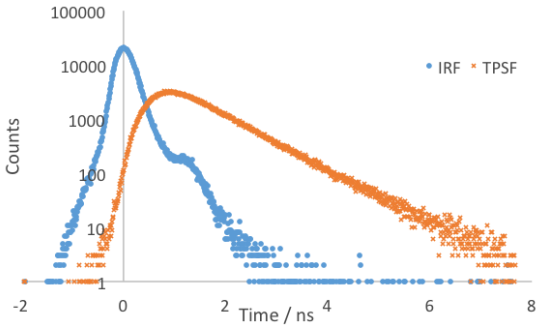

FIGURE 5.5: Instrument response function (IRF) at 800nm, and an example of a temporal point spread function (TPSF) during the perturbation study. The TRS-20 sets the time axis at t=0 to the peak of the IRF.

The experimental phantom setup used a 3-axis translation stage scanning system (Zaber LSR160A) to relocate a small local absorber in a diluted intralipid solution, as shown in Figure 5.6. The system has a 1 mm resolution in the x and y planes to ensure accurate relocation of the absorber controlled by a custom Labview (National Instruments) program. The absorber is a polyester based cylinder with dimensions 5mm x 5mm x 10 mm, with a reduced scattering coefficient (μ_s') of 10 cm^{-1}and an absorption coefficient of 0.14 cm^{-1}. The solution is enclosed in a clear glass tank contained 1% intralipid diluted with distilled water, with an absorption coefficient (μ_a) of 0.029 cm^{-1}and a reduced scattering coefficient of 10 cm^{-1}. The tank itself had 2 mm thick walls; the sensitivity maps therefore start at a minimum distance of 5 mm corresponding to the centre of the inclusion, and a total depth of 25 mm. For each location of the absorber, five measurements were taken and their average used in the calculations.

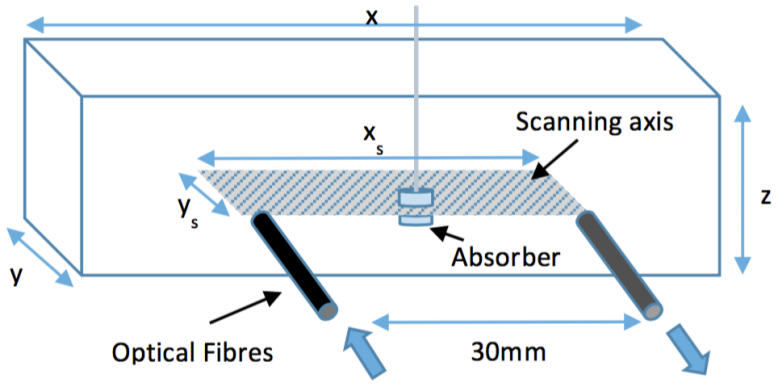

FIGURE 5.6: Experimental setup showing the input and output fibre locations with respect to the scanning plane. x, y and z correspond to the dimensions of the tank, which has dimensions 170mm x 50mm x 110mm, respectively. x_s and y_s correspond to the scanning area dimensions of 30mm x 20mm, starting at the inside of the tank.

The source and detector separation was set at 3 cm as this is a typical spacing for functional NIRS studies in the adult head, and the default spacing for the TRS-20. The absorber was raster scanned in two axes (x and y) in the tank, a reference measurement was performed after each scan along the x axis by removing the absorber from the phantom. This was required in order to correct for settling of the intralipid over time. At each absorber position a TPSF was measured. The depth sensitivity of the system was then measured using the percentage change in intensity for a specified region of the TPSF.

5.4 Intensity gating method for depth selectivity

Other studies have shown that by inspecting the late arriving photons of the TPSF the mean penetration depth of the measurement can be improved [73]. These photons have a longer time of flight so the assumption is that they have, on average, travelled through deeper tissue than the early photons.

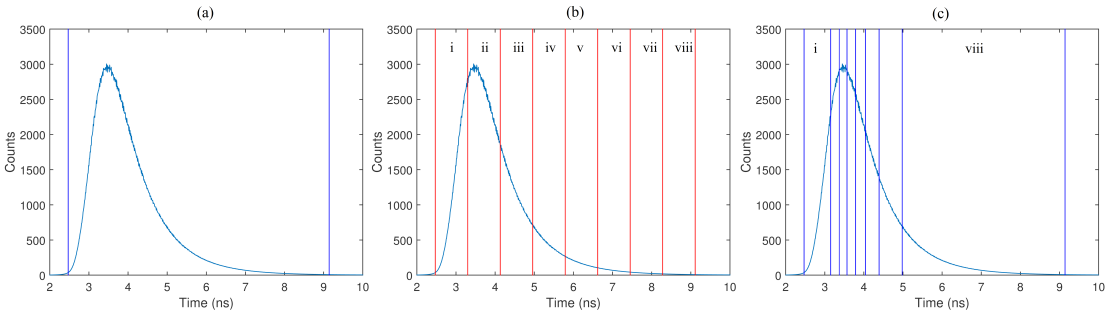

FIGURE 5.7: Time gating windows shown on averaged temporal spread point function. (A) Full time gate; (B) Equal time gates; (C) Time gates based on equal photon counts.

Two methods were used to determine the sizes of the gates used in our investigation. For the first method, the TPSF was divided into eight equal time-sized gates [115]. As the measurements were performed in an optically isolated black enclosure, there is very little noise in the signal, allowing the start and end of each TPSF to be easily identified. For the second method, the TPSF was also divided into eight gates, but in this case the gate boundaries were set so that each of them contained an equal number of photons [139]. The beginning and end of each TPSF was defined at 0.01% and 99.9% of the cumulative counts. This method of defining the TPSF proved to be a robust method of distinguishing between background noise and the signal. The total number of counts in each gate varied depending on the total counts in the TPSF. Examples of the gate boundaries arising from these methods are shown in Figure 5.7, with a full time gate shown for comparison.

The sensitivity of the measurement for the selected gate was calculated using

$$J_{gate}(x,y) = \frac{I^{ref}_{gate}(x) - I_{gate}(x,y)}{I^{ref}_{gate}(x)} \times 100\%, \tag{5.8}$$

where I_{gate} is the total number of photon counts recorded between the gate boundaries, and $I^{ref}_{gate}(x)$ is the intensity of photons recorded in the reference measurement for each relevant gate.

The mean penetration depth $\langle y \rangle$ is calculated using the equation

$$\langle y \rangle = \frac{\Sigma \langle J(y_i) \rangle . y_i}{\Sigma J(y_i)}. \tag{5.9}$$

5.4.1 Results

The ungated (Figure 5.7(A)) depth sensitivity to changes in the intensity of all three wavelengths of the TRS system can be seen in Figure 5.8. It is noted that the intensity changes calculated from the whole TPSF are equivalent to those of a CW system. The mean depth sensitivities are 11.6 mm, 11.9 mm and 11.4 mm for the three wavelengths 760 nm, 800 nm and 830 nm, respectively. The scale of each graph was kept distinct to more clearly highlight the sensitivity region.

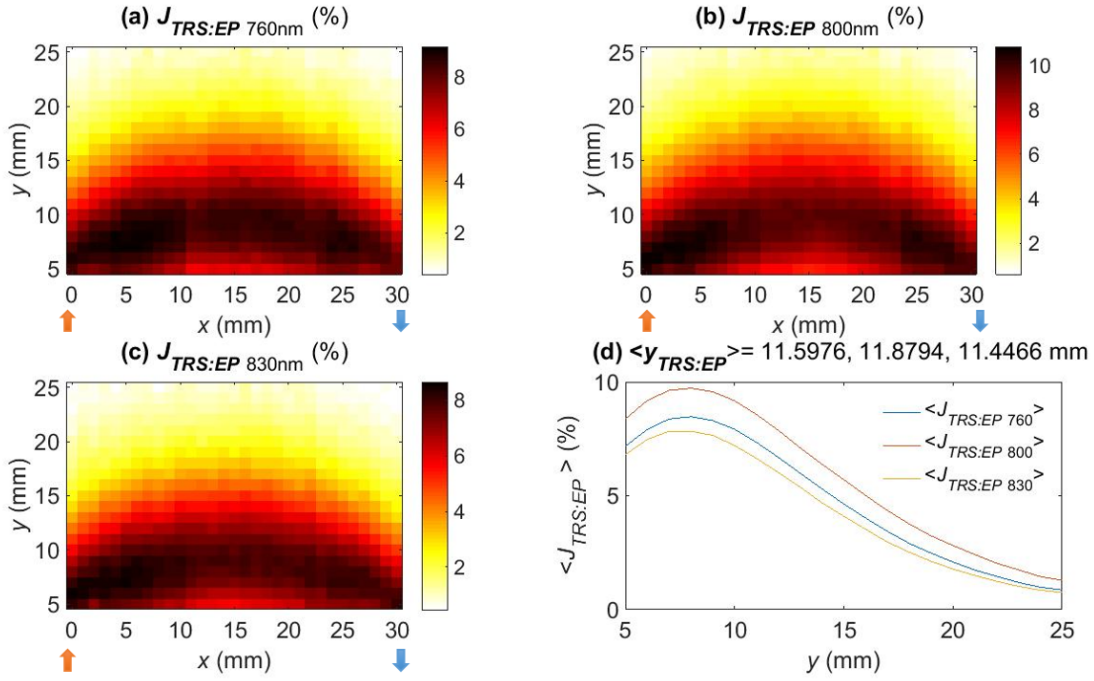

FIGURE 5.8: (A-C) Spatial intensity sensitivity when the entire TPSF is used for the three wavelengths 760 nm, 800 nm, and 830 nm; (D) Average depth sensitivity $\langle J(\text{TRS}) \rangle$ across the x axis.

The gating procedure was performed on the TPSFs using the two methods described above (Figure 5.7(B), (C)), with fixed time gate and equal photon gates. The result is

shown in Figure 5.9.

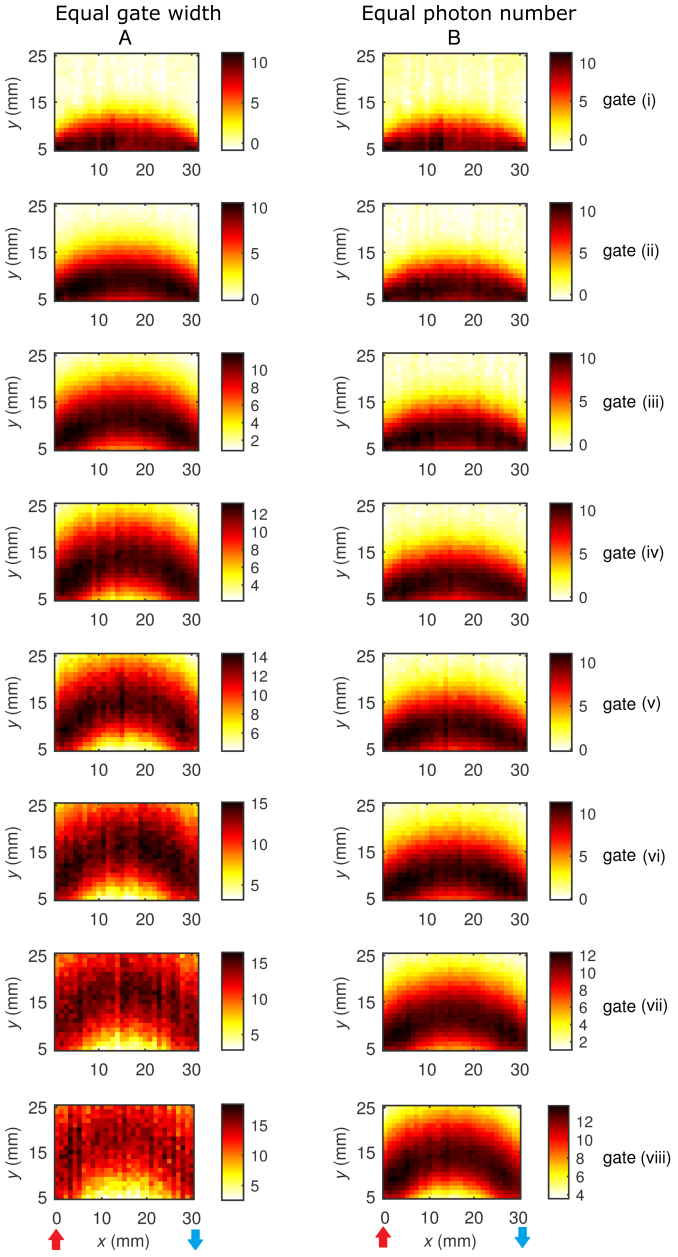

FIGURE 5.9: Column A: Mean depth sensitivity of equal gates size as in 5.7(B). Column B: Depth sensitivity for gates of equal photon counts as in 5.7(C).

The scale of each graph was again kept distinct to highlight features in the sensitivity maps. Both methods clearly show a 'banana' shaped profile for the sensitivity, which at the early gates almost entirely encompasses the superficial layer. As later gates are chosen, the sensitivity becomes higher for deeper regions. The mean penetration depth

for the fixed gates (i)-(viii) are 7.54, 10.52, 12.62, 13.83, 14.56, 15.04, 15.37, and 15.6 mm, respectively. The sensitivity maps show an increase of noise as later gates are used, as these include far fewer photons than the early gates. This is vastly improved with the use of equal photon gates, which have mean penetration depth of 6.77, 8.53, 9.52, 10.47, 11.24, 12.02, 12.92, and 14.32 mm for gates (i)-(viii), respectively.

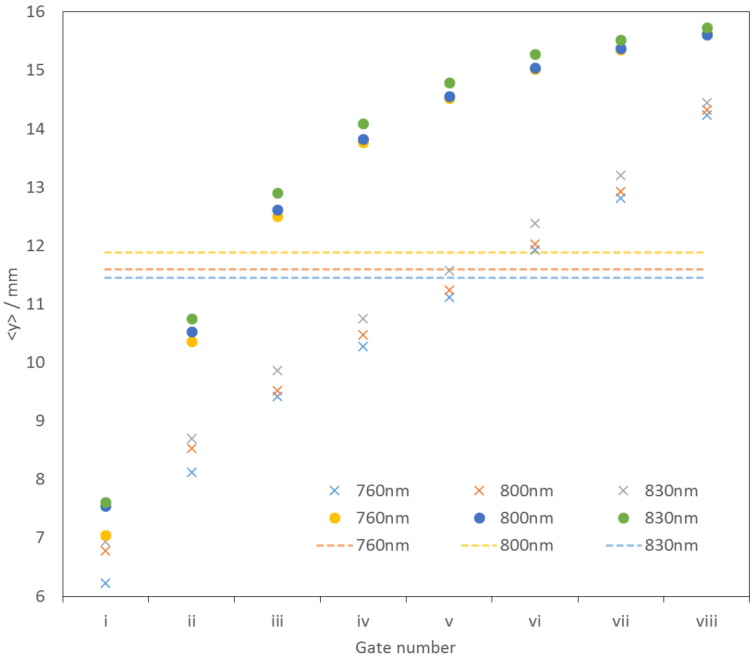

FIGURE 5.10: Mean sensitivity to narrow gated TPSF depth measurements. (Circles for fixed gate; crosses for equal photons. Dashed lines show mean depth penetration for entire TPSF.)

These results can be seen for all wavelengths in Figure 5.10. The fixed gate has the deepest mean depth penetration compared to the equal photon gates when eight gates are used, however, the noise encountered is significantly greater at later gates.

5.4.2 Conclusions

These results show that the TPSF can be gated in relatively small gates to adjust the mean penetration depth in a homogeneous phantom. Two methods are used to determine the gate size: fixed gating and equal photon gates. The latter method is advantageous over

the former, as the signal to noise ratio remains constant throughout the time gates. The time gating intensity results are in agreement with simulations using finite element methods performed by Montcel et al., and Monte Carlo simulations by Selb et al., where later photons detected in the TPSF are shown to pass through deeper layers in homogenous media [72, 140]. These results are also observed in a number of in vivo functional experiments where functional haemodynamic changes can be isolated from systemic variations by using late photon gates in analysis [115, 133].

5.5 Gated fitting of TPSF

One technique used to minimise the influence of the superficial layers on μ_{a} when fitting the diffusion equation to the TPSF is to reduce the fitting region of the TPSF [139]. In Selb et al. the TPSF is fitted to data starting at 50% of the highest value on the leading edge and finishing at 0.5% on the tail [72]. This section describes an investigation into the impact that these fitting gates have on the depth resolution of the measurement when resolving μ_{a}. Four gates, shown in Figure 5.11(a-d) are used in the data analysis; the entire TPSF, the start of the TPSF to 0.5% of the peak on the tail, 50% on the leading edge to 0.5% on the tail, and 50% on the leading edge to the end of the TPSF.

The spatial sensitivity to absorption was measured using the equation

$$J(x,y) = \frac{\mu_{\mathrm{a}}(x,y) - \mu_{\mathrm{a}}^{ref}(x)}{\mu_{\mathrm{a}}^{ref}(x)} \times 100\%, \tag{5.10}$$

where $J(x,y)$ is the sensitivity at (x,y), μ_{a} is the average of five measurements with the absorber at position (x, y), and $\mu_{\mathrm{a}}^{ref}(x)$ is the measurement of absorption with the absorber removed from the liquid phantom. As before with the intensity measurements, the reference measurement was performed at each pass along the x axis to reduce any drift through the measurement. The layer sensitivity (the sensitivity of the entire scan

along x) was calculated in two parts. The boundaries of the superficial layer were defined as y = 5-12 mm, due to the limits of our experimental setup, and an estimate for scalp thickness [128]. A deeper layer sensitivity in the region of interest is also calculated with the boundaries y = 12-25mm, again due to the limits of our setup. A high ratio of deeper sensitivity to superficial layer sensitivity will indicate a good fitting procedure.

5.5.1 Results

The effect of the gating on the fitting of the TPSF is shown in Figure 5.11. Figure 5.11(e-h) show the respective effect on mean penetration depth at 800 mn. Figure 5.11(i-l) show sensitivity profiles at all three wavelengths. Table 5.1 shows values for the mean penetration depth of all three wavelengths, and the sensitivity ratio of the region of interest to the superficial layer. The gate resulting in the deepest mean penetration depth is found where the entire TPSF is used with an average $\langle y \rangle$ over the three wavelengths of 19.93 mm. The next best performing gates are the gates in Figure 5.11(b) and Figure 5.11(d), with an average $\langle y \rangle$ of 19.28 mm and 18.82 mm, respectively. The worst gate for depth penetration is the gate seen in Figure 5.11(c) where the leading edge and tail are not included in the fit, with a mean depth of 17.39 mm over the three wavelengths. The ratio of the superficial layer to the region of interest follows the same order as the mean penetration depth, with the full TPSF fit producing the lower ratio. As can be seen in Figure 5.11(g), the noise of the sensitivity maps increases as the size of the gate reduces.

5.5.2 Conclusions

The impact of gated fitting of the TPSF on the depth penetration of time resolved NIRS measurements has been investigated using four different gating windows. There were small differences between the sensitivity maps for the fitting gates chosen with the

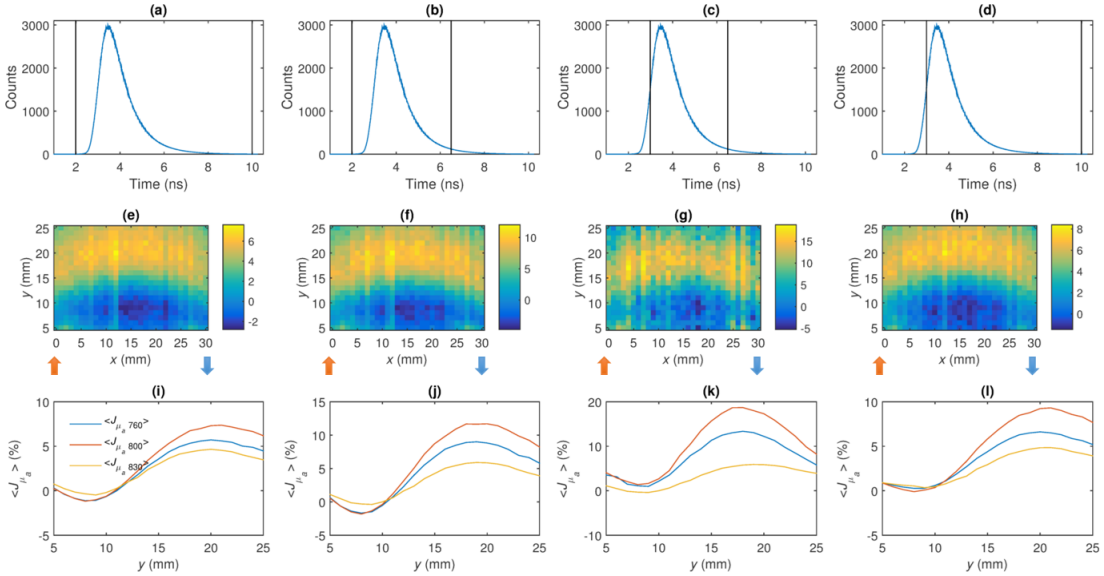

FIGURE 5.11: (a) Full TPSF used in fitting procedure; (b) Start of TPSF to 0.5% of the peak on the tail; (c) 50% of peak on the rising edge to 0.5% of the peak on the tail; (d) 50 % on the rising edge to the end of the TPSF; (e-h) Sensitivity maps of absorption at 800nm for the respective gated fits shown in (a-d); (i-l) Average sensitivity profiles for the gated fits (a-d) for all three wavelengths (760, 800, 830).

Gate	Mean depth sensitivity <y> /mm			<J(SPL)> (800nm)(%)	<J(ROI)> (800nm) (%)	<J(SPL)> / <J(ROI)> (%)
	760nm	800nm	830nm			
Full TPSF	20.26	20.21	19.33	0.25	6.14	4.12
Start:0.5% tail	19.53	19.5	18.82	0.54	10.74	4.98
50% rising edge:0.5% tail	17.31	17.49	17.37	4.06	17.61	23.06
50% rising edge : end of TPSF	18.71	19.19	18.57	0.87	7.81	11.09

TABLE 5.1: Mean penetration depth for different gated fits for 3 wavelengths. Sensitivity to the region of interest ($\langle J(\text{ROI})\rangle$) and the ratio of sensitivity to the region of interest to the superficial layer ($\langle J(\text{SPL})\rangle$).

highest penetration and the best layer selectively achieved when the entire TPSF was fitted. Several papers have shown that fitting to a late window of the TPSF has produced more accurate results for μ_a at deeper tissue, however, we have found that using this technique does not improve the depth penetration of the measurement [73, 139].

The value calculated for the mean penetration depth of the TRS-20 can only be used to compare against other values using the perturbation method using the same or a similar phantom setup. As we used a liquid phantom, which would not accurately represent the geometry and absorption coefficient of the human brain, we cannot translate the values found in this investigation to the values expected from clinical measurements on the head.

Due to practical reasons, the range of the sensitivity map was set at 5 mm to 25 mm. Ideally, this would have started closer to the optodes to simulate the contact that fibres would have with skin, and continued until there was a detected sensitivity to the absorber. The absorber itself presented a large change in absorption that would not typically be seen in the brain, and is discussed in detail by Gunadi et al., where the same absorber was used in their investigation [130]. However, as the absorber was used to compare between different methods used in this paper, the large μ_{a} was beneficial to provide good contrast in the measurement.

In future work, scanning the local absorber in the z direction would provide interesting insight into the sensitivity of the measurement to changes occurring off the plane between the source and detector. Unfortunately this was not a feasible option in the current setup, as it would require significantly more measurements, and the intralipid solution would not maintain the same optical properties for this length of time.

5.6 Discussion

In this chapter, transport models of light in a scattering medium are introduced. The radiative transfer equation is described, and an explanation of how each of its terms describes the loss or gain in energy due to absorption and scattering as light travels through biological tissue is included. The diffusion approximation to the RTE is presented, and the Green's function solution to the diffusion approximation is compared to a Monte

Carlo simulation. We include a step-by-step explanation of how the Green's function can be used in an optimisation method to determine values of μ_{a} and μ_{s}' from time resolved spectroscopy measurements, taking into account the instrument function.

A short study into possible techniques that can be used to improve the mean penetration depth of experimental time resolved measurements has also been reported. The study uses the experimental perturbation method to show that intensity gating the TPSF can provided higher sensitivity to deeper layers in a homogeneous medium. The study also found that fitting the Green's function solution to the entire TPSF maximises the mean penetration depth of the measurement.

Chapter 6

System calibration studies

In Chapter 4 we described the design choices and evaluated the performance of each component of the system individually. In this chapter, the performance of the system is characterised as a whole. The temporal stability, instrument response function (IRF), random noise, cross talk and temperature stability are all measured or calibrated before testing the basic function of the system by measuring the speed of light and performing several phantom studies.

6.1 Random noise

Random noise is present in all optical measurements due to Poisson or shot noise in the detection of photons. In this system, other contributions to the total noise are made by background noise from stray room light, spontaneously emitted photoelectrons from the cathode and dynodes within the PMT, and electrical noise in the system. The shot noise, arising from the stochastic nature of photon detection, will be a limiting factor to the signal to noise ratio. The shot noise measured will be equal to the square root of the signal (shot noise $= \sqrt{\text{signal}}$).

The majority of dark counts measured are produced by thermionic emission of electrons in the PMT in the absence of light. We can reduce the dark count rate by cooling the PMTs, minimising the probability of thermionic emission [141]. The specifications of the PMT state that the dark count rate for the Hamamatsu PMTs is 125 s^{-1}at room temperature. The majority of dark counts will be due to thermally emitted electrons from secondary dynodes inside the PMT, as the multiplication of signal for these events is not as great as an incoming photon, we can reduce the measured counts due to these events by utilising a threshold cutoff on the incoming signal line at the constant fraction discriminators (CFD).

Figure 6.1 shows the noise detected under different light conditions. In Figure 6.1(A) we see the detected noise in the system with no room lighting and the VOAs in the closed position. For a second exposure we see a total count rate of 3 photon counts. This low background noise can be attributed to careful calibration of threshold values on both the router and TCSPC card. This is a typical outcome of the counts with the system in a dark lab with a mean count rate of 3.4 s^{-1}. When the room is illuminated with ceiling lights the background noise detected can be seen in Figure 6.1(B) and Figure 6.1(C), where the VOA is fully closed and fully open, respectively, with the end of the fibre covered in the IRF module. Here we see an increase in the background noise, which must be due to light entering the PMMA fibre between the VOA and the PMT. With the VOA closed (Figure 6.1(A)) and open (Figure 6.1(B)) we achieve a mean count rate of 142 s^{-1} and 343 s^{-1}, respectively. When the fibre is placed on tissue with one of the optode holders seen in 4.20, we see typical background noise as shown in Figure 6.1(D), with an average count rate of 5077 s^{-1}.

We can see that the dark counts due to thermally emitted electrons from the PMT can effectively be eliminated from the measurement, and nearly all of the background noise measured is due to background room light. This light shielding in the system itself is not perfect, however, the vast majority of stray light enters the system at the end of the

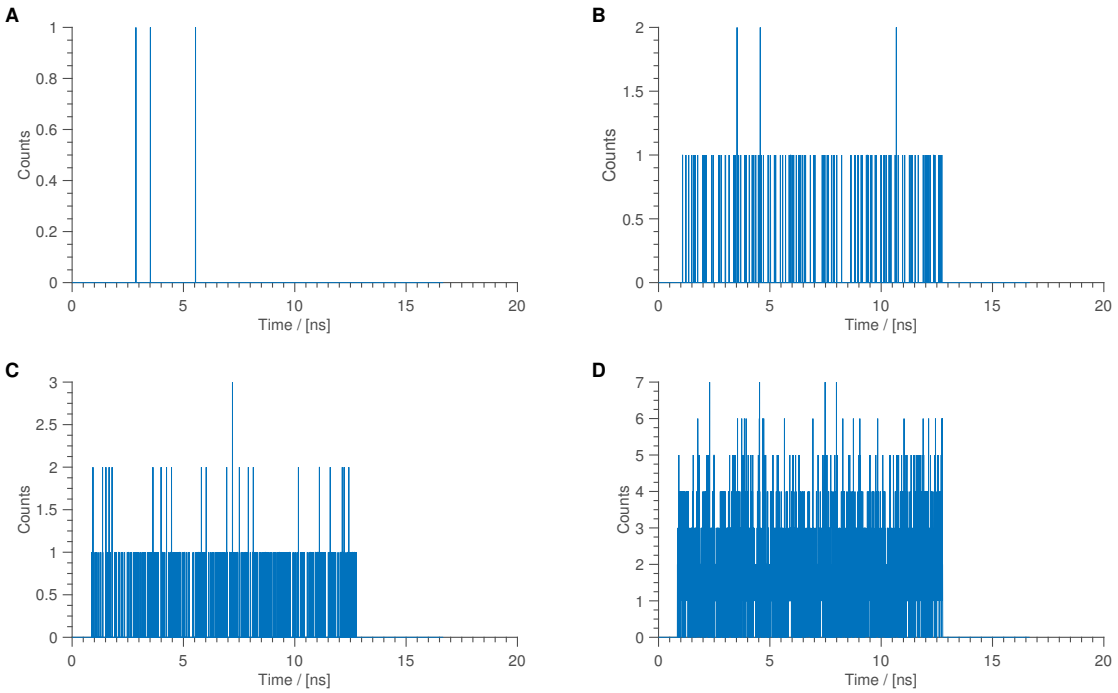

FIGURE 6.1: Noise floor measurements for 1s collection time with no source input under different lighting conditions. Noise floor measured (A) room lights off and the VOAs in closed positions, (B) room lights on and VOA in closed position, (C) room lights on and VOAs fully opened but with end of fibre shut off, and (D) end of fibre placed on phantom to simulate typical measurement conditions.

fibre which is placed on the skin. The best solution for reducing background noise is to therefore make sure there is highly effective light shielding around the fibre end on the skin and/or to conduct experiments in minimal lighting conditions.

6.2 Instrument response function

As discussed in earlier sections, the measured signal in a time resolved system is a temporal spread point function (TPSF), corresponding to the true TPSF of the medium being investigated convolved with the temporal response of the system itself. The TPSF is therefore given by

$$TPSF_{measured} = TPSF_{true} \otimes IRF. \tag{6.1}$$

In order to remove the IRF from the measurement, it is necessary to record the IRF immediately before or after every measurement. The shape and width of the IRF depends on the broadening of the pulse due to the detector fibre bundles, PMMA fibre and thermal dispersion of the photoelectrons in the PMTs. The largest source of scattering in the system is from the temporal response of the PMTs due to the process of electron multiplication. As the photoelectrons are emitted from the cathode and the dynodes, the path that they travel in the vacuum to the anode is not defined and varies from photon to photon. This difference in paths for the photons will mean the measured flight time of each photon will differ and cause the short pulse emitted by the laser to be detected as a broadned pulse. This is called the transit time spread of the photomultiplier tube and is measured by the full width half maximum (FWHM) of the signal generated by the PMT. The Hamamatsu H7422-50P have a transit time spread of up to 300 ps [51]. The IRF is measured by directing the output from the source fibre directly into the detector fibre through a diffuser and a neutral density filter, as shown in Figure 6.2. The diffuser is used to uniformly fill the detection fibre with light in the same manner as it is typically used in experiments; this is important as it has been shown that measurements of scattering and absorption using this method can be overestimated by 90% without the diffuser [142].

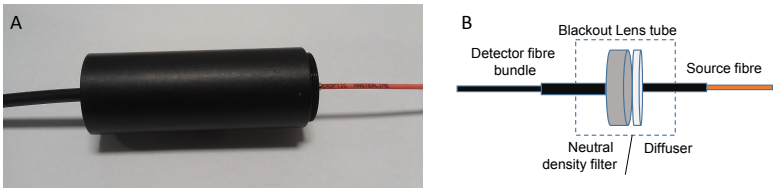

FIGURE 6.2: (A) Instrument response function module; (B) Diagram of module showing 5 OD neutral density filter and diffuser.

The FWHM of the IRF should be as small as possible. This is mainly achieved by proper calibration of the timing electronics of the system. A typical IRF measured for 16 wavelengths by this system is shown in Figure 6.3. The average FWHM of the measured IRFs is 370.0ps. As the initial pules from the light source have a FWHM of 4ps, the

broadening of the response function is mainly due to the PMT (∼300ps), and the detection fibres. There is a small reflection peak occurring at an average of 2487ps after the main peak, which is most likely due to a reflection in the optical fibre, which is common in time resolved systems. ([48, 57, 73]). The magnitude of the reflection peak is around two orders of magnitude less than the main TPSF, and so should not affect the measurements significantly. The IRF differs slightly in measurements taken at different times due to temperature variations, therefore a new IRF should be measured as close to the measurement as possible to avoid any difference in the source light or detector conditions.

Stability studies, described later in this chapter, show that the IRF, after improvements to the cooling in the system (6.4), remains stable over a long period of time.

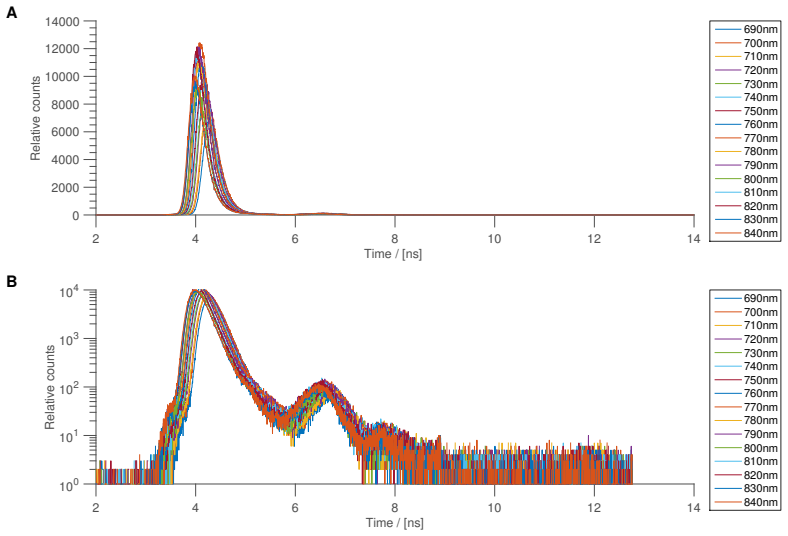

FIGURE 6.3: (A) Instrument response function of 16 wavelengths measured using IRF module (linear scale); (B) Instrument response function of 16 wavelengths measured using IRF module (log scale).

6.3 Crosstalk

Crosstalk in multichannel near infrared systems occurs where photon counts are registered in a different channel to that of the incoming photon. Crosstalk can occur optically

or electronically in the system between different channels. Source crosstalk occurs in systems that have source switches, such as a fibre switch or galvanometer, to angle the light into the end of the fibre [48, 72]. In this system, however, there is no fibre switch and the source channels are kept separate from the initial beam splitter in the acousto-optic tunable filters (AOTF). If source multiplexing is required, the RF frequency sent to the AOTF can be cut off effectively by blocking the light path for that source. There is then no possibility that the light from one source channel could affect the other. However, crosstalk is still likely to occur in the detection process due to shared components.

There is unlikely to be any source of significant optical crosstalk in the system due to the optical paths of each detector being kept separate. The only component the optics share is the VOA housing which is a solid machined piece of black Delrin. The tolerances of the machining are very tight, and hence it is unlikely that any light is crossing optical paths in this part of the system.

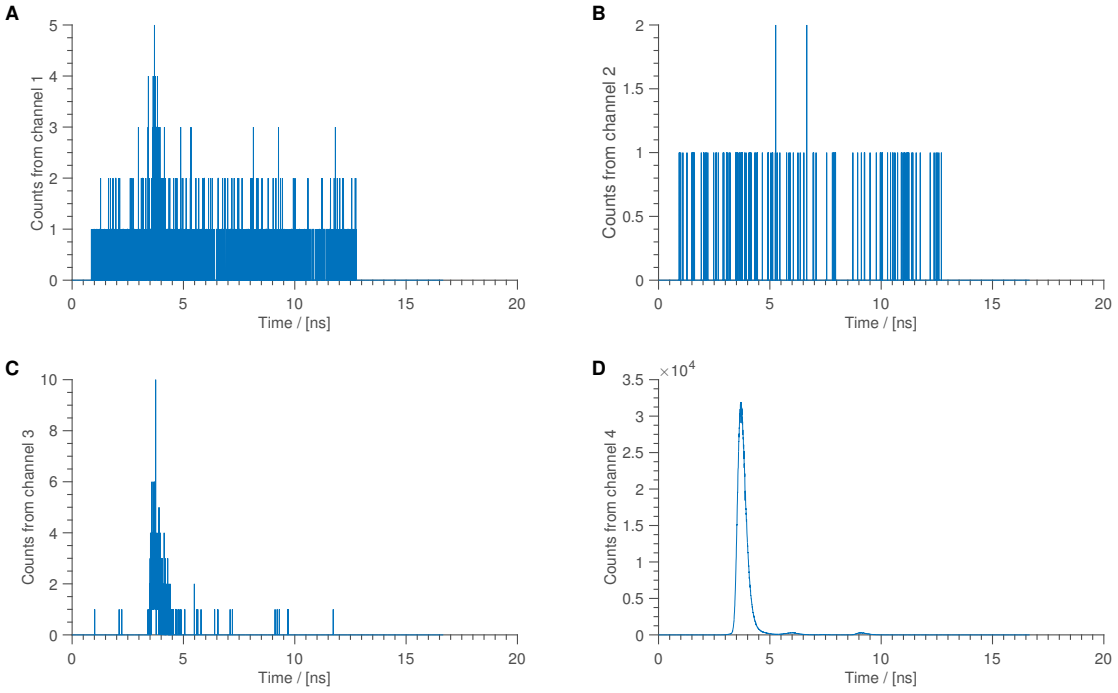

FIGURE 6.4: Crosstalk in 3 channels when measuring PMT 4's IRF. (A) Cross talk in channel 1 (PMT 1); (B) Cross talk in channel 2 (PMT 2); (C) Cross talk in channel 3 (PMT 3); (D) IRF measurement in channel 4 (PMT 4).

Electrical crosstalk arises due to either electrical noise from photon counts in a different channel or the router and TCSPC cards allocate a photon to the wrong TPSF in the memory. Electrical crosstalk is much more likely to occur then optical crosstalk, as the detected electrical pulses produced by the PMTs are all directed into the same 4-way router [112]. The router itself has threshold comparators which are adjusted by a trimpot in the module. This is used to ensure that the router discriminators are only triggered from pulses triggered from the detection of a photon. The threshold is also used to lower the cross talk between channels. Figure 6.4 show the photon counts for all 4 channels when only a single channel is illuminated. In this experimental setup channel 4 is highly illuminated, with a peak count of 32135. Typical measurements in tissue would see a photon count an order of magnitude less. The crosstalk measured in channels one, two and three accounts for 0.015%, 0.006% and 0.028% of the measured peak, respectively.

6.4 Stability study

Long-term stability of the measurement system is of high importance for the application of the instrument. Studies can be performed over periods of time of up to several hours, and maintaining high temporal stability over each measurement is therefore critical. The IRF can only be measured before or after the experiment takes place and is assumed to remain constant throughout the measurement. As the system is comprised of a number of different components, there are many possibilities for instability or drift to occur with fluctuations in temperature and laboratory conditions. We can test the stability and performance of the system by measuring the calibration IRF repeatedly over a 1 hour period for 16 wavelengths in the near infrared region every minute.

A stable system would produce a consistent IRF for all wavelengths for the duration of the experiment. The measurement was started 1 hour after the laser was switched on to allow the system to stabilise. From these measurements we calculate four parameters:

total counts, peak counts, mean time of flight, and variance of the TPSF, all of which are calculated after the removal of noise from the data. The initial results before optimisation of the design can be seen in Figure 6.5.

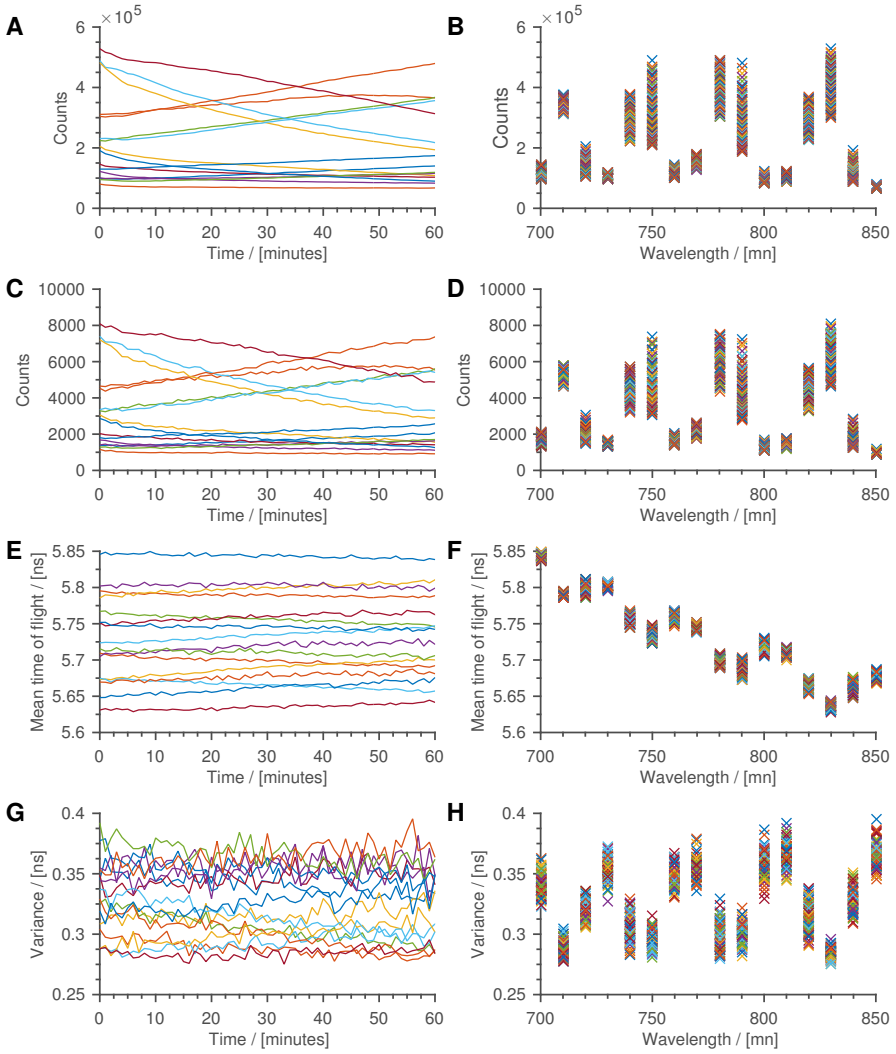

FIGURE 6.5: Different data types taken from IRFs of a stability test, where significant drift is seen throught measurement. (A) Total counts vs time; (B) Total counts vs wavelength; (C) Peak counts vs time; (D) Peak counts vs wavelength; (E) Mean time of flight vs time; (F) Mean time of flight vs wavelength; (G) Variance vs time; (H) Variance vs wavelength.

The results from the initial stability study display considerable instability in the system. The total counts of the TPSFs contain a number of distinct patterns for different wavelengths. In several wavelengths the total counts decreases by over 50%, whereas in

a number of wavelength channels the total counts increases by a similar amount (Figure 6.5). There is also drift in other wavelengths by a smaller amount, whilst wavelength 850nm experienced zero drift. The peak counts (Figure 6.5(C) & (D)) display the same behaviour. The mean time of flight show more consistent trends, however, drift is still seen in all wavelengths. Again, these drifts occur in different directions and there is no global trend.

This stability proved to be a major issue in the development and calibration of the system as there was no clear indication as to its cause. A number of further experiments were therefore carried out in order to investigate the source of this problem, and the following observations were made:

- The laser stability test described in Section 4.1.3 and Figure 4.11 was repeated, and very similar results found. Over an 8 hour period the maximum drift was measured at $\pm$3%. We conclude that the issues here cannot be due to drift in the power of the laser source.
- The sync (seed) pulse shows no sign of drift either, with similar findings as in Figure 4.10. Over the same 8 hour period the sync pulse had a frequency range of less than 1%.
- This issue is unlikely to be due to an error in the TCSPC card, as this would most likely create a global response.
- Similarly, errors in the IRF measurement module or VOAs would produce a global trend.
- In some repeated measurements over long periods, the PMTs would occasionally shut down due to overheating or excessive light.

The shut down of the PMTs indicate a possible number of scenarios: i) the PMTs are being overloaded with photon counts, or ii) the ambient temperature inside the system

is in excess of the PMTs operating range. The cause of the error is very unlikely to be due to the overload of the PMT with photon counts, as the incident light on the PMTs during the IRF measurement is significantly lower than the PMTs' limit.

A device was created to allow the temperature to be measured in several areas of the system simultaneously during normal operation. The results from this test can be seen in Figure 6.6. The temperature can be seen to increase rapidly in the first 90 minutes of operation, with the inside of the detector box reaching over 30 degrees Celsius. The initial design of the detector enclosure contained a metal light shield that covered the entire sub rack with a section cut out in order to leave the heatsinks above the PMTs exposed. This light shield was thought to be causing excessive heating in the surrounding enclosure of the PMT due to a lack of air flow. This covered section also contains the VOAs (although these do not move during the experiment, so do not produce any heat), PMT controllers and USB hub. Therefore, the light shield was removed and a fabric covering placed over the VOAs and polymer fibre leaving the entire PMT modules exposed. This improved the cooling of the PMTs and significantly reduced the number of incidents of PMT overheating. However, the cooling of the system as a whole remains a concern, and future work with the system would benefit from the addition of active cooling elements, as well as integrated temperature sensors. The best way to achieve this would be to incorporate fans in the top panel to remove hot air from the systems environment.

This alteration to the heat flow improved the stability of the PMTs significantly. A repeat measurement of the IRF (Figure 6.5) was conducted and the results are shown in Figure 6.7. The improvement of air flow and cooling in the detector box removed any drift in the measurement of total and peak intensities, mean time of flight, and variance of the IRFs measured. The total and peak counts show very little jitter throughout the measurement. The mean time of flight for the IRFs show a clear improvement on the measurement in Figure 6.5, with very little noise over the hour period. In Figure 6.7(F),

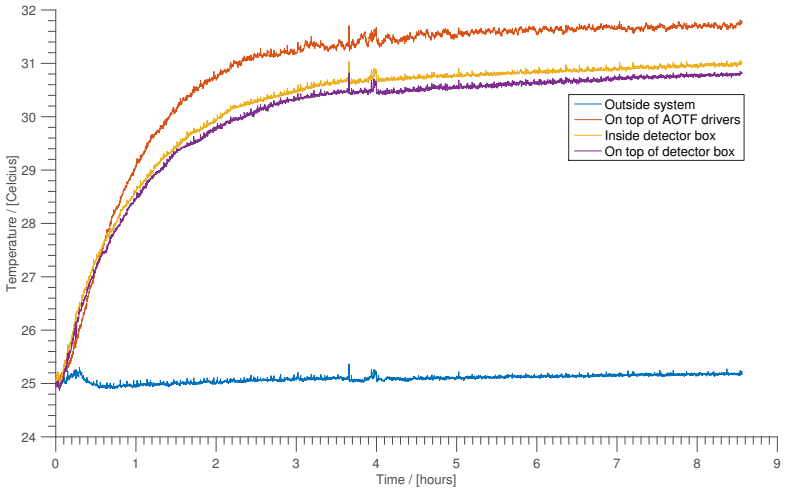

FIGURE 6.6: Temperature measured at different positions in system from the initial warm up period.

the data shows a steady decrease in time of flight as wavelength increases. This is expected due to the scattering decreasing in the optical fibres as wavelength increases due to Rayleigh scattering. These results show the importance of cooling on the system and ambient temperature of the room. This is especially critical as the system is expected be used in different environments.

6.5 Temporal stability

Good temporal stability of the mean time of flight is required for accurate measurements. In order to more clearly assess the temporal stability of the measurements shown in Figure 6.7, the mean time of flight delay has been set to 0 s for all wavelengths at time 0 minute, and subsequent measurements are relative to this time point (Figure 6.8). The difference between the minimum and maximum mean time of flight was 11.7ps. There is also no significant drift over the measured period, confirming that the measurement is sufficiently consistent over time.

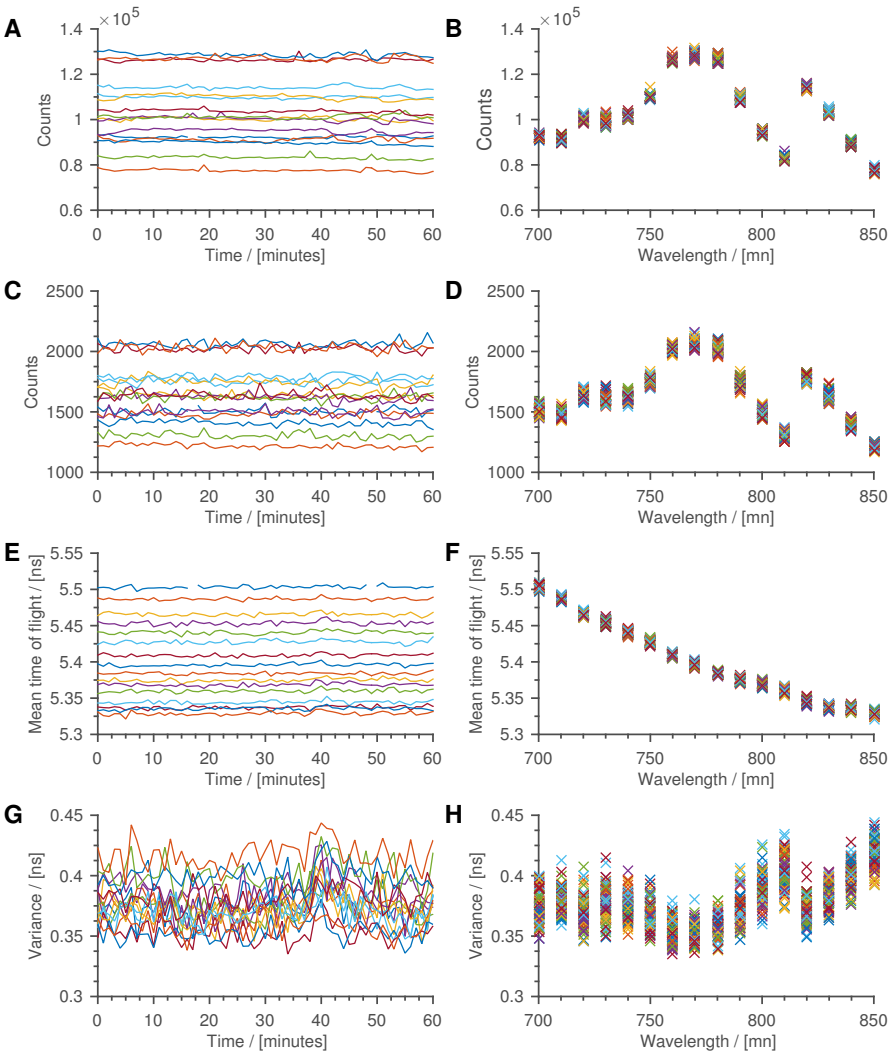

FIGURE 6.7: Different data types taken from IRFs of stability test after improving the cooling in the system by increasing the airflow over the PMTs. (A) Total counts vs time; (B) Total counts vs wavelength; (C) Peak counts vs time; (D) Peak counts vs wavelength; (E) Mean time of flight vs time; (F) Mean time of flight vs wavelength; (G) Variance vs time; (H) Variance vs wavelength.

6.6 Speed of light measurements

The temporal accuracy of the system can be verified by measuring the mean time of flight for different source-detector separations in air and comparing it with the known speed of light. Figure 6.9(A) shows the mean times-of-flights for 16 wavelengths and 6.9(B) shows the calibrated results and the expected line. A good agreement between the results and calculated distance from the speed of light was found. The system measured the

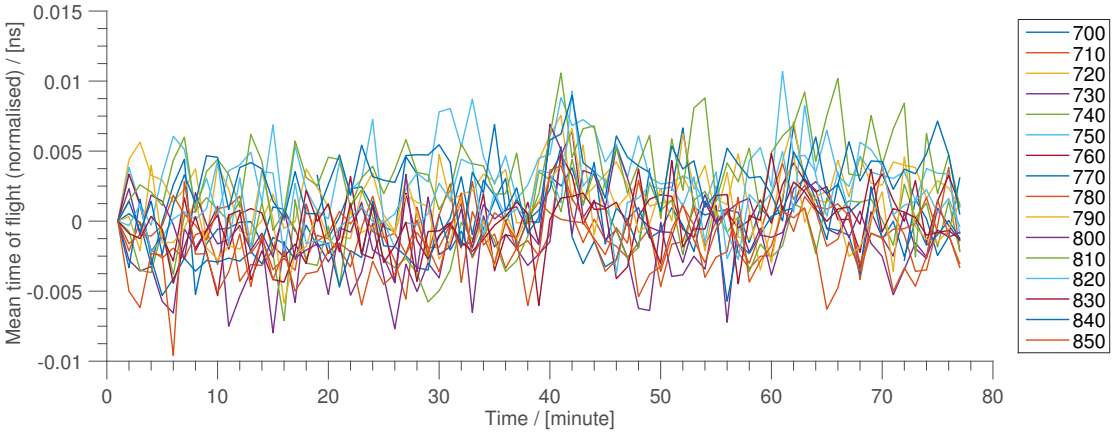

FIGURE 6.8: Mean time of flight of IRF measurements with a normalised initial delay.

speed of light with a 5% error from the true value in a vacuum. The cause of this error is most likely an experimental error caused by movement of the detector fibres away from the source fibre.

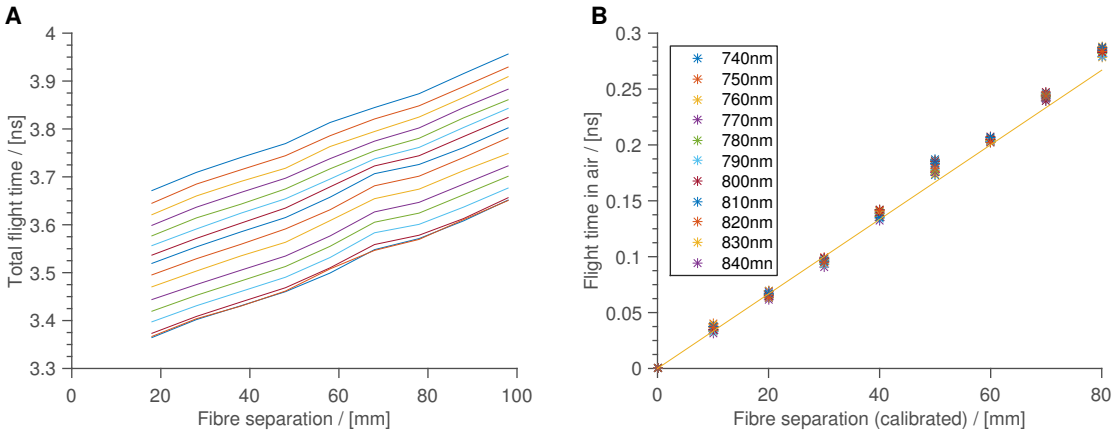

FIGURE 6.9: (A) Total mean time of flight for different wavelengths; (B) Calibrated mean time of flight for fibre separations showing calculated flight times.

6.7 Phantom studies

In Chapter 4, the calibration of the system was described along with evaluation the performance of individual components of the system. In Sections 6.1 to 6.6, the sensitivity and response of the system was evaluated as a whole. This section evaluates the

system's ability to perform accurate measurements on optical phantoms. Phantoms are manufactured, tissue-like structures with known quantities of ingredients for which the optical properties are known. By using a phantom with a known, uniform absorption and scattering coefficient, the ability of the system to recover these values can be determined. The phantoms used in this study are all made in the Department of Medical Physics and Biomedical Engineering at UCL. The aim of the system is to accurately measure the coefficient of absorption and scattering at multiple wavelengths in the near infrared range. While a large challenge of this task is to detect the TPSFs of all wavelengths over a short period of time, we can use a static phantom to see the ability to resolve absorption and scattering over longer periods of time.

6.7.1 Epoxy resin Phantom

Epoxy resin is often used as a basis for optical phantoms as it offers a rigid, easily manufactured and stable material for creating optical slabs. The epoxy resin used in the first phantom is a clear two part araldite resin which produces a strongly exothermic reaction when mixed. The mixture is then combined with Titanium Dioxide (TiO_2) pigment in order to increase the scattering properties of the material to tissue-like levels (1 mm^{-1}at 800 nm). A light absorbing dye is also added, called Projet 900NP, in order to increase the coefficient of absorption of the phantom to between 0.0044$mm^{-1}$and 0.0112mm^{-1}in the near infrared range. Further details on the fabrication of this phantom can be found in papers by Firbank et al. [143, 144]. The procedure used for making this epoxy resin phantom is expected to produce optical properties to within 5% of the specified values. As with all measurements detailed in Section 6.2, a calibration IRF for all wavelengths is measured first (Figure 6.10(A)). To measure the accuracy of the system against the expected absorption, a wide range of wavelengths between 690nm and 840nm with 10nm separation were used.

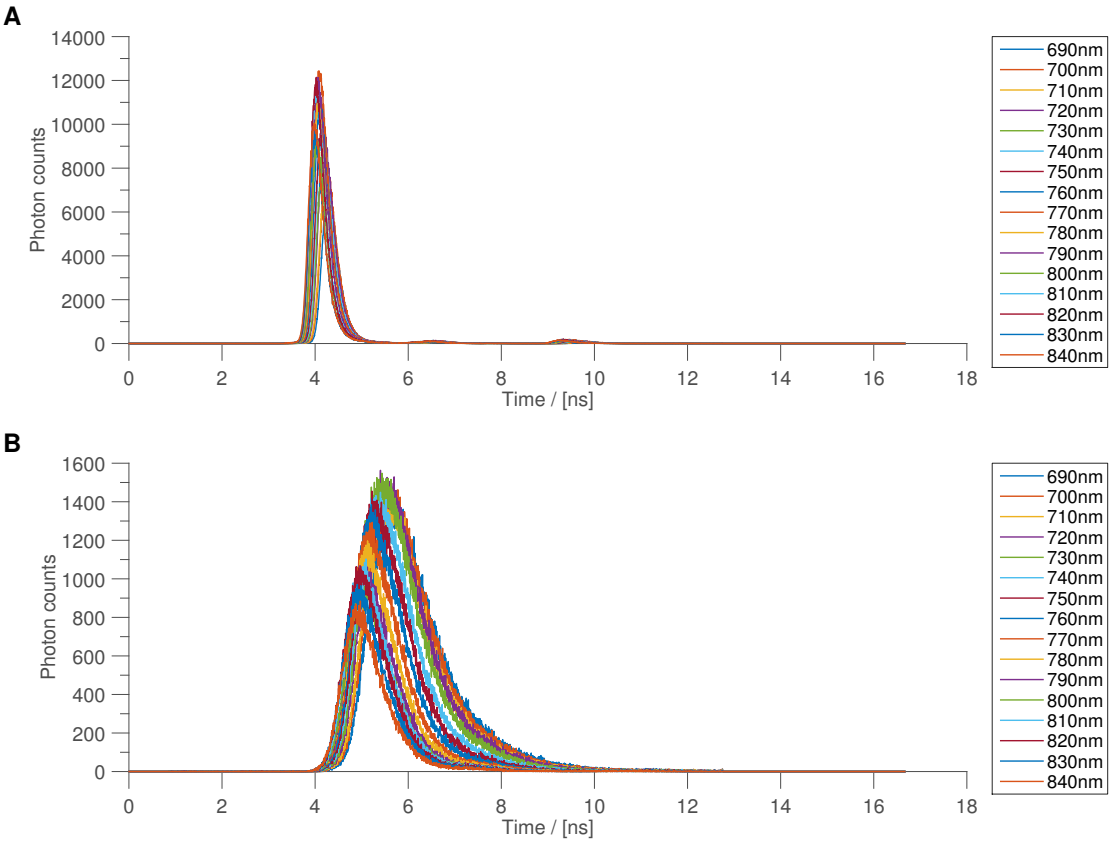

FIGURE 6.10: (A) IRF measurements for 16 wavelengths using IRF module; (B) TPSFs measured in reflection mode on Epoxy resin phantom.

6.7.1.1 Results

TPSFs were measured in a simple reflection mode using the optode holders shown in Section 4.4.1 and a source-detector separation of 30 mm from centre to centre. The TPSFs were recorded with a 2 second collection time and are shown in Figure 6.10(B). These TPSFs were processed by removing the average background noise, and a fitting process as described in Section 5.2 was employed to recover the absorption and reduced scattering coefficients. Figure 6.11(A) shows the absorption coefficient at each wavelength calculated using the system measurements, and the expected values of absorption (solid line) in the phantom. The expected values are calculated from the manufacturer specifications of the materials used. The recovered absorption and scattering produced using the system is indicated by point markers on both graphs. The measured values for

the absorption coefficient largely agree with the expected values of the phantom with a mean error of 5% and a maximum error of 9% at 690 nm. The calculated values of μ_a range from 0.005 mm^{-1}at 690 nm to 0.011 mm^{-1}at 840 nm, compared with the expected values of 0.004 $mm^{-1}$and 0.011 mm^{-1}.

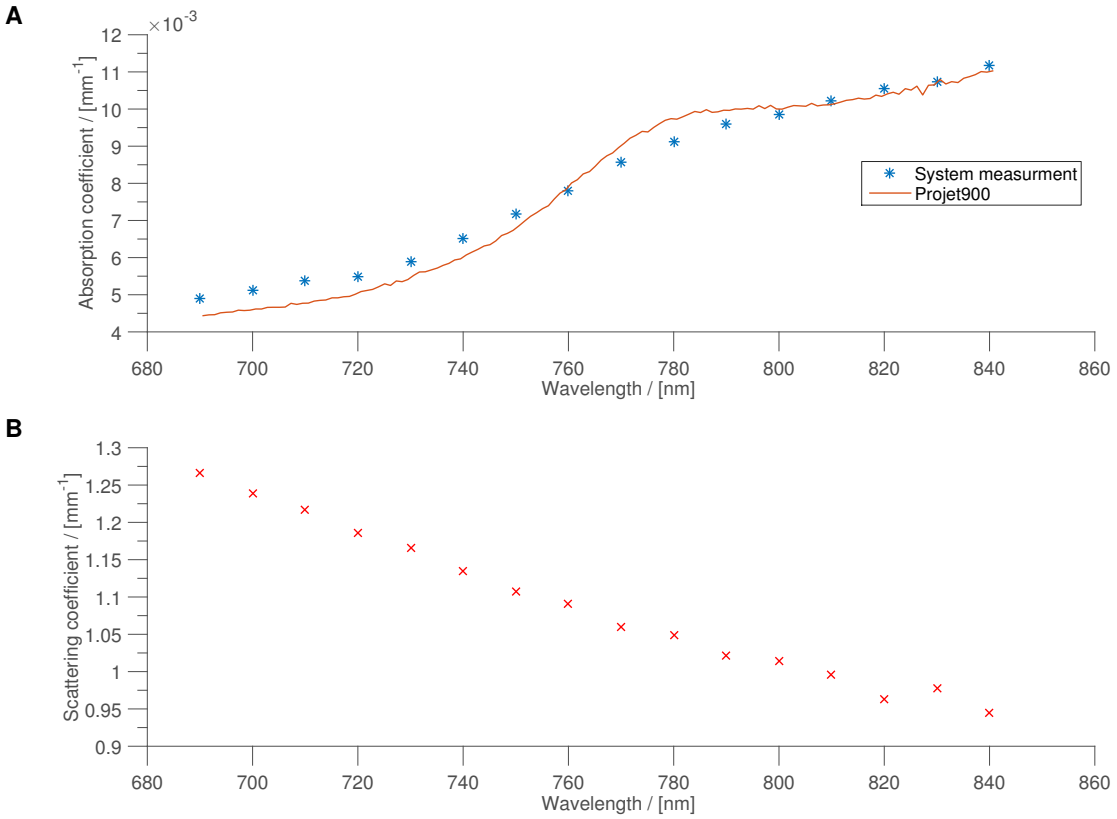

FIGURE 6.11: (A) Absorption coefficient calculated from the system measurements (points) and the expected absorption (solid line) in the epoxy resin phantom; (B) Reduced scattering coefficient calculated from the system measurements (points) in the same phantom. The reduced scattering coefficient is expected to be 1 mm^{-1}at 800nm, at which point the system produces an estimation of 1.01 mm^{-1}.

As the expected values are predicted to only be calculated to within 5% of their true values due to fabrication error, the small difference in absorption spectra is not unexpected and most values of μ_a are within this error. The expected values of μ_a are also calculated with the absorption spectra of the Projet 900 absorbing dye without consideration of the other ingredients in the phantom. This may therefore alter the predicted absorption curve as the resin and the Titanium dioxide introduce a small contribution to the overall absorption coefficient. The reduced scattering coefficient was expected to have a value

of 1 mm^{-1}at 800nm, and the system measures the value at 1.01 mm^{-1}Figure 6.11(B). The trend of μ_s' is exactly what we expect due to Mie scattering, as discussed in Section 2.2.2.

Three other phantom studies were also carried out achieving similar results to these findings, calculating the absorption and scattering of the phantoms with a comparable accuracy.

6.8 Conclusion

In this chapter the system is characterised and evaluated as a whole. The random noise was found to increase mainly due to poor light shielding around the end of the fibre optic, but also the interface between the VOAs and the PMTs. Effective light shielding over these parts is recommended and can reduce the random counts in a measurement to 142 s^{-1}.

Crosstalk was found to occur in the detector channels, and is most likely due to the router which combines the pulses from the four detectors into a single line. This crosstalk was found to be fairly small in comparison to the signal, however, a possible solution is to used a shorter cable between the router and the TCSPC card and could be easily added in future upgrades.

Temporal stability of the instrument is of high importance in a time resolved system. Initially, there was significant drift found in the measurement over long periods of time. This was discovered to be due to inadequate cooling of the PMTs, and once the airflow around the PMTs was increased by removing some of the light shielding the drift in the temporal stability over time was removed. The variation in the mean time of flight is measured as $\pm$ 6ps. The speed of light was measured to within a 5% error.

Finally, measurements on a homogeneously absorbing and scattering tissue phantom with known absorption and scattering coefficients were taken over the wavelength range 690nm - 840nm. From these measurements, the absorption and reduced scattering coefficients were calculated using the method described in Section 5.2. The results show an excellent recovery of the expected absorption coefficient of the phantom over the full wavelength range; the mean error for the absorption coefficient was 5%, which is comparable to the error in the calculation of the expected value when creating the phantom. Furthermore, the system was able to determine the reduced scattering coefficient to within 1% of its known expected value of 1 mm^{-1}at 800nm, and produced the expected, roughly linear decrease that is expected over this wavelength range.

Chapter 7

In vivo studies

In previous chapters we have analysed the performance of individual components used in the system and evaluated the instrument as a whole on a static phantom with tissue-like properties. In the first section of this chapter we discuss the operation of the system, detailing how the wavelengths are multiplexed for in vivo measurements, and then describing the results of in vivo measurements on adults. Multiple baseline measurements have been made with healthy volunteers on the forehead and arm, and the optical properties of the tissues are calculated. The system is then used for several physiology experiments, including a cuff occlusion and a visual cortex stimulation, where we demonstrate that the system is able to detect the expected changes in optical properties of the brain due to changes in haemoglobin concentration and metabolism during functional activation.

7.1 Measurement protocol

Time resolved near infrared measurements on biological tissue pose a much greater challenge than measuring a static phantom. As only a single wavelength illuminates the subject at any one time, the measurement must ensure every temporal point spread

function (TPSF) from each wavelength contains information about the tissue under the same biological conditions. Depending on the conditions of the measurement, recording the TPSFs with sufficient photon counts for sixteen wavelengths can take several seconds, in which time the biological properties of the tissue may have changed substantially. The acousto-optic tunable filters (AOTF) allow fast switching of the wavelength using external TTL signals which are controlled with National Instruments DAQ cards as discussed in Chapter 6.

To overcome this issue, we employ a multiplexing procedure to ensure that the TPSFs acquired for each wavelength are effectively measured over the same period of time. Figure 7.1 shows this multiplexing procedure and how its incorporation into the main software can be seen in Figure 4.40. Each wavelength is illuminated for a very short period of time (such as 20-50 ms) in sequence. This is called 'micro time' in the software, to avoid confusion with the total collection time. The choice of this time period depends on the intended study, how many wavelengths are used, and whether fast biological changes are expected. A lower micro time of 20ms is recommended for functional tests where the haemoglobin change might occur rapidly, although if resting baseline measurements are being taken, a larger micro time in the region of 50 ms is recommended. The switching of each wavelength contributes several milliseconds to the total dead time of the measurement, and smaller micro times therefore increase the amount of dead time for a measurement which decreases the signal to noise ratio. For this reason, micro times shorter than 20 ms are not suitable for these measurements. While these data could be collected as a single measurement after one sequence of eight or sixteen wavelengths, it would not produce accurate results as the last wavelengths will measure the tissue at a different time to the first. By implementing the multiplexing shown in 7.1 with a small micro time, the first and last wavelength are only separated by 160 ms - 200 ms over which time no significant physiological change should have occurred.

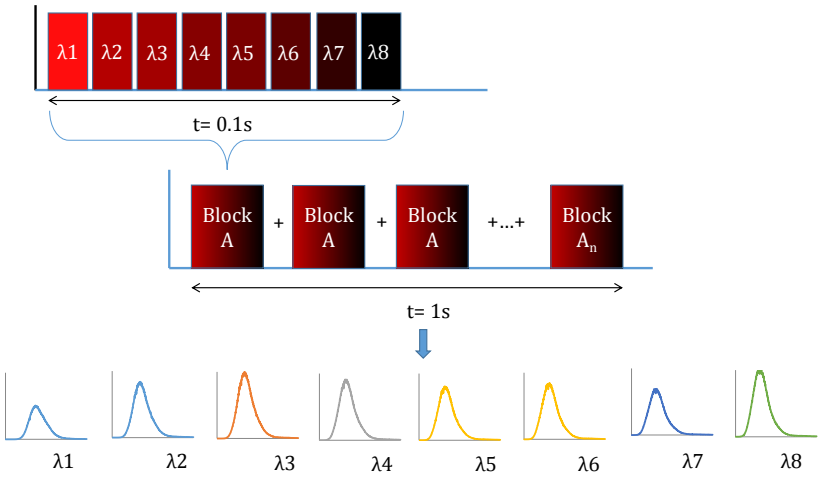

FIGURE 7.1: Simplified data and operation flow of the system for eight wavelengths.

7.2 Arm Measurements

The first in vivo studies using the system produced time-resolved near infrared measurements of a human forearm, from which absolute concentrations of oxy- and deoxy-haemoglobin were obtained. The arm is a relatively easy area to measure, as the subject can remain motionless in a seated position with good control of the fibres and light shielding.

Five different healthy volunteers aged between 20 and 28 were used to obtain the measurements. The measured area of the forearm was just below the elbow, with the probes placed on the largest part of the muscle, found by tensing the arm. The location of the optodes is seen in Figure 7.2. The fibres are held in the 3D optode holders described in Section 4.4.1, which were attached to the skin using clear double-sided tape. The tape is skin safe, and does not affect the measurement in any way. After the optodes are attached to the skin with the tape, the arm is covered with Coban bandage and black cloth to hold the fibres in place and to provide optical shielding.

Before each arm measurement the IRFs were measured, since information from these will need to be deconvolved from the measurement later as described in 5.2. 16 wavelengths between 690nm and 894nm were recorded for each measurement to get a broad spread over the near infrared range. As there was no dynamic element to the measurement, a relatively long exposure time was used, with a micro time of 20 ms and 60 repetitions to maximise the quality of the data. The total time for a single measurement of 16 wavelengths was 20 seconds.

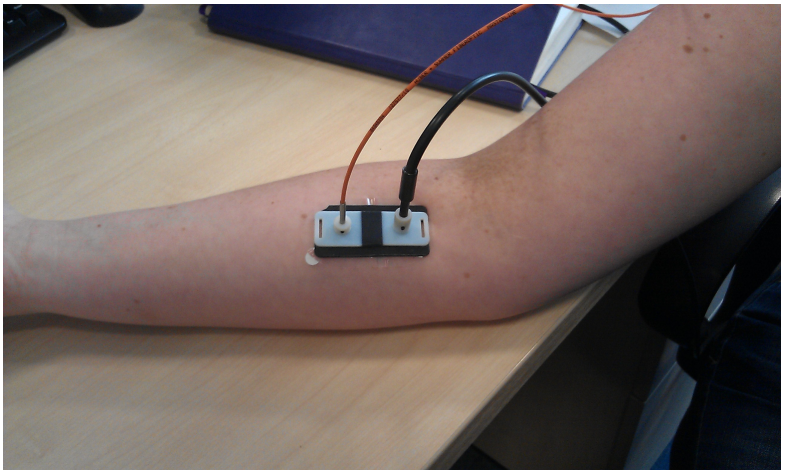

FIGURE 7.2: Picture of optode and fibre placement on the forearm. Light shielding is placed wrapped around the arm after the optodes are attached using clear double-sided tape.

7.2.1 Results

The measured TPSFs were processed by removing the background noise. This is achieved by identifying an area of the window before the arrival of the first signal photon. The average of 100 time bins is then calculated and subtracted from the entire TPSF. The mean time of flight and the variance of the TPSFs are shown in Figure 7.3. The mean time of flight and variance of the TPSF are calculated using the temporal and central moments, given by

$$M = S^{-1} \int_0^\infty \Gamma(t)\ t\ dt \tag{7.1}$$

and

$$V = S^{-1} \int_0^\infty \Gamma(t)(t - M)^2 \, dt \tag{7.2}$$

where M is the mean time-of-flight, V is the variance, S is the total intensity of the TPSF (calculated by integrating over time) and $\Gamma(t)$ is the temporal distribution of light [127]. The mean time of flight shows a steady decrease as wavelength increases in the results from all subjects. The peak in the deoxyhaemoglobin absorption spectrum at 760 nm can be seen as a small dip in the mean time of flight of all the subjects (Figure 7.3(A)). The variance shows a significant amount of noise, especially in Subject 2 where there were three times fewer photon counts in the measurement than the others. This is likely to be due to a poor contact with the skin. The variance is shown as it is a datatype that can be used in the data analysis and gives an indication to the scattering in the tissue [127]. However we see that the variance does not produce as consistent results as the mean time of flight.

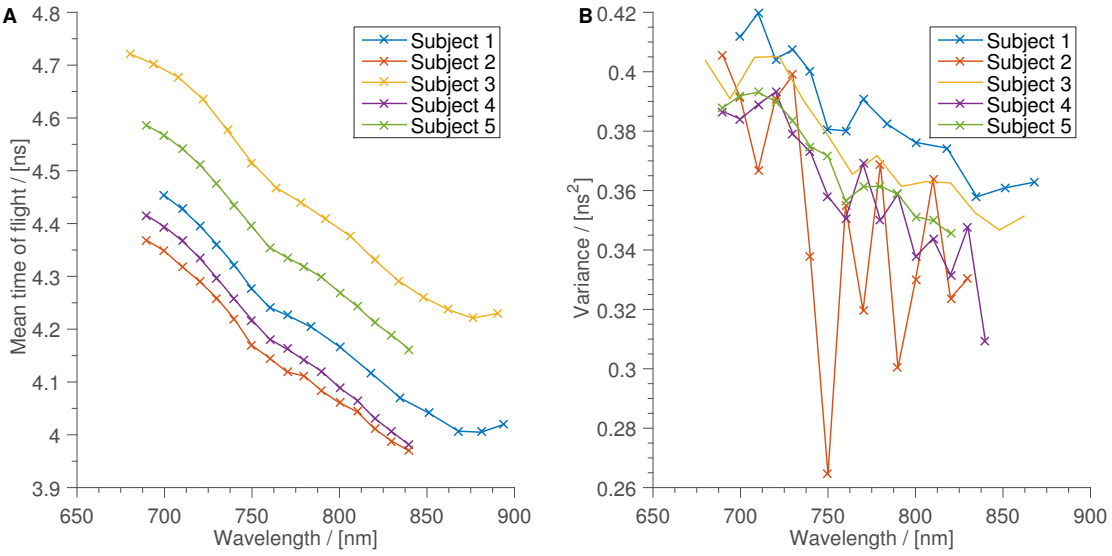

FIGURE 7.3: (A) Mean time of flight and (B) Variance of the TPSFs produced by measurements on five subjects using 16 wavelengths between 690nm and 894 nm.

The full width half maximum (FWHM) of the TPSFs measured on the arm is shown in Figure 7.4. The FWHMs of the five subjects have a range of 0.53 to 0.91 ns. All of the

FWHM's are far greater than the FWHM of the system IRF, which has an average FWHM of 370 ps. This difference is beneficial, since a FWHM of comparable size to the FWHM of the IRF would hinder the deconvolution of the IRF from the TPSF measurement. The FWHM of the TPSFs decreases with wavelength, which is as expected as the absorption increases over this range.

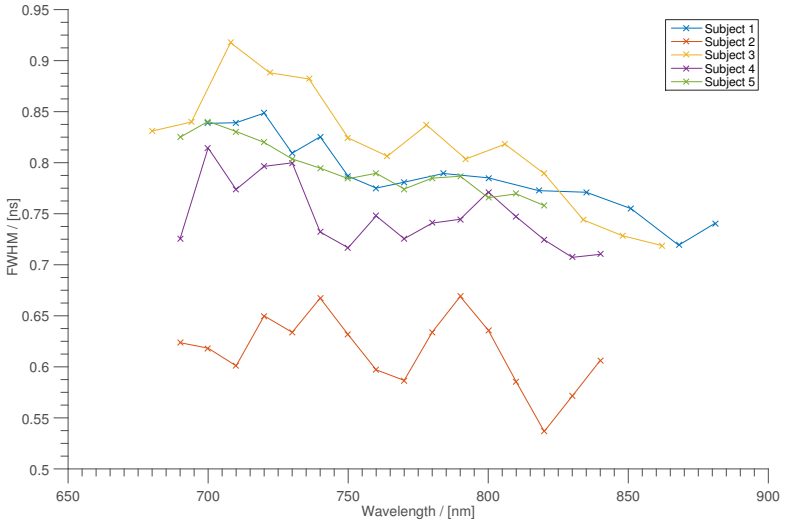

FIGURE 7.4: Full width half maximum of the noise-corrected TPSFs measured on the forearm of five healthy volunteers.

The mean pathlength of light in tissue is derived by first calculating the mean time of flight of the measured TPSF and IRF using Equation 7.1. To remove the time taken for the photons to travel down the fibres, the mean time of flight of the IRF is subtracted from the mean time of flight of the TPSF, giving the actual mean time of flight in tissue. This is then converted to a distance using a refractive index of 1.4, which is the typical refractive index of tissue [116, 145]. The pathlengths of light in the measurements of the 5 subjects ranges from 0.13 m to 0.20 m, with a mean pathlength at 750 nm of 0.16$\pm$0.02 m. The source-detector separation of the measurement was fixed at 3 cm, which results in an average differential pathlength of 5.3$\pm$0.3 m at 750 nm.

The absorption (μ_a) and reduced scattering (μ_s') coefficients were obtained by fitting a solution of the diffusion equation to the measured TPSFs. This process is described in detail in Section 5.2. Briefly, the Green's function was convolved with the measured IRF

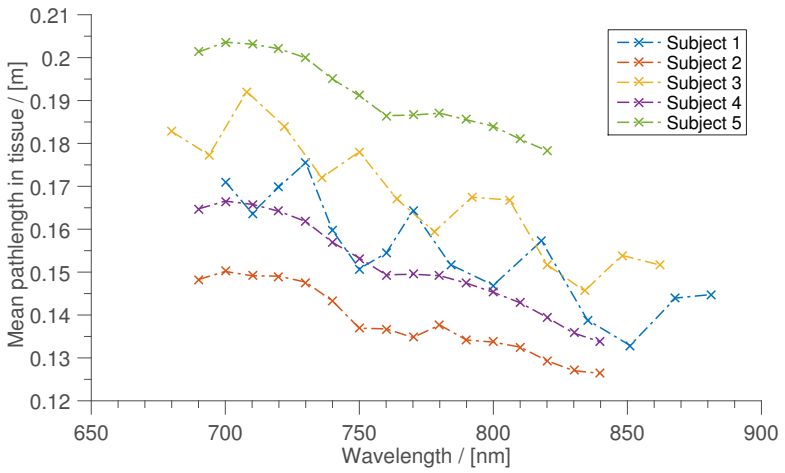

FIGURE 7.5: Calculated mean pathlength in tissue of five healthy volunteers.

for each wavelength and fitted to the TPSF using a least squares algorithm, in order to minimise the sum of the deviations. This optimises μ_a and μ_s' for the function to provide a best fit to the measured data. The initial guesses for μ_a and μ_s' were 0.01 mm^{-1}, and 1 mm^{-1}, respectively, based on an order-of-magnitude estimate of their typical values in tissue. Figure 7.6 shows the coefficients of absorption (A, C, E, G and I) and scattering (B, D, F, H and J) of 5 subjects calculated using the multiwavelength measurements from the system, which were taken under the conditions detailed above. The absorption coefficients of all subjects arms show a general rise in μ_a as wavelength increases from 700 nm to 850 nm.

A small peak can be seen at 760 nm which is consistent with the high absorption in deoxy-haemoglobin expected at that wavelength. At the lower wavelengths there is a small rise in μ_a, which is again representative of the absorption spectrum of deoxyhaemoglobin. The optical absorption properties range from μ_a = 0.013 to 0.022 mm^{-1} between 680 and 894 nm, which is within the range expected in biological tissue [146, 147].

The shape of the absorption coefficient spectrum can be predicted if we estimate the ratio of chromophores in tissue. If the concentrations by volume of water, lipids and haemoglobin are estimated to be 75%, 25% and 1% respectively, with a SaO_2 of 95% [12]. A predicted normalised absorption spectrum can be obtained by using the known

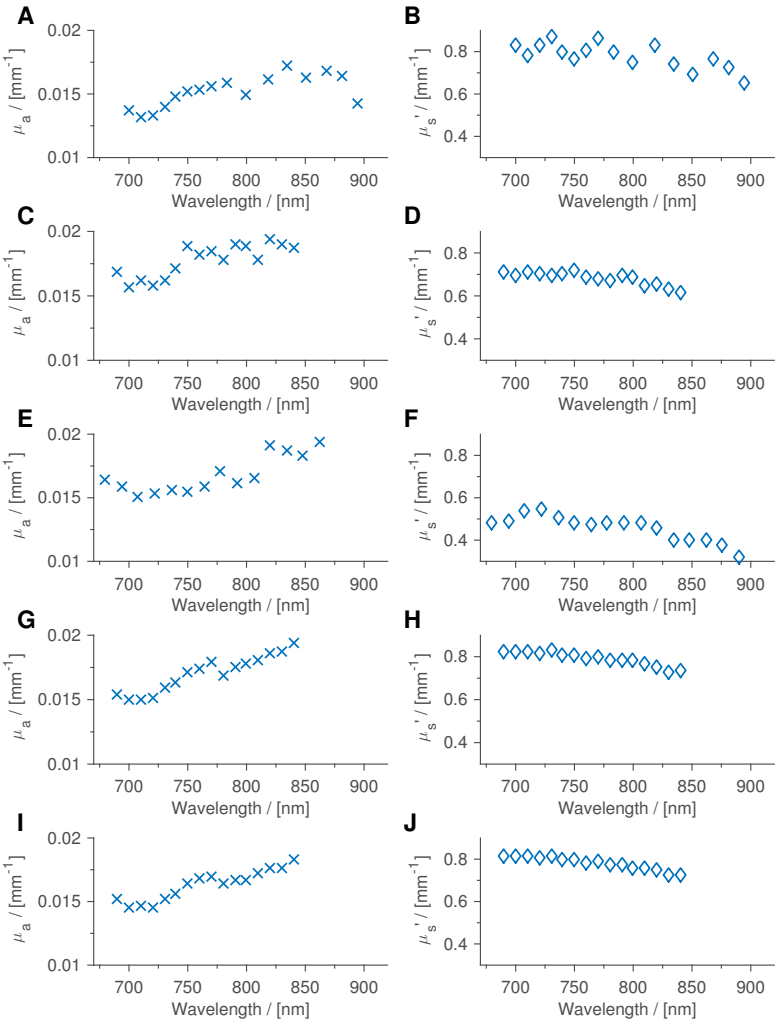

FIGURE 7.6: (A, C, E, G, I) show the absorption coefficient (μ_a) calculated from in vivo spectroscopic measurements in the arm tissue of subjects 1-5 respectively. (B, D, F, H, J) show the corresponding calculations for the reduced scattering coefficient (μ_s'). The values of μ_a and μ_s' were calculated by fitting the solution of the diffusion equation over a semi infinite homogenous medium to the measured TPSFs.

absorption spectrum of each chromophore which is shown in Figure 7.7. As can be seen in the predicted absorption spectrum, there is an overall increase in the absorption with wavelength as well as two distinct features. There is a small increase at the low end of the spectrum around 690 nm and a small 'peak' at 760 nm. The rise in absorption with wavelength is due to the absorption spectra of water and lipids, whereas the small increases at 690 nm and 760 nm are mainly due to the absorption spectrum of HHb.

Both these features can be seen in all of the resolved μ_a from the measured data in

Subject	HbO_2 [μM]	HHb [μM]	SO_2 [%]
1	59.0	29.3	66.8
2	60.7	28.8	67.7
3	57.6	24.4	70.2
4	48.0	25.0	65.7
5	61.1	26.0	70.1

TABLE 7.1: Absolute concentrations of oxyhaemoglobin (HbO_2) and deoxyhaemoglobin (HHb) and oxygen saturation determined from in vivo measurements on the forearm on 5 subjects.

addition to the overall trend in absorption. There is a good agreement in the shape of the absorption spectra which means that the system and analysis technique are effective at accurately resolving μ_a.

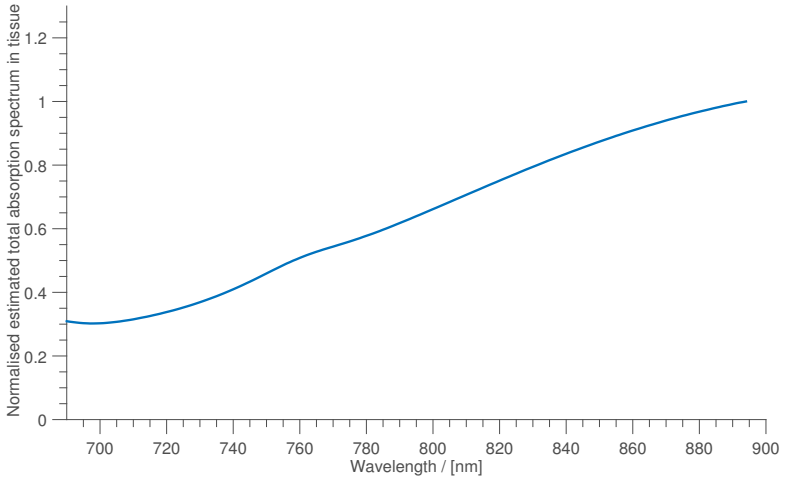

FIGURE 7.7: The predicted normalised absorption spectrum in tissue using estimated concentrations of water, lipid, HbO_2 and HHb.

The fitted scattering coefficient in all 5 subjects appears linear over the wavelength range measured. The minimum value of μ_s' is 0.31 mm^{-1}, and the maximum μ_s' calculated was 0.88 mm^{-1}. The distinctive effects of absorption seen at 760 nm and 690 nm are not visible in the fitted scattering coefficient, suggesting that the method has removed the crosstalk typically observed between the recovered absorption and scattering coefficients. Mean values of 0.74$\pm$0.08 mm^{-1} at 700 nm and 0.69$\pm$0.07 mm^{-1} at 800nm are observed.

The absolute concentrations of deoxyhaemoglobin and oxyhaemoglobin were calculated for the five arm measurements using the Beer-Lambert law, correcting for water concentration. The results of the conversion to absolute oxyhaemoglobin and deoxyhaemoglobin concentrations can be seen in Table 7.1. The mean values of oxyhaemoglobin and deoxyhaemoglobin concentrations are 57.2$\pm$2.4 μM and 26.7$\pm$1.0 μM. The SO_2 values calculated show a mean of 68.1% which is a typical value for SO_2.

7.3 Head Measurements

Baseline measurements of optical properties were measured in ten healthy volunteers between the ages of 20 and 32. The fibres were placed on the forehead using the same optode holder as shown in Figure 7.2 with a 30 mm source-detector separation. The optode holder was attached with skin-safe, double-sided tape and wrapped around with Coban tape to secure it onto the head. As the fibres protrude at 90 degrees to the skin there is significant force pulling the fibres from the skin. The weight of the fibres was therefore relieved by taping the fibre onto the subjects shoulder or a nearby support. The optode was positioned off-centre on the forehead in order to avoid the frontal (supratrochlear) vein and to be located above the frontal lobe of the brain. A photograph of the typical placement of the probe is seen in Figure 7.8.

For all ten measurements, 16 wavelengths were used between 680 and 894 nm, with a total collection time of between 1 and 2 seconds for each wavelength. The collection time was multiplexed as described in Section 7.1, with a small micro time of between 20 and 50 ms. Total collection time for the 16 wavelengths was between 16 and 32 seconds.

FIGURE 7.8: Photograph of the typical optode and fibre placement on the forehead.

7.3.1 Results

The data were analysed in a very similar method to that for the arm measurements; TPSFs were recorded for each wavelength, with the inclusion of an individual IRF prior to each subject measurement. The TPSF window was trimmed, and background noise was removed from the measurement. The Green's function solution was convolved with the IRF and fitted to the measured TPSF using a non linear least squares Levenberg-Marquardt algorithm.

The mean times of flight for the 10 subjects are shown in Figure 7.9. All mean times of flight show a smooth decrease over the wavelength range as seen in the arm measurements. The mean time of flight measured in the head is higher overall than that measured in the arm, which is expected since the scattering of light would be increased due to the skull.

The variance of the head measurements of ten subjects is shown in Figure 7.10. The majority of subjects have a mean variance between 0.37 and 0.43 ns^2, except the measurement from Subject 5 which has a mean variance of 0.82 ns^2. This higher variance

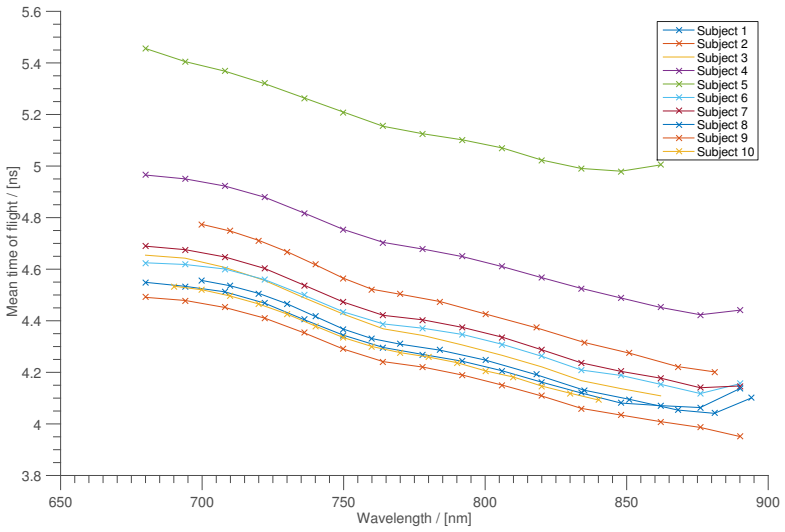

FIGURE 7.9: Mean times of flight of light travelling through the forehead, obtained from in vivo measurements from ten subjects.

is likely to be the result of a low signal to noise ratio. The measurements taken at high wavelengths above 880 nm can also be seen to produce high variance, which is due to low photon counts in this range.

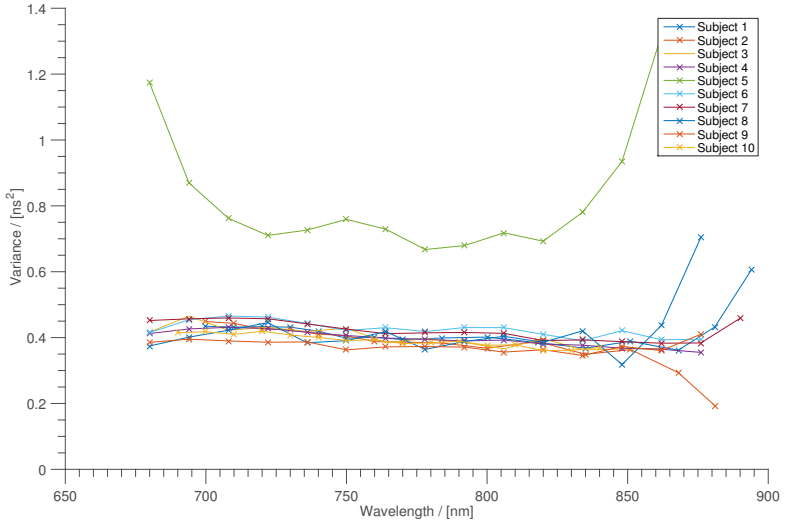

FIGURE 7.10: Variance of the the TPSFs for all ten subjects. The measurement on Subject 5 displays a significantly higher variance than the other subjects, possibly due to a low signal to noise ratio.

The mean pathlengths of light were calculated by converting the mean times of flight for the IRF and TPSF to a distance in tissue, by using a typical refractive index of 1.4 and subtracting the total pathlength of the IRF from the total pathlength of the TPSF. The

result pathslengths for each of the ten subjects can be seen in Figure 7.11(A). The mean pathlengths measured in the forehead range from 0.22 m and 0.13 m between 680 and 890 nm, which corresponds to a differential pathlength factor (DPF) of 7.33 and 4.33, respectively. A mean DPF of 6.05±0.02 is measured at 750 nm. The mean differential pathlength factor with standard error is shown in Figure 7.11(B). Also shown is the differential pathlength factor dependency measured by Cope et al., with the error bars and initial point taken from [1, 28] at 807 nm as 6.26(± 14.1%). The data show that there is an overall increase in pathlength compared to that measured by Duncan et al., although, the pathlengths measured by this system fall well within the standard error. The trend of the two data sets, however, show very similar characteristics, including a dip around 760 nm due to the peak in the absorption spectrum of deoxyhaemoglobin. Overall, we see a smooth decrease in pathlength from 700 nm to 860 nm.

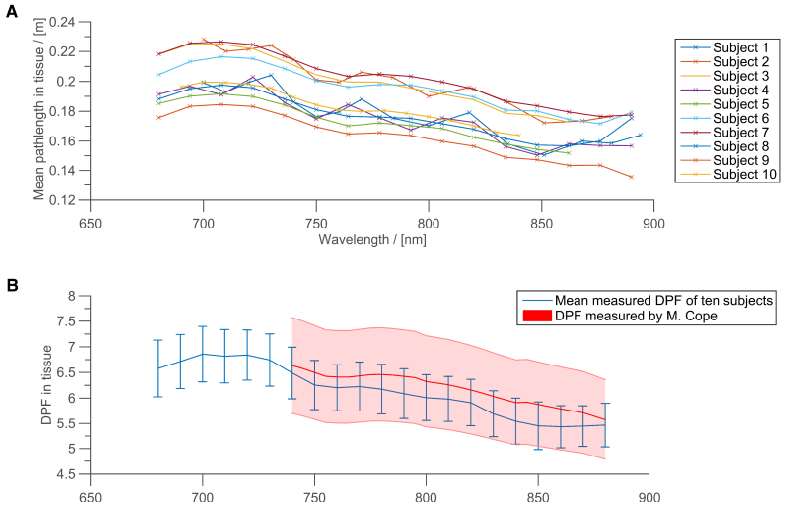

FIGURE 7.11: (A) Mean pathlengths of light calculated from in vivo measurements in the heads of ten subjects; (B) Calculated average differential pathlength from the forehead measurements, showing standard error and differential pathlength factor (DPF) and error from Cope and Duncan [1, 28].

The absorption and scattering coefficients were calculated using the same technique as for the arm measurements, by convolving the solution to the diffusion equation using the IRF, and fitting to the measured TPSF after noise correction. The initial guess for μ_a and μ_s' were kept at 0.01 mm^{-1}and 1 mm^{-1}, as the fitting method proved to be very

robust with regards to the initial conditions of the model. A typical fit of the convolved model to the measured TPSF can be seen in Figure 7.12(A), and the difference between the two fits is shown in 7.12(B). The model convolved with the IRF shows a good fit to the measured TPSF, with only a small difference around the tail of the signal.

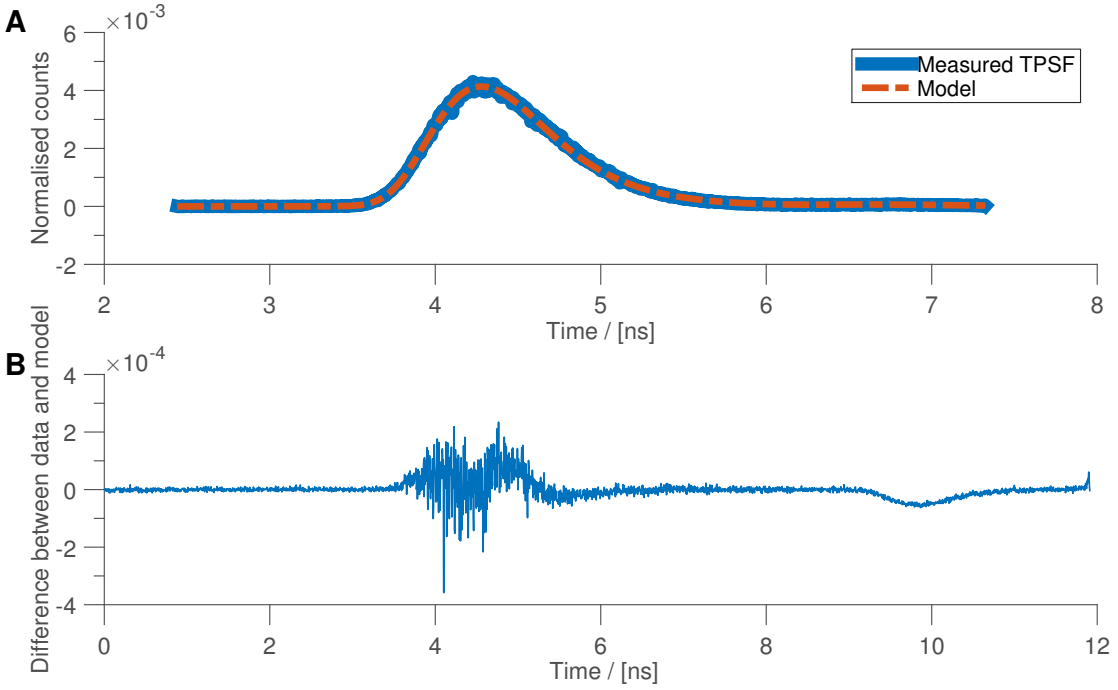

FIGURE 7.12: (A) Normalised measured TPSF with the least-squares fitted model plotted over the top. The model has been convolved with the real measured IRF and normalised to match the intensity of the TPSF; (B) Difference between the measured TPSF and fitted model.

The absorption and scattering coefficient determined from the in vivo measurements on ten subjects can be seen in Figure 7.13 and Figure 7.14, respectively. The coefficients of absorption show a similar trend in all subjects, with a range from 0.011 and 0.019 mm^{-1}. The data show an increase in μ_a from 700 nm to 880 nm, with a peak at 760 nm due to the haemoglobin absorption peak. Several of the data show a very low μ_a at the highest wavelength above 890 nm, which is most likely due to the inability of the PMT to measure a good enough signal at these wavelengths, resulting in a poorly fitted TPSF.

The reduced scattering coefficients shown in 7.14(A-J) correspond to the same subjects shown in 7.13. All data show a gradual decrease in μ_s' over the wavelength range of 680

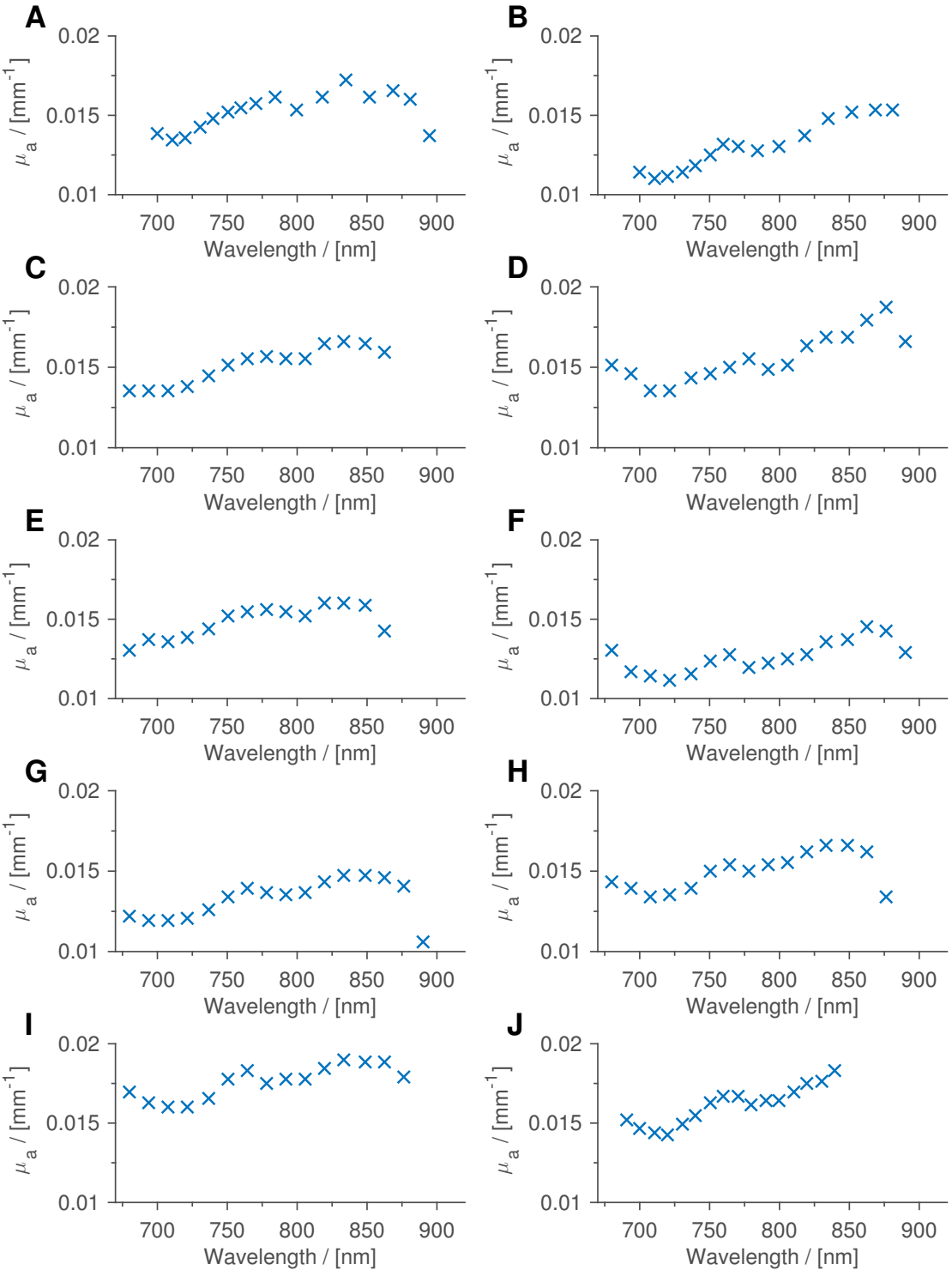

FIGURE 7.13: (A) - (J) show the absorption coefficients (μ_a) calculated from in vivo spectroscopic measurements performed on the heads of Subjects 1-10, respectively.

Subject	HbO_2 [μM]	HHb [μM]
1	39.2	29.6
2	38.8	22.0
3	61.5	23.3
4	48.8	23.5
5	29.9	27.5
6	37.4	20.3
7	38.8	21.2
8	49.6	22.3
9	45.2	30.2
10	62.1	25.8

TABLE 7.2: Absolute concentrations of oxyhaemoglobin and deoxyhaemoglobin determined from in vivo measurements on the forehead on ten subjects.

to 890 nm, as expected according to Mie theory. The scattering of all subjects range from 1.21 to 0.66 mm^{-1}, with a mean of 0.82 mm^{-1}($\pm$ 18.7%) at 800 nm. There is a small amount of noise in the scattering coefficient for Subjects 1, 2 and 4 ((A), (B) and (D), respectively) over the wavelength range which correlates with a similar noise effect seen in the FWHMs of the TPSFs. The exact cause of this is unknown, but could be caused by variations in the temporal stability of those measurements.

The calculated absolute chromophore concentrations of oxyhaemoglobin and deoxyhaemoglobin are shown in Table 7.2 for each of the ten subjects. The values for HbO_2 have a fairly large distribution with a mean of 45.15 μM and standard error of $\pm$23.3%. Deoxyhaemoglobin has a mean of 24.61μM and a much smaller standard error of $\pm$14.3%. These mean values of haemoglobin concentrations are lower than that found in the arm.

7.3.2 Conclusions

In this section the system was used to perform multiwavelength, time resolved, near infrared measurements of the optical properties of the arm and forehead of 5 and 10 healthy volunteers, respectively. This study found a mean differential pathlength factor of 5.3$\pm$0.3 in the arm and 6.05$\pm$0.02 in the forehead at 750 nm. These results are in

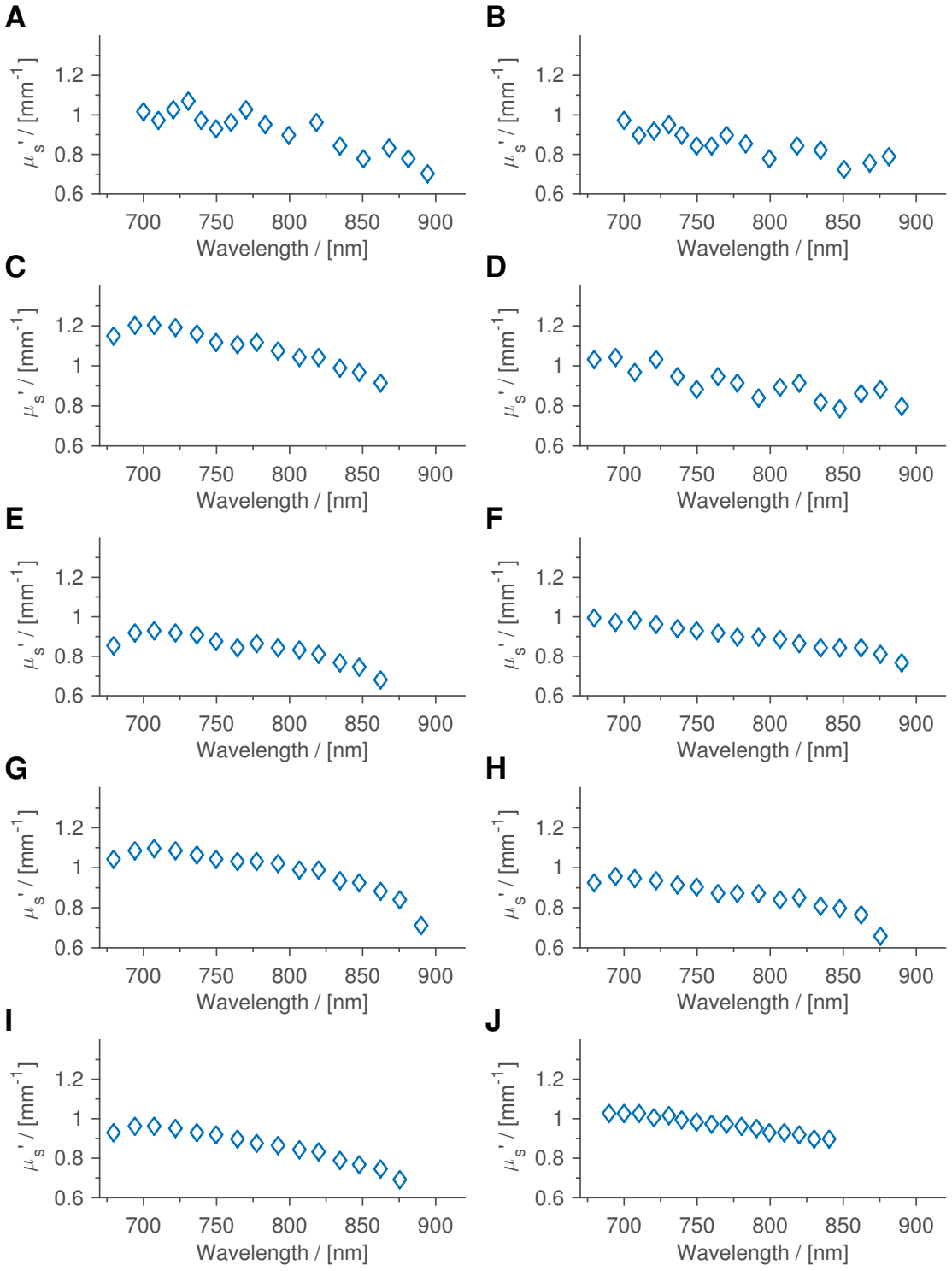

FIGURE 7.14: (A-J) show the reduced scattering coefficients (μ_s') calculated from in vivo spectroscopic measurements performed on the heads of Subjects 1-10, respectively.

agreement with other work on determining the pathlength of tissue [1]. The absorption and scattering coefficients of light in the tissue were calculated for up to 16 wavelengths, and demonstrated little cross talk between the recovered absorption and scattering. The shape of the absorption spectrum of tissue measured in all subjects shows good agreement with the expected total absorption spectrum calculated with known absorption spectra of chromophores.

Some of the measurements highlighted the importance of the positioning and attachment of the optode holder to the tissue; several measurements experienced high levels of noise, most likely due to poor contact between the fibre end and the tissue. This could be improved with the use of right-angled fibre optics which are much easier to fix in place.

7.4 Cuff Occlusion Measurements

Cuff occlusions are commonly used to assess the function of near infrared systems and techniques, [63, 77, 148–152]. The procedure has a relatively consistent and reproducible outcome, and haemodynamic changes during the occlusion are well documented. Performing an arterial cuff occlusion on the upper arm prevents any blood entering or leaving the arm, the total haemoglobin will then remain constant and the oxyhaemoglobin will be converted to deoxyhaemoglobin.

7.4.1 Method

In order to perform the cuff occlusion a healthy volunteer was seated with forearm laid at rest on a surface roughly at chest height. A sphygmomanometer (pressure cuff) was located above the Brachial artery and inflated to 200 mm Hg on the right arm. The measurement protocol involved recording 2 minutes of resting baseline then inflating to 200 mm Hg and occluding the artery for 5 minutes, before releasing and recording

a further 2 minutes of recovery. The optical probes were attached to the underside of the forearm on the largest muscle below the elbow using the 3D printed optode holders shown in Figure 4.4.1 and double sided tape. The area around the probes was wrapped with Coban tape and covered with black cloth, and the source and detector had a separation of 30 mm. The total collection time for each wavelength was set to 1 second recorded over 20 blocks of 200 ms. The measurement setup consisted of sixteen wavelengths between 690 and 840 nm. The spread of these wavelengths is shown in Figure 7.15. These wavelength were chosen to give an even spread over the near infrared range so that anaylsis of the data could be performed over a wide spectrum.

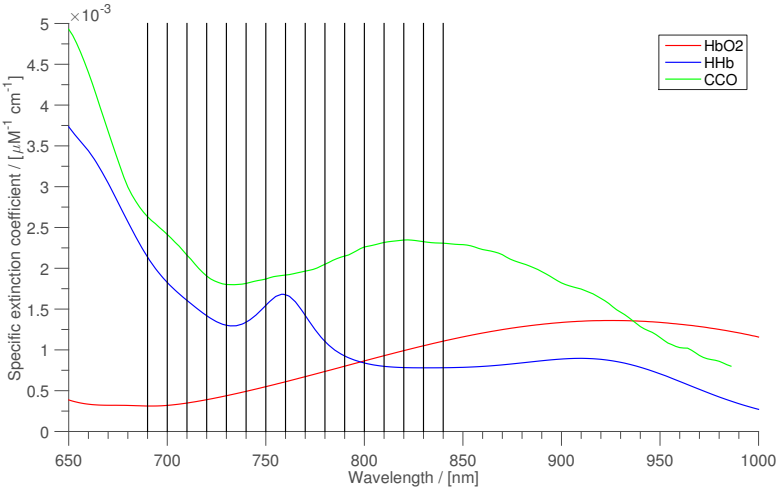

FIGURE 7.15: Wavelengths between 690-840 nm used to perform the cuff occlusion measurement.

7.4.2 Results

Due to a system error, the 690 nm measurements failed on 5 occasions out of the 40 measurements. Therefore, the TPSFs measured corresponding to the 690 nm wavelength have been removed from the data set.

The total intensity of the TPSFs during the pressure cuff inflation are shown in Figure 7.16. The change in the intensity spectrum can be seen in 7.16(A) which shows the photon counts for each wavelength. The change in intensities of individual wavelengths

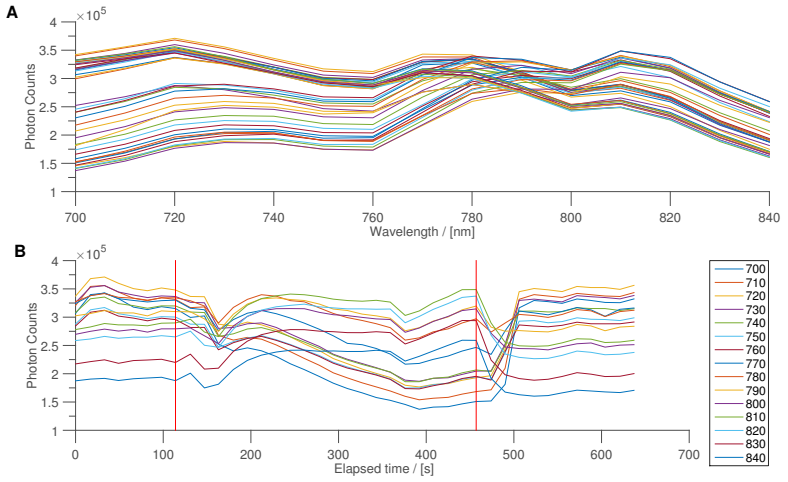

FIGURE 7.16: (A) Total photon counts at different wavelengths. Different plots represent counts at different measurement times in the cuff occlusion; (B) Change in total intensity of 15 wavelengths during cuff occlusion. The first vertical red line indicates the initial inflation of the cuff, and the second indicates when it is released.

over time can be seen in 7.16(B). Relatively large changes in the attenuation of light can be clearly seen due to due to the changes of haemoglobin concentrations in the arm. The photon counts from the lowest wavelength (700 nm), where absorption due to deoxyhaemoglobin dominates, experiences a decrease of 56% from the average baseline to the lowest measurement during the occlusion. The 840 nm wavelength intensity measurement increases by 34% during the cuff occlusion.

All wavelengths display a small decrease in intensity shortly after the start of the occlusion. This is most likely to be due to the inflation of the pressure cuff; as it is not an instantaneous process, blood can be forced back into the lower arm.

The mean times of flight of the photons through the system is shown in Figure 7.17(A), and the variance of the TPSFs in 7.17(B). The mean time of flight is corrected for the IRF time of flight and converted into its pathlength in tissue (Figure 7.18). The maximum decrease in mean time of flight is measured at 0.12 ns, which corresponds to a change in pathlength of 0.03 m at 700 nm. The maximum increase in mean time of flight and pathlength is recorded for the 840 nm wavelength 0.03 ns 0.01 m. As we would expect, near the isosbestic point (the wavelength at which the oxy and deoxyhaemoglobin

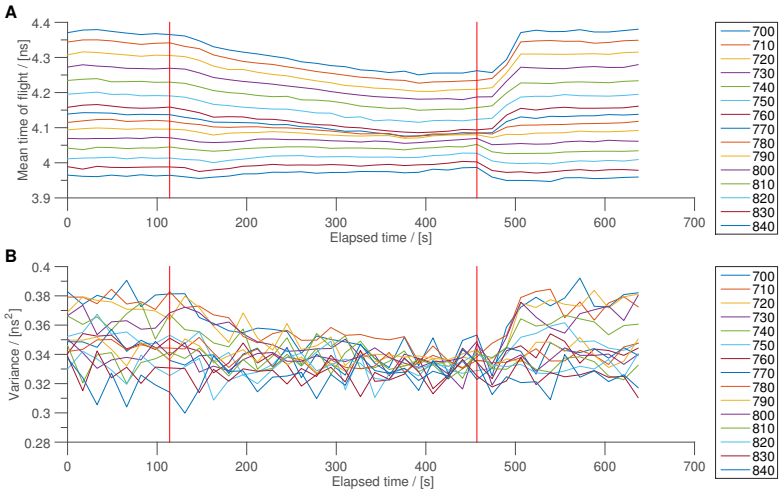

FIGURE 7.17: (A) Mean times of flight for each of the 15 wavelengths; (B) Variance of the TPSFs for the 15 wavelengths over time during a cuff occlusion. The first vertical red line indicates the initial inflation of the cuff, and the second indicates when it is released.

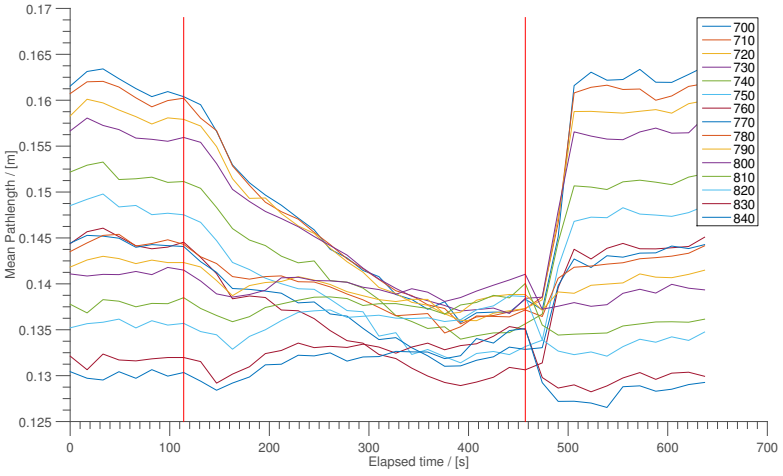

FIGURE 7.18: Optical mean pathlength changes during a cuff occlusion procedure. The first vertical red line indicates the initial inflation of the cuff, and the second indicates when it is released. The pathlengths can be seen to change significantly during the procedure, and return to the baseline quickly after the cuff is released.

absorptions cross), the pathlength shows no change, as the pure conversion of HbO_2 to HHb does not change the total absorption.

The absorption and scattering spectrum for all measurements is shown in Figure 7.19(A) and (B), respectively, and the absorption and scattering over time is shown in Figure 7.19(C) and (D). There is a small mean change of -4% in the scattering coefficient

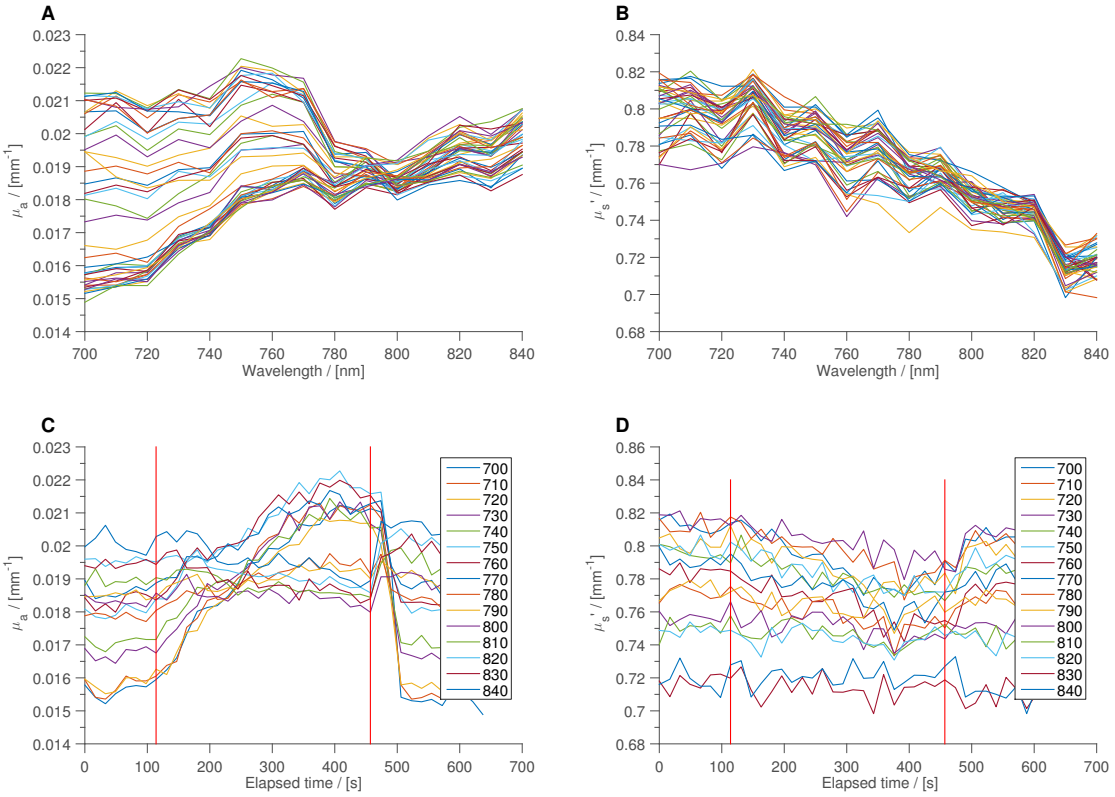

FIGURE 7.19: (A) Absorption and (B) scattering coefficient spectrum for all measurements during the cuff occlusion. Changes in coefficient of (C) absorption (μ_a) and (D) scattering (μ_s') in the forearm during a cuff occlusion. The first vertical red line indicates the initial inflation of the cuff, and the second indicates when it is released.

of certain wavelengths, however, there is an error on the baseline measurements of $\pm$2-3%, such that this change may not be significant. A larger change can be seen in the absorption coefficient during the occlusion. The greatest change is seen in the 700 nm measurement, which increases from 0.015 $mm^{-1}$to 0.021 $mm^{-1}$with an increase of 0.006 mm^{-1}. The shorter wavelengths show a greater change than the measurements at longer wavelengths due to greater differences in the absorption spectrum of both chromophores.

Figure 7.20 shows the concentration changes of chromophores in tissue during the cuff occlusion. Figure 7.20(A) shows the absolute concentrations of oxy and deoxy-haemoglobin. When resolving for absolute HbO_2 and HHb , all other chromophores are assumed to be constant, and the results are corrected for the absorption of water with

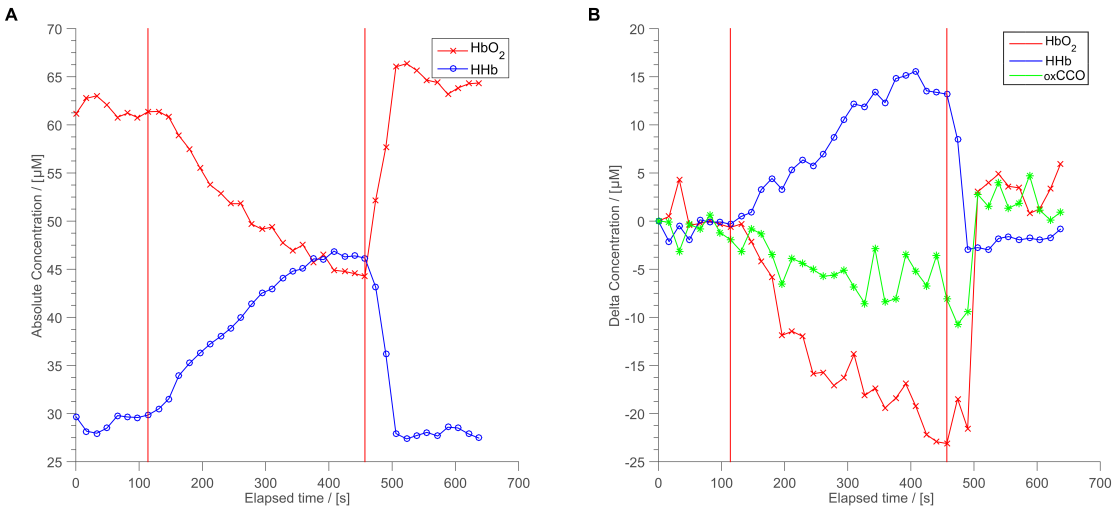

FIGURE 7.20: (A) Absolute concentrations of oxyhaemoglobin and deoxyhaemoglobin during a cuff occlusion; (B) Concentration changes of oxyhaemoglobin, dexoyhaemoglobin and cytochrome c oxidase during a cuff occlusion.

an estimated concentration of 80%. The changes in concentrations of HbO_2 , HHb and redox state of cytochrome c oxidase are shown in Figure 7.20(B). The change in delta concentrations were also corrected for the water concentration. In both graphs, a similar trend is shown for the concentration changes of HbO_2 and HHb . As the arm is occluded, the outflow of HHb through the veins and inflow of HbO_2 is inhibited. This results in the total haemoglobin remaining constant while a desaturation process occurs. Therefore, we expect the concentrations of HbO_2 and HHb to be decreasing and increasing, respectively, which is what is observed in these measurements. The results show a maximum decrease in the oxyhaemoglobin from the mean baseline of 16μM, and an increase in deoxyhaemoglobin of 17μM. When releasing the cuff, we see an overshoot in HbO_2 on return to baseline.

We also expect to see a small, delayed reduction in the oxidise state of cytochrome c oxidase (oxCCO), due to the low oxygen consumption in resting muscle [152, 153]. In Figure 7.20(B), we see a slow decrease in the oxCCO throughout the occlusion as expected, with an overall maximum decrease of 10μM. However, the oxCCO shows some evidence of crosstalk with the oxyhaemoglobin, as there is an overshoot in the signal

when the cuff is released which you would not expect to see in the oxCCO measurement.

7.4.3 Low wavelength count analysis

In order to see the benefit of using a large number of wavelengths to resolve for HbO_2, HHb and oxCCO the data has be analysed using only three wavelengths 760, 800, and 830 nm as these are the most wavelengths used by the TRS-20 [76, 77]. The data is processed using the same method as used for Figure 7.20.

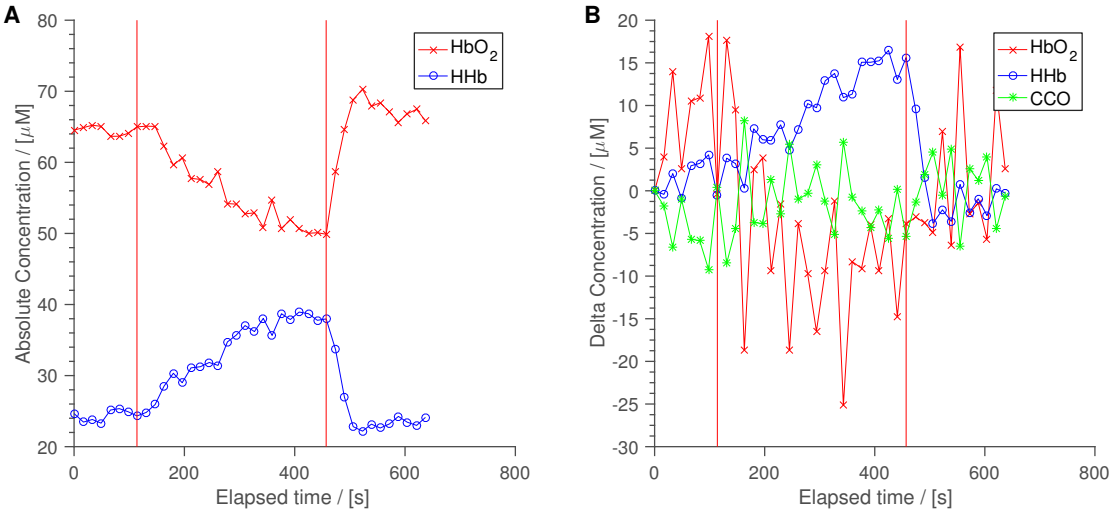

FIGURE 7.21: Data analysis using three wavelengths (760, 800, 830 nm)(A) Absolute concentrations of oxyhaemoglobin and deoxyhaemoglobin during a cuff occlusion with three wavelength analysis; (B) Concentration changes of oxyhaemoglobin, dexoyhaemoglobin and cytochrome c oxidase during a cuff occlusion with three wavelength analysis.

As can be seen, when calculating the absolute concentration of HbO_2 and HHb a very similar outcome is achieved to using to complete 15 wavelengths as in Figure 7.20. This is expected as the majority of fNIRS systems use only two or three wavelengths to resolve for these chromophores. However when the change in concentrations of haemoglobin and oxCCO is calculated, in this case we see that although the overall shape remains the same, the HbO_2 signal becomes significantly noisy. There is no oxCCO signal however, and only noise can be seen throughout the cuff occlusion.

Similar results are also found when using different combination of wavelengths out of the original 15 measured. This analysis shows the importance of multiple wavelengths when resolving for cyctochrome-c-oxidase. Quantification is needed to fully understand the ideal combination and number of wavelengths used when resolving for changes in oxCCO. This will require further measurements with either a well known oxCCO signal or a phantom replicating a changing oxCCO concentration.

7.4.4 Conclusions

The haemodynamic changes during an arterial cuff occlusion were measured on a healthy volunteer. The concentration change observed shows a desaturation process occurring in the tissue as expected. A small decrease in oxCCO is also observed, however, there is some indication of crosstalk between the oxCCO and HbO_2 signal.

The system experienced some technical difficulties during the measurement, as the data for the 690 nm could not be recovered. The cause of this error was found to be due to a software and hardware timing mismatch. When a complete TPSF is measured and stored into memory, the TCSPC card must populate the individual time channel memory with zeros, which takes a small amount of time. The software appeared to be restarting the time of flight measurement of the first wavelength (690 nm) before this process had completed, causing the error. This has been fixed by increasing the wait time before the restart of the next measurement, but timing constraints meant that the cuff occlusion measurement were not able to be repeated.

7.5 Visual Cortex Measurements

Functional measurements of the visual cortex using near infrared spectroscopy were first reported in 1993 by Kato et al. and Villringer et al. [154, 155]. Measurements

taken from optical probes positioned over the occipital lobe (7.22) at the posterior of the head showed that there is a haemodynamic response to a visual or photonic stimulus. The results show an increase in total and oxyhaemoglobin and small decrease in deoxy-haemoglobin during the stimulus which returns to baseline when at rest. Since these initial observations, other measurements using imaging systems have agreed with the findings [156, 157]. As the changes in haemoglobin concentrations are relatively small during a visual stimulus, an effective method for showing the haemodynamic response is to perform multiple stimulation blocks and average the results ([157]).

Changes in the oxidation state of cytochrome c oxidase in visual stimulation experiments have been observed by Heekeren et al. using a broadband continuous wave near infrared system [158]. This was discovered since the spectral changes in the light travelling through the occipital lobe could not be explained fully by just changes in HbO_2 and HHb . Heekeren et al. found a small increase in the oxidised state of cytochrome c oxidase, thought to be due increased neuronal activity causing accelerated activity of ion pumps in the electron transport chain. The paper, however, uses continuous wave measurements, which have to assume that the scattering and pathlength are constant throughout the measurement. Uludag et al. discuss how crosstalk can influence the calculations of chromophores when using attenuation as the data type using Monte Carlo simulations [159], and they proposed using the changes in the mean time of flight as an alternative data type. In 2004, however, Uludag et al. stated that, while cross talk between HbO_2 and oxCCO can often contribute to a cytochrome signal, it cannot explain all of the observed changes [160].

In this section, preliminary measurements taken during the stimulation of the visual cortex using multiwavelength near infrared spectroscopy.

7.5.1 Methods

In order to measure photons travelling through the occipital lobe, the source-detector separation was increased from previous measurements to provide greater depth penetration. Initial measurements with a 30 mm source-detector separation over the visual cortex presented no change in intensity or mean time of flight when visual stimulus was provided, and so a longer source-detector separation of 40 mm was used. This will reduce the intensity of light measured but will increase the mean depth penetration of light detected.

The stimulation protocol consisted of a rotating black and white checker board pattern with a frequency of 5 Hz displayed on a large monitor in front of the subject. The visual stimulus was displayed for 40 seconds, followed by a 40 second block consisting of a black screen. This protocol was repeated seven times after an initial 60 baseline acquisition period.

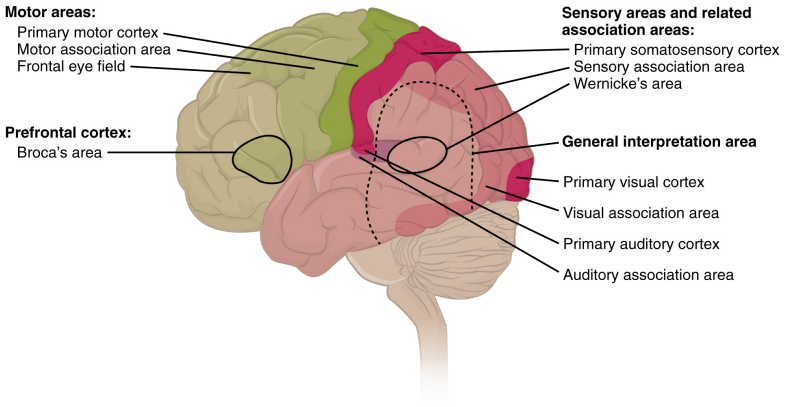

FIGURE 7.22: Anatomy of the brain, showing the location of the visual cortex in the posterior of the head.

The positioning of the optodes is critical for the success of this measurement. The occipital lobe is located at the rear of the brain, as shown in Figure 7.22. Several attempts to locate the optodes directly over the visual cortex were required to acquire successful data. The optodes were located over the right occipital region above the inion. Once the correct positions for the optodes were found, the optode holder was attached

to the head with Coban tape and the area covered with black material to prevent light from the monitor being detected. The subject was seated in a comfortable position in a dark quiet room.

A relatively short total collection time was required to see a response in a 40 second block. Therefore a total collection time of 300 ms was used for each wavelength. This was measured over 15 blocks of 20 ms as described in Section 7.1. This resulted in a total collection time of 3.5 seconds for all eight wavelengths after the switching time of the light source is accounted for.

7.6 Results

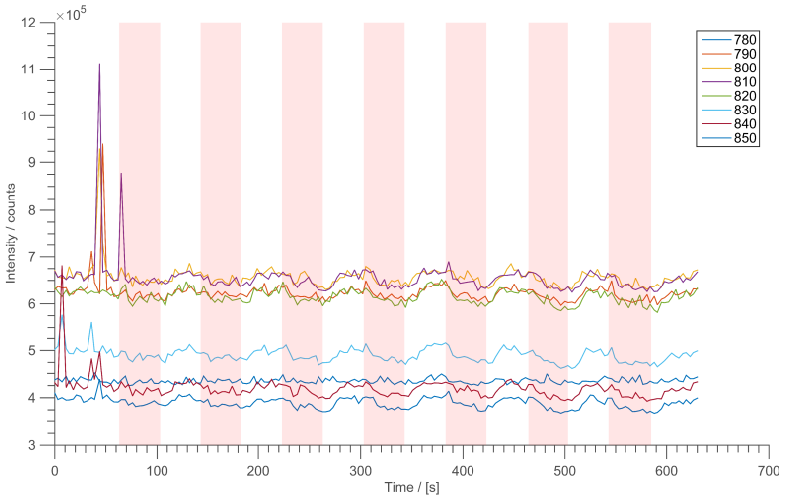

FIGURE 7.23: Intensity of measured photons during the visual stimulation experiment. Visual stimulus occurred for 40 seconds during the shaded period with 40 seconds of rest in between.

The intensity of light detected for each wavelength during the visual stimulation is shown in Figure 7.23. The stimulation period is indicated by a shaded region and the rest periods are unshaded. There is significant noise generated in the initial baseline period which is due to electrical noise in the system, however, this is shown to not affect any other data type. If these anomalous data points are ignored, the intensities measured range from

4×10^5 to 6.8×10^5. An average increase of 4%±2% is seen during visual stimulation blocks.

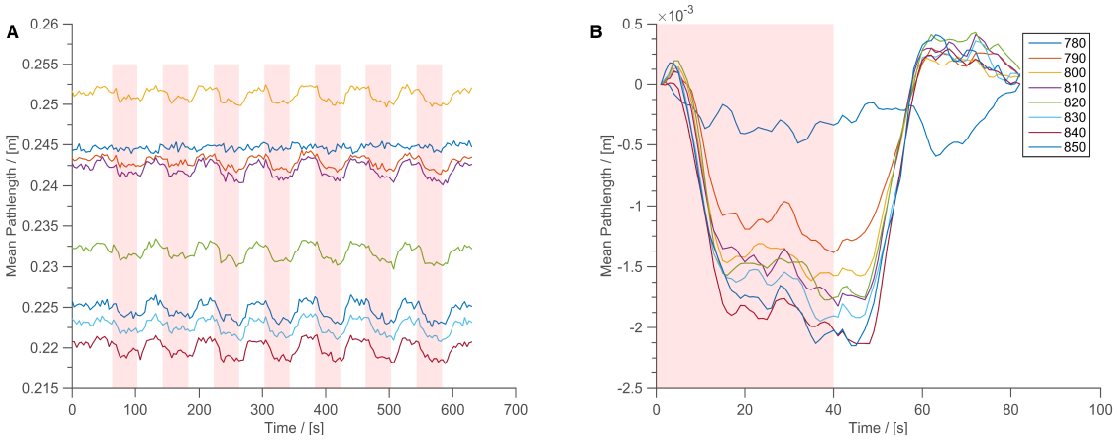

FIGURE 7.24: Mean pathlength of light over the occipital lobe during a visual stimulation experiment. (A) shows the mean pathlength over the entire measurement, while (B) shows an averaged stimulation and rest block. The visual stimulation occurs during the shaded region.

The changes of the mean pathlength of light in the head during a visual stimulation protocol are shown in Figure 7.24. 7.24(A) shows the absolute mean pathlength for each wavelength during the entire measurement, and 7.24(B) shows the protocol averaged over the seven blocks. These measurements clearly show a consistent change in pathlength during the visual stimulation. The pathlength generally decreases during the stimulus with a mean decrease of 1.4 mm±0.4 mm, corresponding to a differential pathlength factor decrease of 0.04. The pathlength of the 760 nm wavelength does not follow the same trend of the other wavelengths. This is most likely due to the fact that the absorption of light by deoxyhaemoglobin dominates at this wavelength, and a small decrease in the concentration of this chromophore will outweigh a larger increase in oxyhaemoglobin concentration.

Figure 7.25 shows the calculated values for the coefficients of absorption and scattering for the visual stimulation experiment. Figure 7.25(A) and (B) show the absolute values of μ_a and μ_s' for the entire measurement, and 7.25(C) and (D) show the changes of μ_a and μ_s' averaged over all stimulus blocks. The values of μ_a and μ_s' were calculated

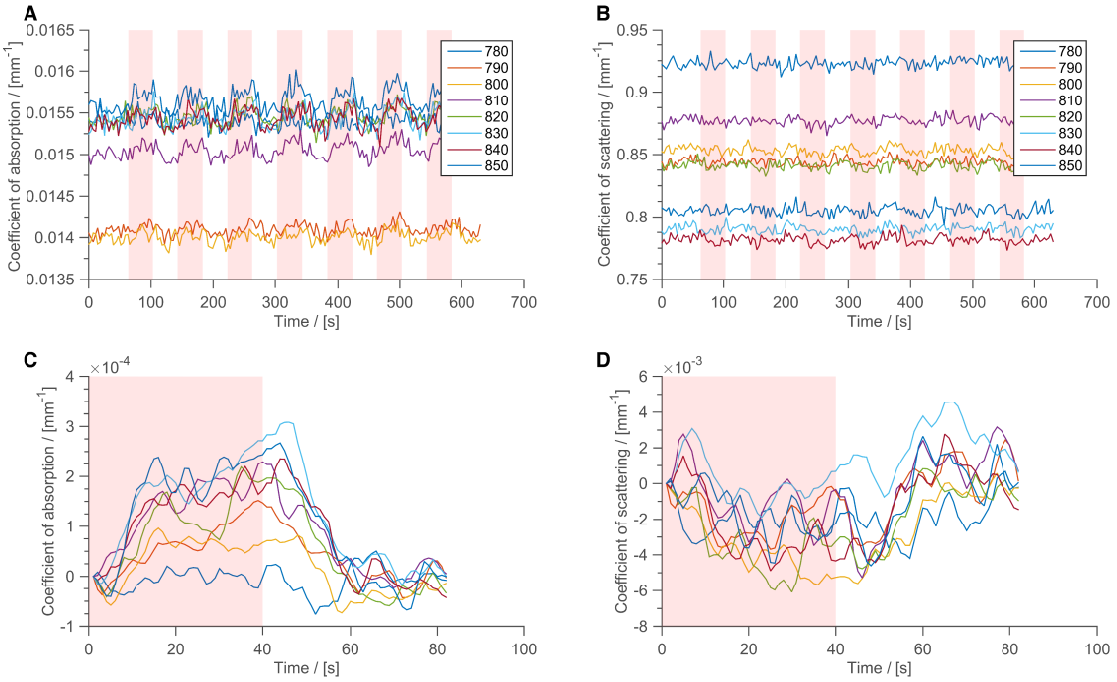

FIGURE 7.25: Coefficient of (A) absorption (μ_a) and (B) scattering (μ_s') for all wavelengths during the entire visual stimulation experiment. (C) and (D) show the change in μ_a and μ_s', respectively, averaged over each block and zeroed from the first point. The visual stimulation occurs during the shaded region.

by fitting the Green's function solution to the measured TPSFs. This is seen to be a consistent method, with little crosstalk between the coefficients and stability in regards to the initial estimation of μ_a and μ_s'. During the visual stimulus a general increase in values of μ_a is seen, with the maximum increase at 830 nm of 0.003 mm^{-1}.

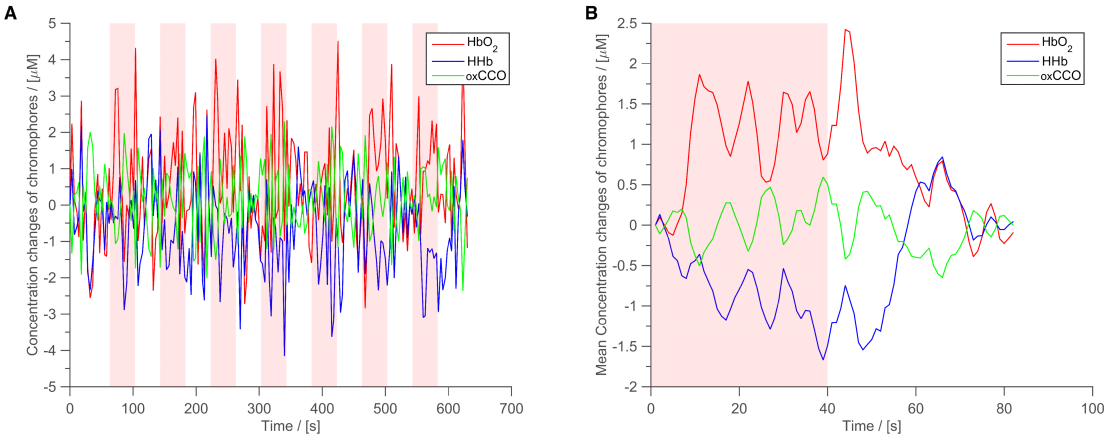

FIGURE 7.26: (A) Change in concentration of oxyhaemoglobin, deoxyhaemoglobin and oxidised cytochrome c oxidase; (B) Mean changes in chromophore concentrations averaged over 7 stimulus blocks. The visual stimulation occurs during the shaded region.

The concentration changes of deoxyhaemoglobin, oxyhaemoglobin, and oxidised cyctochrome c oxidase over the course of the experiment are shown in Figure 7.26(A). The averaged block of visual stimulus and rest period is shown in Figure 7.26(B). Both plots show considerable noise on all concentration changes, however, the averaged block clearly shows an increase in HbO_2 and a decrease in HHb during the stimulus. The averaged blocks, however, do not show any significant changes in oxCCO over the stimulation block. If the stimulus and rest blocks are heavily filtered, a small rise and fall, respectively, can be seen, which is expected according to the literature. However, the signal to noise ratio is too low to confirm these results.

7.7 Discussion

This preliminary study shows the measurement of haemodynamic changes that occur in the visual cortex during a visual stimulus. The results show a small but measurable increase and decrease in HbO_2 and HHb , respectively. There is also a very small but clear change in optical pathlength during the stimulus. The literature suggests that there is also a change in oxCCO, however, during this measurement, this finding could not be replicated. The most likely reason for this is the high noise level in the concentration changes. As the concentration of cytochrome c oxidase is an order of magnitude lower than haemoglobin, a change in the absorption spectrum due to oxCCO can be dominated by other signals. A different approach to the data analysis could be taken to try and improve on the sensitivity to changes in the cortex. For example, several groups have investigated the use of layered models for data analysis, which could be adapted for use with data from this system [128, 129, 135, 161]. Furthermore, the choice of wavelengths used in the measurement could also be used to help improve the calculation of oxCCO; Arifler et al. show that specific combinations of wavelengths can be used to improve the accuracy of oxCCO concentration [3].

Chapter 8

Discussion

In this chapter a brief summary of the work is given, highlighting the key development aspects of the system and the novel elements to the design. A review of the system's performance and experimental phantom and in vivo studies are discussed. Finally, future work to be carried out is discussed, and suggestions for improvements and upgrades are made.

8.1 Instrument

The major goal of this PhD was to develop a novel, multiwavelength, time resolved near infrared spectrometer for measuring the absorption and scattering of light in tissue. This would allow the absolute concentrations of individual chromophores in tissue to be determined, and the pathlength in tissue at multiple wavelengths in the near infrared region to be measured. An important requirement for the system, and one of the significant challenges, is the ability to measure more than 8 wavelengths simultaneously over different areas of the brain, enabling the functional measurements of haemodynamic and metabolism changes. The system was also required to be portable and allow movement around a clinical environment with a reasonable warm up time.

8.1.1 System summary

The multiwavelength time resolved near infrared spectrometer design was based on the use of a supercontiuum laser to output a broadband spectrum, which can be filtered into narrowband light for use in spectroscopic measurements. A Fianium SC480 6W supercontinuum laser is used with two Gooch and Housego acousto-optic tunable filters (AOTF) as a multiwavelength light source. Using these two components together results in a source that produces wavelength selectable, picosend pulses of light with a repetition rate of 60 MHz and a bandwidth of 2-4 nm in the near infrared region (650-1000 nm). The two sources are individually controllable, and optical fibres deliver the light to the subject which are held in place by custom designed 3D printed flexible optode holders.

The detection of light is performed by four Hamamatsu photomultiplier tubes (PMTs) which are protected from overexposure by custom built variable optical attenuators. The arrival time of the photons is measured by a Becker and Hickl time correlated single photon counting card. I have written software to control the entire system, focusing on speed of acquisition and reduction of dead time in the measurement due to computational processes.

8.2 Performance

The performance of individual electronics in the system is evaluated in Chapter 4 and the system as a whole is discussed in Chapter 6. The most significant specifications, performance, and sources of errors are reviewed here.

8.2.1 Light source

The Fianium supercontinuum laser has an optical range of 400-2600 nm. The laser has good temporal stability over long periods of time after a 1 hour warm up period, with

the output intensity only varying by a maximum of $\pm$3% over 15 hours. At the ends of the two source fibres an output power of up to 4mW is achievable. The wavelength of light can be individually selected, and the output power reduced using the software. The AOTFs allow fast switching of up to 16 wavelengths in the near infrared region.

It is worth noting that, while the AOTF are vibration isolated, during the course of this study the internal optics became misaligned for no obvious reason. This may be a concern in the future if the system is required to be transported, and should therefore be taken into consideration. The task of refocusing the optics is not trivial and may take days to achieve. A possible solution is to change the wheels on the system to provide an extra element of 'suspension' for the optics.

The bandwidth of light measured was slightly higher than the manufacturer specifications of 2-3 nm between 600-1000 mn, with a full-width half maximum of 4.4 nm at 890nm observed. Section 4.2.2 shows the full range of bandwidths of light. While this is not ideal, it satisfied the required system specifications of $<$5 nm which is needed for accurate chromophore concentration calculations.

8.2.2 Photon detection

The system uses four Hamamatsu photomultiplier tubes (PMTs) to detect the arrival of photons and generate an amplified electrical pulse for the timing measurement. The PMT has a peak sensitivity at 800 nm and a usable range of between 400-880 nm. The PMT can detect photons at slightly longer wavelengths, however, the quantum efficiency of the cathode is too low for wavelengths above 880 nm resulting in a low signal to noise of the measurements. This is a current limitation of the system; a greater wavelength range would prove advantageous for the measurements of the cytochrome c oxidase and water concentration [3, 162]. A possible solution to this is discussed in Section 8.3.

8.2.3 Timing electronics

The precise timing of photon time-of-flights is achieved by a Becker and Hickl SPC-130-EM time correlated single photon counting card. This card has a timing resolution of 4 ps and can measure up to 64 temporal point spread functions from four input channels simultaneously. A good temporal stability is seen in the system with a mean error of ± 6 ps over all wavelengths and no drift occurring over time. Phantom measurements show that the absorption and scattering can be accurately resolved with an error of 5%.

8.2.4 In vivo studies

Baseline measurements were made on the arm and forehead of five and ten healthy volunteers, in order to resolve absolute concentrations of oxyhaemoglobin and deoxyhaemoglobin in tissue. An arterial cuff occlusion shows the measurement of haemodynamic changes and reduction in cellular metabolism. Finally, a preliminary visual cortex measurement showed that the optical pathlength and change in absorption can be detected due to visual stimulus.

8.3 Future system upgrades

In the near future, I do not foresee any need to change the light source in the system, as the current laser produces sufficient optical power and is found to have good stability over time. The flexibility of the AOTF means that many different wavelength configurations can be tested, and has a range greater than the detectors at this time. The possible need for a different light source may arise if a significantly smaller device was needed. Laser diodes would provide the compactness required, but would lack the flexibility of the current configuration.

The main limitation of the system is the quantum efficiency of the photomultiplier tubes at longer wavelengths around 900 nm. Other detectors, such as single photon avalanche diodes (SPADs), could replace or be used in addition to the PMTs to provide a greater wavelength range of measurement. The disadvantages of a SPAD over a PMT is a smaller detection area and a greater transit time spread. If the system changes to incorporate a hybrid detection configuration, the appropriate detector could be used for different measurements. This upgrade could be relatively easily achieved as there is space in the detection rack to accommodate additional detectors.

The variable optical attenuators used in the system provide variable optical density up to 3.7 OD. Unfortunately the optical density does not increase linearly over this range. This is not a significant problem with the system, as the source-detector separations do not change during measurements. The high dynamic range needed in imaging systems is therefore not required. A better design was shown by Cooper et al., where the optical discs are made using transparent film and and inkjet printers [57]. This could be relatively easily implemented in the current system with little need for modifications if a better dynamic range is required.

A practical change which would increase the ergonomics of a measurement would be to used fibre optics with right angle connectors. The straight end fibres are not very easy to secure on the subjects due to the weight of the fibre pulling on the optode holder. This is currently prevented by taping the fibre onto the shoulder of the volunteer. As this would not be possible in a clinical measurement, right angle fibres offer a better solution.

8.4 Future work

The results from phantom studies, in vivo measurements on tissue and preliminary visual cortex measurements show that the multiwavelength time resolved system is capable of

reaching a high level of accuracy when measuring the optical properties of tissue. The system could be used in many studies for measuring absorption and scattering of light from which the concentrations of individual chromophores such as oxy-, deoxyhaemoglobin and cytochrome c oxidase can be determined.

The system uses up to 16 wavelengths in order to measure changes in CCO as well as HbO_2 and HHb , however in order to streamline the data collection process and instrumentation needed. Further work into the optimum and minimum number of wavelengths would enable much smaller systems to be produced and enable a much greater impact by creating real-time bedside monitoring.

This can provide valuable insight into the current health of the tissue region of interest, using a relatively inexpensive and portable piece of equipment that could be used at the bedside. Furthermore, improvements to the speed and methods applied when performing the data analysis could facilitate the measurements of these quantities in real time, progressing the field of near infrared spectroscopy by providing a safe, non-invasive diagnostic tool.

Appendix A

Publications and presentations

November 2012 *Poster Presentation*

Functional Near Infrared Spectroscopy, UCL, UK

"Development of a new fNIRS multi-wavelength, multi-channel time resolved spectrometer using a supercontinuum laser for measuring brain tissue haemodynamics and metabolism"

June 2013 *Oral Presentation*

International Society of Oxygen Transport to Tissue (ISOTT), Dartmouth, USA

"New time resolved system to measure cerebral metabolism and haemodynamics using multi-wavelength NIRS"

July 2013 *Oral Presentation*

PG Biomed 13, University of Surrey, UK

"Measuring cerebral metabolism and haemodynamics using multi-wavelength NIRS"

2014 *Paper*

"Development of a near infrared multi-wavelength, multi-channel, time-resolved spectrometer for measuring brain tissue haemodynamics and metabolism"

L. Dunne, J. Hebden, I. Tachtsidis

Advances in Experimental Medicine and Biology, 812, 181-186, (2014)

June 2014 *Poster Presentation*

Optical Society of America (OSA), Miami, USA

"Supercontinuum multiwavelength multi-channel time resolved near infrared spectrometer"

October 2014 *Poster Presentation*

fNIRS, Montreal, Canada

"Investigation of time gated methods to control depth sensitivity in fNIRS time resolved data"

October 2014 *Oral Presentation*

British Medical Laser Association, Brighton, UK

"Measurement of absorption and scattering of light in tissue using time resolved spectroscopy"

In preparation *Paper*

"Investigation of time gated methods to quantify depth sensitivity in fNIRS time resolved data"

Development of a Near Infrared Multi-Wavelength, Multi-channel, Time-Resolved Spectrometer for Measuring Brain Tissue Haemodynamics and Metabolism

Luke Dunne, Jem Hebden, Ilias Tachtsidis

Department of Medical Physics & Bioengineering, Malet Place Eng. Building, University College London, Gower Street, London, WC1E 6BT, UK

Abstract We present a novel time domain functional near infrared spectroscopy system using a supercontinuum laser allowing us to measure the coefficient of absorption and scattering of up to 16 multiplexed wavelengths in the near infrared region. This is a 4 detector system that generates up to 3mW of light for each wavelength with a narrow 2-3nm FWHM bandwidth between 650-890nm; each measurement of 16 wavelengths per channel can be performed up to a rate of 1Hz. We can therefore quantify absolute haemoglobin changes in tissue and are currently investigating which and how many wavelengths are needed to resolve additional chromophores in tissue, such as water and the oxidation state of cytochrome-c-oxidase.

1 Introduction

Near infrared spectroscopy (NIRS) is commonly used for non-invasive measurements of the concentration changes of oxyhaemoglobin (HbO_2) and deoxyhaemoglobin (HHb) in tissue. Typically, continuous wave (CW) systems are used where a reflected/transmitted change in light attenuation through tissue is measured. If the scattering of light in the tissue is assumed constant and the differential path length factor estimated, the modified Beer-Lambert law can be used to calculate changes in chromophore concentrations [1]. CW systems have the benefit of requiring relatively simple and inexpensive components, and can be made into easy to use compact devices.

Time-resolved spectroscopy operates by pulsing short picosecond pulses of light into the tissue through optical fibres. Fast single photon detectors and highly accurate timing electronics are then used to measure the time-of-flight (TOF) of each photon escaping the tissue surface. By repeating this TOF measurement

many times a histogram called a temporal point spread function (TPSF) can be generated. We can obtain much more detailed information about the tissue from the TPSF than is possible using a CW technique, including mean path length and the absolute absorption and scattering coefficients [2].

Advances in technology have reduced the cost and size of the timing electronics needed for TOF measurements, making the technique reasonably accessible. Time-resolved systems are therefore becoming increasingly popular for tissue diagnostics.

In addition to haemoglobin, cytochrome-c-oxidase (CCO) the terminal electron accepter of the respiratory chain is a strong absorber of near infrared light [3]. The absorption spectrum of CCO depends on whether the enzyme is in its oxidised or reduced state; NIRS utilises this to measure the changes in its oxidation state (oxCCO). Although there is a clear optical signature in the difference between the reduced and oxidised forms of CCO, the measurement of oxCCO is considerably more difficult than haemoglobin as the concentration in tissue is of an order of magnitude less [4]. Therefore, in order to decouple the haemoglobin and oxCCO changes accurately it is necessary to enhance the spectroscopic resolution of the NIRS system and measure independently absorption and scattering in many wavelengths [5]. CW broadband [6] and recently hybrid broadband and frequency domain systems have been used to measure oxCCO [7]. Zhu and colleagues using computational techniques and data from a CW broadband system during severe hypoxic-ischaemia in piglets have found that not only is the number of wavelengths important but there is significant improvement in the estimation of chromophores if specific combinations of wavelengths are used [8].

In order to address these issues we have designed and built a near infrared time domain multiwavelength spectrometer using a supercontinuum laser source. This enables us to measure the coefficient of absorption (μ_a) and the reduced coefficient of scattering (μ_s') for 16 wavelengths between 650 and 890nm. Here we describe the hardware of the system, discuss the theory of operation and present some preliminary results from the use of the system to monitor haemodynamic changes in the muscle during an arm cuff occlusion experiment.

2 Instrumentation and Methods

A custom designed supercontinuum laser (SC-480-6, Fianium, UK) with a repetition rate of 60 MHz producing white light over a range of 400nm to 2100nm is used. The light is passed via optical fibre into a dual acoustic optic tunable filter (AOTF) system. As seen in fig. 1, the light is collimated in free space and split by a polarising beam splitter. These beams are then passed through two AOTFs mounted at right angles to each other. As the devices only filter light in one plane this is the most efficient way of maximising the output power. The filters consist of piezo-electric transducers bonded to a birefringent quartz crystal that create a

standing wave at a driven frequency. This modulates the refractive index of the crystal creating a phase grating, splitting the light from the laser into its different diffraction orders. A desired frequency can thus be directed and focused into an optical fibre. Custom AOTFs are used in the system to give narrow band filtered light of 2-3nm FWHM in the region of 600nm to 1100nm, these can provide an output power of 3mW per wavelength.

For spectroscopy of tissue, each wavelength is multiplexed so that the TPSFs are averaged over the total desired measurement duration. The AOTF fast switches between 16 wavelengths at 160Hz allowing time domain measurements with any combination of wavelengths between 650-890nm. Two source fibres are used simultaneously when the detectors are placed on either hemisphere of the adult head. The light is passed into a 70μm high NA single fibre which is attached to the patient via a custom designed 3D printed optode holder (fig. 2d).

The light is collected by 4 glass fibre bundles (Loptek) with a diameter of 3mm and is passed through custom made variable optical attenuators (VOAs) with a range of 0-3.7OD to 4 Hamamatsu H7442-50P photomultiplier tube (PMT) modules. As the PMTs have a high gain the VOAs protect against over exposure during the experiment increasing the dynamic range. The signal from the PMTs is passed through a 4 way router (HRT-41) and the arrival time of each photon is measured with a Becker and Hickl SPC-130-EM time correlated single photon counting card.

The TSPF obtained in time resolved measurements contains information not only from the tissue but also the instrument itself. Therefore, a correction has to be made before the true optical properties of the tissue can be obtained. An instrument response function (IRF, fig. 2a) is recorded before each measurement using neutral density filters (fig. 2c) in order to characterise the factors which contribute towards the broadening of the IRF (laser pulse, optical fibres, photon detectors, and timing electronics).

In order to quantify the optical properties of the tissue, the solution to the diffusion equation for a semi-infinite homogenous medium was convolved with the IRF (fig. 2b) [9]. The convolved model is fitted to the measured TPSF using a non-linear curve fitting function and the absorption coefficient, μ_a and reduced scattering coefficient, μ_s' obtained. The Beer-Lambert law was then used to calculate chromophore concentrations [10]. To test the hardware and theory of operation we performed an arterial cuff-occlusion on the upper arm in one volunteer to induce flow and oxygenation changes in the forearm flexor muscles. The probe was placed on the forearm and measurements were done in reflection mode with source and detector fibres 3cm apart. After 100 seconds of baseline measurements we inflated the cuff at 200mmHg for 300 seconds, following cuff deflation we continue monitoring the muscle recovery for 5 minutes.

Data were collected every second for 8 common wavelengths used in near infrared spectroscopy [690 750 761 790 801 834 850 870]. The average count rate over the experiment was kept at over 10^6/s to provide a good enough SNR for

each wavelength. The diffusion equation model was then fitted to each TPSF to resolve absorption and scattering.

3 Results

Time series data for the changes in scattering and absorption for all 8 wavelengths are shown in fig. 3b and 3c, respectively. The standard deviation of the scattering and absorption during baseline was $0.0002mm^{-1}$. During the occlusion there were large changes in the absorption in some wavelengths, in particular there was a significant rise in absorption of 690nm (sensitive to HHb) and significant decreases in 870nm (sensitive to HbO_2). The scattering also demonstrated some hetereogeneous large changes and we are currently investigating whether these might be due to crosstalk or other factors. Finally, the absorption data were fitted for HbO_2 and HHb, the baseline total haemoglobin was $84.8\pm0.3\mu Ml^{-1}$ and the absolute tissue saturation was 51.8±0.5%, comparable to previous studies in muscle [11]. Figure 3d shows the absolute concentration of oxyhaemoglobin and deoxyhaemoglobin during the study.

4 Conclusion

We have developed a four-channel NIR time-resolved spectrometer using a supercontinuum laser source and tunable narrow band filter system capable of measuring the TPSFs of 16 wavelengths between 650-890nm every second in order to quantify the scattering and absorption independently for tissue. This offers us the ability to extract changes in haemoglobin and other chromophores in tissue such as CCO. We have presented preliminary results of the operation of the system for one channel and 8 wavelengths during an arm cuff occlusion test. We are currently using the system to investigate wavelength selection optimisation for resolving HbO_2, HHb and oxCCO and will be carrying out a series of functional activation studies.

Acknowledgments The authors would like to thank The Wellcome Trust (088429/Z/09/Z) for the financial support of this work.

References

1. D. T. Delpy, et al. (1988) Estimation of optical pathlength through tissue from direct time of flight measurement. Physics in medicine and biology, 33:1433–42

2. D. T. Delpy (1997) Quantification in tissue near-infrared spectroscopy. Philosophical Transactions: Biological Sciences 352:649–659
3. J. Lee, et al. (2007) Non-invasive in vivo diffuse optical spectroscopy monitoring of cyanide poisoning in a rabbit model. Physiological measurement 28:1057–66
4. C. E. Cooper (1997) Measurement of cytochrome oxidase redox state by near infrared spectroscopy. Optical Imaging of Brain Function and Metabolism II:63–73
5. S. Matcher (1995) Performance comparison of several published tissue near-infrared spectroscopy algorithms. Analytical Biochemistry 227:54–68
6. M. Tisdall, et al. (2007) Near-infrared spectroscopic quantification of changes in the concentration of oxidized cytochrome c oxidase in the healthy human brain during hypoxemia. Journal of Biomedical Optics 12:024002
7. F. Bevilacqua, et al. (2000) Broadband absorption spectroscopy in turbid media by combined frequency-domain and steady-state methods. Applied optics 39:6498–507
8. T. Zhu, et al. (2012) Optimal Wavelength Combinations for Resolving in-vivo Changes of Haemoglobin and Cytochrome-c-oxidase Concentrations with NIRS. Biomedical Optics and 3D Imaging OSA
9. D. Contini, et al. (1997) Photon migration through a turbid slab described by a model based on diffusion approximation. I. Theory. Applied optics 36:4587–99
10. S. J. Matcher, et al. (1994) Use of the water absorption spectrum to quantify tissue chromophore concentration changes in near-infrared spectroscopy. Physics in medicine and biology 39:177–96
11. S. J. Matcher et al. (1994) Absolute quantification of deoxyhaemoglobin concentration in tissue near infrared spectroscopy. Physics in medicine and biology 39:1295–312

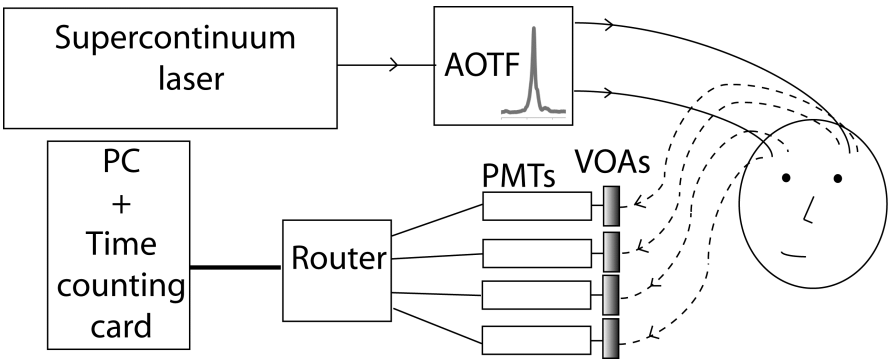

Fig. 1. Schematic of time resolved multiwavelength near infrared spectrometer. The light is tuned using acousto-optic tunable filters (AOTF) and detected with 4 photomultiplier tubes (PMTs) each protected by variable optical attenuators (VOAs).

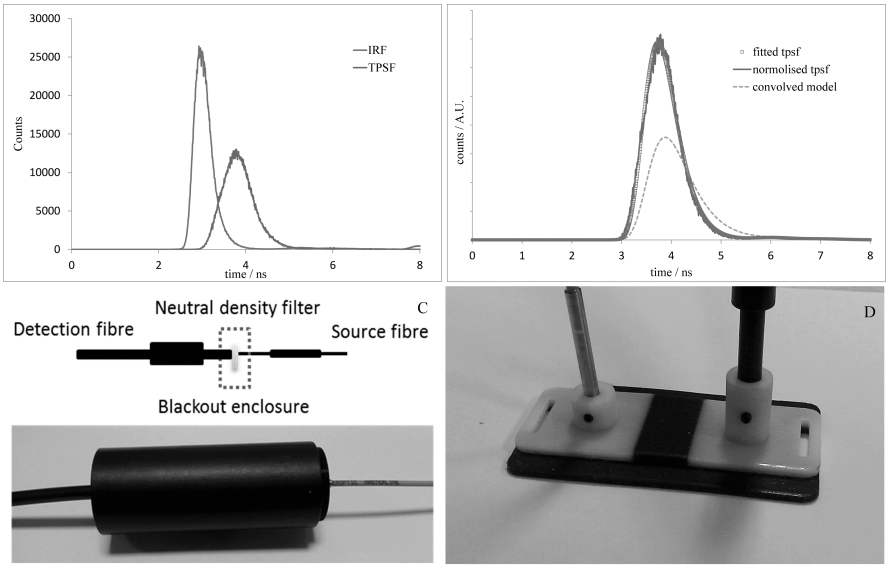

Fig. 2. (a) Raw TPSF(scaled) and IRF, (b) Theoretical model convolved with the IRF, the real TPSF and fitted curve using the lsqcurvefit function returning μ_a and μ_s' as 0.0224 and 1.0655 mm^{-1}. (c) Method of measuring IRF. (d) 3D printed optode holder.

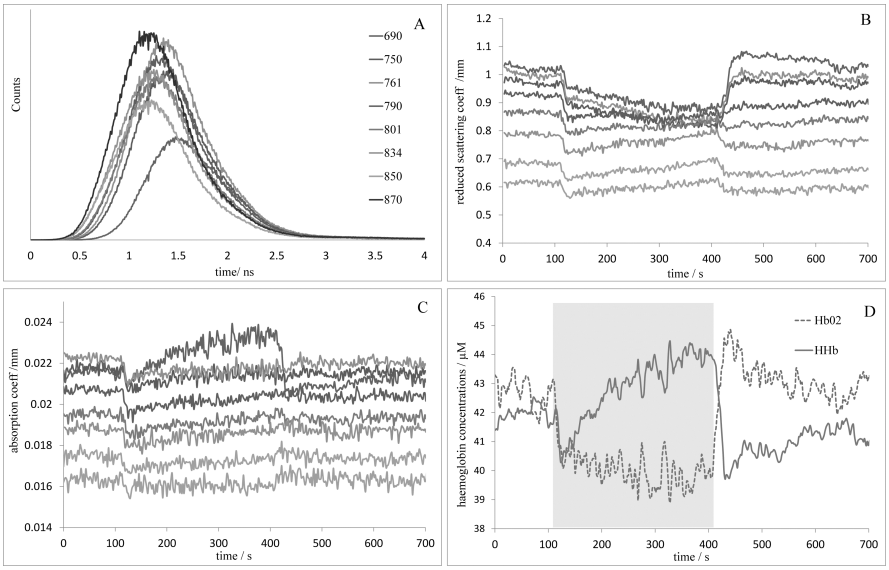

Fig. 3. (a) Example TPSFs for single measurement. (b) Reduced coffecient of scattering for 8 wavelengths over course of cuff occlusion. (c) Coffecient of absorption for 8 wavelengths over course of cuff occlusion. (d) Concentration changes for HbO_2 and HHb,with a cuff inflation time of 4 seconds.

Bibliography

[1] A Duncan, J H Meek, M Clemence, C E Elwell, L Tyszczuk, M Cope, and D T Delpy. Optical pathlength measurements on adult head, calf and forearm and the head of the newborn infant using phase resolved optical spectroscopy. *Physics in medicine and biology*, 40(2):295–304, 1995. ISSN 0031-9155. doi: 10.1088/0031-9155/40/2/007.

[2] Johannes D. Johansson. Spectroscopic method for determination of the absorption coefficient in brain tissue. *Journal of Biomedical Optics*, 15(5):057005, 2010. ISSN 10833668. doi: 10.1117/1.3495719.

[3] Dizem Arifler, Tingting Zhu, Sara Madaan, and Ilias Tachtsidis. Optimal wavelength combinations for near-infrared spectroscopic monitoring of changes in brain tissue hemoglobin and cytochrome c oxidase concentrations. *Biomedical Optics Express*, 6(3):933, 2015. ISSN 2156-7085. doi: 10.1364/BOE.6.000933. URL `http://www.opticsinfobase.org/abstract.cfm?URI=boe-6-3-933`.

[4] F. Jobsis. Noninvasive , Infrared Monitoring of Cerebral and Myocardial Oxygen Sufficiency and Circulatory Parameters. *Science*, 198(4323):1264–1267, 1977.

[5] M. Ferrari, I. Giannini, G. Sideri, and E Zanette. Continuous non invasive monitoring of human brain by near infrared spectroscopy. *Oxygen Transport to Tissue VII*, 191(7):873–882, 1985. doi: 10.1007/978-1-4684-3291-6. URL `http://www.springerlink.com/index/10.1007/978-1-4684-3291-6`.

[6] Jane E Brazy, V Lewis, H Mitnick, and F. Jobsis. Noninvasive Monitoring of Cerebral Oxygenation on Preterm Infants: Preliminary Observations. *Pediatrics*, 75(2):217–225, 1985.

[7] D T Delpy, M Cope, P van der Zee, S Arridge, S Wray, and J Wyatt. Estimation of optical pathlength through tissue from direct time of flight measurement. *Physics in medicine and biology*, 33(12):1433–42, dec 1988. ISSN 0031-9155. URL http://www.ncbi.nlm.nih.gov/pubmed/3237772.

[8] Marco Ferrari and Valentina Quaresima. A brief review on the history of human functional near-infrared spectroscopy (fNIRS) development and fields of application. *NeuroImage*, 63(2):921–35, nov 2012. ISSN 1095-9572. doi: 10.1016/j.neuroimage.2012.03.049. URL http://www.ncbi.nlm.nih.gov/pubmed/22510258.

[9] S. Lloyd-Fox, A. Blasi, and C. E. Elwell. Illuminating the developing brain: The past, present and future of functional near infrared spectroscopy. *Neuroscience and Biobehavioral Reviews*, 34(3):269–284, 2010. ISSN 01497634. doi: 10.1016/j.neubiorev.2009.07.008.

[10] Martin Wolf, Marco Ferrari, and Valentina Quaresima. Progress of near-infrared spectroscopy and topography for brain and muscle clinical applications. *Journal of biomedical optics*, 12(6):062104, 2011. ISSN 1083-3668. doi: 10.1117/1.2804899. URL http://www.ncbi.nlm.nih.gov/pubmed/18163807.

[11] S Lloyd-Fox, M Papademetriou, M K Darboe, N L Everdell, R Wegmuller, A M Prentice, S E Moore, and C E Elwell. Functional near infrared spectroscopy (fNIRS) to assess cognitive function in infants in rural Africa. *Scientific Reports*, 4: 4740, 2014. ISSN 2045-2322. doi: 10.1038/srep04740. URL http://www.ncbi.nlm.nih.gov/pubmed/24751935.

[12] Paul Beard. Biomedical photoacoustic imaging. *Interface focus*, 1 (4):602–31, 2011. ISSN 2042-8901. doi: 10.1098/rsfs.2011.0028. URL http://www.pubmedcentral.nih.gov/articlerender.fcgi?artid=3262268{&}tool=pmcentrez{&}rendertype=abstract.

[13] Felix Scholkmann, Stefan Kleiser, Andreas Jaakko Metz, Raphael Zimmermann, Juan Mata Pavia, Ursula Wolf, and Martin Wolf. A review on continuous wave functional near-infrared spectroscopy and imaging instrumentation and methodology. *NeuroImage*, 85:6–27, 2014. ISSN 10538119. doi: 10.1016/j.neuroimage.2013.05.004. URL http://dx.doi.org/10.1016/j.neuroimage.2013.05.004.

[14] Martini, Nath, and Bartholomew. *Fundamentals of Anatomy & Physiology: Pearson New International Edition*. Pearson Education, 2013. ISBN ISBN 9781292038872. URL https://www-dawsonera-com.libproxy.ucl.ac.uk/abstract/9781292038872.

[15] OpenStax. *Anatomy and Physiology*. OpenStax College, 2016. URL http://cnx.org/contents/14fb4ad7-39a1-4eee-ab6e-3ef2482e3e22@8.1.

[16] Larry W Swanson. Mapping the human brain: past, present, and future. *Trends Neuroscience*, 18:471–474, 1995.

[17] Lippincott. *Anatomy and Physiology*. Lippincott Williams & Wilkins, 2002. ISBN 1582551804. URL https://books.google.com/books?id=H8{_}z-XaS{_}d0C{&}pgis=1.

[18] Elaine Nicpon Marieb and Katja Hoehn. *Human Anatomy & Physiology*. Pearson Benjamin Cummings, 2007. ISBN 0321372948. URL https://books.google.com/books?hl=en{&}lr={&}id=x1uEB68iitwC{&}pgis=1.

[19] Lord Rayleigh. On the light from the sky, its polarization and colour. *Philos. Mag.*, 41:107–120, 1871.

[20] G Mie. Beiträge zur Optik trüber Medien speziell kollodialer Metallösungen. *Ann. Phys.*, 25:377–445, 1908.

[21] W F Cheong, S A Prahl, and A J Welch. A review of the optical properties of biological tissues, 1990.

[22] Wai-Fung Cheong, Scott A. Prahl, and Ashley J. Welch. A Review of the Optical Properties of Biological Tissues. *Journal of Quantum Electronics*, 26(12):2166–2185, 1990.

[23] D. T. Delpy and M Cope. Quantification in tissue near-infrared spectroscopy. *Philosophical Transactions: Biological Sciences*, 352(1354):649–659, 1997.

[24] Henry. McIlwain and H. S. Bachelard. *Biochemistry and the central nervous system*. Churchill Livingstone, 1972. URL `http://agris.fao.org/agris-search/search.do?recordID=US201300484341`.

[25] Linhong Kou, Daniel Labrie, and Petr Chylek. Refractive indices of water and ice in the 065- to 25-micrometer spectral range. *Applied Optics*, 32(19):3531, 1993. ISSN 0003-6935. doi: 10.1364/AO.32.003531. URL `https://www.osapublishing.org/ao/abstract.cfm?uri=ao-32-19-3531`.

[26] J M Conway, K H Norris, and C E Bodwell. A new approach for the estimation of body composition: infrared interactance. *The American journal of clinical nutrition*, 40(6):1123–30, dec 1984. ISSN 0002-9165. URL `http://www.ncbi.nlm.nih.gov/pubmed/6507337`.

[27] R van Veen, H. Sterenborg, A Pifferi, A. Torricelli, and R. Cubeddu. Determination of VIS- NIR absorption coefficients of mammalian fat, with time- and spatially resolved diffuse reflectance and transmission spectroscopy. In *Biomedical Topical Meeting*, page SF4, Washington, D.C., apr 2004. OSA. ISBN 1-55752-769-5. doi: 10.1364/BIO.2004.SF4. URL `http://www.osapublishing.org/abstract.cfm?uri=BIO-2004-SF4`.

[28] Mark Cope. *The Application of Near Infrared Spectroscopy to Non Invasive Monitoring of Cerebral Oxygenation in the Newborn Infant*. PhD thesis, UCL, 1991.

[29] G C Brown, M Crompton, and S Wray. Cytochrome oxidase content of rat brain during development. *Biochimica et biophysica acta*, 1057(2):273–5, mar 1991. ISSN 0006-3002. URL http://www.ncbi.nlm.nih.gov/pubmed/1849741.

[30] N Sato, B Hagihara, T Kamada, and H Abe. A Sensitive Method for the Quantitative Estimation of Cytochromes a and a3 in Tissues. *Analytical Biochemistry*, 117: 105–117, 1976.

[31] S R Arridge, M Cope, and D T Delpy. The theoretical basis for the determination of optical pathlengths in tissue: temporal and frequency analysis. *Physics in medicine and biology*, 37(7):1531–60, jul 1992. ISSN 0031-9155. URL http://www.ncbi.nlm.nih.gov/pubmed/1631197.

[32] Hellmuth Obrig and Arno Villringer. Beyond the visible - Imaging the human brain with light. *Journal of Cerebral Blood Flow and Metabolism*, 23(1):1–18, 2003. ISSN 0271-678X. doi: 10.1097/01.WCB.0000043472.45775.29. URL http://dx.doi.org/10.1097/01.WCB.0000043472.45775.29$\delimiter"026E30F$nhttp://www.scopus.com/inward/record.url?eid=2-s2.0-0037215482{&}partnerID=tZOtx3y1.

[33] N. L. Everdell, a. P. Gibson, I. D. C. Tullis, T. Vaithianathan, J. C. Hebden, and D. T. Delpy. A frequency multiplexed near-infrared topography system for imaging functional activation in the brain. *Review of Scientific Instruments*, 76 (9):093705, 2005. ISSN 00346748. doi: 10.1063/1.2038567. URL http://scitation.aip.org/content/aip/journal/rsi/76/9/10.1063/1.2038567.

[34] Harsimrat Singh, Robert J. Cooper, Chuen Wai Lee, Laura Dempsey, Andrea Edwards, Sabrina Brigadoi, Dimitrios Airantzis, Nick Everdell, Andrew Michell,

David Holder, Jeremy C. Hebden, and Topun Austin. Mapping cortical haemodynamics during neonatal seizures using diffuse optical tomography: A case study. *NeuroImage: Clinical*, 5:256–265, 2014. ISSN 22131582. doi: 10.1016/j.nicl.2014.06.012. URL http://dx.doi.org/10.1016/j.nicl.2014.06.012.

[35] R. J. Cooper, Jeremy C. Hebden, H. O'Reilly, S. Mitra, A. W. Michell, N. L. Everdell, A. P. Gibson, and T. Austin. Transient haemodynamic events in neurologically compromised infants: A simultaneous EEG and diffuse optical imaging study. *NeuroImage*, 55(4):1610–1616, 2011. ISSN 10538119. doi: 10.1016/j.neuroimage.2011.01.022. URL http://dx.doi.org/10.1016/j.neuroimage.2011.01.022.

[36] Sarah Lloyd-Fox, Anna Blasi, Agnes Volein, Nick Everdell, Claire E. Elwell, and Mark H. Johnson. Social perception in infancy: A near infrared spectroscopy study. *Child Development*, 80(4):986–999, 2009. ISSN 00093920. doi: 10.1111/j.1467-8624.2009.01312.x.

[37] A Blasi, S Fox, N Everdell, a Volein, L Tucker, G Csibra, a P Gibson, J C Hebden, M H Johnson, and C E Elwell. Investigation of depth dependent changes in cerebral haemodynamics during face perception in infants. *Physics in medicine and biology*, 52(23):6849–6864, 2007. ISSN 0031-9155. doi: 10.1088/0031-9155/52/23/005.

[38] Sarah Lloyd-Fox, Anna Blasi, Nick Everdell, Clare E Elwell, and Mark H Johnson. Selective cortical mapping of biological motion processing in young infants. *Journal of cognitive neuroscience*, 23(9):2521–32, 2011. ISSN 1530-8898. doi: 10.1162/jocn.2010.21598. URL http://www.mitpressjournals.org/doi/abs/10.1162/jocn.2010.21598.

[39] N Everdell. Gowerlabs, 2016. URL www.gowerlabs.co.uk.

[40] Mamadou Diop, Jonathan T. Elliott, Kenneth M. Tichauer, Ting Yim Lee, and Keith St. Lawrence. A broadband continuous-wave multichannel near-infrared

system for measuring regional cerebral blood flow and oxygen consumption in newborn piglets. *Review of Scientific Instruments*, 80(5), 2009. ISSN 00346748. doi: 10.1063/1.3123347.

[41] Martin M Tisdall, Ilias Tachtsidis, Terence S Leung, Clare E Elwell, and Martin Smith. Near-infrared spectroscopic quantification of changes in the concentration of oxidized cytochrome c oxidase in the healthy human brain during hypoxemia. *Journal of biomedical optics*, 12(2):024002, 2007. ISSN 1083-3668. doi: 10.1117/1.2718541. URL http://www.ncbi.nlm.nih.gov/pubmed/17477717.

[42] Gemma Bale, Subhabrata Mitra, Judith Meek, and Nicola Robertson. A new broadband near-infrared spectroscopy system for in-vivo measurements of cerebral cytochrome-c-oxidase changes in neonatal brain injury. *Biomedical Optics Express*, 36(10):663–676, 2014. ISSN 21567085. doi: 10.1364/BOE.5.003450.

[43] Britton Chance, M. Cope, Enrico Gratton, Nirmala Ramanujam, and Bruce J Tromberg. Phase measurement of light absorption and scatter in human tissue. *Review of Scientific Instruments*, 69(10):3457–3481, 1998. ISSN 00346748. doi: 10.1063/1.1149123. URL http://link.aip.org/link/?RSINAK/69/3457/1.

[44] Joseph R. Lakowicz and Klaus Berndt. Frequency-domain measurements of photon migration in tissues. *Chemical Physics Letters*, 166(3):246–252, 1990. ISSN 00092614. doi: 10.1016/0009-2614(90)80024-8.

[45] B Chance, J S Leigh, H Miyake, D S Smith, S Nioka, R Greenfeld, M Finander, K Kaufmann, W Levy, and M Young. Comparison of time-resolved and -unresolved measurements of deoxyhemoglobin in brain. *Proceedings of the National Academy of Sciences of the United States of America*, 85(14):4971–4975, 1988. ISSN 0027-8424. doi: 10.1073/pnas.85.14.4971.

[46] Britton Chance, Shoko Nioka, Jane Kent, Kevin McCully, Michael Fountain, Robert Greenfeld, and Gary Holtom. Time-resolved spectroscopy of hemoglobin and

myoglobin in resting and ischemic muscle. *Analytical Biochemistry*, 174(2):698–707, 1988. ISSN 10960309. doi: 10.1016/0003-2697(88)90076-0.

[47] J Hebden, S Arridge, and D Delpy. Optical imaging in medicine .1. Experimental techniques. *Physics in Medicine and Biology*, 42:825–840, 1997. ISSN 0031-9155. doi: 10.1088/0031-9155/42/5/007. URL `http://discovery.ucl.ac.uk/179661/`.

[48] Florian E W Schmidt. *Development of a Time-Resolved Optical Tomography System for Neonatal Brain Imaging*. PhD thesis, UCL, 1999.

[49] M Essenpreis, C E Elwell, M Cope, P van der Zee, S R Arridge, and D T Delpy. Spectral dependence of temporal point spread functions in human tissues. *Applied optics*, 32(4):418–425, 1993. ISSN 0003-6935. doi: 10.1364/AO.32.000418.

[50] Wolfgang Becker, Axel Bergmann, Giovanni Biscotti, and Angelika Rück. Advanced time-correlated single photon counting technique for spectroscopy and imaging in biomedical systems. In *SPIE*, volume 5340, pages 1–9, 2004.

[51] Wolfgang Becker and Axel Bergmann. Detectors for high-speed photon counting. *Becker & Hickl GmbH Application Note*, pages 1–22, 2002. URL `http://scholar.google.com/scholar?hl=en{&}btnG=Search{&}q=intitle:Detectors+for+High-Speed+Photon+Counting{#}6`.

[52] Wolfgang Becker. *The bh TCSPC Handbook*. Becker and Hickl, 2010. URL `http://www.becker-hickl.de/handbook.htm`.

[53] Rinaldo Cubeddo. nEUROPt Report Summary disease by pulsed near infrared light). Technical report, Politecnico di Milano, 2012.

[54] Heidrun Wabnitz and Alexander Jelzow. Performance assessment of time-domain optical brain imagers: a multi-laboratory study. *Proc. SPIE*, 8583: 85830L–1 – 85830L–14, 2013. ISSN 16057422. doi: 10.1117/12.

2002438. URL http://proceedings.spiedigitallibrary.org/proceeding.aspx?articleid=1658718.

[55] Heidrun Wabnitz, Dieter Richard Taubert, Mikhail Mazurenka, Oliver Steinkellner, Alexander Jelzow, Rainer Macdonald, Daniel Milej, Piotr Sawosz, Michal Kacprzak, Adam Liebert, Robert Cooper, Jeremy Hebden, Antonio Pifferi, Andrea Farina, Ilaria Bargigia, Davide Contini, Matteo Caffini, Lucia Zucchelli, Lorenzo Spinelli, Rinaldo Cubeddu, and Alessandro Torricelli. Performance assessment of time-domain optical brain imagers, part 1: basic instrumental performance protocol. *Journal of biomedical optics*, 19(8):86010, aug 2014. ISSN 1560-2281. doi: 10.1117/1.JBO.19.8.086010. URL http://www.ncbi.nlm.nih.gov/pubmed/25121479.

[56] Heidrun Wabnitz, Alexander Jelzow, Mikhail Mazurenka, Oliver Steinkellner, Rainer Macdonald, Daniel Milej, Norbert Zolek, Michal Kacprzak, Piotr Sawosz, Roman Maniewski, Adam Liebert, Salavat Magazov, Jeremy Hebden, Fabrizio Martelli, Paola Di Ninni, Giovanni Zaccanti, Alessandro Torricelli, Davide Contini, Rebecca Re, Lucia Zucchelli, Lorenzo Spinelli, Rinaldo Cubeddu, and Antonio Pifferi. Performance assessment of time-domain optical brain imagers, part 2: nEUROPt protocol. *Journal of biomedical optics*, 19(8):86012, aug 2014. ISSN 1560-2281. doi: 10.1117/1.JBO.19.8.086012. URL http://www.ncbi.nlm.nih.gov/pubmed/25121480.

[57] Robert J Cooper, Elliott Magee, Nick Everdell, Salavat Magazov, Marta Varela, Dimitrios Airantzis, Adam P Gibson, and Jeremy C Hebden. MONSTIR II: a 32-channel, multispectral, time-resolved optical tomography system for neonatal brain imaging. *The Review of Scientific Instruments*, 85(5):053105, may 2014. ISSN 1089-7623. doi: 10.1063/1.4875593. URL http://www.ncbi.nlm.nih.gov/pubmed/24880351.

[58] Florian E. W. Schmidt, Martin E. Fry, Elizabeth M. C. Hillman, Jeremy C. Hebden, and David T. Delpy. A 32-channel time-resolved instrument for medical optical tomography. *Review of Scientific Instruments*, 71(1):256, 2000. ISSN 00346748. doi: 10.1063/1.1150191. URL http://scitation.aip.org/content/aip/journal/rsi/71/1/10.1063/1.1150191.

[59] Jeremy C Hebden, Adam Gibson, Rozarina Md Yusof, Nick Everdell, Elizabeth M C Hillman, David T Delpy, Simon R Arridge, Topun Austin, Judith H Meek, and John S Wyatt. Three-dimensional optical tomography of the premature infant brain. *Physics in medicine and biology*, 47(23):4155–66, dec 2002. ISSN 0031-9155. URL http://www.ncbi.nlm.nih.gov/pubmed/12502040.

[60] A. P. Gibson, T. Austin, N. L. Everdell, M. Schweiger, S. R. Arridge, J. H. Meek, J. S. Wyatt, D. T. Delpy, and J. C. Hebden. Three-dimensional whole-head optical tomography of passive motor evoked responses in the neonate. *NeuroImage*, 30 (2):521–528, 2006. ISSN 10538119. doi: 10.1016/j.neuroimage.2005.08.059.

[61] Jeremy C Hebden, Marta Varela, Salavat Magazov, Nick Everdell, Adam Gibson, and Topun Austin. Diffiuse optical imaging of the newborn infant brain. In *Proc. of 9th IEEE In- ternational Symposium, Biomedical Imaging: from Nano to Macro*, pages 503–505, 2012. ISBN 9781457718588.

[62] Davide Contini, Alessandro Torricelli, Antonio Pifferi, Lorenzo Spinelli, Floriano Paglia, and Rinaldo Cubeddu. Multi-channel time-resolved system for functional near infrared spectroscopy. *Optics express*, 14(12):5418–32, 2006. ISSN 1094-4087. doi: 10.1364/OE.14.005418. URL http://www.ncbi.nlm.nih.gov/pubmed/19516708.

[63] Rebecca Re, Davide Contini, Matteo Caffini, Rinaldo Cubeddu, Lorenzo Spinelli, and Alessandro Torricelli. A compact time-resolved system for near infrared spectroscopy based on wavelength space multiplexing. *The Review of scientific*

instruments, 81(11):113101, nov 2010. ISSN 1089-7623. doi: 10.1063/1.3495957. URL http://www.ncbi.nlm.nih.gov/pubmed/21133455.

[64] Federico Aletti, Rebecca Re, Vincenzo Pace, Davide Contini, Erika Molteni, Sergio Cerutti, Anna Maria Bianchi, Alessandro Torricelli, Lorenzo Spinelli, Rinaldo Cubeddu, and Giuseppe Baselli. Deep and surface hemodynamic signal from functional time resolved transcranial near infrared spectroscopy compared to skin flowmotion. *Computers in Biology and Medicine*, 42(3):282–289, 2012. ISSN 00104825. doi: 10.1016/j.compbiomed.2011.06.001. URL http://dx.doi.org/10.1016/j.compbiomed.2011.06.001.

[65] D. Contini, R. Re, M. Turola, L. Spinelli, G. Romano, R. Cubeddu, and A. Torricelli. Multi-channel time-resolved functional near infrared spectroscopy system. *SPIE*, 8578:857832, 2013. doi: 10.1117/12.2004967. URL http://proceedings.spiedigitallibrary.org/proceeding.aspx?doi=10.1117/12.2004967.

[66] Agathe Puszka, Laura Di Sieno, Alberto Dalla Mora, Antonio Pifferi, Davide Contini, Gianluca Boso, Alberto Tosi, Lionel Hervé, Anne Planat-Chrétien, Anne Koenig, and Jean-Marc Dinten. Time-resolved diffuse optical tomography using fast-gated single-photon avalanche diodes. *Biomedical optics express*, 4(8):1351–65, 2013. ISSN 2156-7085. doi: 10.1364/BOE.4.001351. URL http://www.pubmedcentral.nih.gov/articlerender.fcgi?artid=3756586{&}tool=pmcentrez{&}rendertype=abstract.

[67] Gianluca Boso, Alberto Dalla Mora, Adriano Della Frera, and Alberto Tosi. Fast-gating of single-photon avalanche diodes with 200 ps transitions and 30 ps timing jitter. *Sensors and Actuators, A: Physical*, 191:61–67, 2013. ISSN 09244247. doi: 10.1016/j.sna.2012.11.042. URL http://dx.doi.org/10.1016/j.sna.2012.11.042.

[68] Laura Di Sieno, Heidrun Wabnitz, Antonio Pifferi, Mikhail Mazurenka, Yoko Hoshi, Alberto Dalla Mora, Davide Contini, Gianluca Boso, Wolfgang Becker, Fabrizio Martelli, Alberto Tosi, Rainer Macdonald, Laura Di Sieno, Heidrun Wabnitz, Antonio Pifferi, Mikhail Mazurenka, and Yoko Hoshi. Characterization of a time-resolved non-contact scanning diffuse optical imaging system exploiting fast-gated SPAD detection. *Review of Scientific Instruments*, 87:025118, 2016. ISSN 0034-6748. doi: 10.1063/1.4944562. URL `http://dx.doi.org/10.1063/1.4944562`.

[69] M. Mazurenka, a. Jelzow, H. Wabnitz, D. Contini, L. Spinelli, a. Pifferi, R. Cubeddu, a. Dalla Mora, a. Tosi, F. Zappa, and R. Macdonald. Non-contact time-resolved diffuse reflectance imaging at null source-detector separation. *Optics Express*, 20 (1):283, 2012. ISSN 1094-4087. doi: 10.1364/OE.20.000283.

[70] M Mazurenka, L Di Sieno, G Boso, D Contini, a Pifferi, a Dalla Mora, a Tosi, H Wabnitz, and R Macdonald. Non-contact in vivo diffuse optical imaging using a time-gated scanning system. *Biomedical optics express*, 4(10):2257–68, 2013. ISSN 2156-7085. doi: 10.1364/BOE.4.002257. URL `http://www.pubmedcentral.nih.gov/articlerender.fcgi?artid=3799683{&}tool=pmcentrez{&}rendertype=abstract`.

[71] Juan Mata Pavia, Martin Wolf, and Edoardo Charbon. Single-photon avalanche diode imagers applied to near-infrared imaging. *IEEE Journal on Selected Topics in Quantum Electronics*, 20(6), 2014. ISSN 1077260X. doi: 10.1109/JSTQE.2014.2313983.

[72] Juliette Selb, Jonathan J Stott, Maria Angela Franceschini, a Gregory Sorensen, and David a Boas. Improved sensitivity to cerebral hemodynamics during brain activation with a time-gated optical system: analytical model and experimental validation. *Journal of biomedical optics*, 10(1):11013, 2005. ISSN 1083-3668. doi: 10.1117/1.1852553. URL `http://www.ncbi.nlm.nih.gov/pubmed/15847579`.

[73] Juliette Selb, Danny K Joseph, and David A Boas. Time-gated optical system for depth-resolved functional brain imaging. *Journal of biomedical optics*, 11 (4):044008, 2006. ISSN 1083-3668. doi: 10.1117/1.2337320. URL http://www.ncbi.nlm.nih.gov/pubmed/16965165.

[74] Juliette Selb, Bernhard B. Zimmermann, Mark Martino, Tyler Ogden, and David a. Boas. Functional brain imaging with a supercontinuum time-domain NIRS system. In Bruce J. Tromberg, Arjun G. Yodh, and Eva M. Sevick-Muraca, editors, *SPIE*, volume 8578, page 857807, 2013. ISBN 1617643513. doi: 10.1117/12.2005348. URL http://proceedings.spiedigitallibrary.org/proceeding.aspx?doi=10.1117/12.2005348.

[75] Juliette Selb, Bernhard Zimmermann, Mark Martino, and David Boas. Design of a Multi-Wavelength Time-Domain Imager Based on a Supercontinuum Laser. In *Biomedical Optics and 3-D Imaging*, page BSu3A.80, Washington, D.C., 2012. Osa. ISBN 978-1-55752-942-8. doi: 10.1364/BIOMED.2012.BSu3A.80. URL http://www.opticsinfobase.org/abstract.cfm?URI=BIOMED-2012-BSu3A.80.

[76] Motoki Oda, Etsuko Ohmae Yamaki, Hiroaki Suzuki, Toshihiko Suzuki, and Yamashita Yutaka. Tissue Oxygenation Measurements Using Near-infrared Time-resolved Spectroscopy. *J Jpn Coll Angiol*, 49:131–137, 2009.

[77] Motoki Oda, Yutaka Yamashita, Tetsuhisa Nakano, and Akihiro Suzuki. Near-infrared Time-Resolved Spectroscopy System for Tissue Oxygenation Monitor. In *SPIE*, volume 3597, pages 611–617, 1999.

[78] Babylux Project, 2016. URL http://www.babylux-project.eu/.

[79] R. N. Hall, G. E. Fenner, J. D. Kingsley, T. J. Soltys, and R. O. Carlson. Coherent light emission from GaAs junctions. *Physical Review Letters*, 9(9):366–368, 1962. ISSN 00319007. doi: 10.1103/PhysRevLett.9.366.

[80] R N Hall. Stimulated emission semiconductor devices, 1966.

[81] R Alfano and L Shapiro, S. Observation of self-phase modulation and small-scale filaments in crystals and glasses. *Physical Review Letters*, 24(11):592–594, 1970.

[82] W. Yu, R.R. Alfano, C.L. Sam, and R.J. Seymour. Spectral broadening of picosecond 1.06 μ pulse in KBr. *Optics Communications*, 14(3):344–347, 1975.

[83] W. Werncke, A. Lau, M. Pfeiffer, K. Lenz, H. J. Weigmann, and C. D. Thuy. An anomalous frequency broadening in water. *Optics Communications*, 4(6):413–415, 1972. ISSN 00304018. doi: 10.1016/0030-4018(72)90113-7.

[84] Paul B. Corkum and Claude Rolland. Femtosecond Continua Produced in Gases. *IEEE Journal of Quantum Electronics*, 25(12):2634–2639, 1989. ISSN 15581713. doi: 10.1109/3.40651.

[85] B P Stoicheff. Characteristics of stimulated Raman radiation generated by coherent light. *Phys Lett*, 7(3):7–9, 1963. ISSN 00319163. doi: 10.1016/0031-9163(63)90377-9.

[86] John M. Dudley, Goëry Genty, and Stéphane Coen. Supercontinuum generation in photonic crystal fiber. *Reviews of Modern Physics*, 78(4):1135–1184, 2006. ISSN 00346861. doi: 10.1103/RevModPhys.78.1135.

[87] R Alfano and S. L. Shapiro. Emission in the Region 4000 to 7000 Å Via Four-Photon Coupling in Glass. *Physical Review Letters*, 24(11):584–588, mar 1970. ISSN 0031-9007. doi: 10.1103/PhysRevLett.24.584. URL `http://journals.aps.org/prl/abstract/10.1103/PhysRevLett.24.584`.

[88] P. Weinberger. John Kerr and his effects found in 1877 and 1878. *Philosophical Magazine Letters*, 88(12):897–907, 2008. ISSN 0950-0839. doi: 10.1080/09500830802526604.

[89] Jamal T. Manassah, Robert R. Alfano, and Mustafa Mustafa. Spectral distribution of an ultrafast supercontinuum laser source. *Physics Letters A*, 107(7):305–309, 1985. ISSN 03759601. doi: 10.1016/0375-9601(85)90641-3.

[90] Stéphane Coen, Alvin Chau, Rainer Leonhardt, John D. Harvey, Jonathan C. Knight, William J. Wadsworth, and Philip St. J. Russell. Supercontinuum generation by stimulated Raman scattering and parametric four-wave mixing in photonic crystal fibers. *Journal of the Optical Society of America B*, 19(4): 753–764, 2002. ISSN 0740-3224. doi: 10.1364/JOSAB.19.000753. URL http://www.opticsinfobase.org/abstract.cfm?URI=josab-19-4-753.

[91] A Devine and A Grudinin. SUPERCONTINUUM SOURCES: An even brighter future awaits supercontinuum fiber lasers, 2013. URL http://www.laserfocusworld.com/articles/print/volume-49/issue-06/features/supercontinuum-sources--an-even-brighter-future-awaits-supercont.html.

[92] Patrice L. Baldeck and Robert R. Alfano. Intensity Effects on the Stimulated Four Photon Spectra Generated by Picosecond Pulses in Optical Fibers. *Journal of Lightwave Technology*, 5(12):1712–1715, 1987. ISSN 15582213. doi: 10.1109/JLT.1987.1075465.

[93] J C Knight, T a Birks, P S Russell, and D M Atkin. All-silica single-mode optical fiber with photonic crystal cladding: errata. *Optics letters*, 22(7):484–5, apr 1997. ISSN 0146-9592. URL http://www.ncbi.nlm.nih.gov/pubmed/18183242.

[94] Philip Russell. Photonic crystal fibers. *Science (New York, N.Y.)*, 299(5605): 358–62, jan 2003. ISSN 1095-9203. doi: 10.1126/science.1079280. URL http://www.ncbi.nlm.nih.gov/pubmed/12532007.

[95] NKT. Photonic crystal fibers, 2016. URL http://www.nktphotonics.com/technology/photonic-crystal-fibers/.

[96] Andrea Bassi, Andrea Farina, Cosimo D Andrea, Antonio Pifferi, Gianluca Valentini, and Rinaldo Cubeddu. system for diffuse optical spectroscopy. *Biomedical optics express*, 15(22):14482–14487, 2007.

[97] S E Harris and R W Wallace. Acousto-Optic Tunable Filter. *J. Opt. Soc. Am.*, 59 (6):744–747, 1969. doi: 10.1364/josa.59.000744. URL `http://dx.doi.org/10.1364/josa.59.000744`.

[98] I. C. Chang. Noncollinear acousto-optic filter with large angular aperture. *Applied Physics Letters*, 25(7):370–372, 1974. ISSN 00036951. doi: 10.1063/1.1655512.

[99] Ling Bei, Glenn I. Dennis, Heather M. Miller, Thomas W. Spaine, and Jon W. Carnahan. Acousto-optic tunable filters: Fundamentals and applications as applied to chemical analysis techniques. *Progress in Quantum Electronics*, 28(2):67–87, 2004. ISSN 00796727. doi: 10.1016/S0079-6727(03)00083-1.

[100] L. Austin and H. Starke. Ueber die Reflexion der Kathodenstrahlen und eine damit verbundene neue Erscheinung secundärer Emission. *Annalen der Physik*, 314(10):271–292, 1902. ISSN 00033804. doi: 10.1002/andp.19023141003. URL `http://doi.wiley.com/10.1002/andp.19023141003`.

[101] VK Zworykin, GA Morton, and L Malter. The secondary emission multiplier-a new electronic device. ... *of the Institute of Radio* ..., 24(3), 1936. URL `http://ieeexplore.ieee.org/xpls/abs{_}all.jsp?arnumber=1686095`.

[102] V.K. Zworykin and J.a. Rajchman. The Electrostatic Electron Multiplier. *Proceedings of the IRE*, 27(9):558–566, 1939. ISSN 0096-8390. doi: 10.1109/JRPROC.1939.228753.

[103] Hamamatsu Photonics. *Photomultiplier tubes*. Hamamatsu, 2006.

[104] Hamamatsu. Photosensor Modules, 2008.

[105] Hamamatsu Photonics. MCP (Microchannel plate) and MCP Assembly, 2016. ISSN 1098-6596.

[106] Massimo Ghioni, Angelo Gulinatti, Ivan Rech, Franco Zappa, and Sergio Cova. Progress in silicon single-photon avalanche diodes. *IEEE Journal on Selected Topics in Quantum Electronics*, 13(4):852–862, 2007. ISSN 1077260X. doi: 10.1109/JSTQE.2007.902088.

[107] A. Goetzberger, B. Mcdonald, R. H. Haitz, and R. M. Scarlett. Avalanche Effects in Silicon p - n Junctions. II. Structurally Perfect Junctions. *Journal of Applied Physics*, 34(6):1591–1600, 1963. ISSN 00218979. doi: 10.1063/1.1702640.

[108] S J Matcher, M Cope, and D T Delpy. Use of the water absorption spectrum to quantify tissue chromophore concentration changes in near-infrared spectroscopy. *Physics in medicine and biology*, 39(1):177–96, jan 1994. ISSN 0031-9155. URL http://www.ncbi.nlm.nih.gov/pubmed/7651995.

[109] Qing Zhao, Lorenzo Spinelli, Andrea Bassi, Gianluca Valentini, Davide Contini, Alessandro Torricelli, Rinaldo Cubeddu, Giovanni Zaccanti, Fabrizio Martelli, and Antonio Pifferi. Functional tomography using a time-gated ICCD camera. *Biomedical optics express*, 2(3):705–16, jan 2011. ISSN 2156-7085. doi: 10.1364/BOE.2.000705. URL http://www.pubmedcentral.nih.gov/articlerender.fcgi?artid=3047374{&}tool=pmcentrez{&}rendertype=abstract.

[110] Desmond O'Connor. *Time-correlated single photon counting*. Academic Press, 1984. ISBN 0323141447. URL https://books.google.com/books?hl=en{&}lr={&}id=ELQ0Mz6Rq1EC{&}pgis=1.

[111] Wolfgang Becker. *Advanced Time-Correlated Single Photon Counting Applications | Wolfgang Becker | Springer*. Springer International Publishing, 2015. URL http://www.springer.com/gb/book/9783319149288.

[112] Wolfgang Becker and Hickl. Routing Modules for Time-Correlated Single Photon Counting. In *Routing Modules for Time-Correlated Single Photon Counting*, volume 23, pages 1–20. Becker and Hickl, 2000.

[113] R Fenske, Du Näther, M Goossens, and Sd Smith. New light sources for time-correlated single-photon counting in commercially available spectrometers. In *Optics East 2006*, volume 6372, pages 1–10, 2006. doi: 10.1117/12.688421.

[114] Fabrizio Martelli, Paola Di Ninni, Giovanni Zaccanti, Davide Contini, Lorenzo Spinelli, Alessandro Torricelli, Rinaldo Cubeddu, Heidrun Wabnitz, Mikhail Mazurenka, Rainer Macdonald, Angelo Sassaroli, and Antonio Pifferi. Phantoms for diffuse optical imaging based on totally absorbing objects, part 2: experimental implementation. *Journal of biomedical optics*, 19(7):076011, jul 2014. ISSN 1560-2281. doi: 10.1117/1.JBO.19.7.076011. URL `http://www.ncbi.nlm.nih.gov/pubmed/25023415`.

[115] Alessandro Torricelli, Davide Contini, Antonio Pifferi, Matteo Caffini, Rebecca Re, Lucia Zucchelli, and Lorenzo Spinelli. Time domain functional NIRS imaging for human brain mapping. *NeuroImage*, 85:28–50, jan 2014. ISSN 1095-9572. doi: 10.1016/j.neuroimage.2013.05.106. URL `http://www.ncbi.nlm.nih.gov/pubmed/23747285`.

[116] Frank P. Bolin, Luther E. Preuss, Roy C. Taylor, and Robert J. Ference. Refractive index of some mammalian tissues using a fiber optic cladding method. *Applied Optics*, 28(12):2297–2303, 1989. ISSN 1530-6992. doi: 10.1021/nl201561u.

[117] Paolo Giacometti and Diamond Solomon G. Compliant head probe for positioning electroencephalography electrodes and near-infrared spectroscopy optodes. *J Biomed Opt*, 18(2):1–11, 2013. ISSN 1560-2281. doi: 10.1117/1.JBO.18. URL `http://www.ncbi.nlm.nih.gov/pubmed/24064948`.

[118] Martin Wolf, Marco Ferrari, and Valentina Quaresima. Progress of near-infrared spectroscopy and topography for brain and muscle clinical applications. *Journal of biomedical optics*, 12(6):062104, 2007. ISSN 1083-3668. doi: 10.1117/1.2804899.

[119] Carl Schubert, Mark C van Langeveld, and Larry a Donoso. Innovations in 3D printing: a 3D overview from optics to organs. *The British journal of ophthalmology*, 98(2):159–61, 2014. ISSN 1468-2079. doi: 10.1136/bjophthalmol-2013-304446. URL http://www.ncbi.nlm.nih.gov/pubmed/24288392.

[120] David K Jennions. *Time-Resolved Optical Tomography Instrumentation for Fast 3D Functional Imaging*. PhD thesis, UCL, 2008.

[121] Steven L Jacques and Lihong Wang. Monte Carlo Modeling of Light Transport in Tissues. In *Optical-Termal Response of Laser-Irradiated Tissue*, pages 73–100. Springer Netherlands, 1995. ISBN 978-90-481-8830-7. doi: 10.1007/978-90-481-8831-4. URL http://link.springer.com/10.1007/978-90-481-8831-4.

[122] Teedah Soonthornsaratoon. *Gradient-based methods for quantitative photoacoustic tomography*. PhD thesis, UCL, 2015.

[123] S R Arridge. Optical tomography in medical imaging. *Inverse Problems*, 15:41–93, 1999.

[124] D Contini, F Martelli, and G Zaccanti. Photon migration through a turbid slab described by a model based on diffusion approximation. I. Theory. *Applied optics*, 36(19):4587–99, 1997. ISSN 0003-6935. URL http://www.ncbi.nlm.nih.gov/pubmed/18259254.

[125] Michael S Patterson, B Chance, and B C Wilson. Time resolved reflectance and transmittance for the noninvasive measurement of tissue optical properties. *Applied Optics*, 28(12):2331–2336, 1989.

[126] Qianqian Fang and David A Boas. Monte Carlo simulation of photon migration in 3D turbid media accelerated by graphics processing units. *Biomedical optics express*, 17(22):20178–20190, 2009.

[127] Jeremy C. Hebden, Simon R. Arridge, and Martin Schweiger. Investigation of alternative data types for time-resolved optical tomography. In *Advances in Optical Imaging and Photon Migration*, page ATuC1, Washington, D.C., mar 1998. OSA. ISBN 1-55752-546-3. doi: 10.1364/AOIPM.1998.ATuC1. URL http://www.osapublishing.org/abstract.cfm?uri=AOIPM-1998-ATuC1.

[128] J Steinbrink, H Wabnitz, H Obrig, a Villringer, and H Rinneberg. Determining changes in NIR absorption using a layered model of the human head. *Physics in medicine and biology*, 46(3):879–896, 2001. ISSN 0031-9155. doi: 10.1088/0031-9155/46/3/320.

[129] Chie Sato, Miho Shimada, Yukari Tanikawa, and Yoko Hoshi. Estimating the absorption coefficient of the bottom layer in four-layered turbid mediums based on the time-domain depth sensitivity of near-infrared light reflectance. *Journal of biomedical optics*, 18(9):097005, sep 2013. ISSN 1560-2281. doi: 10.1117/1.JBO.18.9.097005. URL http://www.ncbi.nlm.nih.gov/pubmed/24057194.

[130] Sonny Gunadi, Terence S Leung, Clare E Elwell, and Ilias Tachtsidis. Spatial sensitivity and penetration depth of three cerebral oxygenation monitors. *Biomedical optics express*, 5(9):2896–912, sep 2014. ISSN 2156-7085. doi: 10.1364/BOE.5.002896. URL http://www.ncbi.nlm.nih.gov/pubmed/25401006.

[131] Donald W. Marquardt. An Algorithm for Least-Squares Estimation of Nonlinear Parameters. *Society for Industrial and Applied Mathematics*, 11(2):431–441, 1963.

[132] Erik Alerstam, Stefan Andersson-Engels, and Tomas Svensson. Improved accuracy in time-resolved diffuse reflectance spectroscopy. *Optics Express*, 16(14):10440–10454, aug 2008. ISSN 1864-0648. doi: 10.1002/jbio.200710025. URL http://www.ncbi.nlm.nih.gov/pubmed/19412969.

[133] Alexander Jelzow, Heidrun Wabnitz, Ilias Tachtsidis, Evgeniya Kirilina, Rüdiger Brühl, and Rainer Macdonald. Separation of superficial and cerebral hemodynamics using a single distance time-domain NIRS measurement. *Biomedical optics express*, 5(5):1465–82, may 2014. ISSN 2156-7085. doi: 10.1364/BOE.5.001465. URL http://www.pubmedcentral.nih.gov/articlerender.fcgi?artid=4026903{&}tool=pmcentrez{&}rendertype=abstract.

[134] Adam Liebert, Heidrun Wabnitz, Jens Steinbrink, Hellmuth Obrig, Michael Moller, Rainer Macdonald, Villringer, Arno, and Herbert Rinneberg. Time-resolved multidistance near-infrared spectroscopy of the adult head: intracerebral and extracerebral absorption changes from moments of distribution of times of flight of photons. *Applied optics*, 43(15):3037–3047, 2004.

[135] Lorenzo Spinelli, Fabrizio Martelli, Samuele Del Bianco, Antonio Pifferi, Alessandro Torricelli, Rinaldo Cubeddu, and Giovanni Zaccanti. Absorption and scattering perturbations in homogeneous and layered diffusive media probed by time-resolved reflectance at null source-detector separation. *Physical Review E*, 74(2):021919, aug 2006. ISSN 1539-3755. doi: 10.1103/PhysRevE.74.021919. URL http://link.aps.org/doi/10.1103/PhysRevE.74.021919.

[136] Davide Contini, Lorenzo Spinelli, Alessandro Torricelli, Antonio Pifferi, and Rinaldo Cubeddu. Novel method for depth-resolved brain functional imaging by time- domain NIRS. In *SPIE-OSA*, volume 6629, page 662908, 2007.

[137] W Cui, N Wang, and B Chance. Study of photon migration depths with time-resolved spectroscopy. *Optics letters*, 16(21):1632–4, nov 1991. ISSN 0146-9592. URL http://www.ncbi.nlm.nih.gov/pubmed/19784091.

[138] Amol V Patil, Javad Safaie, Hamid Abrishami Moghaddam, Fabrice Wallois, and Reinhard Grebe. Experimental investigation of NIRS spatial sensitivity. *Biomedical optics express*, 2(6):1478–93, jun 2011. ISSN 2156-7085. doi: 10.1364/BOE.2.001478. URL http://www.pubmedcentral.nih.gov/articlerender.fcgi?artid=3114217{&}tool=pmcentrez{&}rendertype=abstract.

[139] Jens Steinbrink. *Near-infrared spectroscopy-on the adult human head with picosecond resolution*. PhD thesis, Freien universitat Berlin, 2000.

[140] Bruno Montcel, Renee Chabrier, and Patrick Poulet. Detection of cortical activation with time-resolved diffuse optical methods. *Applied optics*, 44(10):1942–7, apr 2005. ISSN 0003-6935. URL http://www.ncbi.nlm.nih.gov/pubmed/15813530.

[141] H O Meyer. Dark Rate of a Photomultiplier at Cryogenic Temperatures. *Physics*, 47405:1–13, 2008. URL http://arxiv.org/abs/0805.0771.

[142] Adam Liebert, Heidrun Wabnitz, Dirk Grosenick, and Rainer Macdonald. Fiber dispersion in time domain measurements compromising the accuracy of determination of optical properties of strongly scattering media. *Journal of biomedical optics*, 8(3):512–516, 2003. ISSN 10833668. doi: 10.1117/1.1578088.

[143] M Firbank and D. T. Delpy. A design for a stable and reproducible phantom for use in near infra-red imaging and spectroscopy. *Physics in medicine and biology*, 847(6):847–853, 1993.

[144] Michael Firbank, Motoki Oda, and David Delpy. An improved design for a stable and reproducible phantom material for use in near-infrared spectroscopy and imaging. *Phys. Med. Biol.*, 40:955–961, 1995.

[145] G J Tearney, M E Brezinski, J F Southern, B E Bouma, M R Hee, and J G Fujimoto. Determination of the refractive index of highly scattering human tissue by optical coherence tomography. *Optics Letters*, 20(21):2258, 1995. ISSN 0146-9592. doi: 10.1364/OL.20.002258. URL https://www.osapublishing.org/ol/abstract.cfm?uri=ol-20-21-2258.

[146] Paola Taroni, Antonio Pifferi, Alessandro Torricelli, Daniela Comelli, and Rinaldo Cubeddu. In vivo absorption and scattering spectroscopy of biological tissues. *Photochemical & Photobiological Sciences*, 2(2):124, 2003. ISSN 1474-905X. doi: 10.1039/b209651j.

[147] Michael S Patterson, J David Moulton, Brian C Wilson, Klaus W Berndt, and Joseph R Lakowicz. Frequency-domain reflectance for the determination of the scattering and absorption properties of tissue. *Applied Optics*, 30(31):4474–4476, 1991. ISSN 0003-6935. doi: 10.1364/AO.30.004474. URL http://ao.osa.org/abstract.cfm?URI=ao-30-31-4474.

[148] M C Van Beekvelt, W N Colier, R Wevers, and B G Van Engelen. Performance of near-infrared spectroscopy in measuring local O(2) consumption and blood flow in skeletal muscle. *Journal of applied physiology*, 90(2):511–519, 2001. ISSN 8750-7587.

[149] R A De Blasi, M Cope, C Elwell, F Safoue, and M Ferrari. Noninvasive measurement of human forearm oxygen consumption by near infrared spectroscopy. *Eur J Appl Physiol Occup Physiol*, 67:20–25, 1993. ISSN 0301-5548. doi: 10.1186/ar4079. URL http://www.ncbi.nlm.nih.gov/entrez/query.fcgi?cmd=Retrieve{&}db=PubMed{&}dopt=Citation{&}list{_}uids=8375359.

[150] T Durduran, G Yu, C Zhou, G Lech, B Chance, and A G Yodh. Quantification of muscle oxygenation and flow of healthy volunteers during cuff occlusion of arm and leg flexor muscles and plantar flexion exercise. *Optical Tomography*

and Spectroscopy of Tissue V, 4955:447–453, 2003. ISSN 0277786X. doi: 10.1117/12.476880. URL {\T1\textless}GotoISI{\T1\textgreater}://WOS:000186054000050.

[151] A. Duncan, T. L. Whitlock, M. Cope, and D. T. Delpy. Measurement of changes in optical pathlength through human muscle during cuff occlusion on the arm. *Optics and Laser Technology*, 27(4):269–274, 1995. ISSN 00303992. doi: 10.1016/0030-3992(95)93756-H.

[152] S J Matcher, C E Elwell, Chris E Cooper, M. Cope, and David T. Delpy. Performance Comparison of Several Published Near-Infrared Spectroscopy Algorithms. *Analytical Biochemistry*, 227:54–68, 1995.

[153] C Honig, R Connett, and T Gayeski. O2 transport and its interaction with metabolism; a system view of aerobic capacity. *Medicine and science in sport and excercise*, 24(1):47–53, 1992.

[154] T Kato, A Kamei, S Takashima, and T Ozaki. Human visual cortical function during photic stimulation monitoring by means of near-infrared spectroscopy. *J Cereb Blood Flow Metab*, 13(3):516–20, 1993. ISSN 0271-678X. doi: 10.1038/jcbfm.1993.66. URL http://www.ncbi.nlm.nih.gov/pubmed/8478409.

[155] A. Villringer, J. Planck, C. Hock, L. Schleinkofer, and U. Dirnagl. Near infrared spectroscopy (NIRS): A new tool to study hemodynamic changes during activation of brain function in human adults. *Neuroscience Letters*, 154(1-2):101–104, 1993. ISSN 03043940. doi: 10.1016/0304-3940(93)90181-J.

[156] Kazumi Takahashi, S Ogata, Y Atsumi, R Yamamoto, S Shiotsuka, Atsushi Maki, Yuichi Yamashita, T Yamamoto, H Koizumi, H Hirasawa, and M Igawa. Activation of the visual cortex imaged by 24 channel near-infrared spectroscopy. *Journal of Biomedical Optics*, 5(1):93–96, 2000.

[157] Martin Wolf, Ursula Wolf, Vlad Toronov, Antonios Michalos, L.Adelina Paunescu, Jee Hyun Choi, and Enrico Gratton. Different Time Evolution of Oxyhemoglobin and Deoxyhemoglobin Concentration Changes in the Visual and Motor Cortices during Functional Stimulation: A Near-Infrared Spectroscopy Study. *NeuroImage*, 16(3):704–712, jul 2002. ISSN 10538119. doi: 10.1006/nimg.2002.1128. URL http://linkinghub.elsevier.com/retrieve/pii/S1053811902911286.

[158] H R Heekeren, M Kohl, H Obrig, R Wenzel, W von Pannwitz, S J Matcher, U Dirnagl, C E Cooper, and a Villringer. Noninvasive assessment of changes in cytochrome-c oxidase oxidation in human subjects during visual stimulation. *Journal of cerebral blood flow and metabolism : official journal of the International Society of Cerebral Blood Flow and Metabolism*, 19(6):592–603, jun 1999. ISSN 0271-678X. doi: 10.1097/00004647-199906000-00002. URL http://www.ncbi.nlm.nih.gov/pubmed/10366189.

[159] K Uludag, M Kohl, J Steinbrink, H Obrig, and a Villringer. Cross talk in the Lambert-Beer calculation for near-infrared wavelengths estimated by Monte Carlo simulations. *Journal of biomedical optics*, 7(1):51–9, 2002. ISSN 1083-3668. doi: 10.1117/1.1427048. URL http://www.ncbi.nlm.nih.gov/pubmed/11818012.

[160] Kâmil Uludag, Jens Steinbrink, Matthias Kohl-Bareis, Rüdiger Wenzel, Arno Villringer, and Hellmuth Obrig. Cytochrome-c-oxidase redox changes during visual stimulation measured by near-infrared spectroscopy cannot be explained by a mere cross talk artefact. *NeuroImage*, 22(1):109–19, may 2004. ISSN 1053-8119. doi: 10.1016/j.neuroimage.2003.09.053. URL http://www.ncbi.nlm.nih.gov/pubmed/15110001.

[161] Tsukasa Funane, Hirokazu Atsumori, Takusige Katura, Akiko N Obata, Hiroki Sato, Yukari Tanikawa, Eiji Okada, and Masashi Kiguchi. Quantitative evaluation of deep and shallow tissue layers' contribution to fNIRS signal using multi-distance

optodes and independent component analysis. *NeuroImage*, 85 Pt 1:150–65, jan 2014. ISSN 1095-9572. doi: 10.1016/j.neuroimage.2013.02.026. URL http://www.ncbi.nlm.nih.gov/pubmed/23439443.

[162] S J Matcher and C E Cooper. Absolute quantification of deoxyhaemoglobin concentration in tissue near infrared spectroscopy. *Physics in medicine and biology*, 39(8):1295–312, aug 1994. ISSN 0031-9155. URL http://www.ncbi.nlm.nih.gov/pubmed/15551568.